Roumen Kountchev · Rumen Mironov ·
Ivo Draganov · Roumiana Kountcheva ·
Kazumi Nakamatsu   *Editors*

New Approaches
for Multidimensional
Signal Processing

Proceedings of International Workshop,
NAMSP 2023

KES International

Springer

Smart Innovation, Systems and Technologies

Volume 385

Series Editors

Robert J. Howlett, KES International, Shoreham-by-Sea, UK

Lakhmi C. Jain, KES International, Shoreham-by-Sea, UK

The Smart Innovation, Systems and Technologies book series encompasses the topics of knowledge, intelligence, innovation and sustainability. The aim of the series is to make available a platform for the publication of books on all aspects of single and multi-disciplinary research on these themes in order to make the latest results available in a readily-accessible form. Volumes on interdisciplinary research combining two or more of these areas is particularly sought.

The series covers systems and paradigms that employ knowledge and intelligence in a broad sense. Its scope is systems having embedded knowledge and intelligence, which may be applied to the solution of world problems in industry, the environment and the community. It also focusses on the knowledge-transfer methodologies and innovation strategies employed to make this happen effectively. The combination of intelligent systems tools and a broad range of applications introduces a need for a synergy of disciplines from science, technology, business and the humanities. The series will include conference proceedings, edited collections, monographs, handbooks, reference books, and other relevant types of book in areas of science and technology where smart systems and technologies can offer innovative solutions.

High quality content is an essential feature for all book proposals accepted for the series. It is expected that editors of all accepted volumes will ensure that contributions are subjected to an appropriate level of reviewing process and adhere to KES quality principles.

Indexed by SCOPUS, EI Compendex, INSPEC, WTI Frankfurt eG, zbMATH, Japanese Science and Technology Agency (JST), SCImago, DBLP.

All books published in the series are submitted for consideration in Web of Science.

Roumen Kountchev · Rumen Mironov ·
Ivo Draganov · Roumiana Kountcheva ·
Kazumi Nakamatsu

Editors

New Approaches for Multidimensional Signal Processing

Proceedings of International Workshop, NAMSP 2023

Editors
Roumen Kountchev
Technical University of Sofia
Sofia, Bulgaria

Ivo Draganov
Technical University of Sofia
Sofia, Bulgaria

Kazumi Nakamatsu
University of Hyogo
Kobe, Japan

Rumen Mironov
Technical University of Sofia
Sofia, Bulgaria

Roumiana Kountcheva
TK Engineering
Sofia, Bulgaria

Preface

This book contains papers presented at the International Workshop "New Approaches for Multidimensional Signal Processing-NAMSP 2023" which was carried out during July 06–08, 2023 at the Technical University of Sofia, Bulgaria. The workshop was a part of the "Days of Science 2023" at the Technical University of Sofia, organized in collaboration of the Research and Development Sector at TU-Sofia, Bulgaria. The workshop was supported by the Bulgarian National Science Fund (BNSF) at the Ministry of Education and Science of Bulgaria. Co-organizers of NAMSP2023 were Interscience Research Network (IRNet) International Academy Communication Center, China; Deenbandhu Chhotu Ram University of Science and Technology, Murthal, Haryana, India, and Interscience Institute of Management and Technology-Bhubaneswar, India. In the workshop scientists participated from China, India, Canada, USA, Hungary, Nigeria and Bulgaria.

The book comprises 25 chapters. The three main topics, on which were focused the accepted papers, are:

(1) Multidimensional Image Tensor Decomposition and Analysis;
(2) Theoretical Approaches in Multidimensional Signal Processing;
(3) Multidisciplinary Applications of Multidimensional Signal Processing in industry, business, medicine, power engineering, ecology, etc.

The aim of the book is to present the latest achievements of the authors in the processing and analysis of multidimensional signals and the related applications, to a wide range of readers: IT specialists, engineers, physicians, Ph.D. students and other specialists.

Sofia, Bulgaria   Roumen Kountchev
Sofia, Bulgaria   Rumen Mironov
Sofia, Bulgaria   Ivo Draganov
Sofia, Bulgaria   Roumiana Kountcheva
Kobe, Japan   Kazumi Nakamatsu
October 2023

The editors express their warmest thanks to the excellent Springer team which made this book possible.

Contents

About the Editors

Prof. Dr. Roumen Kountchev Ph.D., D.Sc. is a professor at the Faculty of Telecommunications, Department of Radio Communications and Video Technologies, Technical University of Sofia, Bulgaria. His areas of interest are digital signal and image processing, image compression, multimedia watermarking, video communications, pattern recognition, and neural networks. He has 360 papers published in magazines and proceedings of conferences; 22 books; 47 book chapters; 21 patents. He had been principle investigator of 38 research projects. At present, he is a member of Euro Mediterranean Academy of Arts and Sciences and President of Bulgarian Association for Pattern Recognition (member of Intern. Association for Pattern Recognition). He has been a plenary speaker at more than 30 international conferences and workshops and edited 28 books published in Springer series.

Prof. Dr. Rumen Mironov received his MSc and PhD in Telecommunications from Technical University of Sofia and MSc in Applied Mathematics and Informatics from Faculty of Applied Mathematics and Informatics. He is currently associated professor in the Department of Radio Communications and Video Technologies, Faculty of Telecommunications, Technical University of Sofia, Bulgaria. His current research focuses on digital signal and image processing, pattern recognition, audio and video communications, information systems, computer graphics, multidimensional signal processing and programming languages. He is a Member of Bulgarian Association of Pattern Recognition (IAPR), Bulgarian Union of Automation and Automation Systems and he is a member of IJBST Journal Group. He participated in more than 20 national and international scientific research projects and he is Author of more than 120 scientific publications in magazines and proceedings of conferences.

Prof. Dr. Ivo Draganov received B.Sc., M.Sc., and Ph.D. in Telecommunications from Technical University of Sofia, Bulgaria, in 2003, 2005, and 2009. Currently, he is an associate professor in the Faculty of Telecommunications and teaches Programming in Assembler, Digital Design, Measurements in Telecommunications, Audio Systems and Speech Coding, Multimedia Systems, Digital Video Broadcasting, and other subjects. His main areas of scientific research are digital image processing,

pattern recognition, multimedia systems, and neural networks. He is a member of the Editorial Board of the Computer and Communications Engineering Journal. During his research activities, he participated in more than 10 national and international projects and published more than 80 papers. He is a member of IEEE.

S.R. Dr. Roumiana Kountcheva is Vice President of TK Engineering. She got her M.Sc. and Ph.D. at the Technical University of Sofia, Bulgaria, and became Senior Researcher (SR) at TIE, in 1993. She had two post-doc trainings in Japan (Fujitsu, 1977, and Fanuc, 1980). She has more than 200 publications (including 28 book chapters and five patents, and presented 22 plenary speeches at international conferences and workshops. She is Member of IRIEM, IDSAI, IJBST Journal Group, and Bulgarian Association for Pattern Recognition. She participated as PI, Co-PI, and Team Member of 47 scientific research projects, from which 14 international. She is Reviewer of WSEAS conferences and journals and edited several books for Springer SIST series. Her scientific areas of interest are in image processing and analysis, image watermarking and data hiding, multidimensional image representation, tensor representation, pyramidal image decompositions, image and video compression, CNC and programmable controllers, etc.

Prof. Dr. Kazumi Nakamatsu received the M.S. Eng. and Dr. Sci. from Shizuoka University, 1976, and Kyushu University, Japan, 1999, respectively. He is Full Professor at School of Human Science and Environment, University of Hyogo, Japan. His research interests encompass various kinds of logic and their applications to Computer Science, especially paraconsistent annotated logic programs and their applications. He is Author of over 150 journal papers, book chapters, and conference papers and edited 14 books published by prominent publishers such as Springer-Verlag. He has chaired various international conferences, workshops, and invited sessions, and he has been a member of numerous international program committees of workshops and conferences in the area of Artificial Intelligence and Computer Science. He has contributed numerous invited lectures at international workshops, conferences, and academic organizations. He also is Recipient of some conference and paper awards. He is Member of Japan AI Society, etc.

Chapter 1
Deep Representation and Analysis of Visual Information, Based on the IDP Decomposition

Lakhmi C. Jain, Roumen K. Kountchev, and Roumiana A. Kountcheva

Abstract We present contemporary methods for image decomposition analysis in the spectrum domain, based on the Inverse Difference Pyramid (IDP) decomposition. The basic IDP implementations in various aspects of visual information processing and analysis are discussed, in the range from 2D images to third-order tensors. Special attention is paid to the main IDP features, which are compared with those of the famous pyramidal decompositions. The basic IDP modifications are presented: the Reduced Branched IDP, which could be implemented on the basis of various 2D orthogonal transforms (WHT, discrete Fourier transform DFT, DCT, KLT, etc.), and the upgrade to the Adaptive IDP, based on neural networks integration. Special approaches are introduced for the IDP-based decomposition for sequences of correlated images, and some important applications in multidimensional image tensor representation are given; the compression of single and groups of correlated multispectral, multi-view, and computer tomography images; and the faster object search in large image databases. The experimental results obtained by the approaches based on the IDP decomposition, confirm its efficiency which is very high for some image classes. In the conclusions the analysis results and the trends for future investigations and implementations are explained.

L. C. Jain
KES International, Selby and University of Arad, Arad, Romania

R. K. Kountchev
Technical University of Sofia, Bul. Kl. Ohridsky 8, Sofia, Bulgaria

R. A. Kountcheva (✉)
TK Engineering, Sofia, Bulgaria
e-mail: kountcheva_r@yahoo.com

1.1 Introduction

The widely used methods for hierarchical image decomposition, based on the pyramidal representation in the pixel domain, comprise of two main approaches, the Non-orthogonal Pyramids and the Orthogonal Pyramids [1, 2]:

– Non-orthogonal Pyramids belong the Gaussian/Laplacian Pyramid (GP/LP); the Reduced/Enhanced Laplacian Pyramid, the Reduced-Sum/Reduced-Difference Pyramid, the Hierarchy-Embedded Differential Pyramid, etc.,
– Orthogonal Pyramids are mainly represented by the Sub-Band Decomposition based on filter banks: the Orthonormal Wavelet Pyramid, the Steerable Pyramid (based on directional filter banks), the Curvelets Pyramid, the Ridgelet Pyramid, etc.

The approaches, based on the Laplacian/Gaussian decompositions are well-known and multiple applications already exist for image compression, analysis, machine learning, etc. [1–3]. Specific for these decompositions is, that in the lowest decomposition level the number of components is the largest, and decreases in each consecutive level (Fig. 1.1). The decomposition ends after the last coefficients of the highest level are calculated. Besides, these decompositions require the execution of multiple decimations and interpolations. Unlike this the IDP decomposition starts with a relatively low number of decomposition components and each level contains a larger number, but the decomposition can stop before the last possible level is executed, depending on the needed quality of the restored image.

The Inverse Difference Pyramid [4] is a kind of hierarchical image decomposition, based on pyramidal representation in the spectrum domain. The IDP structure is based on orthogonal deterministic or statistic transforms, such as the Discrete Fourier Transform (DFT), the Discrete Cosine Transform (DCT), the Walsh-Hadamard Transform (WHT), the Complex Hadamard Transform (CHT), the Karhunen–Loeve Transform (KLT), etc. One modification of IDP is the Adaptive Inverse Difference Pyramid (AIDP), which could be based on the following: Back-Propagation Neural Networks (BPNN), Gaussian Radial Basis Function Networks (GRBFN), Self-Organizing Feature Mapping Vector Quantization (SOFM-VQ). Another kind of IDP decomposition is the Non-linear Inverse Difference Pyramid (NL-IDP), based on the Discrete Modified Mellin-Fourier Transform (MMFT).

A simplified structure of the basic IDP decomposition is shown on Fig. 1.2.

The processing of the input (original) 2D image starts at the lowest level. For this, the image is represented by the matrix, [B]. To simplify the calculations, the image is divided into smaller pieces (sub-blocks), each of size $2^n \times 2^n$, and on the figure is shown the processing of one of these blocks only. For the decomposition any 2D orthogonal transform could be used like the Walsh-Hadamard Transform (WHT), the Discrete Fourier Transform (DFT), the Discrete Cosine Transform (DCT), the Karhunen–Loève Transform (KLT) or Principal Component Analysis (PCA), etc. In order to reduce the number of calculated transform coefficients, the "truncated" orthogonal transform is used, i.e., part of the coefficients are not calculated because
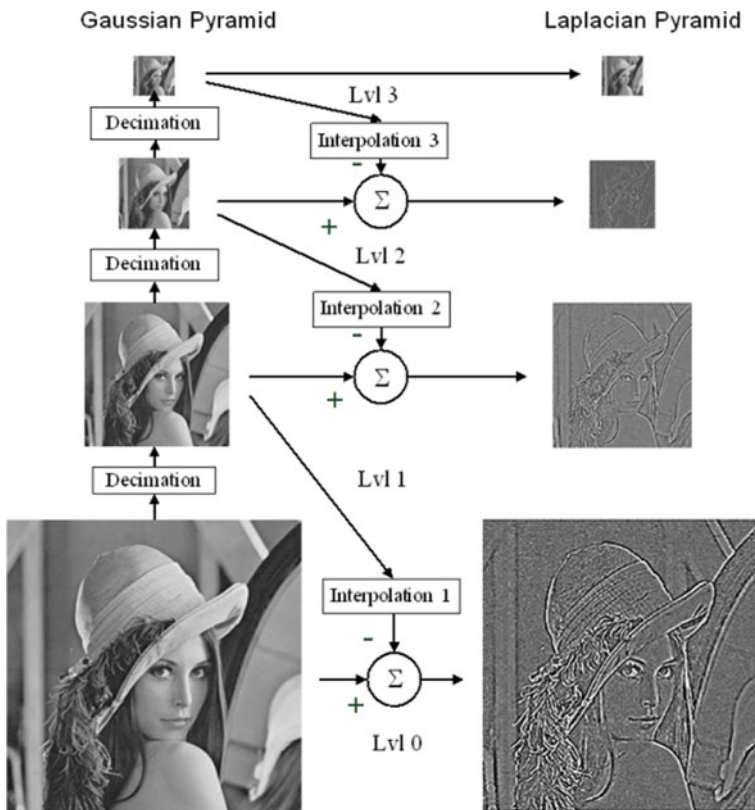
Fig. 1.1 Image decomposition based on Gaussian/Laplacian pyramid

(after analysis) their values are evaluated as too small to influence the quality of the restored image. The corresponding block in the figure is denoted as Truncated Orthogonal Transform, "TOT". The values of the calculated coefficients are saved in the block $[\hat{\boldsymbol{S}}]$ (in the figure are used correspondingly: $[\hat{\boldsymbol{S}}_0]$—for the start level; $[\hat{\boldsymbol{S}}_1]$—for level 1, etc.). From the start level in this example 4 coefficients are retained, $\hat{s}_0(u, v)$ only, as shown in the lower right part of the figure. The processing continues with the preparation of the data for the next decomposition level. For this, on the coefficient s_0 Inverse Orthogonal Transform (the block "IOT") is executed, and the first is obtained, which is the coarse approximation of the processed image block, $[\hat{\boldsymbol{B}}_0]$. This approximation (i.e., the restored image sub-block) is subtracted from the original in "$\sum$" and the difference (error) image is calculated. For this level, the "Error" image matrix is denoted as $[E_0]$. In the second level it is divided into smaller sub-blocks, of size $2^{n-1} \times 2^{n-1}$, and after that processed with TOT again. The values of the calculated coefficients are saved in the corresponding blocks $[\hat{\boldsymbol{S}}_1]$. The calculated 16 coefficients for this level, are saved in the block $\hat{s}_1(u, v)$. The coefficients in the next level are calculated in a similar way and the obtained corresponding 256
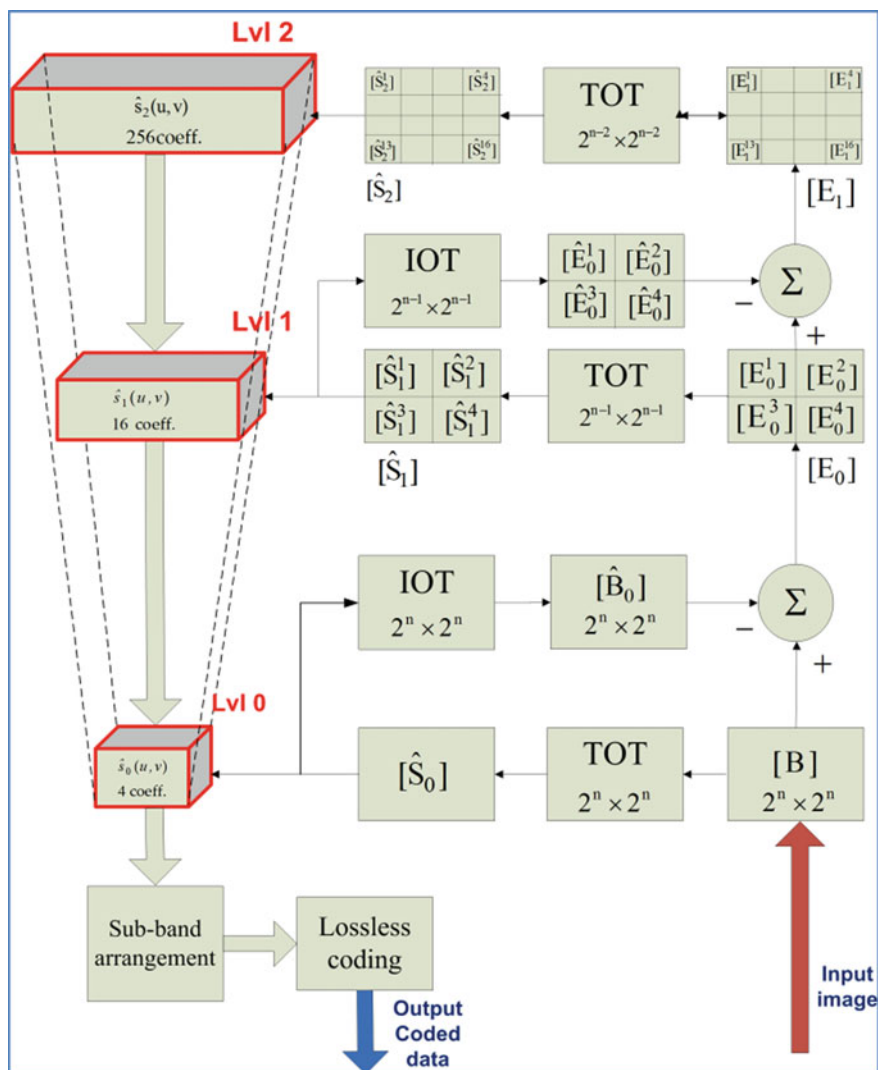
Fig. 1.2 Basic structure of the inverse difference pyramid

coefficients are retained and saved in the block $\hat{s}_2(u, v)$. As it is shown, the number of coefficients is higher in each consecutive decomposition level, and this is why the decomposition is called "Inverse Difference Pyramid". The decomposition can stop in any decomposition level, depending on the achieved quality of the restored image, or on the values calculated for the "difference" image. When the decomposition is stopped, the values of the coefficients, retained in all levels, are arranged in accordance with their spatial frequencies and are then losslessly coded through Adaptive Run-length Encoding (ARLE), followed by a Modified Huffman (MH) coding. The

ARLE and the MH coding were specially developed for the IDP decomposition, in accordance with the specifics of the processed data [5]. The restoration of the decomposed image is executed in reverse order.

The main advantage of IDP is its efficiency when used for the compression of 2D or 3D visual information. Unlike Laplacian/Gaussian pyramids, the IDP decomposition does not use decimations and interpolations, because it is based on some kind of orthogonal transform. The computational cost of the process depends on the number of needed operations, analyzed in previous research of the authors [6]. The authors also proved theoretically the low computational complexity for the tensor representation of multidimensional visual information [7, 8]. One important disadvantage of IDP is, that if all coefficients are retained, the decomposition is over-complete. To avoid this, the properties of the used orthogonal transform, are used. For example, for the WHT it is not necessary to calculate all neighbor coefficients in a group, because for each 4 coefficients is necessary to calculate 3 only (the fourth is calculated by using the values of the remaining three). On the basis of this property, the problem with the decomposition over-completeness, is solved.

1.2 Branched IDP

To achieve a better performance for the processing and analysis of sequences of correlated images, the Branched Inverse Difference Pyramid (BIDP) was developed. This approach is extremely useful for processing sequences of medical images (computer tomography images, magnetic resonance images, etc.), and groups of multispectral or multi-view images. In all these cases, the processed groups of images have high mutual correlation. The BIDP block diagram is shown on Fig. 1.3. In this case, the basic IDP diagram is retained (the red rectangle), but some new relations between images in the processed group, are introduced.

In the case shown on Fig. 1.3, one sequence of $(2N + 1)$ images (representing same object or scene) is processed bound together by similarity, and one of the images is used as a reference.

To select the reference image, various approaches could be used, for example, through PSNR comparison, etc. For video sequences, the middle image in the group is usually the most suitable, and this is the easiest solution. Another approach is based on the analysis of the images histograms for the group: the image, whose histogram is most similar with these of the remaining in the group, is chosen to be used as a reference (R).

The image decomposition starts with this reference image, which is processed with some kind of orthogonal transform, using a limited number (preset) of transform coefficients. After inverse transform of the so calculated coefficients, the coarse approximation of the processed image is obtained. The IDP decomposition then branches out into several decompositions, whose number corresponds to the number of images in the group. The first approximation for all multispectral images is that calculated for the reference image. In case that IDP comprises of 2 levels only, each
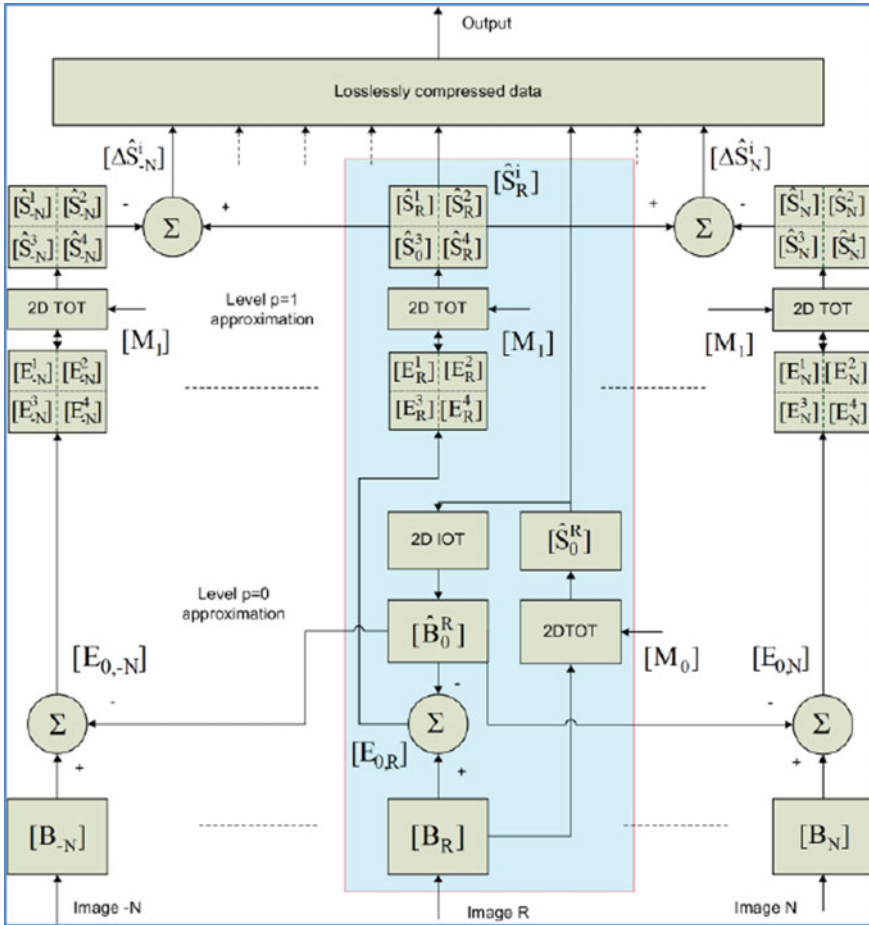
Fig. 1.3 Block diagram of BIDP

branch is built individually in the next level. For IDP of more levels, the reference image approximation could be used also in the second level, etc. The similarity between the processed images, permits the same coarse approximation to be used for the whole group. Depending on the visual contents, the number of images in one group could be different and is set in relation to their mutual correlation. For example, for video sequences, the highest correlation usually exists between each 8–12 sequential frames, and for CT and MRI sequences, longer groups could be used. Due to the result of the processing based on BIDP, high compression and very good visual quality of the restored images are achieved, as confirmed by the experimental results.

1.3 Multi-layer Tensor Decomposition Trough 3D IDP

The common practice in image representation is based on the use of a 2D matrix, where each pixel corresponds to one matrix element. Together with this, many contemporary applications exist, where video sequences and groups of correlated images, obtained from various sources must be stored, analyzed or searched, and for this, the most suitable approach is that they are to be treated as 3D arrays of matrices. Recently tensors, and specially the third-order tensors, are most suitable to represent such sequences. The main obstacle for the wide tensor decomposition implementation in real time applications is the high computational complexity. Tensor decompositions are usually based on deterministic discrete transforms of the kind: Discrete Wavelet Transform (DWT), or the Discrete Cosine Transform (DCT) followed by SVD in the frequency domain [9]. In part of the related publications [10–13], algorithms are proposed for cubical decomposition based on the 3D separable discrete transforms: Discrete Fourier Transform, Discrete Hartley Transform, Discrete Cosine Transform, etc. To reduce the computational complexity, in many cases "fast" algorithms are used, one of which is the 3D Fast Fourier Transform (FFT). Compared to the SVD/PCA-based algorithms, the tensor decomposition based on deterministic orthogonal transforms offers lower energy concentration in the first decomposition components but accelerates the computations. This is why, the tensor decomposition based on orthogonal transforms is reasonable in cases when real-time processing of various multidimensional data is needed.

The approach, presented here, is the hierarchical third-order tensor decomposition based on the 3D-IDP. For this, the tensors are transformed into the 3D-WHT spectrum space. The basic concept is to represent each third-order tensor X of size N × N × N through a 3D Reduced IDP (3D-RIDP) [14] of the kind, shown on Fig. 1.4. For this, the tensor X is initially divided into Q sub-tensors X_q for $q = 1, 2, …, Q$, each of size M × M × M, where M $= \lfloor N/\sqrt[3]{Q} \rfloor$. The value of M is defined in accordance with the condition $M = 2^m$. For the calculation of each sub-tensor X_q of size $N × N × N$ ($N = 2^n$) is built the individual n-level 3D-RIDP. In result, the tensor X is transformed into the corresponding spectrum tensor S, which comprises n levels of coefficients. The coefficients in the initial level have the highest energy concentration, while the energy in the next levels decreases quickly. In correspondence with Parseval's theorem, where the total energy of the coefficients of the tensor S is equal to that of the elements of the tensor X, but is redistributed. The main advantages of the method are the lower computational complexity because the only mathematical operations, which are needed, are "additions" and their number is relatively low. Furthermore, the main part of the tensor energy is concentrated in a small number of coefficients from the first pyramid level which permits significant information redundancy reduction, after neglecting the low-energy elements.

The properties of the 3D-RIDP open new possibilities for implementation in various application areas related to processing and analysis of 3D data: sequences of correlated images (video, multi-spectral, multi-view, medical images from various sources), multichannel signals, etc.
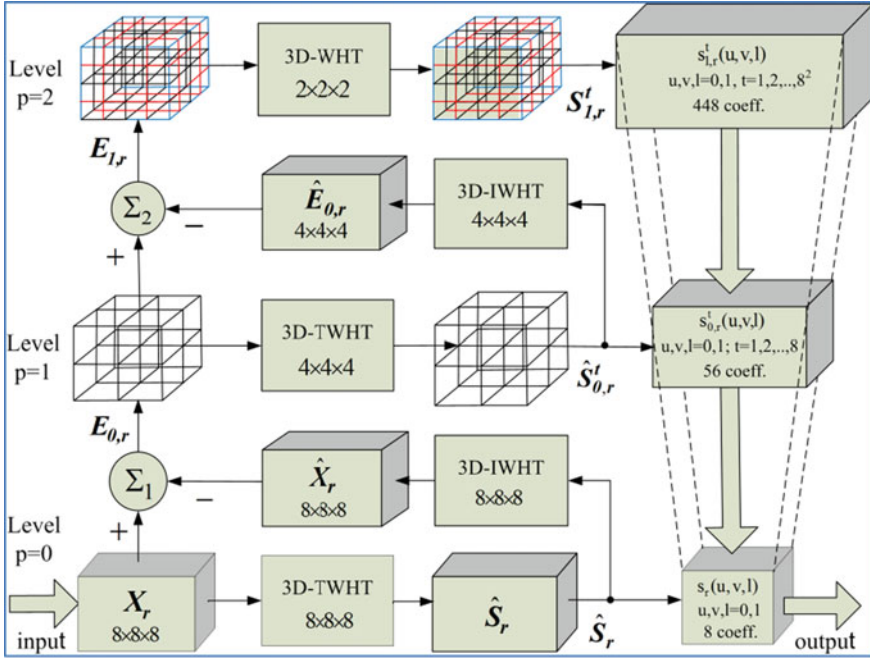
Fig. 1.4 Block diagram of 3D reduced IDP

1.4 Multi-layer Tensor IDP, Based on Hierarchical SVD

To achieve computational complexity reduction, a new non-iterative approach for multi-dimensional tensor representation based on the Multi-layer Tensor Spectrum Pyramid (MLTSP) [15] is proposed, with embedded 3D orthogonal transforms (3D OT) and Hierarchical Tensor SVD (HTSVD) [8]. This approach is illustrated by an example for the representation of a tensor of size $8 \times 8 \times 8$ through a two-layer tensor spectrum pyramid (2LTSP), with embedded 3D Frequency-Ordered Fast Walsh-Hadamard Transform (3D FO-FWHT) [7] and HTSVD for a tensor of size $2 \times 2 \times 2$ (HTSVD$_{2 \times 2 \times 2}$) [8]. To explain the multi-layer TSP structure, as an example here is used the two-layer tensor spectrum pyramid (2LTSP), which comprises a coder and a decoder. The structure of the decoder is mirror-symmetrical to that of the coder. Both block diagrams are shown on Fig. 1.5, a, b. The block diagram of the computational graph of the algorithm HTSVD$_{2 \times 2 \times 2}$ of two hierarchical levels for the decomposition of the elementary tensor $S_{2 \times 2 \times 2}$ of size $2 \times 2 \times 2$, is shown in Fig. 1.6. The decomposition is based on SVD for the matrix $[X]$ of size 2×2, denoted as SVD$_{2 \times 2}$. The SVD$_{2 \times 2}$ decomposition is executed through simple relations, of low computational complexity [15]. After the decomposition of $S_{2 \times 2 \times 2}$ is finished, the tensors in the resulting sum are arranged following the decrease of the variances for the sub-matrices obtained after the unfolding.

a. 2LTSP Encoder   b. 2LTSP Decoder
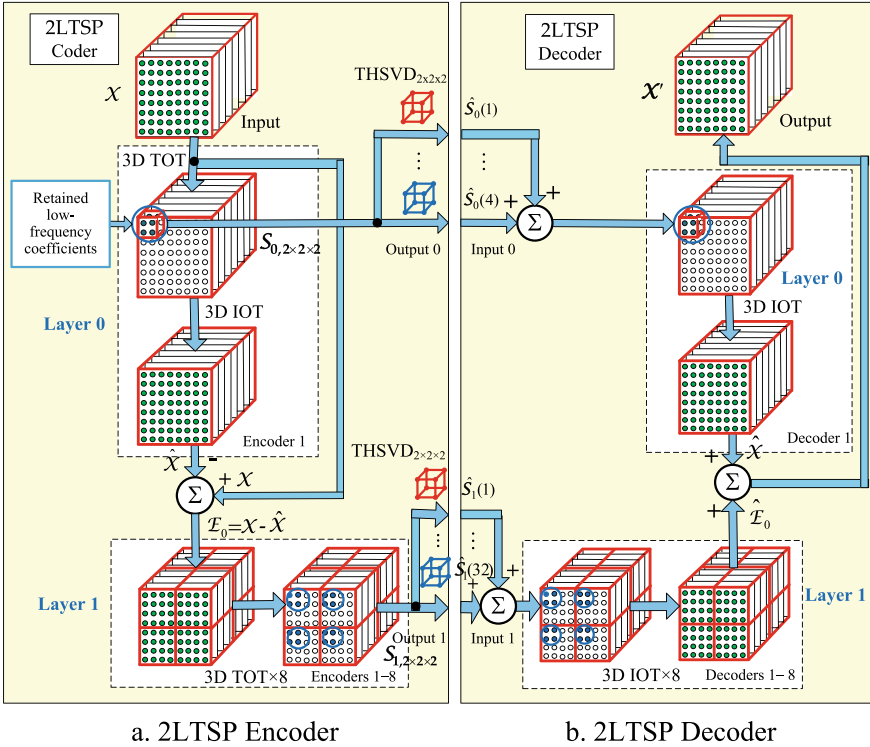
Fig. 1.5 2LTSP based on 3D OT and HTSVD$_{2\times2\times2}$ for input tensor X of size $N \times N \times N$, for $N = 8$

The voxels of higher values in the $S_{2\times2\times2}$ decomposition in Fig. 1.6, are colored in red, and these of lower—in blue. The main advantages of the MLTSP algorithm are the low computational complexity, the high flexibility regarding the choice of their parameters, and the high ability for information redundancy reduction in the input tensor.

1.5 3D Adaptive Inverse Difference Pyramid with Convolutional Auto Encoder/Decoder

This adaptive IDP version is based on the use of a Convolutional Auto Encoder/ Decoder (CED) [16]. The two components of the CED neural network are ained by deep learning. These are the Convolutional Coder (CE), is used to compress the input data, and the Convolutional Decoder (CD), which restores the already compressed input data. On Fig. 1.7, the block diagram of one multi-layer CED is shown, of the kind $m^3 \rightarrow n \rightarrow m^3$, i.e., it comprises m^3 input cells, n cells in the hidden layer (the
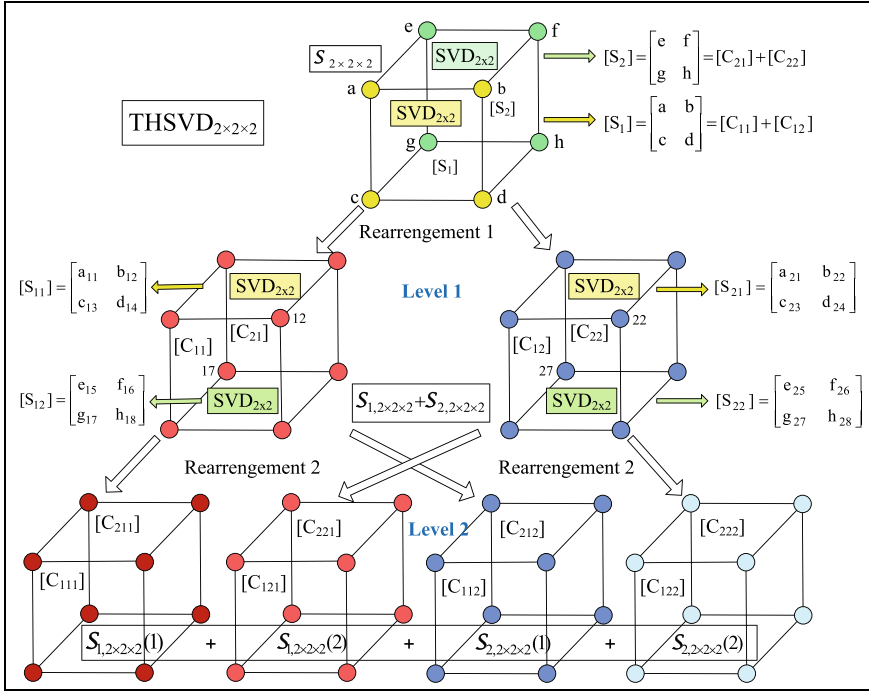
Fig. 1.6 HTSVD$_{2\times2\times2}$ algorithm for the tensor $S_{2\times2\times2}$ decomposition

output of the coder and the input of the decoder, respectively), and m^3 output cells. After the end of the iterative CED training, the values obtained for the output cells approximate these from the input cells, at minimum root mean square error.

Two new approaches are offered here for the compression of a single third-order (cubical) tensor.

The *First approach* is based on the Adaptive Inverse Difference Pyramid (AIDP) structure, combined with CED. On Fig. 1.8 the corresponding three-level block diagram is shown. Here the third-order tensor of size $m \times m \times m$, enters the AIDP input. In the initial (zero) hierarchical AIDP level, the elements of the input tensor are arranged as a sequence of length m^3, following a preselected rule. This sequence defines the m^3-dimensional vector, which enters the auto-encoder CED-0. In this case, the hidden layer contains n cells (for $n << m^3$), while the output layer is of m^3 cells. From them, after inverse rearrangement, the output third-order tensor of size $m \times m \times m$ is restored. After the CED-0 self-training is finished, the so obtained output tensor approximates the input tensor, of size $m \times m \times m$. In the first summator (Σ_1), the approximated tensor is subtracted element-by-element from the input tensor, and as a result the difference tensor is obtained, which corresponds to the approximation error. In the first hierarchical AIDP level, the difference tensor is divided into 8 sub-tensors, each of size $(m/2) \times (m/2) \times (m/2)$. The elements of these sub-tensors are
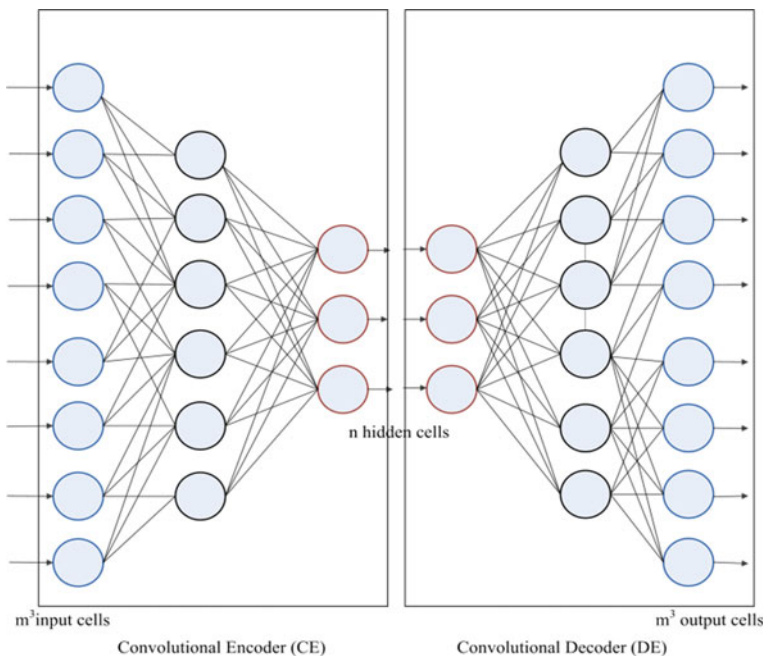
Fig. 1.7 Convolutional E/D (CED)

transformed into eight $(m^3/8)$-dimensional vectors respectively. They enter sequentially the input of CED-1, whose hidden layer contains $(n/2)$ cells, and the output layer—$(m^3/8)$ cells. After the self-training of CED-1 for these sub-tensors is finished, the corresponding 8 sub-tensors of length $(m^3/8)$ are restored, which comprise the approximating difference tensor. In the second summator (Σ_2), the approximated difference tensor is subtracted element-by-element from the first approximation, and in the end the second difference tensor, i.e., the second approximation of the tensor is obtained. In the second hierarchical AIDP level, the difference tensor is divided into 64 sub-tensors, each of size $(m/4) \times (m/4) \times (m/4)$, which are then transformed into the corresponding $(m^3/64)$-dimensional vectors. They enter sequentially the auto-encoder CED-2, whose hidden layer comprises $(n/4)$ cells, and the output layer, $(m^3/64)$ cells.

After the end of the CED-2 self-training, from the so calculated 64 output vectors of length $(m^3/64)$, the corresponding 64 sub-tensors are restored which build the approximated second difference tensor. Each of the restored tensors in the AIDP levels, has a corresponding feedback to the CED-0, CED-1, and CED-2 coders. These connections are used in the self-training process of the auto-encoders. At the output of the AIDP zero level, an n-dimensional vector is obtained, which comprises the cells of the hidden layer of the trained CED-0. At the output of the AIDP first level, the $(4n)$-dimensional vector which is the concatenation of the elements of the 8 vectors is obtained, each of length $(n/2)$, built by the cells of the CED-1 hidden
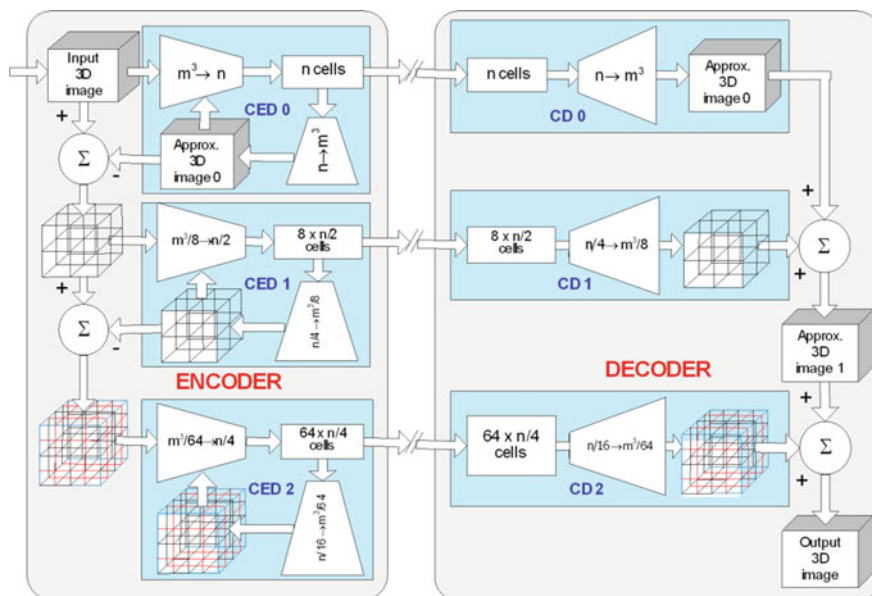
Fig. 1.8 Block diagram of the two-level adaptive IDP with convolutional Encoder/Decoder

layer, for the corresponding input vector. At the output of the AIDP second level, the $(16n)$-dimensional vector is obtained which is the concatenation of the elements of the 64 vectors, (each of length $(n/4)$), built by the cells of the hidden layer of the trained CED-1, for the corresponding input vector. The output n-dimensional vector for the zero AIDP level is the shortest, but it carries the largest information volume for the input tensor of size $m \times m \times m$. The output vectors from the first and second AIDP level, are correspondingly 4 and 16 times longer than these from the zero level, but they carry much less information about the input tensor. This permits significant reduction of the data obtained from the AIDP outputs, without noticeable information loss; i.e., the meaningless information is filtered (neglected). The number of AIDP levels together with the size growth of the input third-order tensor, should be increased.

The *Second approach*, aimed at tensors sequence compression (for example, color RGB images), as illustrated in Fig. 1.9. Here, a tensor decomposition is shown, based on the 2-level 3D Branched IDP (3D BIDP). The levels numbers are $p = 0.1$ [17], in correspondence to the block diagram from Fig. 1.3. Each tensor is of size $M \times N \times 3$; the input sequence is denoted as X_{t-1}, X_t, X_{t+1} for $k = 1$, and in the time moments $t - 1, t, t + 1$, where it contains 3 matrices of size $M \times N$. For the moment, at the input of the trained CED arrives the tensor X, and at the output is obtained the approximated tensor, $\hat{X}$. The approximation accuracy depends both on the CED training, and on the neuron number (n) in the hidden layer. These neurons are the components of the corresponding output n-dimensional vector, s.
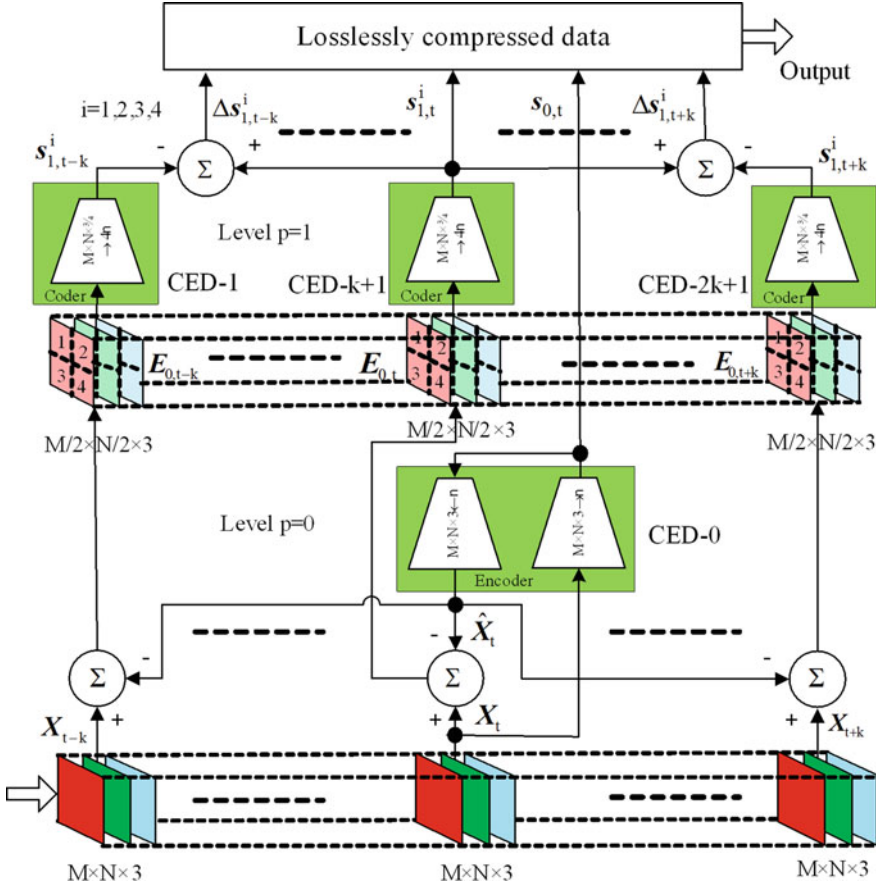
Fig. 1.9 Block diagram of the two-level 3D BIDP based on the convolutional Encoder/Decoder

Due to the result of the 3D BIDP implementation for the tensor sequence X_{t-1}, X_t, X_{t+1}, the output vectors $s_{0,t}$, $\Delta s^i_{1,t-1}$, and $\Delta s^i_{1,t+1}$ for $i = 1, 2, 3, 4$ are obtained of total length $n + 4n + 4n + 4n = 13n$. Due to high correlation existing between the sequential tensors X_{t-1}, X_t, X_{t+1}, the values of the significant part of the components in the difference vectors $\Delta s^i_{1,t+1}$ and $\Delta s^i_{1,t+1}$ are close to zero. In this way, the input tensors are transformed into an output vector of small length which contains many zero values, i.e., the features' space is reduced at minimum computational cost. For the calculations reduction the mutual correlation between the tensors is used, which determines the relation $\hat{X}_t \approx \hat{X}_{t-1} \approx \hat{X}_{t+1}$. In the result, the calculation of tensors $\hat{X}_{t-1}$ and $\hat{X}_{t+1}$ through the corresponding CEDs, is not necessary. In the second level ($p = 1$) of the 3D BIDP, each difference tensor $E_{0,t} = X_t - \hat{X}_t$, $E_{0,t-1} = X_{t-1} - \hat{X}_t$, and $E_{0,t+1} = X_{t+1} - \hat{X}_t$, is divided into four sub-tensors of size $(M/2) \times (N/2) \times 3$, and for each, a corresponding CED is used. The neurons in the hidden layers of all CED in the level $p = 1$ are represented by the vectors $s_{1,t}$, $s_{1,t-1}$, and $s_{1,t+1}$.

Applications

In this part of our work, the experimental results obtained for some of the most important applications are shown: for compression and image content protection, and for efficient object search in large image databases.

1.5.1 Compression of Multidimensional Images

The compression algorithms are developed both for single images, and for groups of correlated images or sequences. The approach is based on the IDP decomposition with Back Propagation Neural Networks (BPNN). In Table 1.1 are shown some comparison results obtained for several widely used test images, when approximately the same quality of the restored images is achieved. The results for the IDP-BPNN decomposition are given for two-level IDP with initial sub-blocks of size 8×8. As it could be noticed, the compression ratio for IDP-BPNN for most of the test images is approximately two times higher, while the quality of the restored images (evaluated by their PSNR) is close or better than this for JPEG 2000.

The use of the BIDP for sequences or groups of correlated images offers similar results, part of which are given in Table 1.2. For the evaluation were used various kinds of medical images. The following abbreviations are used: CT—computer tomography; MG—mammography; NM—nuclear magnetic; US—ultrasound; dcm—Dicom; and jp2—JPEG2000. The "idp" format was specially created for the IDP decomposition [18]. The header contains detailed information about the decomposition structure—the number of levels, the used transform for each level (for example, DCT WHT, etc.), the arrangement of the retained coefficients, and the kind of lossless compression applied on the compressed image data. The lossless compression method is based on adaptive run-length coding, which corresponds to the data statistics. The results show that IDP offers higher compression ratio than Dicom, and is comparable in efficiency with JPEG 2000, but at lower computational cost (the wavelet transform is more complicated than WHT or DCT). Additional advantage of IDP is the sub-block structure, which offers high flexibility in observing medical images, and permits enlargement (on request) of a selected Region Of Interest (ROI). This is an important feature in case of remote diagnostics and medical decision support applications.

1.5.2 Content Protection of Visual Information
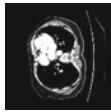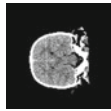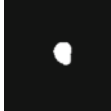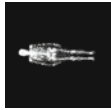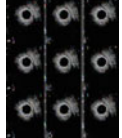
The IDP-based decomposition permits the insertion of invisible resistant watermark (WM) [19]. The block diagram of a two-level WM insertion algorithm, is shown in Fig. 1.10. In this case, the IDP structure is retained, but the decomposition is based on the Complex Hadamard Transform (CHT). The watermark is prepared in the same

Table 1.1 Comparison results for JPEG2000 and IDP-BPNN

No	Name	8 bpp 512 × 512	JPEG 2 K (Matlab)		IDP-BPNN(8 × 8)	
			CR	PSNR [dB]	CR	PSNR [dB]
1	Boy		25.23	28.98	60.40	29.05
2	Fruits		32.64	32.69	60.29	32.89
3	Tracy		54.13	35.66	59.93	35.32
4	Vase		35.75	27.20	60.18	26.83
5	Clown		31.71	31.47	60.01	31.81
6	Peppers		38.39	30.70	60.23	30.94
7	Text		17.86	18.35	60.22	18.69
8	Lena		32.10	29.20	59.57	29.15

way, as the image (i.e. decomposed into 2 or 3 levels), and in the watermarking process, its coefficients are added to the image decomposition coefficients. To retain the image quality unchanged (i.e., "invisible" watermarking), the WM information is inserted in the phases of selected coefficients, and could be extracted by using a special decoding software. The watermark "depth" depends on the phase rotation

Table 1.2 Compression results for various kinds of medical images

Image size, KB Type: CTI, MGI, NMI, USI	CTI 512 × 512 14 images	CTI 512 × 512 14 images	CTI 512 × 512 14 images	MGI 1914 × 2294	NMI 1024 × 1024	USI 1020 × 818	USI 1020 × 818
dcm	545	545	545	4190	2000	1800	1800
jp2	52.2	49.6	3.92	820	103	700	189
idp	50.5	46.9	2.3	801	71	388	134
dcm/jp2	10.44	10.98	139.03	5.11	19.41	3.48	22.16
dcm/idp	10.79	11.62	236.95	5.23	28.17	6.28	31.26

angle, for example, for rotations in the range 0–20°, the PSNR is always higher than 35 dB, i.e., the visual quality of the watermarked test images is retained. In Fig. 1.10, the following notations are used: $w_0(r)$—the decomposed watermark data for level 0; $w_1(r)$—the decomposed watermark data for level 1; $Z_0(r)$—the calculated coefficients for the initial (zero) level, with the inserted watermark; $Z_1(r)$—the calculated coefficients for level 1, with the inserted watermark. For a decomposition of higher number of levels, the structure is retained. The so calculated coefficients are arranged following their spatial frequency, and are losslessly coded. With this, the coding procedure is finished. The decoding is executed in reverse order.

The main advantages of the algorithm [19], are:

– The algorithm is highly resistant against attacks, based on high-frequency filtration (JPEG compression), which is confirmed by the almost constant MSE value for the extracted watermark.
– The algorithm permits insertion of significant amounts of data (the number of inserted bits could be approximately equal to ¾ of the total number of pixels).
– The algorithm is highly resistant against attacks related to image editing of the kind: crop, rotations, etc.
– The algorithm permits to insert different watermarks in each consecutive decomposition level, which is an additional tool to ensure hierarchical access control.
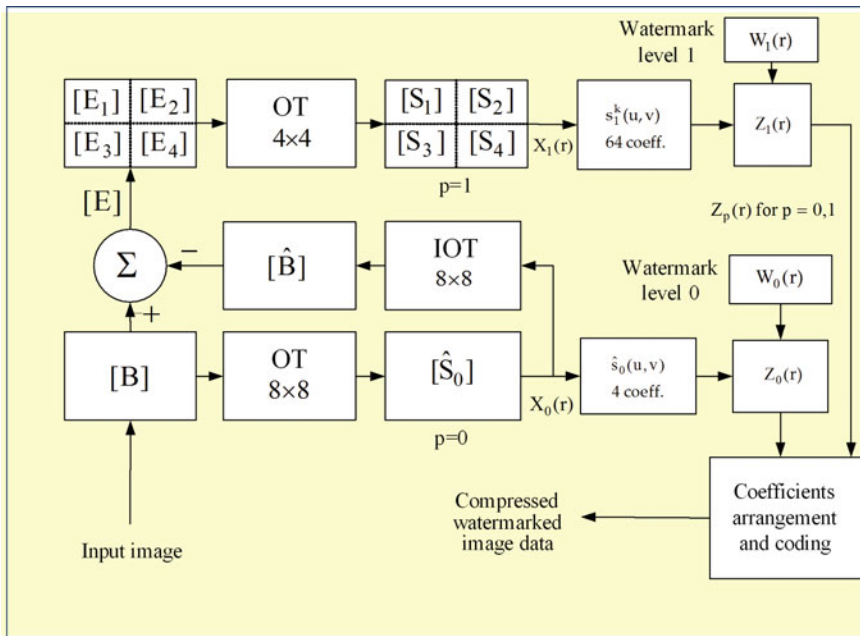
Fig. 1.10 Block diagram for 2-layer WM insertion in one IDP sub-block of size 8 × 8

1.5.3 Object Search in Large Image Databases

Contemporary databases contain huge number of images, video sequences, etc., and sometimes the search needs too much time. The layered structure of the IDP-based decomposition gives significant abilities for the search process enhancement.

For this, the images in the database and the query image are decomposed in a similar way. The retained decomposition coefficients from all decomposition levels, which represent the query image, constitute the "Cognitive 3D IDP model" (Fig. 1.11). The retained coefficients are used for the layer-by-layer comparison and evaluation in the search process.

In case that the search is aimed at a specified group of images, the method permits to select in advance the most suitable group of coefficients (which ensure the highest similarity), so as to enhance the process significantly.

The model is based on the n-level IDP decomposition under Neural Network (NN) control, shown on Fig. 1.12. The accuracy of the 3D model in the IDP level p is defined by the NN in the preceding level $p - 1$, and as a result the minimum
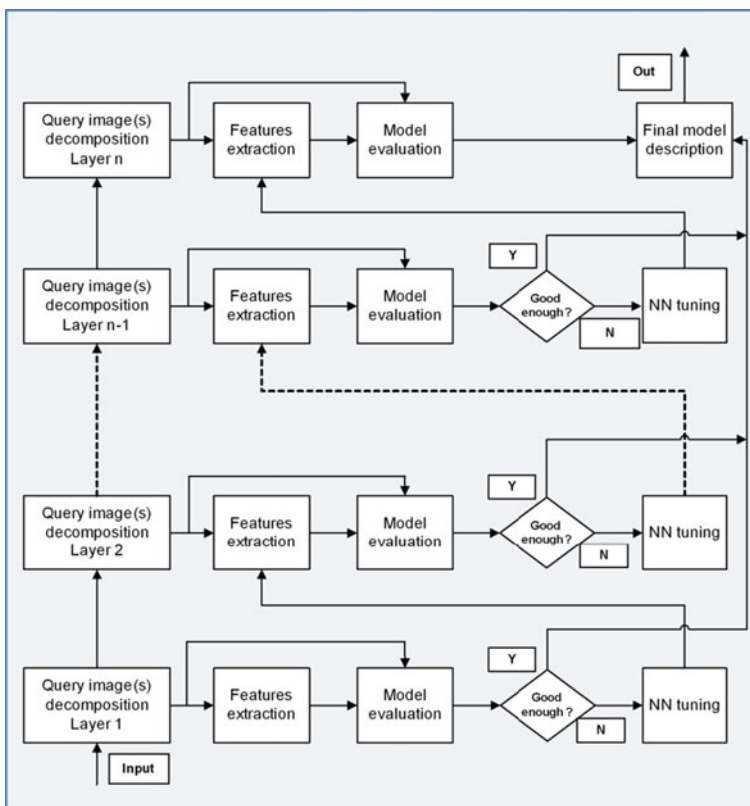
Fig. 1.11 Creation of the cognitive 3D IDP model

mean-square approximation error in the restored image for the corresponding level is obtained.

The comparison starts in the initial (lowest) decomposition level. The similarity of the first approximations of the query image and the images in the database is evaluated, and for the search in the next level the closest images only are retained. Thus, the number of analyzed images in each consecutive level is reduced, which enhances the process efficiency.
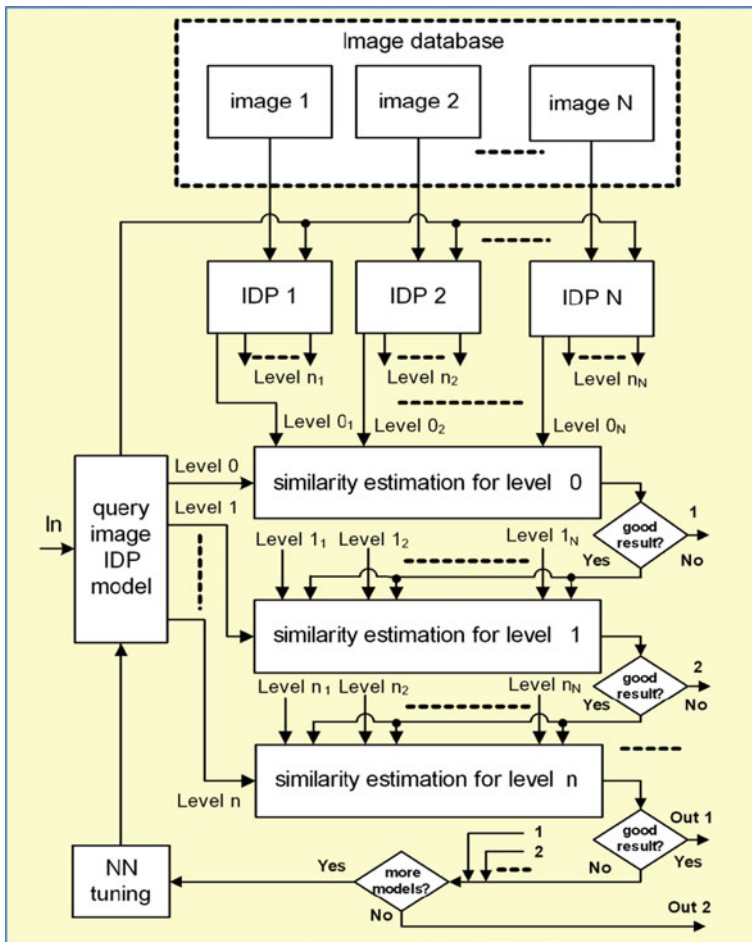
Fig. 1.12 Block diagram of the algorithm for layered IDP-based object search

1.6 Conclusions

In this work, the basic IDP implementations in various aspects of visual information processing and analysis are discussed, starting with single images, and upgrading to the third-order tensor representation of multidimensional visual information. The main advantages of IDP compared to other well-known decompositions, are the lower computational complexity, the feasible hardware implementation and the application flexibility. Very good results are achieved in processing and compression of correlated sequences of medical images.

The analysis and the related experiments show that the basic pyramidal structure of the IDP decomposition suits the 2D and 3D (tensor) implementations in various applications: compression of visual information; content protection, efficient object search, etc. The layered architecture permits adaptive processing and flexible approach, with changeable structure.

The future work will be mostly aimed at the implementation in new medical devices based on the IDP decomposition, which will support remote diagnostics and medical decision support integrated in the contemporary smart communications. Special interest attract some new technologies, which need processing of continuously changing information, among which are the Digital twins and the Mip-Map technology. The flexibility of the IDP structure permits easy development of adaptive decomposition architectures.

References

1. Burt, P., Adelson, E.: The Laplacian pyramid as a compact image code. IEEE Trans. Commun. **31**(4), 532–540 (1983)
2. Lin, T., Ma, Z., Li, F., He, D., Li, X., Ding, E., Wang, N., Li, J., Gao, X.: Drafting and revision: Laplacian pyramid network for fast high-quality artistic style transfer. Sci. Comput. Vis. Pattern Recogn. arXiv:2104.05376 [cs.CV] (2021)
3. Liang, H., Gong, Y., Kervadec, H., Li, C., Yuan, J., Liu, X., Zheng, H., Wang, S.: Laplacian pyramid-based complex neural network learning for fast MR imaging. In: Proceedings of Machine Learning Research (Proceedings of the Third Conference on Medical Imaging with Deep Learning), vol. 121, pp. 454–464 (2020)
4. Kountchev, R., Rubin, S., Milanova, M., Kountcheva, R.: Comparison of image decompositions through inverse difference and Laplacian pyramids. J. Multimed. Data Eng. Manag. **6**(1), 19–38 (2015)
5. Milanova, M., Todorov, V.L., Kountcheva, R.: Lossless data compression for image decomposition with recursive IDP algorithm. In: 17th International Conference on Pattern Recognition (ICPR), Cambridge, UK, pp. 823–826 (2004)
6. Kountchev, R., Mironov, R., Kountcheva, R.: Complexity estimation of cubical tensor represented through 3D frequency-ordered hierarchical KLT. MDPI Symmetry **12**(10), 1605, SI "Advances in Symmetric Tensor Decomposition Methods" (2020)

7. Kountchev, R., Mironov, R., Kountcheva, R.: Hierarchical cubical tensor decomposition through low-complexity orthogonal transforms. Symmetry **12**, 864 (2020)
8. Kountchev, R., Kountcheva, R.: Comparative analysis of the hierarchical 3D-SVD and reduced inverse tensor pyramid in regard to famous 3D orthogonal transforms. In: Kountchev, R., Mironov, R., Li, S. (Eds.) Proceedings of NAMSP 2020, Springer SIST Series, pp. 35–56 (2021)
9. Grasedyck, L.: Hierarchical singular value decomposition of tensors. SIAM J. Matrix Anal. Appl. **31**(4), 2029–2054 (2010)
10. Bergqvist, G., Larsson, E.: The higher-order singular value decomposition: theory and an application. IEEE Signal Process. Mag. **27**(3), 151–154 (2010)
11. Cichocki, A., Mandic, D., Phan, A., Caiafa, C., Zhou, G., Zhao, Q., De Lathauwer, L.: Tensor decompositions for signal processing applications: from two-way to multi-way component analysis. IEEE Signal Process. Mag. **32**(2), 145–163 (2015)
12. Sakai, T., Sedukhin, S.: 3D discrete transforms with cubical data decomposition on the IBM Blue Gene/Q. Technical Report 2013-001, Graduate School of Computer Science and Engineering, The University of Aizu, 31 p. (2013)
13. Woods, J.: Multidimensional Signal, Image, and Video Processing and Coding, 2nd edn. Academic Press, Elsevier, Amserdam (2012)
14. Kountchev, R., Kountcheva, R.: Low computational complexity third-order tensor representation through inverse spectrum pyramid. In: Kountchev, R., Patnaik, S., Shi, J., Favorskaya, M. (Eds.) Advances in 3D Image and Graphics Representation, Analysis, Computing and Information Technology - Methods and Algorithms, vol. 1, pp. 63–76. Springer (2020)
15. Kountcheva, R., Mironov, R., Kountchev, R., MLTSP: New 3D framework, based on the multilayer tensor spectrum pyramid. MDPI Symmetry **12**(14), 1909, September (2022)
16. Girin, L., Leglaive, S., Bie, X., Diard, J., Hueber, T., Alameda-Pineda, X.: Dynamical variational autoencoders: a comprehensive review. Found. Trends Mach. Learn. **15**(1–2), 1–175 (2021)
17. Kountchev, R., Kountcheva, R.: Tensor spectral pyramid for color video sequences representation, based on 3D FO-AHKLT. In: Kountchev, R., Mironov, R., Nakamatsu, K. (eds.) New Approaches for Multidimensional Signal Processing (NAMSP'22). Springer SIST series, vol. 332, Chap. 4, pp. 31–42 (2022)
18. Todorov, Vl., Kountcheva, R.: New format for coding of still images based on the IPD. In: Kountchev, R. (Ed.) New Approaches in Intelligent Image Processing, pp. 198–200. WSEAS Books (2013)
19. Kountchev, R., Todorov, Vl., Kountcheva, R.: Fragile and resistant image watermarking based on inverse difference pyramid decomposition. WSEAS Trans. Signal Process. **3**(6), 101–112 (2010)

Chapter 2
Some Trends in Application of Geometric Approaches in Multimodal Medical Image Fusion

Veska Georgieva and **Diana Tsvetkova**

Abstract The multimodal medical fusion combines data from different medical modalities, and thus can improve clinical information from medical images for a better understanding of the content of the image and to obtain a more precise diagnosis. The multimodal registration task is not easy, since images obtained from different modalities may have exceptional differences. This type of regeneration produces images that combine physiological and anatomical information. The aim of this paper is to present some trends in application of geometric approaches in fusion of multimodal medical images. For the efficient extraction of geometric characteristics, some trends are related to the use of structure tensors in combination with other transformations. The problem is considered in two main directions, namely registration and sparse representation and their role for obtaining better results in multimodal medical image fusion.

2.1 Introduction

In recent years, progress in medical image technology has been based on receiving high resolution images and more information about anatomical and functional changes in patients. Precise diagnosis should be based on the possibility of seeing different depths and structures of the human body, which are usually not visible from just one modality. The main purpose of such a system is to effectively combine various diagnostic modal images to bring out a representation that can help experts (radiologists, oncologists, interventionists) in the process of diagnostics and decision making. Fusion algorithms are associated with many challenges, conditioned

V. Georgieva (✉)
Faculty of Telecommunications, Technical University of Sofia, 8 Kl. Ohridski Blvd., 1000 Sofia, Bulgaria
e-mail: vesg@tu-sofia.bg

D. Tsvetkova
Faculty of German Engineering Education and Industrial Management, Technical University of Sofia, 8 Kl. Ohridski Blvd., 1000 Sofia, Bulgaria

not only with theoretical origin, but also to the nature of medical images, which in most cases are low contrast, poor quality and show ambiguous information.

The multimodal medical image fusion (MMIF) is described as a process that combines two or more geometrically registered images of a single or multiple modalities. The main purpose is to generate a composed fused image with improved quality and clear characteristics [1–4]. In addition, the rapid progress in medical imaging techniques (Computed Tomography (CT), Positron Emission Tomography (PET), Magnetic Resonance Imaging (MRI), and Single Photon Emission Computed Tomography (SPECT)) can help the researcher to fuse different modalities to be useful in making decisions by experts during biopsy, applying computer diagnostics and therapy. Moreover, fused images can help solve other tasks such as detection, segmentation and classification.

The aim of this survey is to focus on some trends in the application of geometric approaches in image registration and sparse representation and their role for obtaining better results in multimodal medical image fusion procedures due to their significance in the medical field. The paper is organized as follows. Section 2.2 describes the main steps in image fusion procedure, and different levels of fusion. In Sect. 2.3 the registration process as an essential step in performing the fusion process and trends in the application of rigid and non-rigid transformations are described. Section 2.4 is focused on multimodal medical image fusion with sparse representation. Finally, Sect. 2.5 concludes the paper with a summary of the brief survey.

2.2   Main Steps in Image Fusion Procedure

The general multimodal medical image fusion procedure consists of some main steps [5]. These steps are described here briefly. First, the body organ of interest is selected for making the multimodal image fusion. Then, two or more imaging modalities are selected to fuse using an appropriate algorithm. Figure 2.1 presents schematically the main steps of the procedure.

An important step in the procedure is to register the input medical images. Image registration is the process of mapping input images using a reference image. The purpose of such mapping is to match the corresponding images based on certain characteristics. The registration step is considered as an optimization problem whose aim is to maximize the similarity. In the registration process, a parametric transformation is applied on the input (target) images in order to maximize their similarity with the reference image. Choosing an appropriate geometric transformation model is extremely important to perform correct registration. It is essential that targeted similarity depends on the defined similarity (cost) function [5].

In the future extraction step, the characteristic features of the registered images are extracting and producing one or more feature maps for each of the input images [5, 6].
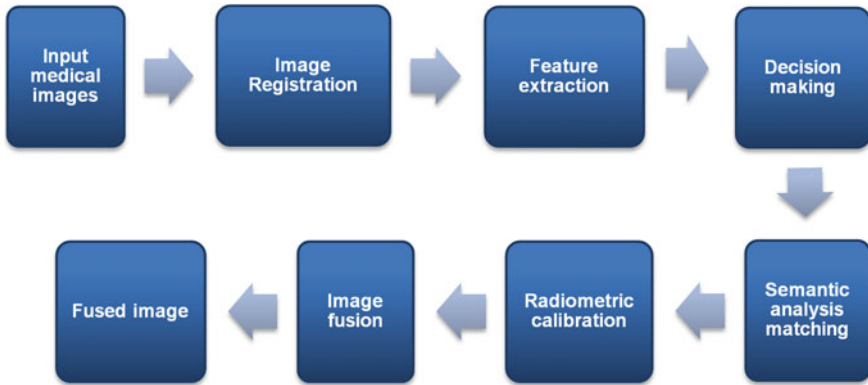
Fig. 2.1 Main steps in medical image fusion procedure

The step for decision making is characterized as follows: when selecting a given criterion, a set of decision maps is created by applying a decision operator that aims to label the pixels of the registered images or feature maps [6].

Semantic analysis matching is needed in cases where the resulting decision maps may not refer to the same object. In these cases, semantic equivalence is applied to associate these maps with a common object to facilitate the merging procedure [7]. Such a procedure is not necessary for input images obtained from the same type of sensors [5].

In the radiometric calibration step, the spatially aligned input images and feature maps are transformed to a common scale. The goal is obtaining a general representation format to act as input to the next step [7].

The final step of the procedure is to combine the images obtained into one output image, which contains a better description of the object than each of the input images. The advantage of image fusion is the quality of the information contained in the fused image.

The fusion process can be performed at three levels, namely: pixel level, feature level and decision level [1]. Pixel-level fusion is a direct process that combines the data from imaging modalities. Fusion at the feature level uses machine learning and statistical approaches for combining the features extracted from different data types. Fusion of decision level is related to a combination of variables that are related to the rules of decision.

Multimodal medical image fusion can be performed in the spatial domain, or in the transform domain. The characteristic of processing in the spatial domain is that we can directly process pixels rather than transform the coefficients. The regions or pixels are selected directly in accordance with some visibility measures, and are then combined with linear or non -linear operations. If more salient features cannot be captured in the spatial domain, the fusion is made in the transformation domain.

2.3 Geometric Approaches in Multimodal Registration

Multimodal medical image registration tasks have an important role in image fusion. The main applications are connected with reconstruction of the 3D images, medical object recognition and analysis. It is connected with correction of different patient positions between scans. Medical image registration allows structural (CT, MRI, US) and functional (PET, SPECT, fMRI) images to be presented and analyzed in the same coordinate system [8]. The registration algorithm includes three components and is presented in Fig. 2.2. The similarity measures are needed to show how well the images are matched. For example, in registration based on patient image content we can use geometric approaches. They build explicit models of anatomical elements, which can be identifying in the images. The elements include important surfaces, curves and point landmarks.

They can be matched with their corresponding elements in the other image [9, 10]. Linear features called ridges are extracted directly from 3D images [11, 12]. Most of the non-rigid registration approaches are based on 3D geometric features, which are anatomical surfaces [9, 13, 14].

The transformation model defines how the source image can be changed to match the other. This model has two main goals: to control how the selected features can be moved to one another for improving the similarity and to interpolate between those features that are known to contain no useful information [9]. For this purpose rigid and non-rigid registrations are used.

The optimization process is connected with adjustment of the transformation to improve the medical image similarity.

The registration methods based on geometric approaches can be classified on three basic criteria: dimensionality, type of transformation and domain of transformation. Figure 2.3 presents this classification.

The dimensionality can be presented for spatial cases as well as for time domains. In multimodal medical image registration, spatial dimensions are typically 3D but they can also be of two-dimensions. The 3D to 3D registration gives most accurate registration results. The 2D to 2D registration is less complicated, easier in implementation and faster than 2D to 3D and 3D to 3D. Dimensionality 2D to 3D is used for positioning of slices from tracked B-mode ultrasound, interventional CT, or interventional MRI images for construction of 3D volume [5, 15]. But in some situations, different from operations and radiotherapy the computational complexity and the speed of applying 2D to 3D registration are not relevant.

Fig. 2.2 Registration algorithm structure
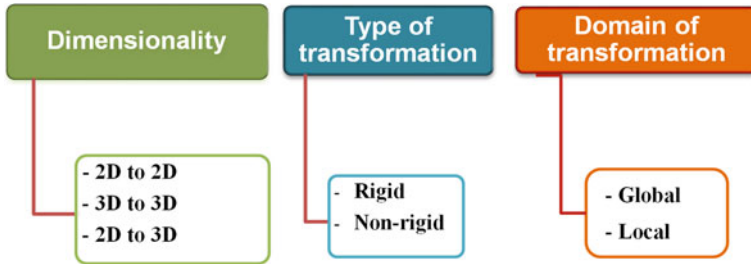
Fig. 2.3 Classification of geometric approaches

The rigid transformation methods are characterized so that the 2D or 3D images are transformed by translating, rotating, scaling and/or shearing of every depicted object in the same way so that distances, lines and angles are preserved [5, 16, 17]. These methods include affine transformation. They can be represented with homogeneous matrices (4×4 matrices) for 3D to 3D mapping [18]. These methods are applied to the images that contain small changes in the object shape and lead to a good approximation in medical image registration. Figure 2.4 presents the US image of esophageal adenocarcinoma [19] and its modification by translating, rotating, and shearing.

But in many cases various body organs have spatially variant geometric differences and require more flexible methods to achieve the multimodal medical registration task. The most used methods nowadays are based on non-rigid registration techniques. They have many applications such as modeling, tissue deformations to anatomical structures' variability [5]. The types of non-rigid registration techniques are presented in Fig. 2.5.

For registration metric is used to determine the distance between corresponding pairs of landmarks, which are obtained from the images. In the case of non-rigid registration, these landmarks are used with thin-plate splines. The landmarks allow to determine the transformation in closed form, but their disadvantages are that we need a large number to try a tightly the deformed field and the localization process can introduce an error. Modern trends are in the use of image similarity measure.

The geometric transformations can be global or local. Global transformations are made with mapping parameters valid for the all image. In the local case, a small part of the image is transformed where the local mapping function parameters are exclusively valid for a small area around the position of the selected control point [5, 15].

In [20] the geometric information is used, such as edges and thin structures, for obtaining a similarity measure for deformable registration models of multimodal images. The idea is to register the template image with the reference one by applying a spatial transformation to the template image. The authors introduce a new similarity term for image registration which is based on the geometric information that is extracted from the images by using the Blake-Zisserman's energy (BZ), an energy that is defined by a second-order derivative [20, 21]. This model is compared to
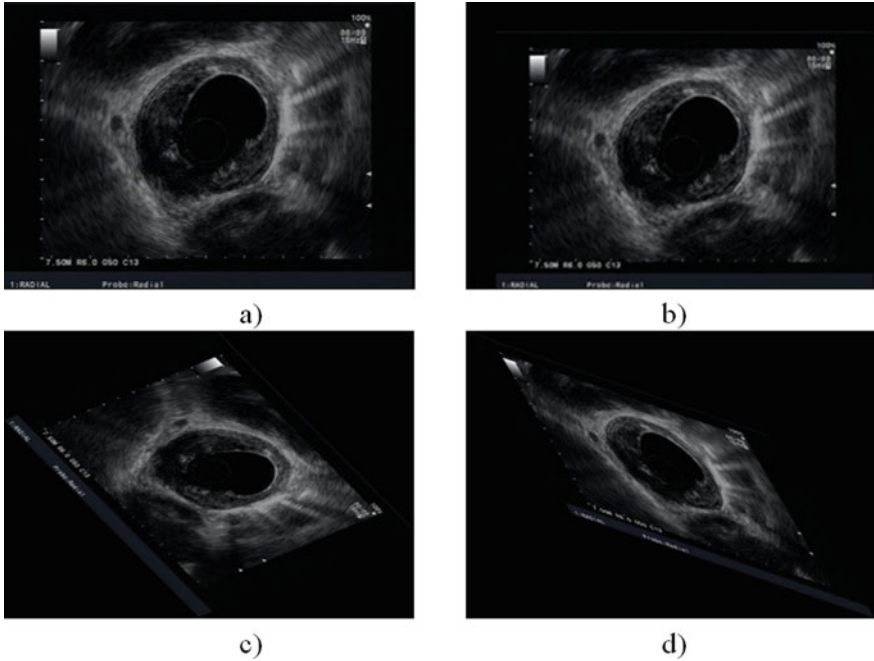
Fig. 2.4 US image of esophageal adenocarcinoma: **a** original; **b** translated; **c** rotated on 30°; **d** after shearing
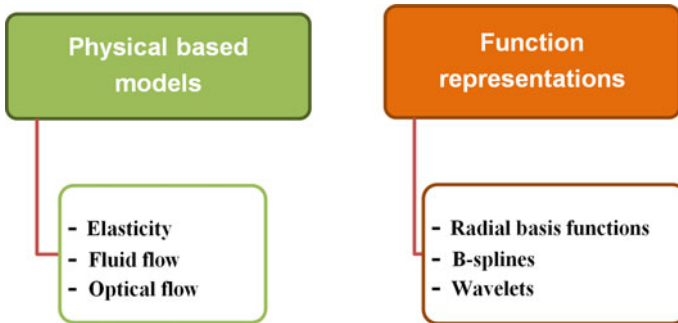
Fig. 2.5 Non-rigid registration techniques

the Mumford-Shah energy model, which uses only first-order derivatives [22]. The model based on first order derivative cannot be useful when the image contains high-order features such as thin structures. The proposed model was tested by MRI cross sections of the brain [20].

On the basis of research presented in [5], the following data on the application of rigid and non-rigid types of transformation for diagnostic features of some diseases are summarized. They are given in Table 2.1.

The main trends of application of geometric approaches are connected to combinations of techniques from different types. Much of researches are in the field of investigation of the normal and pathological structure of the brain [23, 24].

By a combination of geometric information from white and gray matter their morphology is investigated and a framework in multimodal brain image fusion from diffusion tensor imaging is proposed [25]. The authors introduce a scale-based white matter geometry method for the analysis. This method is an intermediate between the tensor gradient method [26] and vector field methods. The advantage is that there is no limit to the tensor model of diffusion and more precise characteristics of macrostructures in different spatial scales. Furthermore this method uses a tangent vector field of tracts and can be compared to the tensor-based model of dispersion in [26]. The advantage is that the analysis of a specific tract can be made independently from other tracts, which are in the neighbor. This method is used to study autism disaster in children.

The multimodal fusion of the brain image based on geometric framework for feature mapping is used in [27]. It is applied by fusing structural MRI and diffusion MRI images for improving statistical analysis. The authors propose to adopt the Riemannian metric for modeling an inherent relation between white and gray matter anatomical features. An adjustment of Riemannian metrics for presenting the original mesh of obtaining the feature embedding is used for this purpose. As result a unified framework for mapping of the surface and volumetric features from neuroimaging data based on geometric methods with defined Riemannian metrics is obtained. This approach is investigated for classifying such diseases as Alzheimer, mild cognitive impairment and Schizophrenia [27].

In [28] a comparative analysis of 3 different gradient geometries for MRI and PET brain image fusion is presented. The proposed approach includes separation of luminance channel from each of the images. The gradients are than selected using

Table 2.1 Types of transformation for diagnostic features of some diseases

Diseases	Modality	Transformation type
Parkinson	MRI/SPECT	Non-rigid/rigid
Cerebral tumor deformations	CT/MRI	Non-rigid
Eye fundus	Ophthalmological images	Rigid
Retinal diseases	Ophthalmological images	Rigid
Tongue disorders	hMR/Cine MR	Non-rigid
Coronary artery diseases	X-ray/CT	Non-rigid
Carotid arteries	US/MRI	Non-rigid/Rigid
Liber tumor	CT/US	Rigid
Prostate Cancer	TRUS/MRI	Non-rigid

various geometries such as Hudgin geometry, Fried geometry, Southwell geometry. Each of these strategies are results of different quality of the fused image that can be used for reconstruction. The reconstruction of the channel from the gradient data is made on the base of the wavelet algorithm proposed in [29], followed by image enhancement with gamma correction. The fusion procedure for grayscale images is the same as for the luminance channel. The experimental results show that the Soutwell geometry provides better quality of the fused MRI and PET image in the case of diagnoses of brain tumor, motor neuron disease, metastatic bronchogenic carcinoma and hypertensive encephalopathy [28].

Another direction of application of geometric approaches is connected to perform all fusion operation in the contourlet, shearlet or wavelet domains.

The fusion of CT/MRI based on multiscale geometric analysis of contourlet transform is presented in [30]. This transform has more advantages over the conventional image representation methods. It is more suitable for the human vision system. Compared with other multi-scale decompositions, the nonsubsampled contourlet transform eliminates the "block-effect" and the "pseudo-effect". It represents the source image in multiple directions and captures the geometric structure of source image in the transform domain [31, 32].

An optimization model for fusing CT and MRI images is proposed in [33]. It is based on structure tensor and nonsubsampled shearlet transform (NSST). The advantage is effective extraction of geometric features. The pre-fused gradient can be obtained from the weighted structure tensor. The final image is a result from solving the constructed optimization problem by the conjugate gradient method [33].

Using multi-scale geometric and multi-resolution geometric analysis an optimized multimodal medical image fusion framework is proposed in [34]. The idea is to obtain high-spectral and high-spectral spatial data. As the solution is proposed a complete fusion system for CT/MRI brain images is obtained according to their multi-resolution, multi-scale transforms. A modified central force optimization (MCFO) technique is used in the optimization step. It is based on Optimized Discrete Wavelet and Dual-Tree as a multi-resolution transform [34].

2.4 Multimodal Medical Fusion with Sparse Representation

In recent years, the multiscale decomposition methods have developed quickly. These are the following methods: discrete wavelet transform (DWT) [35, 36], framelet transform [37], contourlet transform [30], and non-subsampled contourlet transform (NSCT) [38, 39]. But transform-based methods give poor fusion results due to the presence of noise and difficulty in choosing the decomposition levels [38, 40, 41].

Sparse representation (SR) has many advantages compared to conventional representation approaches. The problem is that image fusion based on joint sparse representation needs much iteration and accordingly many resources in terms of memory

and time. The decision map can help to solve this task by extracting the local structure feature of the image blocks [42, 43].

In [38], three decision maps are constructed. They include structure information map and energy information map, as well a composite structure and energy map with the goal to reserve more energy and edge information. For medical image fusion of CT/MRI, MRIT1/MRIT2 and CT/PET based on SR with the decision map, the local structure and energy information of images is added. The proposed approach improves the speed of processing and the quality of the fused images.

In [44], the authors proposed a multimodal medical fusion algorithm with geometric algebra based sparse representation. In the traditional sparse representation fusion method, the color channels usually are processed separately. This destroys the correlation between image channels and results in loss of color in the fused image. Geometric algebra (GA) has many applications. The geometric algebra space does not work with coordinate information [45]. All geometric operators are included in the space. The multimodal medical image can be represented as a multi-vector. The proposed model for medical image fusion based on geometric algebra and sparse representation has the advantage of preventing the loss of channels correlation of the image [44, 46, 47]. For obtaining the sparse coefficient matrix is proposed to apply an orthogonal matching pursuit algorithm based on geometric algebra. For a more specific disease information that can be used for diagnosis, the dictionary learning method based on geometric algebra is applied. The fusion procedure was made on SPECT-T1 and SPECT-TC1 medical images for neoplastic disease of brain tumor [44].

2.5   Conclusion

In this paper we present some trends in the application of geometric approaches in the fusion of multimodal medical images. The application of geometric approaches is shown primarily in the registration processes as in sparse representation. This includes both geometric transformations themselves as well as the processes of extracting geometric features and the use of geometric models. The brief survey shows that the main trends are related to the use of hybrid methods. They are characterized by the following:

- They combine purely geometric models with transformation models in order to obtain a better quality of the multimodal medical fused image;
- For the optimization step in the registration process, a model based on structure tensor and nonsubsampled shearlet transform for fusing is proposed. The advantage is effective extraction of geometric features;
- Another advantage is that in this way the computational resources in terms of memory and time can be reduced;

- There are in the literature mainly described results related to the application of geometric approaches in multimodal image fusion in the field of brain diseases, but opportunities for their use in other diseases are increasingly sought;
- Another major trend is their application in the fusion of nuclear medicine images and images from other modalities.

References

1. Hermessi, H., Mourali, O., Zagrouba, E.: Multimodal medical image fusion review: theoretical background and recent advances. Signal Process. **183**, 1–27 (2021)
2. Du, J., Li, W., Lu, K., Xiao, L.: An overview of multi-modal medical image fusion. Neurocomputing **215**, 3–20 (2016)
3. Li, Sh., Kang, H., Fang, L., Hu, J., Yin, H.: Pixel-level image fusion: a survey of the state of the art. Inf. Fusion **33**, 100–112 (2017)
4. Liu, Y., Chen, X., Wang, Z., Wang, Z.J., Ward, R., Wang, X.: Deep learning for pixel-level image fusion: recent advances and future prospects. Inf. Fusion **42**, 158–173 (2018)
5. El-Gamal, F., Elmogy, M., Atwan, A.: Current trends in medical image registration and fusion. Egypt. Inf. J. **17**(1), 99–124 (2016)
6. Mitchel, H.: Image Fusion: Theories, Techniques and Applications. Springer, Heidelberg (2010)
7. Mitchel, H.: Data Fusion: Concepts and Ideas, 2nd edn. Springer, Heidelberg (2012)
8. Crum, W., Hartkens, T., Hill, D.: Non-rigid image registration: theory and practice. Br. J. Radiol. **77**, 140–153 (2004)
9. Johnson, H.J., Christensen, G.E.: Consistent landmark and intensity-based image registration. IEEE Trans. Med. Imaging **21**, 450–461 (2002)
10. Crum, W., Griffin, L., Hill, D., Hawkes, D.: Zen and the art of medical image registration: correspondence, homology, and quality. Neuroimaging **20**, 1425–1437 (2003)
11. Rohr, K., Stiehl, H., Sprengel, R., Buzug, T., Weese, J., Kuhn, M.: Landmark-based elastic registration using approximating thin-plate splines. IEEE Trans. Med. Imaging **20**, 526–534 (2001)
12. Rohr, K., Fornefett, M., Stiehl, H.: Spline-based elastic image registration: integration of landmark errors and orientation attributes. Comput. Vis. Image Underst. **90**, 153–168 (2003)
13. Ferrant, M., Nabavi, A., Macq, B., Jolesz, F., Kikinis, R., Warfield, S.: Registration of 3-D intraoperative MR images of the brain using a finite-element biomechanical model. IEEE Trans. Med. Imaging **20**, 1384–1397 (2001)
14. Liu, T., Shen, D., Davatzikos, C.: Deformable registration of cortical structures via hybrid volumetric and surface warping. Neuroimaging **22**, 1790–1801 (2004)
15. Mani, V., Arivazhagan, Dr.: Survey of medical image registration. J. Biomed. Eng. Technol. **1**(2), 8–25 (2013)
16. Khalifa, F., Beache, G., Gimel'farb, G., Suri, J., El-Baz, A.: State-of-the-art medical image registration methodologies: a survey. In: Multimodality State-of-the-Art Medical Image Segmentation and Registration Methodologies, pp. 235–280. Springer, Boston (2011)
17. Goshtasby, A.: Image Registration: Principles, Tools and Methods. Springer, London (2012)

18. Holden, M.: A review of geometric transformations for non-rigid body registration. IEEE Trans. Med. Imaging **27**(1), 111–128 (2008)
19. https://radiopaedia.org/
20. Lajili, M., Theljani, A., Moakher, M., Rjaibi, B.: Multimodal image registration based on geometric similarity term. In: Proceeding of African Conference on Research in Computer Science and Applied Mathematics – CARI 22, pp. 1–8 Tunis-Yaoundé-Dschang (2022)
21. Zanetti, M., Vitti, A.: The Blake-Zisserman model for digital surface models segmentation. ISPRS Ann. Photogramm. Remote Sens. Spatial Inf. Sci., II-5/W2, 355–360 (2013)
22. Mumford, D., Shah, J.: Optimal approximation by piecewise smooth functions and associated variational problems. Commun. Pure Appl. Math. **42**, 577–685 (1989)
23. Diwakar, M., Singh, P., Ravi, V., Maurya, A.: A non-conventional review on multi-modality-based medical image fusion. Diagnostics **13**(820), 1–21 (2023)
24. Haribabu, M., Guruviah, V., Yogarajah, P.: Recent advancements in multimodal medical image fusion techniques for better diagnosis: an overview. Current Med. Imaging **19**(7), 673–694 (2023)
25. Savadjiev, P., Rathib, Y., Bouixb, S., Smithc, A., Schultzd, R., Vermac, R., Westin, C.F.: Fusion of white and gray matter geometry: a framework for investigating brain development. Med. Image Anal. **18**(8), 1349–1360 (2014)
26. Savadjiev, P., Kindlmann, G.L., Bouix, S., Shenton, M.E., Westin, C.F.: Local white matter geometry from diffusion tensor gradients. Neuroimaging **49**(3), 175–3186 (2010)
27. Zhang, W., Mi, L., Thompson, P., Wang, Y.: A geometric framework for feature mappings in multimodal fusion of brain image data. Inf. Process. Med. Imaging **11492**, 617–630 (2019)
28. Edith, J., Nithya, N., Palani, B., Thanaraj, K.: Evaluation of gradient geometry for multimodal medical image fusion. Int. J. Adv. Res. **5**(3), 1098–1105 (2017)
29. Sevcenco, I., Hampton, P., Agathoklis, P.: A wavelet based method for image reconstruction from gradient data with applications, multidimensional system and signal processing. Multidimension. Syst. Signal Process. **26**, 717–737 (2015)
30. Yang, L., Guo, B., Ni, W.: Multimodality medical image fusion based on multiscale geometric analysis of contourlet transform. Neurocomputing **72**(1–3), 203–211 (2008)
31. Liu, C., Chen, S., Fu, Q.: Multimodal image fusion using nonsubsamplet contourlet transform. IEICE Trans. Inf. Syst. **96**(10), 2215–2223 (2013)
32. Mei, Q., Li, M.: Nonsubsampled contourlet transform and adaptive PCNN for medical image fusion. J. Appl. Sci. Eng. **26**(2), 213–220 (2022)
33. Liu, X., Mei, W., Du, H.: Structure tensor and nonsubsampled shearlet transform based algorithm for CT and MRI image fusion. Neurocomputing **235**, 131–139 (2017)
34. Faragallah, O.S., El-Hoseny, H., El-Shafai, W., et al.: Optimized multimodal medical image fusion framework using multi-scale geometric and multi-resolution geometric analysis. Multimed. Tools Appl. **81**, 14379–14401 (2022)
35. Liu, Z., Yin, H., Chai, Y., Yang, S.: A novel approach for multimodal medical image fusion. Expert Syst. Appl. **41**(16), 7425–7435 (2014)
36. Shen, R., Cheng, I., Basu, A.: Cross-scale coefficient selection for volumetric medical image fusion. IEEE Trans. Biomed. Eng. **60**(4), 1069–1079 (2013)
37. Bhatnagar, G., Wu, Q., Liu, Z.: Human visual system inspired multi-modal medical image fusion framework. Expert Syst. Appl. **40**(5), 1708–1720 (2013)
38. Fei, Y., Wei, G., Zongxi, S.: Medical image fusion based on feature extraction and sparse representation. Int. J. Biomed. Imaging **2017**, 1–11 (2017)
39. Gomathi, P., Kalaavathi, B.: Multimodal medical image fusion in non-subsampled contourlet transform domain. Circuits Syst. **7**(8), 1598–1610 (2016)
40. Kim, M., Han, D., Ko, H.: Joint patch clustering-based dictionary learning for multimodal image fusion. Inf. Fusion **27**, 198–214 (2016)
41. Yao, Y., Guo, P., Xin, X., Jiang, Z.: Image fusion by hierarchical joint sparse representation". Cogn. Comput. **6**(3), 281–292 (2014)
42. Yang, Y., Tong, S., Huang, S., Lin, P.: Multifocus image fusion based on NSCT and focused area detection. IEEE Sens. J. **15**(5), 2824–2838 (2015)

43. Liu, Y., Liu, S., Wang, Z.: Multi-focus image fusion with dense SIFT. Inf. Fusion **23**, 139–155 (2015)
44. Li, Y., Fang, N., Wang, H., Wang, R.: Multi-modal medical image fusion with geometric algebra based sparse representation. Front. Genet. **13**, 1–9 (2022)
45. Batard, T., Saint-Jean, C., Berthier, M.: A metric approach to Nd images edge detection with Clifford algebras. J. Math. Imaging Vis. **33**, 296–312 (2009)
46. Rocha, R., Vaz, J.: Extended Grassmann and Clifford algebras. Adv. Appl. Clifford Algebras **16**, 103–125 (2006)
47. López-González, G., Altamirano-Gómez, G., Bayro-Corrochano, E.: Geometric entities voting schemes in the conformal geometric algebra framework. Adv. Appl. Clifford Algebras **26**, 1045–1059 (2016)

Chapter 3
Weighted Tensor Least Angle Regression for Solving Sparse Weighted Multilinear Least Squares Problems

Ishan M. Wickramasingha, Biniyam K. Mezgebo, and Sherif S. Sherif

Abstract Sparse weighted multilinear least-squares is a generalization of the sparse multilinear least-squares problem, where prior information about, e.g., parameters and data is incorporated by multiplying both sides of the original problem by a typically diagonal weights matrix. However, the introduction of arbitrary diagonal weights would result in a non-Kronecker least-squares problem that could be very large to store or solve practically. In this paper, we generalize our recent Tensor Least Angle Regression (T-LARS) algorithm to efficiently solve either L_0 or L_1 constrained multilinear least-squares problems with arbitrary diagonal weights for all critical values of their regularization parameter. To demonstrate the validity of our new Weighted Least Angle Regression (WT-LARS) algorithm, we used it to successfully solve three different image inpainting problems by obtaining sparse representations of binary-weighted images.

3.1 Introduction

Weighted least squares is a generalization of the least-squares (LS) problem, where prior information about parameters and data is incorporated by multiplying both sides of the original LS problem by a typically diagonal weights matrix. Applications of weighted least-squares in Signal Processing include signal restoration [1, 2], source localization in wireless networks [3–6], adaptive filters [4, 7–9], and image smoothing [10]. In Statistics, weighted least-squares regression is often used to reduce bias from non-informative data samples [11, 12]. Also, a best linear unbiased estimator (BLUE) is obtained by using the inverse of the data covariance matrix as the weights matrix [13].

Recently, sparsity has become a commonly desired characteristic of a least-squares solution [14, 15]. Because of its relatively small number of non-zero values, a sparse

I. M. Wickramasingha · B. K. Mezgebo · S. S. Sherif (✉)

Department of Electrical and Computer Engineering, University of Manitoba, Winnipeg, Canada

e-mail: Sherif.Sherif@umanitoba.ca

solution could result in faster processing with lower computer storage requirements [14, 15]. A sparse solution is usually obtained by solving a least-squares problem while minimizing either the L_0 norm of the solution (non-convex optimization problem) or minimizing the L_1 norm of the solution (convex optimization problem), where the L_0 norm of a vector is its number of non-zero elements and the L_1 norm of a vector is the sum of the magnitude of its elements [14].

Several methods have been proposed to solve sparse least-squares problems, including the *Method of Frames* [16], *Matching Pursuit* (MP) [17], *Orthogonal Matching Pursuit* (OMP) [18], *Best Orthogonal Basis* [19], *Least Absolute Shrinkage and Selection Operator* (LASSO) that is also known as *Basis Pursuit* [20, 21], and *Least Angle Regression* (LARS) [21]. Both MP and OMP solve the L_0 constrained least-squares problem [22] using sequential heuristic steps that add solution coefficients in a greedy, i.e., non-globally optimal, way. LASSO relaxes the non-convex L_0 constrained least-squares problem to solve the convex L_1 constrained least-squares problem instead [20]. Among the above solution methods, only *Least Angle Regression* could efficiently solve both the L_0 and, with a slight modification, L_1 constrained least-squares problem for all critical values of their regularization parameters. This parameter is required to balance the minimization of the LS residual with the minimization of the norm of the solution [21].

In addition to incorporating a priori information, weights also could be introduced to sparse least-squares problems to improve the L_1 minimization problem results [23, 24]. Candès et al. also used a reweighted L_1 minimization approach to enhance sparsity in compressed sensing [25]. Also, weighted L_1 constrained least-squares regression has been used to extract information from large data sets for statistical applications [26, 27]. We note that sparse weighted least-squares problems could be solved using any of the above optimization methods.

Multilinear least-squares is a multidimensional generalization of least-squares [28–30], where the least-squares matrix has a Kronecker structure [31, 32]. Sparse multilinear least-squares could be either an L_0 constrained or an L_1 constrained multilinear least-squares problem. Caiafa and Cichocki introduced a generalization of OMP, *Kronecker-OMP*, to solve the L_0 constrained sparse multilinear least-squares problem [32]. Elrewainy and Sherif [33] developed *Kronecker Least Angle Regression* (K-LARS) to efficiently solve both L_0 and L_1 constrained sparse least-squares having a specific Kronecker matrix form, $A \otimes I$, for all critical values of the regularization parameter. To overcome this limitation, the authors further developed Tensor Least angle Regression (T-LARS) [30], a generalization of K-LARS that does not require any special form of the LS matrix beyond being Kronecker. T-LARS solves either large L_0 or large L_1 constrained, sparse multilinear least-squares problems (underdetermined or overdetermined) for all critical values of the regularization parameter λ with significantly lower computational complexity and memory usage than Kronecker-OMP.

Weighted multilinear least-squares is a generalization of multilinear least-squares that introduces a typically diagonal weight matrix to both sides of the original LS problem. Since an arbitrary diagonal weight matrix would not be Kronecker, the

weighted LS matrix would lose its original Kronecker structure, resulting in a potentially very large non-Kronecker LS matrix. Thus solving these weighted sparse multilinear least-squares problems could become highly impractical, as it would require significant memory and computational power.

Therefore, in this paper, we extend T-LARS to Weighted Tensor Least Angle Regression (WT-LARS) that could solve efficiently both L_0 and L_1 constrained sparse weighted multilinear least-squares problems for all critical values of the regularization parameter. It is organized as follows: Sect. 3.2 includes a brief introduction to the sparse weighted multilinear least-squares problem. In Sect. 3.3, we describe our new Weighted Tensor Least Angle Regression (WT-LARS) algorithm in detail. Section 3.4 provides results of applying WT-LARS to solve three different image inpainting problems by obtaining sparse representations of binary-weighted images. We present our conclusions in Sect. 3.5.

3.2 Problem Formulation

3.2.1 Sparse Weighted Multilinear Least-Squares Problem

A multilinear transformation of a tensor $\mathcal{X}$ could be defined as, $\mathcal{Y} = \mathcal{X} \times_1 \mathbf{\Phi}^{(1)} \times_2 \cdots \times_N \mathbf{\Phi}^{(N)}$, where $\mathcal{Y} \in \mathbb{R}^{J_1 \times \cdots \times J_n \times \cdots \times J_N}$ and $\mathcal{X} \in \mathbb{R}^{I_1 \times \cdots \times I_n \times \cdots \times I_N}$ are N^{th} order tensors, with the equivalent vectorized form

$$\Phi vec(\mathcal{X}) = vec(\mathcal{Y}) \tag{3.1}$$

where $\mathbf{\Phi} \in \mathbb{R}^{J \times I}$, and $\mathbf{\Phi} = \mathbf{\Phi}^{(N)} \otimes \cdots \otimes \mathbf{\Phi}^{(1)}$, and $\otimes$ is the Kronecker product operator [34].

Let $\mathbf{W} = \mathbf{S}^H \mathbf{S}$, be a diagonal weight matrix. We could obtain a weighted linear transformation [35] of (1) as

$$\mathbf{S}\Phi vec(\mathcal{X}) = S vec(\mathcal{Y}) \tag{3.2}$$

A sparse solution of the weighted linear system in (2) could be obtained by solving an L_p ($p = 0$ or $p = 1$) minimization problem,

$$\overset{\sim}{\mathcal{X}} = \underset{\mathcal{X}}{\operatorname{argmin}} \|\mathbf{S}\mathbf{\Phi} vec(\mathcal{X}) - \mathbf{S} vec(\mathcal{Y})\|_2^2 + \lambda \|vec(\mathcal{X})\|_p \tag{3.3}$$

where λ is a regularization parameter.

If $\mathbf{S}$ is a Kronecker matrix, then $\mathbf{S}\mathbf{\Phi} = \left(\mathbf{S}^{(N)}\mathbf{\Phi}^{(N)} \otimes \cdots \otimes \mathbf{S}^{(1)}\mathbf{\Phi}^{(1)}\right)$ and we could use T-LARS [30] to obtain a sparse solution for either L_0 or L_1 optimization problem in (3) efficiently. However, $\mathbf{S}$ is not typically Kronecker, so $\mathbf{S}\mathbf{\Phi}$ would not have a Kronecker structure, and (3) should be solved as a potentially very large vectorized

(one-dimensional) sparse least-squares problem which could be very challenging in terms of memory and computational power requirements. Therefore, in this paper, we develop Weighted Tensor Least Angle Regression (WT-LARS), a computationally efficient method, to solve either L_0 or L_1 constrained sparse weighted multilinear least-squares problems in (3) for an arbitrary diagonal weights matrix $W = S^H S \in \mathbb{R}^{J \times J}$.

3.3 Weighted Tensor Least Angle Regression

In this section, we develop Weighted Tensor Least Angle Regression (WT-LARS) by extending T-LARS to solve the sparse weighted multilinear least-squares problem in (3), for weights $W = S^H S$ and Kronecker dictionaries $\boldsymbol{\Phi}$.

Inputs to WT-LARS are the data tensor $\mathcal{Y} \in \mathbb{R}^{J_1 \times \cdots \times J_n \times \cdots \times J_N}$, mode-$n$ dictionary matrices $\boldsymbol{\Phi}^{(n)}$; $n \in \{1, \cdots, N\}$ where $\boldsymbol{\Phi} = \boldsymbol{\Phi}^{(N)} \otimes \cdots \otimes \boldsymbol{\Phi}^{(1)}$, the diagonal weight matrix $W = S^H S$, and the stopping criterion as a residual tolerance ε or the maximum number of non-zero coefficients K (K-sparse representation). The output is the solution tensor $\mathcal{X} \in \mathbb{R}^{I_1 \times \cdots \times I_n \times \cdots \times I_N}$.

WT-LARS requires weighted data $S\text{vec}(\mathcal{Y})$, and columns of the weighted dictionary $S\boldsymbol{\Phi}$ to have a unit L_2 norm. Normalized weighted data could be easily calculated by $\mathcal{Y}_W = S\text{vec}(\mathcal{Y})/\|S\text{vec}(\mathcal{Y})\|_2$. However, the dictionary matrix $S\boldsymbol{\Phi}$ does not have a Kronecker structure. Hence, normalizing mode-n dictionary matrices $\boldsymbol{\Phi}^{(n)}$ does not ensure normalization of the columns of $S\boldsymbol{\Phi}$. Therefore, in WT-LARS, we use the normalized weighted dictionary matrix $\boldsymbol{\Phi}_W = S\boldsymbol{\Phi} Q$ instead of the normalized dictionary matrix $\boldsymbol{\Phi}$ in T-LARS, where Q is a diagonal matrix,

$$Q_{i,i} = \frac{1}{\|(S\boldsymbol{\Phi})_i\|_2} \tag{3.4}$$

where $(S\boldsymbol{\Phi})_i$ is the ith column of the weighted dictionary matrix $S\boldsymbol{\Phi}$. We can efficiently calculate the diagonal matrix Q as,

$$diag(Q) = 1./\sqrt{\left(\boldsymbol{\Phi}^{*2}\right)^T diag(W)} \tag{3.5}$$

where, $\boldsymbol{\Phi}^{*2}$ [36] denotes the Hadamard square of $\boldsymbol{\Phi}$, such that $\boldsymbol{\Phi}_{i,j}^{*2} = \left(\boldsymbol{\Phi}_{i,j}\right)^2$, "./" denotes elementwise division, and $diag(Q)$ and $diag(W)$ are diagonal vectors of Q and W respectively. We could efficiently calculate $\left(\boldsymbol{\Phi}^{*2}\right)^T diag(W)$ using the full multilinear product.

WT-LARS solves the L_0 or L_1 constrained minimization problems in (3) for all critical values of the regularization parameter λ. WT-LARS starts with a large value of λ, that results in an empty active set $I = \{\}$, and a solution $\widetilde{\mathcal{X}}_{t=0} = 0$. The set I denotes an active set of columns of the dictionary $\boldsymbol{\Phi}_W$, i.e., column indices where the optimal solution $\widetilde{\mathcal{X}}_t$ at iteration t, is nonzero, and I^c denotes its corresponding

inactive set. Therefore, $\boldsymbol{\Phi}_{W\,I}$ contains only the active columns of the dictionary $\boldsymbol{\Phi}_W$ and $\boldsymbol{\Phi}_{W\,I^c}$ contains only its inactive columns.

At each iteration t, a new column is either added (L_0) to the active set I or a new column is either added or removed (L_1) from the active set I, and λ is reduced by a calculated value δ_t^*.

As a result of such iterations, new solutions with an increased number of coefficients that follow a piecewise linear path are obtained until a predetermined residual error ε or a predetermined number of active columns K is obtained.

The regularization parameter λ is initialized to the maximum of the correlation $\boldsymbol{c}_1$, between the columns of $\boldsymbol{\Phi}_W$ and the initial residual $\boldsymbol{r}_0 = \mathrm{vec}(\mathcal{Y})$.

$$\boldsymbol{c}_1 = \boldsymbol{\Phi}_W^T \boldsymbol{r}_0 \tag{3.6}$$

Since $\boldsymbol{\Phi}_W^T = \boldsymbol{Q}\boldsymbol{\Phi}^T\boldsymbol{S}$, we can easily calculate $\boldsymbol{\Phi}^T\boldsymbol{S}\boldsymbol{r}_0$ using the full multilinear product as

$$\mathcal{C}_1' = \mathcal{R}_{\mathcal{S}_0} \times_1 \boldsymbol{\Phi}^{(1)^T} \times_2 \ldots \times_N \boldsymbol{\Phi}^{(N)^T} \tag{3.7}$$

where $\mathrm{vec}(\mathcal{R}_{\mathcal{S}_0}) = \boldsymbol{S}\boldsymbol{r}_0$ and $\boldsymbol{c}_1 = \boldsymbol{Q}\mathrm{vec}(\mathcal{C}_1')$. The column index corresponding to the maximum correlation $\boldsymbol{c}_1$ is added to the active set. For a given active set I, the optimal solution $\widetilde{\mathcal{X}}_t$ at any iteration t, could be written as

$$\mathrm{vec}\left(\widetilde{\mathcal{X}}_t\right) = \begin{cases} \left(\boldsymbol{\Phi}_{W_{I_t}}^T \boldsymbol{\Phi}_{W_{I_t}}\right)^{-1}\left(\boldsymbol{\Phi}_{W_{I_t}}^T \mathrm{vec}(\mathcal{Y}) - \lambda_t \boldsymbol{z}_t\right), & \text{on } I \\ 0, & \text{Otherwise} \end{cases} \tag{3.8}$$

where, $\boldsymbol{z}_t$ is the sign sequence of $\boldsymbol{c}_t$ on the active set I, and $\boldsymbol{c}_t = \boldsymbol{\Phi}_W^T \boldsymbol{r}_{t-1}$ is the correlation vector of all columns of the dictionary $\boldsymbol{\Phi}_W$ with the residual $\boldsymbol{r}_{t-1}$ at any iteration t.

The optimal solution at any iteration, t must satisfy the following two optimality conditions,

$$\boldsymbol{\Phi}_{W_{I_t}}^T \boldsymbol{r}_t = -\lambda_t \boldsymbol{z}_t \tag{3.9}$$

$$\left\|\boldsymbol{\Phi}_{W_{I_t^c}}^T \boldsymbol{r}_t\right\|_\infty \leq \lambda_t \tag{3.10}$$

where, $\boldsymbol{r}_t = \mathrm{vec}(\mathcal{Y}) - \boldsymbol{\Phi}_W \mathrm{vec}\left(\widetilde{\mathcal{X}}_t\right)$ is the residual at iteration t, and $\boldsymbol{z}_t$ is the sign sequence of the correlation $\boldsymbol{c}_t$ at iteration t, on the active set I. The condition in (9) ensures that the magnitude of the correlation between all active columns of $\boldsymbol{\Phi}_W$ and the residual is equal to $|\lambda_t|$ at each iteration, and the condition in (10) ensures that the magnitude of the correlation between the inactive columns of $\boldsymbol{\Phi}_W$ and the residual is less than or equal to $|\lambda_t|$.

At each iteration t, λ_t is reduced by a small step size, δ_t^*, until a condition in either (9) or (10) violates. For L_0, and L_1 constrained minimization problems, if an inactive column violates the condition (10), it is added to the active set, and for L_1 constrained minimization problems, if an active column violates the condition (9), it is removed from the active set.

As λ is reduced by δ_t^*, the solution $\widetilde{\mathcal{X}}_t$ changes by $\delta_t^* \boldsymbol{d}_t$ along a direction $\boldsymbol{d}_t$, where $\boldsymbol{d}_{I_t^c} = 0$ and $\boldsymbol{d}_{I_t} = \boldsymbol{G}_t^{-1}\boldsymbol{z}_t$, and $\boldsymbol{G}_t^{-1}$ is the inverse of the Gram matrix of the active columns of the dictionary $\boldsymbol{G}_t = \boldsymbol{\Phi}_{W\,I_t}^T \boldsymbol{\Phi}_{W\,I_t}$.

The size of this Gram matrix would either increase (dictionary column addition) or decrease (dictionary column removal) with each iteration t. Therefore, for computational efficiency, we use the *Schur complement* inversion formula to calculate $\boldsymbol{G}_t^{-1}$ from $\boldsymbol{G}_{t-1}^{-1}$ thereby avoiding its full calculation [30, 37].

The smallest step size for L_1 constrained sparse least-squares problem $\delta_t^* = \min\{\delta_t^+, \delta_t^-\}$ is the minimum of δ_t^+, minimum step size for adding a column, and δ_t^-, minimum step size for removing a column. The minimum step size for removing a column from the active set is given by,

$$\delta_t^- = \min_{i \in I}\left\{-\frac{x_{t-1}(i)}{d_t(i)}\right\} \tag{3.11}$$

The minimum step size for adding a new column to the active set is given by,

$$\delta_t^+ = \min_{i \in I^c}\left\{\frac{\lambda_t - c_t(i)}{1 - v_t(i)}, \frac{\lambda_t + c_t(i)}{1 + v_t(i)}\right\} \tag{3.12}$$

where

$$v_t = \boldsymbol{\Phi}_W^T \boldsymbol{\Phi}_W \boldsymbol{d}_t \tag{3.13}$$

Since $\boldsymbol{\Phi}_W = \boldsymbol{S}\boldsymbol{\Phi}\boldsymbol{Q}$, We can efficiently calculate v_t using two full multilinear products.

Let $v_t = \boldsymbol{Q}\text{vec}(\mathcal{V}_t\prime)$, where

$$\mathcal{V}_t' = \mathcal{U}_{w_t} \times_1 \boldsymbol{\Phi}^{(1)^T} \times_2 \ldots \times_N \boldsymbol{\Phi}^{(N)^T} \tag{3.14}$$

and $\text{vec}(\mathcal{U}_{w_t}) = \boldsymbol{W}\text{vec}(\mathcal{D}_t\prime \times_1 \boldsymbol{\Phi}^{(1)} \times_2 \ldots \times_N \boldsymbol{\Phi}^{(N)})$, and $\text{vec}(\mathcal{D}_t\prime) = \boldsymbol{Q}\boldsymbol{d}_t$.

The residual $\boldsymbol{r}_{t+1}$ is calculated at the end of each iteration using,

$$\boldsymbol{r}_{t+1} = \boldsymbol{r}_t - \delta_t^* \boldsymbol{\Phi}_W \boldsymbol{d}_t \tag{3.15}$$

where we can efficiently calculate $\boldsymbol{\Phi}_W \boldsymbol{d}_t$ using

$$\boldsymbol{\Phi}_W \boldsymbol{d}_t = \boldsymbol{S}vec(\mathcal{D}_t\prime \times_1 \boldsymbol{\Phi}^{(1)} \times_2 \cdots \times_N \boldsymbol{\Phi}^{(N)}) \tag{3.14}$$

WT-LARS stops at a predetermined residual error $\boldsymbol{r}_{t+1} \leq \varepsilon$ or when a predetermined number of active columns K is obtained.

3.3.1   Weighted Tensor Least Angle Regression Algorithm

Algorithm 1: Weighted Tensor Least Angle Regression (WT-LARS)

Input: *WT-LARS_mode = L_1 or L_0, normalized tensor $\mathcal{Y} \in \mathbb{R}^{J_1 \times \ldots \times J_n \times \ldots \times J_N}$; Mode-n dictionary matrices $\boldsymbol{\Phi}^{(n)} \in \mathbb{R}^{J_n \times I_n}$; $n \in \{1, \ldots N\}$;*

Diagonal Weights Matrix $\boldsymbol{W} \in \mathbb{R}^{(J_1 \times \ldots \times J_N) \times (J_1 \times \ldots \times J_N)}$; Stopping criterion: residual tolerance: ε or number of non-zero coefficients: K

Initialization: $\boldsymbol{S} = \sqrt{\boldsymbol{W}}$, Residual: $\boldsymbol{r}_0 = \boldsymbol{S}vec(\mathcal{Y})$; $\boldsymbol{x}_0 = 0$; $I = \{\}$;

1. $diag(\boldsymbol{Q}) = \boldsymbol{1}./\sqrt{(\boldsymbol{\Phi}^2)^T\, diag(\boldsymbol{W})}$
2. $vec(\mathcal{R}_{S_0}) = \boldsymbol{S}\boldsymbol{r}_0$
3. $\mathcal{C}_1 = \mathcal{R}_{S_0} \times_1 \boldsymbol{\Phi}^{(1)T} \times_2 \ldots \times_N \boldsymbol{\Phi}^{(N)T}$
4. $\boldsymbol{c}_1 = \boldsymbol{Q}vec(\mathcal{C}_1)$
5. $[\lambda_1, column\_idx] = max(\boldsymbol{c}_1)$
6. $I = \{column\_idx\}$
7. **while** $(\|\boldsymbol{r}_t\|_2 < \varepsilon$ or $length(I) < K)$**:**
8. $\boldsymbol{z}_t = sign\,(\boldsymbol{c}_t(I))$
9. $\boldsymbol{G}_t^{-1} = updateWeightedInverseGramMatrix(\ \boldsymbol{G}_{t-1}^{-1},\ \boldsymbol{W}\ ,\ \boldsymbol{Q}\ ,\ \{\ \boldsymbol{\Phi}^{(1)},\ \ldots,\ \boldsymbol{\Phi}^{(N)}\},\ I,$ $add\_column,\ column\_idx)$ % See reference [30]
10. $\boldsymbol{d}_{I_t} = \boldsymbol{G}_t^{-1}\boldsymbol{z}_t$
11. $vec(\dot{\mathcal{D}}_t) = \boldsymbol{Q}\boldsymbol{d}_t$
12. $\mathcal{U}_t = \dot{\mathcal{D}}_t \times_1 \boldsymbol{\Phi}^{(1)} \times_2 \ldots \times_N \boldsymbol{\Phi}^{(N)}$
13. $vec(\mathcal{U}_{w_t}) = \boldsymbol{W}vec(\mathcal{U}_t)$
14. $\mathcal{V}_t = \mathcal{U}_{w_t} \times_1 \boldsymbol{\Phi}^{(1)T} \times_2 \ldots \times_N \boldsymbol{\Phi}^{(N)T}$
15. $\boldsymbol{v}_t = \boldsymbol{Q}vec(\mathcal{V}_t)$
16. $\delta_{t\,1}^+ = (\lambda_t - \boldsymbol{c}_t(I^c))./(1 - \boldsymbol{v}_t(I^c))$ % "./" - Elementwise division
17. $\delta_{t\,2}^+ = (\lambda_t + \boldsymbol{c}_t(I^c))./(1 + \boldsymbol{v}_t(I^c))$
18. $\delta_t^- = -\boldsymbol{x}_{t-1}./\boldsymbol{d}_t$
19. $[\delta_t^*,\ column\_idx] = min\,(\delta_{t\,1}^+, \delta_{t\,2}^+)$
20. $add\_column == True$
21. **if** *WT-LARS_mode == L_1 && $min\,(\delta_t^-) < \delta_t^*$***:**
22. $[\delta_t^*,\ column\_idx] = min\,(\delta_t^-)$
23. $add\_column = False$
24. **end**
25. $\boldsymbol{x}_t = \boldsymbol{x}_{t-1} + \delta_t^* \boldsymbol{d}_t$
26. $\lambda_{t+1} = \lambda_t - \delta_t^*$
27. $\boldsymbol{c}_{t+1} = \boldsymbol{c}_t - \delta_t^* \boldsymbol{v}_t$
28. $\dot{\mathcal{R}}_t = \dot{\mathcal{D}}_t \times_1 \boldsymbol{\Phi}^{(1)} \times_2 \cdots \times_N \boldsymbol{\Phi}^{(N)}$
29. $\boldsymbol{r}_{t+1} = \boldsymbol{r}_t - \delta_t^* \boldsymbol{S}vec(\dot{\mathcal{R}}_t)$
30. **if** $add\_column == True:$ $I = I + \{column\_idx\}$
31. **else:** $I = I - \{column_{idx}\}$ **end**
32. **end while**
33. **return** I, $\boldsymbol{x}$

3.4 Experimental Results

In this section, we present experimental results for WT-LARS as a tensor completion problem [38–40], using inpainting as an example. Image inpainting has progressed significantly during last few years, specifically using machine learning methods [41–43]. However, as far as we know, no other tensor-based method is available for solving the image inpainting problem as a weighted tensor least squares problems.

For experiments shown in Figs. 3.2 and 3.1, we obtained fenced images from the Image datasets for MSBP deformable lattice detection Algorithm [44], and for the experiment shown in Fig. 3.1, we obtained a landscape image from the DIV2K dataset [45].

Our experimental results were obtained using a MATLAB implementation of WT-LARS using the MATLAB version R2017b on an MS-Windows machine: 2 Intel Xeon CPUs E5-2637 v4, 3.5 GHz, 32 GB RAM, and NVIDIA Tesla P100 GPU with 12 GB memory.
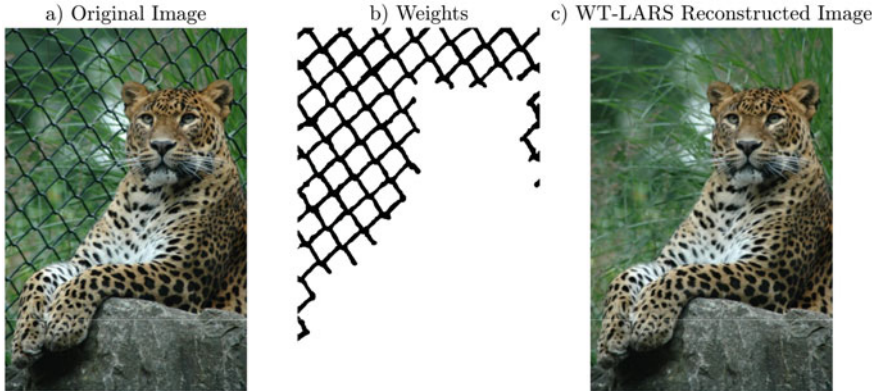
Fig. 3.1 **a** Original image with a fence **b** weights image with zero weights for the fence **c** WT-LARS reconstructed image (Fence Removed)
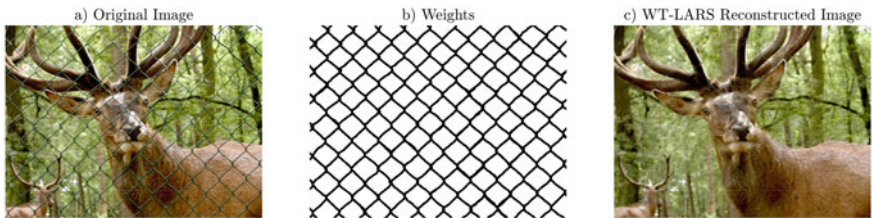
Fig. 3.2 **a** Original image with a fence **b** weights image with zero weights for the fence **c** WT-LARS reconstructed image (Fence Removed)

3.4.1 Inpainting

In this experiment, we use WT-LARS for inpainting. We obtained a sparse representation of the inpainted image using WT-LARS after applying zero weights to the missing data.

In our experimental results shown in Figs. 3.1 and 3.2, we obtained a fenceless image by considering pixels behind the fences as missing data. Figures 3.1a and 3.2a show the original image with a fence, and Figs. 3.1b and 3.2b show the respective masks applied to each pixel of the original image, where black indicates zero and white indicates one. Figures 3.1c and 3.2c show the obtained sparse representation of images behind fences using WT-LARS.

We obtained RGB image patches, $200 \times 200 \times 3$ pixels, from the original images in Figs. 3.1a and 3.2a. For each patch, we obtained a weighted K-sparse representation using WT-LARS, with 10% nonzero coefficients, for three fixed *mode-n* overcomplete dictionaries, $\boldsymbol{\Phi}^{(1)} \in \mathbb{R}^{200 \times 400}$, $\boldsymbol{\Phi}^{(2)} \in \mathbb{R}^{200 \times 400}$ and $\boldsymbol{\Phi}^{(3)} \in \mathbb{R}^{3 \times 4}$, by solving a L_1 constrained sparse weighted least squares problem. Weights consists of zeros for the pixels that belong to the fence in the original images and ones for everywhere else. Used fixed *mode-n* overcomplete dictionaries were a union of a Discrete Cosine Transform (DCT) dictionary and a Symlet wavelet packet with four vanishing moments dictionary. In the experimental results shown in Figs. 3.1 and 3.2, the RGB patches with the minimum number of nonzero samples had 79, 834 and 92, 748 nonzero samples, respectively. We collected 60 image patches from the image in Fig. 3.1a and 35 image patches from the image in Fig. 3.2a, where on average WT-LARS took 476 s to collect 12,000 (10% of $200 \times 200 \times 3$) non-zero coefficients from each image patch.

In the experimental results shown in Fig. 3.3, we use WT-LARS to obtain a landscape image occluded by a person in Fig. 3.3a. Figure 3.3b shows the weights, and Fig. 3.3c shows the inpainting result after removing the person from the foreground of the landscape image.

The RGB images in Fig. 3.3a is a scaled version of the original image with $200 \times 300 \times 3$ pixels. We obtained a weighted K-sparse representation for the scaled image in Fig. 3.3a using WT-LARS, with 20% non-zero coefficients, for three fixed *mode-n* overcomplete dictionaries, $\boldsymbol{\Phi}^{(1)} \in \mathbb{R}^{200 \times 400}$, $\boldsymbol{\Phi}^{(2)} \in \mathbb{R}^{300 \times 604}$ and $\boldsymbol{\Phi}^{(3)} \in$

a) Original Image   b) Weights   c) WT-LARS Reconstructed Image

Fig. 3.3 **a** Original image with a person **b** weights image with zero weights for the person **c** WT-LARS reconstructed image (Person Removed)

$\mathbb{R}^{3\times4}$, by solving a weighted L_1 constrained sparse least squares problem. Weights consist of zeros for the pixels belonging to the person in the original image and ones for everywhere else. Used fixed *mode-n* overcomplete dictionaries were a union of a Discrete Cosine Transform (DCT) dictionary and a Symlet wavelet packet with four vanishing moments dictionary. In the experimental results shown in Fig. 3.3, a total of 170,829 nonzero samples have been used to obtain the sparse signal representation of the landscape image. The WT-LARS took 20,625 s to collect 36,000 non-zero coefficients, which is 20% of the size of the image tensor in Fig. 3.3a. Therefore, inpainting results in, Figs. 3.1c, 3.2c and 3.3c clearly show that WT-LARS can be successfully used to approximate missing/incomplete data.

3.5   Conclusions

Sparse weighted multilinear least-squares is a generalization of the sparse multilinear least-squares problem, where both sides of the Kronecker LS system are multiplied by an arbitrary diagonal weights matrix. These arbitrary weights would result in a potentially very large non-Kronecker least-squares problem that could be impractical to solve as it would require significant memory and computational power.

This paper extended the T-LARS algorithm, earlier developed by the authors [28], to become the Weighted Tensor Least Angle Regression (WT-LARS) algorithm that could solve efficiently either L_0 or L_1 constrained multilinear least-squares problems with arbitrary diagonal weights for all critical values of their regularization parameter. To validate our new WT-LARS algorithm, we used it to solve three image inpainting problems. In our experimental results using WT-LARS shown in Figs. 3.1 and 3.2, we obtained the exact sparse signal representation of RGB images behind fences after applying zero weights to the pixels representing the fences. In the experimental result using WT-LARS shown in Fig. 3.3, we successfully obtained an exact sparse signal representation of an RGB landscape image occluded by a person by applying zero weights to the pixels representing this person. These results demonstrate the validity and usefulness of our new Weighted Least Angle Regression (WT-LARS) algorithm.

Possible future applications of WT-LARS include efficiently solving weighted least-squares applications for tensor signals. Such examples include tensor completion, image/video inpainting, image/video smoothing, and tensor signal restorations.

A MATLAB GPU-based implementation of our Weighted Tensor Least Angle Regression (WT-LARS) algorithm, Algorithm 1, is available at https://github.com/SSSherif/Weighted-Tensor-Least-Angle-Regression.

References

1. Repetti, A., Chouzenoux, E., Pesquet, J.C.: A penalized weighted least squares approach for restoring data corrupted with signal-dependent noise. Eur. Signal Process. Conf., 1553–1557 (2012)
2. Wang, J., Lu, H., Wen, J., Liang, Z.: Multiscale penalized weighted least-squares sinogram restoration for low-dose X-ray computed tomography. IEEE Trans. Biomed. Eng. **55**, 1022–1031 (2008). https://doi.org/10.1109/TBME.2007.909531
3. Cheung, K.W., So, H.C., Ma, W.K., Chan, Y.T.: Least squares algorithms for time-of-arrival-based mobile location. IEEE Trans. Signal Process. **52**, 1121–1128 (2004). https://doi.org/10.1109/TSP.2004.823465
4. Zou, Y., Liu, H., Wan, Q.: An iterative method for moving target localization using TDOA and FDOA measurements. IEEE Access. **6**, 2746–2754 (2017). https://doi.org/10.1109/ACCESS.2017.2785182
5. Tarrío, P., Bernardos, A.M., Besada, J.A., Casar, J.R.: A new positioning technique for RSS-based localization based on a weighted least squares estimator. ISWCS'08 - Proc. 2008 IEEE Int. Symp. Wirel. Commun. Syst., 633–637 (2008). https://doi.org/10.1109/ISWCS.2008.4726133
6. Wang, W., Tan, W., Shi, W., Zhang, Q., Li, H.: Direction finding based on iterative adaptive approach utilizing weighted ℓ_2 $\ell 2$ -norm penalty for acoustic vector sensor array. Multidimens. Syst. Signal Process. **331**(33), 247–261 (2021). https://doi.org/10.1007/S11045-021-00797-6
7. Chan, S.C.K.: Adaptive weighted least squares algorithm for Volterra signal modeling. IEEE Trans. Circuits Syst. I Fundam. Theory Appl. **47**, 545–554 (2000). https://doi.org/10.1109/81.841856
8. De Courville, M., Duhamel, P.: Adaptive filtering in subbands using a weighted criterion. IEEE Trans. Signal Process. **45**, 1675 (1997). https://doi.org/10.1109/icassp.1995.480341
9. Zhao, R., Lai, X.: A fast matrix iterative technique for the WLS design of 2-D quadrantally symmetric FIR filters. Multidimens. Syst. Signal Process. 2010 224. 22, 303–317 (2010). https://doi.org/10.1007/S11045-010-0128-X
10. Min, D., Choi, S., Lu, J., Ham, B., Sohn, K., Do, M.N.: Fast global image smoothing based on weighted least squares. IEEE Trans. Image Process. **23**, 5638–5653 (2014). https://doi.org/10.1109/TIP.2014.2366600
11. Ruppert, D., Wand, M.P.: Multivariate locally weighted least squares regression. Ann. Stat. **22**, 1346–1370 (2007). https://doi.org/10.1214/aos/1176325632
12. Magee, L.: Improving survey-weighted least squares regression. J. R. Stat. Soc. Ser. B Stat. Methodol. **60**, 115–126 (1998). https://doi.org/10.1111/1467-9868.00112
13. Romano, J.P., Wolf, M.: Resurrecting weighted least squares. J. Econom. **197**, 1–19 (2017). https://doi.org/10.1016/j.jeconom.2016.10.003
14. Wickramasingha, I., Sobhy, M., Sherif, S.S.: Sparsity in Bayesian Signal Estimation. In: Tejedor, J.P. (ed.) Bayesian Inference. InTech (2017)
15. Mallat, S.: A Wavelet Tour of Signal Processing. Elsevier (2009)
16. Daubechies, I.: The wavelet transform, time-frequency localization and signal analysis. IEEE Trans. Inf. Theory **36**, 961–1005 (1990). https://doi.org/10.1109/18.57199
17. Mallat, S.G., Zhang, Z.: Matching pursuits with time-frequency dictionaries. IEEE Trans. Signal Process. **41**, 3397–3415 (1993). https://doi.org/10.1109/78.258082
18. Pati, Y.C., Rezaiifar, R., Krishnaprasad, P.S.: Orthogonal matching pursuit: recursive function approximation with applications to wavelet decomposition. In: Conference Record of the Asilomar Conference on Signals, Systems & Computers, pp. 40–44. IEEE Comput. Soc. Press (1993)
19. Coifman, R.R., Wickerhauser, M.V.: Entropy-based algorithms for best basis selection. IEEE Trans. Inf. Theory **38**, 713–718 (1992). https://doi.org/10.1109/18.119732
20. Chen, S.S., Donoho, D.L., Saunders, M.A.: Atomic decomposition by basis pursuit. SIAM J. Sci. Comput. **20**, 33–61 (1998). https://doi.org/10.1137/S1064827596304010

21. Efron, B., Hastie, T., Johnstone, I., Tibshirani, R., Ishwaran, H., Knight, K., Loubes, J.M., Massart, P., Madigan, D., Ridgeway, G., Rosset, S., Zhu, J.I., Stine, R.A., Turlach, B.A., Weisberg, S., Johnstone, I., Tibshirani, R.: Least angle regression. Ann. Stat. **32**, 407–499 (2004). https://doi.org/10.1214/009053604000000067

22. Tropp, J.A.: Greed is good: algorithmic results for sparse approximation. IEEE Trans. Inf. Theory **50**, 2231–2242 (2004). https://doi.org/10.1109/TIT.2004.834793

23. Friedlander, M.P., Mansour, H., Saab, R., Yilmaz, Ö.: Recovering compressively sampled signals using partial support information. IEEE Trans. Inf. Theory **58**, 1122–1134 (2012). https://doi.org/10.1109/TIT.2011.2167214

24. Khajehnejad, M.A., Xu, W., Avestimehr, A.S., Hassibi, B.: Weighted l1 minimization for sparse recovery with prior information. IEEE Int. Symp. Inf. Theory - Proc. 483–487 (2009). https://doi.org/10.1109/ISIT.2009.5205716

25. Candès, E.J., Wakin, M.B., Boyd, S.P.: Enhancing sparsity by reweighted ℓ1 minimization. J. Fourier Anal. Appl. **14**, 877–905 (2008). https://doi.org/10.1007/s00041-008-9045-x

26. Bergersen, L.C., Glad, I.K., Lyng, H.: Weighted lasso with data integration. Stat. Appl. Genet. Mol. Biol. **10** (2011). https://doi.org/10.2202/1544-6115.1703

27. Shimamura, T., Imoto, S., Yamaguchi, R., Miyano, S.: Weighted lasso in graphical Gaussian modeling for large gene network estimation based on microarray data. Genome Inform. **19**, 142–153 (2007). https://doi.org/10.1142/9781860949852_0013

28. Kolda, T.G., Bader, B.W.: Tensor decompositions and applications. SIAM Rev. **51**, 455–500 (2009). https://doi.org/10.1137/07070111X

29. Cichocki, A., Mandic, D., De Lathauwer, L., Zhou, G., Zhao, Q., Caiafa, C., Phan, H.A.: Tensor decompositions for signal processing applications: from two-way to multiway component analysis (2015)

30. Wickramasingha, I., Sobhy, M., Elrewainy, A., Sherif, S.S.: Tensor least angle regression for sparse representations of multidimensional signals. Neural Comput. **32**, 1697–1732 (2020). https://doi.org/10.1162/neco_a_01304

31. Sulam, J., Ophir, B., Zibulevsky, M., Elad, M.: Trainlets: dictionary learning in high dimensions. IEEE Trans. Signal Process. **64**, 3180–3193 (2016). https://doi.org/10.1109/TSP.2016.2540599

32. Caiafa, C.F., Cichocki, A.: Computing sparse representations of multidimensional signals using Kronecker bases. Neural Comput. **25**, 1–35 (2012). https://doi.org/10.1162/NECO_a_00385

33. Elrewainy, A., Sherif, S.S.: Kronecker least angle regression for unsupervised unmixing of hyperspectral imaging data. Signal, Image Video Process. **14**, 359–367 (2020). https://doi.org/10.1007/s11760-019-01562-w

34. Schäcke, K.: On the Kronecker product, 1–35 (2013)

35. Moon, T.K., Stirling, W.C.: Mathematical methods and algorithms for signal processing (1999)

36. Bocci, C., Carlini, E., Kileel, J.: Hadamard products of linear spaces. J. Algebr. **448**, 595–617 (2016). https://doi.org/10.1016/j.jalgebra.2015.10.008

37. Zhao, Q., Caiafa, C.F., Mandic, D.P., Chao, Z.C., Nagasaka, Y., Fujii, N., Zhang, L., Cichocki, A.: Higher order partial least squares (HOPLS): A generalized multilinear regression method. IEEE Trans. Pattern Anal. Mach. Intell. **35**, 1660–1673 (2013). https://doi.org/10.1109/TPAMI.2012.254

38. Phan, A., Cichocki, A., Tichavsk, P., Luta, G., Brockmeier, A.: Tensor completion through multiple Kronecker product decomposition Institute of Information Theory and Automation. Proc. ICASSP. c, 3233–3237 (2013)

39. Bugg, C., Chen, C., Aswani, A.: Nonnegative Tensor Completion via Integer Optimization. (2021)

40. Yu, Q., Zhang, X., Chen, Y., Qi, L.: Low Tucker rank tensor completion using a symmetric block coordinate descent method. Numer. Linear Algebra. with Appl. **30**, e2464 (2022). https://doi.org/10.1002/nla.2464

41. Elharrouss, O., Almaadeed, N., Al-Maadeed, S., Akbari, Y.: Image inpainting: a review, https://link.springer.com/article, https://doi.org/10.1007/s11063-019-10163-0 (2020)

42. Xiang, H., Zou, Q., Nawaz, M.A., Huang, X., Zhang, F., Yu, H.: Deep learning for image inpainting: A survey. Pattern Recognit. **134**, 109046 (2023). https://doi.org/10.1016/j.patcog.2022.109046

43. Romero, A., Castillo, A., Abril-Nova, J., Timofte, R., Das, R., Hira, S., Pan, Z., Zhang, M., Li, B., He, D., Lin, T., Li, F., Wu, C., Liu, X., Wang, X., Yu, Y., Yang, J., Li, R., Zhao, Y., Guo, Z., Fan, B., Li, X., Zhang, R., Lu, Z., Huang, J., Wu, G., Jiang, J., Cai, J., Li, C., Tao, X., Tai, Y.W., Zhou, X., Huang, H.: NTIRE 2022 Image Inpainting Challenge: Report. In: IEEE Computer Society Conference on Computer Vision and Pattern Recognition Workshops, pp. 1149–1181 (2022)
44. Park, M., Brocklehurst, K., Collins, R.T., Liu, Y.: Deformed lattice detection in real-world images using mean-shift belief propagation. IEEE Trans. Pattern Anal. Mach. Intell. **31**, 1804–1816 (2009). https://doi.org/10.1109/TPAMI.2009.73
45. Agustsson, E., Timofte, R.: NTIRE 2017 challenge on single image super-resolution: dataset and study. In: IEEE Computer Society Conference on Computer Vision and Pattern Recognition Workshops, pp. 1122–1131 (2017)

Chapter 4
Research on Behavior Control Method in 3D Virtual Animation Design Based on the Purpose of Improving the Effect of Overseas Dissemination

Nan Zhang and Xu Liu

Abstract In order to improve the overseas dissemination effect of 3D (Three-dimensional) animation, this paper starts from the perspective of animation character behavior control to improve the dynamic texture of animation and enhance the audience's visual experience. Moreover, this paper designs and verifies the behavior control system of mobile animation character model based on the mathematical model. In addition, the initial animated character model is used to collect and summarize the working data, and the targeted hierarchical behavior design method is formulated by analyzing and adjusting the target tasks of the moving animated character model, which can generate the real-time behavior track meeting the requirements, strengthen the motion control, pose data estimation and safety control of the behavior, and realize more efficient reaction control. Finally, the experimental results verify the effectiveness of this method, which has a certain effect on improving the overseas dissemination effect of animation.

4.1 Introduction

At present, the top three countries in the global animation industry are the United States, Japan, South Korea. Among them, there are eight animation companies in the United States. Moreover, advanced technology, sufficient funds, fully supported policies and excellent talents make its animation industry develop rapidly, which can be said to be the largest animation country in the world. Japan has a strong development

N. Zhang
School of Theater, Film and Television, Communication University of China, BeiJing 100000, China

X. Liu (✉)
Animation Art College, Jilin Animation Institute, Changchun 130000, Jilin, China
e-mail: liuxu@jlai.edu.cn

© The Author(s), under exclusive license to Springer Nature Singapore Pte Ltd. 2024
R. Kountchev et al. (eds.), *New Approaches for Multidimensional Signal Processing*,
Smart Innovation, Systems and Technologies 385,
https://doi.org/10.1007/978-981-97-0109-4_4

momentum in recent years. With the strong support of its government, social recognition and excellent talents, it produces a large number of exquisite and high-quality animation works almost every year. Since the financial crisis, the government of South Korea also began to focus on the development of animation economy, and has now leapt to the third animation country. In addition, France, Britain, the Netherlands and other countries have strong creative and cultural industries.

From the perspective of animation companies, the transformation is difficult. Even though the country has gradually attached importance to the animation industry and provided strong policy support, there are significant shortcomings in China's animation companies themselves: firstly, there is a lack of original animation. Animation itself is a creative and cultural industry, and creativity occupies a large proportion, which can be said to be the soul of the entire industry. However, most animation companies in our country are processing companies and do not have a complete production chain, which leads to a situation where "skillful women cannot cook without rice", even with the best technology, it cannot be solved. Secondly, due to insufficient investment, animation works require a large amount of capital investment, which can directly lead to the production and quality of the works. According to international practice, the recovery of animation costs should account for 20 to 30% of production costs, and the return on investment in peripheral product development should be 70 to 80%. In China, the cost of playing original animated films is low, accounting for only 10% of the cost, making it difficult to recover production costs and continue operating, creating a vicious cycle. Once again, professional talents have withered, and the subject of animation education in China has just started. There is a shortage of animation talents, especially those who are skilled in creation and technology, which directly restricts the development of animation in China. Due to the inadequate development of animation companies, hard work and low wages, the temptation of the animation market demand is directly weakened. The cultivation of animation talents cannot be completed overnight and requires a short period of time. Finally, the domestic environment is chaotic, and vicious competition often occurs. Due to the increasing number of animation companies that draw well and cheaply, with an average cost of 5 yuan per animation, many people are willing to pay 2 or 3 yuan. Therefore, in order to compete for business, the industry has started vicious competition, forcing the entire industry's profit and income to decrease.

Technology is one of the important elements in the development of the animation industry, especially for some countries with relatively backward animation industry development, the advantages of technology are bound to become one of the shortcuts to accelerate industrial development. Currently, with the increasing use of computer technology in the field of animation, especially 3D and Flash technologies, significant breakthroughs have been made in the production of animation [1].

Traditional animation visual stimulation experiments play an important role in behavioral experiments, while other sensory stimulation experiments (such as hearing, smell, touch, etc.) are relatively less applied due to technical limitations [2]. Visual stimulation experiments are the largest and most diverse work to date, and commonly used visual stimuli can be divided into three different types: static stimuli, abstract stimuli, and video stimuli. Static stimuli are some of the earliest

stimuli used in behavioral experiments. Stimulation often involves related animals, which are presented as a static object, such as animal models, images, etc. [3]. We used cardboard models of adult seagulls to simulate the begging behavior of seagull chicks. The chicks responded naturally to the model, just like begging for food from their parents. Reference [4] used a predator model to study the alarm behavior of animals. When the eagle's model moved above the cage, the chicken emitted an alarm sound. Scientists speculate that the test animals may view static models as real animals and react to them. The main advantage of reference [5] is that the same stimulus can be applied to different animals, and its visual characteristics can be modified between different experiments, which can control the time and frequency of stimulus transmission. The main limitation is that there is no interactive feedback between the stimulus and the tested individual, and over time, the individual becomes accustomed to the stimulus and stops responding to it [6].

This paper combines the design technology of three-dimensional virtual animation design to improve the behavior control in animation design, improve the overall design quality of animation, and promote the overseas dissemination effect of animation.

4.2 Behavior Control Algorithm of 3D Animation

4.2.1 Mathematical Model of Behavior Control

Due to the limitation of technology, the control of some kinds of animation character behavior is still a single form of control, and the average control efficiency is low and the stability is poor. Traditional control instruction is relatively independent. Although it is a single control unit, but in the process of practical application, in the face of complex execution and processing environment, it will still produce certain errors and problems, resulting in more or less influence. In order to innovate the execution process, expand the control range of interactive instructions and form a more modular design idea, it is necessary to introduce the instructions of real-time data sharing area into the original initial control system, so as to create a more active, systematic and comprehensive execution environment, and use mathematical models to determine the task execution range of animation characters, and calculate the execution range through mathematical linear equations, as shown in the following formula (4.1) [7]:

$$\begin{cases} K = \frac{r}{3} + 6\varphi - \sqrt{2a + 1} \\ \quad P = 2\beta + 4\omega \end{cases} \tag{4.1}$$

In the formula, K represents the execution range, r represents the hierarchy ratio, φ represents the degree of shared control, a represents existing control errors, P represents the linear execution range, β represents the execution limit value, and ω represents the interaction coefficient. Through the above calculation, the actual execution range of animated characters can be finally obtained. Taking the obtained execution range as the actual processing range of the animation character behavior control system, on the basis of the above and combining with the actual control requirements, the limit edge control coefficient of the animation character is calculated, as shown in the following formula (4.2) [8]:

$$H = -\chi + 1.5 - \frac{e - 2\pi}{7} \tag{4.2}$$

In the formula, H represents the limit edge control coefficient, χ represents the value of edge distance, e represents the strain control ratio, and π represents the interaction area. Through the above calculation, the actual limit edge control coefficient can be finally obtained. According to the calculated value, the specific edge control range is set to form the limit internal control standard. It is set in the behavior control system processing model of moving animation characters, and according to the actual situation, the corresponding interactive control instructions are formed [9].

The control structure diagram of multi-behavior cooperative synthesis is shown in Fig. 4.1 [10].

After completing the design of interactive control instructions under the mathematical model, it is necessary to design the hierarchical module of the mathematical model of mutual class function. First of all, we need to build a linear mutual class environment according to the actual control requirements and execution conditions
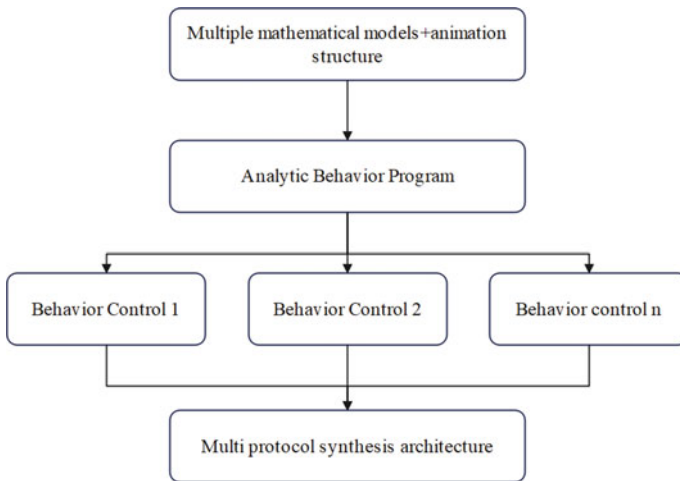
Fig. 4.1 Illustration of multi-behavior cooperative synthesis control structure

of animation characters [11]. In essence, this part delineates the instruction import area of animation characters under the mutual class mode, and associates the functional mathematical model with the related execution and processing instructions to form a more stable module control program. Therefore, we can first determine the cross-class control range and calculate the cross-class control ratio, as shown in the following formula (4.3) [12]:

$$G = (5\xi + 0.25) - \frac{1}{x} \qquad (4.3)$$

In the formula, G represents the mutual class control ratio, ξ represents the coefficient of linear change, and x represents the controllable weight value. Through the above calculation, the actual cross-class control ratio can be finally obtained. According to the control ratio, the mathematical control model is created, and the mutual class function modules at different levels are designed. The mutual class function module is different from the common system execution module, and the mutual class module has stronger flexibility and can increase the connection between animation characters. It is necessary to first calculate the terminal deviation coefficient of the executive control section of the mutual class function module, as shown in the following formula (4.4):

$$O = \frac{Q}{2\varphi + 1} - 2\sqrt{3} + 7\varsigma \qquad (4.4)$$

In the formula, O represents the terminal deviation coefficient, φ represents the number of interactive control sections, Q represents the actual behavior control range of animation characters, and ς represents the change protocol side.

Through the above calculation, the actual terminal deviation coefficient can ultimately be obtained. Construct a NAO processing program within the hierarchical module of the mathematical model, utilize the obtained data information, and combine it with choreography software to develop corresponding animation character behavior control instructions. This section is mainly divided into basic control commands, travel commands, jump commands, arm lift commands, etc. All commands are added to the control module to form a stable command control group. Under the influence of mathematical models, mathematical mobile programs are added to the instruction control group. The program is interconnected with instructions at each level and has a certain degree of adjustability. Changes can be made at any time according to actual needs. In the process of motion, control, and even inspection of animated characters, there are also different levels of mutual control commands. Similar to mathematical mobile programs, interclass control instructions execute tasks assigned by the system in a predetermined order, requiring fixed execution standards and levels to form initial functional modules, secondary functional modules, and top-level functional modules. Each functional module is independent of each other and has a certain degree of correlation, enhancing the stable operation of the system and ensuring clear execution goals, further improving the

final design of the hierarchical module of the mathematical model for optimizing interclass functions.

4.2.2   Multi Behavior Collaborative Design

After completing the design of the hierarchical module of the mathematical model for mutual class functions, it is necessary to carry out the design of multi-behavior collaboration for mobile animation characters. Due to the fact that the animation characters designed in this article are multi-level control programs, supplemented by inter class control instructions, the control of animation character behavior also needs to be set to bidirectional or multiple to ensure the comprehensive control effect within the system.

Usually, when implementing behavior settings for animated characters, 3D technology is combined to establish a comprehensive coordinate system centered around themselves, using the animated character's abdomen as a preset reference to construct WDS (Wireless Distribution System) coordinates. W represents the horizontal axis for forward behavior control, D represents the vertical axis for backward behavior control of the animated character, and S represents the core axis for mid-range behavior control. When observing, the forward, backward, left, and right movements of animated characters are generally basic habits that can be completed in conjunction with mutual control commands. However, for jumping, forward, and other movements, joint coordination is required.

Generally, there are 30 joints in the animated character itself. By using bus association and timing control program, the joints are demarcated in the same control area, the timing access protocol is designed, and the specific number of timing protocol nodes is calculated, as shown in the following formula (4.5):

$$E = -j - \left(\sqrt[4]{g} + 2.5\right) - \frac{1}{b} \tag{4.5}$$

In the formula, E represents the number of timing protocol nodes, j represents the main control coefficient, g represents an access weighting value, and b represents the central control standard value. Through the above calculation, we can finally get the actual number of timing protocol nodes. Meanwhile, we set nodes in the main control area of the system according to the number. Combined with Choregraphe software animation character development software, we change the related index parameters and interface functions of animation character behavior control in the system, and adjust the running function and coverage control range of animation character ontology. Moreover, in the control system, the complex behavior of animation characters is also divided into several small behavior combinations, which can reduce the internal pressure of animation characters' behavior control to a certain extent. In addition, small behavior combinations consist of behavior units, so we can calculate unit behavior units first, as shown in the following formula (4.6).

$$N = \sqrt{5\gamma - \frac{\sqrt{2I}}{3} + R - o} \tag{4.6}$$

In the formula, N represents the unit of the unit line, γ represents the integration ratio, I represents the behavior synthesis ratio, R represents the standard value of behavior activation limit, and o represents the limit mathematical priority series. Through the above calculation, the actual unit behavior unit can be finally obtained. According to the above coordinate system, the behavior units are added to the hierarchical structure of the system and associated with the set mathematical model to form a multi-behavior cooperative synthesis control structure. The design of multi-behavior cooperative synthesis control structure can be completed. After completion, different behavior cooperation goals are set up in each control level, and different goals represent the corresponding behaviors of animation characters. So far, the multi-behavior cooperation construction is realized and the software design is completed.

4.2.3 Behavior Characteristic Selection

The quality of feature selection results directly affects the lightness and quality of the constructed human behavior recognition model. Excessive redundancy and irrelevant features are not only detrimental to the improvement of model generalization, but also easy to increase modeling difficulty and computational load This article proposes a feature selection technique based on Neighborhood Component Analysis (NCA) to perform high correlation feature selection on the original human behavior recognition feature set Therefore, from the perspective of correlation between behavioral features, this article uses NCA to select the highly correlated optimal feature subset from the human behavioral feature set, thereby improving the lightness of the behavior recognition model calculation process. NCA is a simple and efficient distance measurement algorithm. It selects the optimal feature subset for human behavior recognition models by maximizing the classification accuracy of the retention method.

The original feature set of human behavior is $S = \{(\tilde{x}_i, \tilde{f}_i), i = 1, 2, ..., n\}$, where $\tilde{x}_i \in \mathbb{R}^m$ is the i-th behavior sample, $\tilde{f} \in \{1, 2, ..., c\}$ is the label of the i-th behavior sample, c is the number of categories and m represents the number of features. The Mahalanobis distance between behavior features $\tilde{x}_i$ and $\tilde{x}_j$ is:

$$d(\tilde{x}_i, \tilde{x}_j) = \sqrt{(A\tilde{x}_i - A\tilde{x}_j)^T (A\tilde{x}_i - A\tilde{x}_j)} \tag{4.7}$$

In the formula, A is the Mahalanobis distance transformation matrix, and T is the matrix transposition, and $j = 1, 2, ..., n$.

Using the method of leaving one to maximize the classification accuracy on the sample set of human behavior, the probability that the sample $\tilde{x}_i$ selects the sample $\tilde{x}_j$ as its reference point is as follows:

$$P_{ij} = \frac{\exp\left(-\left\|A\tilde{x}_i - A\tilde{x}_j\right\|^2\right)}{\sum_{q \neq i} \exp\left(-\left\|A\tilde{x}_i - A\tilde{x}_j\right\|^2\right)}, \ P_{ii} = 0 \tag{4.8}$$

In the formula, $q = 1, 2, ..., n$ represents the probability that the sample $\tilde{x}_i$ chooses the sample $\tilde{x}_j$ as its reference point. The probability that the sample $\tilde{x}_i$ is correctly classified is:

$$P_i = \sum_{i=1, j\neq 1} P_{ij}\tilde{f}_{ij} \tag{4.9}$$

Among them, $\tilde{f}_i \neq \tilde{f}_j$, $\tilde{f}_{ij} = 0$, and vice versa $\tilde{f}_{ij} = 1$.

The objective function is to maximize the number of correctly classified behavioral features, so it is defined as follows:

$$F(A) = \sum_i p_i \tag{4.10}$$

We use conjugate gradient method to solve A:

$$\frac{\partial F}{\partial A} = -2A \sum_i \sum_{j\in \tilde{f}_i} p_{ij}\left(\tilde{x}_{ij}\tilde{x}_{ij}^T - \sum_q P_{iq}\tilde{x}_{ij}\tilde{x}_{ij}^T\right) \tag{4.11}$$

Among them, $\tilde{x}_{ij} = \tilde{x}_i - \tilde{x}_j$.

Using the optimized A, the feature subset after NCA selection is obtained

$$X = \tilde{X} \cdot A \tag{4.12}$$

In the formula, $\tilde{X} = \{\tilde{x}_1, \tilde{x}_2, ..., \tilde{x}_n\}$ and $X = \{x_1, x_2, ..., x_n\}$ represents the optimal feature subset selected by NCA.

4.3 Behavior Control Model of 3D Virtual Animation Design

When the three-dimensional virtual character external building is completed, it is necessary to adjust and control its movements to achieve the required authenticity. The control process is shown in Fig. 4.2. First of all, the action of the character material is captured, and the trajectory is copied by the method of physics, so that the 3D virtual animation can realize the movement and adjustment corresponding to the real character, thus realizing the fidelity of the three-dimensional virtual animation character. After that, through system feedback, the control parameters suitable
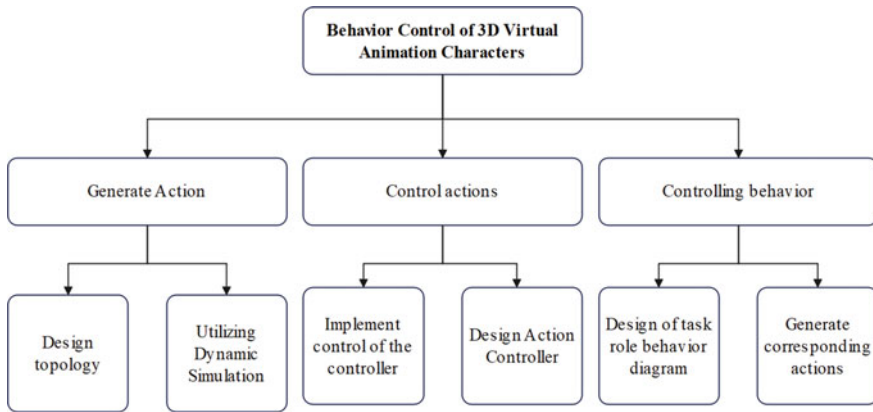
Fig. 4.2 Behavior control process of 3D simulation animation image

for 3D simulated character animation joints are set, which realizes the combination of external information and 3D virtual animation in proportion, avoids external interference as much as possible, realizes the conversion of relative data, increases the similarity between character image and real image, and satisfies the constraint control conditions for 3D virtual animation.

The visual perception model simulates the visual cone of real human eyes, and sets the appropriate visual field angle and range. Usually, the comfortable visual field of human eyes is within 30°, and only objects in the visual cone can be perceived by agents. Figure 4.3 is a visual perception model of intelligent characters. We assume P is a point on the object, O is the origin of the agent's line of sight, the distance between other objects and the agent character is d, and R represents the visual field angle. If $\|O - P\| \leq d$ and the angle between the ray OP and the z axis (directly in front of the agent's line of sight) is less than $R/2$, the object is within the visual field of the agent character. In the virtual environment, it is necessary to judge whether the object is in the field of vision and whether the object is occluded. In this paper, point occlusion detection method is used for line-of-sight detection.

The auditory perception model of intelligent characters simulates the real auditory region through a spherical region, as shown in Fig. 4.4. If the agent can hear the sound, it makes behavior decision by the sound and makes appropriate behavior response. In order to increase the authenticity, we also need to consider the intensity range of sound.

Fig. 4.3 Visual perception
model
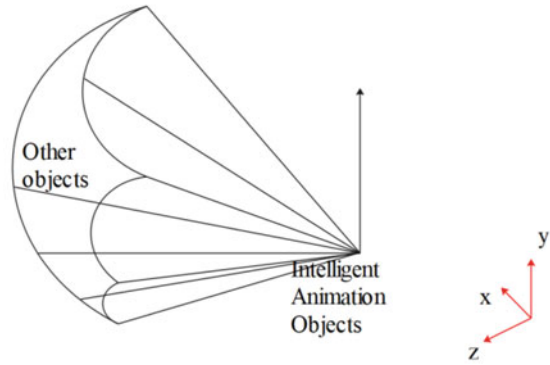
(a) Visual stereoscopic images
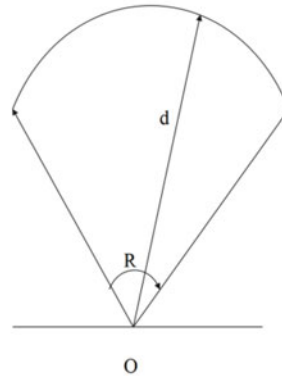
(b) Planar decomposition image

4.4   Model Validation

Currently, the operation of 3D virtual animation design is mostly based on MAYA software. Therefore, this article chooses MAYA software as the system software and combines the algorithm in the second part to improve 3D virtual animation design and automate the processing of intelligent characters.

After constructing the above model, the effect of the model is verified. Firstly, the behavior control simulation analysis of domestic animation is carried out through the model constructed by the simulation system. The following Fig. 4.5 shows an example of simulation analysis through this model, and the case comes from the characters in domestic animation "Kuiba". With this method, the role reconstruction and behavior control analysis can be carried out from multiple angles, and behavior control can be carried out, and finally the following model is obtained.

After building the above model, we verify the effect of the model, and use multiple groups of simulation to verify the effect of this model in animation character behavior control, and finally get the verification results shown in Table 4.1 and Fig. 4.6.

Fig. 4.4 Auditory
perception model
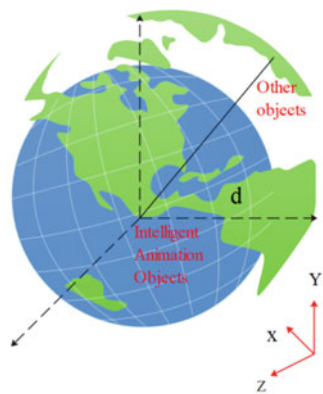
(a) Auditory stereogram
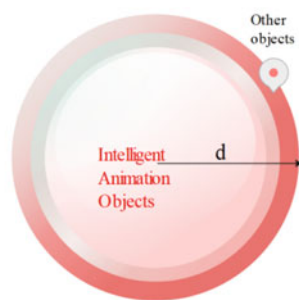
(b) Horizontal exploded view

From the above analysis results, we can see that the behavior control method in 3D virtual animation design proposed in this paper has a good effect on the behavior control of animation characters, so it can promote the look and feel of animation and have a certain positive effect on promoting the overseas dissemination effect of animation.

Fig. 4.5 Example of
behavior control model

(a) Model sketches
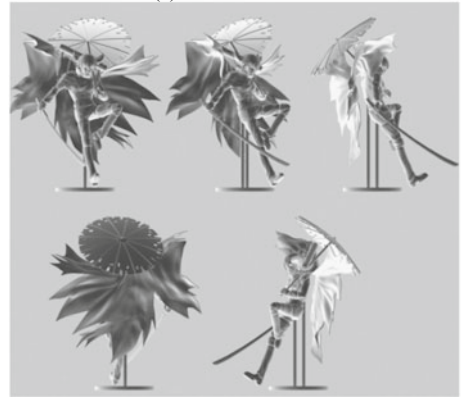
(b) Behavior control model

Table 4.1 Simulation analysis of behavior control

Simulation serial number	Behavioral control	Simulation serial number	Behavioral control	Simulation serial number	Behavioral control
1	79.83	13	83.54	25	83.60
2	81.71	14	88.56	26	80.90
3	79.14	15	86.90	27	85.09
4	78.03	16	86.12	28	84.60
5	86.32	17	82.80	29	81.66
6	86.19	18	79.96	30	79.64
7	80.51	19	83.08	31	81.88
8	78.98	20	82.63	32	88.75
9	78.74	21	82.80	33	80.27
10	86.49	22	79.06	34	81.32
11	87.99	23	87.69	35	82.22
12	88.84	24	78.51		
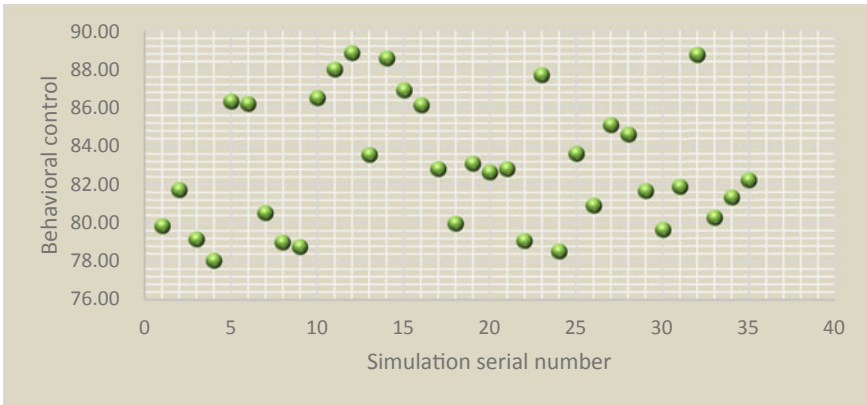
Fig. 4.6 Statistical diagram of behavior control simulation data

4.5 Conclusion

This paper combines with 3D virtual animation design technology to improve the behavior control in animation design to improve the overall design quality of animation and promote the effect of animation overseas dissemination. Moreover, this paper designs and verifies the behavior control system of mobile animation character model based on the mathematical model. Under the aided design of the mathematical model, the behavior control program of animation character model is innovated, and the initial animation character model is used to collect and summarize the working data. Moreover, by analyzing and adjusting the objectives and tasks of moving animation character model, a targeted hierarchical behavior design method is formulated, which can generate real-time behavior trajectory meeting the requirements, strengthen the motion control, pose data estimation and safety control of behavior, and realize more efficient reaction control. From the analysis results, we can see that the behavior control method in 3D virtual animation design proposed in this paper is very good for improving the effect of animation character behavior control, which is helpful to promote the overseas dissemination effect of animation.

References

1. Abbasi, A., Chen, H., Salem, A.: Sentiment analysis in multiple languages: Feature selection for opinion classification in web forums. ACM Trans. Inf. Syst. (TOIS) **26**(3), 1–34 (2008)
2. Agrawal, S., Singh, R.K., Murtaza, Q.: Prioritizing critical success factors for reverse logistics implementation using fuzzy-TOPSIS methodology. J. Ind. Eng. Int. **12**(1), 15–27 (2016)
3. Bosc, P., Dubois, D., Prade, H.: Fuzzy functional dependencies and redundancy elimination. J. Am. Soc. Inf. Sci. **49**(3), 217–235 (1998)
4. Carrasco, R., Ordaz, M.G., López, F.J.M.: Science fiction and bodies of the future: alternative gender realities in Hollywood Cinema. J. Futur. Stud. **20**(2), 67–80 (2015)

5. Cohen, R.D.: The delinquents: Censorship and youth culture in recent US history. Hist. Educ. Q. **37**(3), 251–270 (1997)
6. Jojola, T.: Absurd reality: hollywood goes to the Indians... film & history: an interdisciplinary. J. Film Telev. Stud. **23**(1), 7–16 (1993)
7. Kaplan, A., Haenlein, M.: Rulers of the world, unite! The challenges and opportunities of artificial intelligence. Bus. Horiz. **63**(1), 37–50 (2020)
8. Kuklick, B.: Fascism comes to America. Int. J. Hist., Cult. Mod. **6**(1), 1–18 (2018)
9. Kumar, S., De, K., Roy, P.P.: Movie recommendation system using sentiment analysis from microblogging data. IEEE Trans. Comput. Soc. Syst. **7**(4), 915–923 (2020)
10. Piryani, R., Gupta, V., Singh, V.K.: Movie prism: a novel system for aspect level sentiment profiling of movies. J. Intell. Fuzzy Syst. **32**(5), 3297–3311 (2017)
11. Porcel, C., Tejeda-Lorente, A., Martínez, M.A., Herrera-Viedma, E.: A hybrid recommender system for the selective dissemination of research resources in a technology transfer office. Inf. Sci. **184**(1), 1–19 (2012)
12. Shon, J.H., Kim, Y.G., Yim, S.J.: Classifying movies based on audience perceptions: MTI framework and box office performance. J. Media Econ. **27**(2), 79–106 (2014)

Chapter 5
The Positive Exertion of "Fuzzy Control" in Art Appreciation Class

Yi Zou and Wenjing Wang

Abstract In order to improve the teaching effect of art appreciation class and promote the development of students' creative thinking, based on ASIFT (Affine Scale-Invariant Feature Transform) algorithm, this paper uses Nelder-Mead method as an optimization tool, introduces fuzzy control according to the characteristics of ASIFT sampling space to realize the self-adaptive adjustment of simplex parameters, and makes the sampling points converge towards the optimal matching direction. Moreover, this paper puts forward that in the process of art appreciation, it is necessary to combine fuzzy control method for image intelligent control, and resample the image by setting discrete sampling points to simulate the deformation caused by visual angle transformation. In addition, this paper gives a teaching model of art appreciation class combined with fuzzy control, demonstrates the display effect of fuzzy control art works through cases, and evaluates the teaching effect of this method combined with teaching evaluation. From the evaluation results, it can be seen that the fuzzy control method proposed in this paper can play an important role in art appreciation class.

5.1 Introduction

Art is a kind of spiritual product created by human beings, which is different from music of auditory art and literature of language art. It is a kind of space art with modeling, visibility, static, and materiality. Because of the above basic characteristics, art works should first be a spatial form that can be perceived by people, which can arouse people's visual perception; Secondly, it shows people a relatively ideal objective world in a static state through its material media, and then triggers people to create specific emotions for the second time.

Y. Zou (✉)
Zhengzhou Vocational College of Finance And Taxation, Zhengzhou 450048, Henan, China
e-mail: yi2768@126.com

W. Wang
Zhengzhou College of Finance and Economics, Zhengzhou 450000, Henan, China

In terms of art appreciation teaching, art is a comprehensive art that combines emotional, formative, visual, static, and material characteristics. These characteristics make its teaching methods correspondingly diverse and flexible. The ways and methods of appreciating art works of different schools and styles also vary. When students first come into contact with a piece of art, their appreciation experience exists in a scattered, free, and uncertain form, a completely subjective appreciation and imagination of the individual. The appreciation process will go through three stages, from "initial perception" to "emotional experience" and finally to "understanding improvement" [1]. Teachers should give students enough tolerance in this process, allowing them to self improve their understanding of themselves and emphasize the psychological process of the subject's emotional experience [2]. Fuzzy teaching method can fully leverage its uncertain advantages and stimulate students' subjective initiative. Fuzzy teaching breaks away from the traditional thinking pattern of "either this or that" binary logic in teaching, and is more conducive to cultivating students' creative thinking [3].

From a psychological perspective, there is a type of thinking that lacks rigorous logical reasoning in its judgments. Instead, the brain constantly experiences conceptual leaps and intersections of light and dark, demonstrating the situation of the problem in an unconscious process [4]. Therefore, psychologists refer to it as fuzzy thinking. Due to the different life experiences of students, it is impossible to have identical experiences with the same artwork. If the teacher only gives one appreciation result, students will not be able to stimulate emotional resonance with the work [5].

Art works, as a bridge between painters and viewers, have an indirect nature. Information can only be obtained visually, and this information is inevitably indirect. The painter's inner emotional world is expressed through external images, and external images only appear meaningful when expressing a person's inner emotions [6]. Therefore, art works serve to express the emotional world of painters. Art mainly appeals to emotions, and the stimulation of emotions inevitably carries a strong personal color. The blurriness of emotions displayed on the screen may attract the viewer in a broader field, causing them to experience the beauty of blurriness and melting their own experience into the blurriness of the work [7].

The application of fuzzy teaching method in art appreciation teaching is determined by the characteristics of art and the existence of students' fuzzy thinking ability. Art appreciation is an aesthetic activity that takes art works as objects and experiences and comprehends the true essence of art through observation and other auxiliary means, thereby obtaining spiritual pleasure. Appreciation teaching holds a significant proportion and holds a significant position in art classes. It not only enriches students' associative and aesthetic abilities, but also enhances their emotional experience and intuition abilities, thereby cultivating students' interest in art, expanding their artistic horizons, and enriching the emotional world [8].

Relatively speaking, students lack rich life experience, lack rigorous logical thinking, and exhibit active and jumping characteristics. However, their ability to think vaguely is quite strong. Their unique and profound perception and understanding of art works can sometimes be surprising. Therefore, in art appreciation

classes, teachers should not accurately explain and depict the "unique" context of the picture, but should broaden the space for art thinking, so that students can have multiple ways of understanding the language, emotional, and meaning levels [9].

Cloud class is a platform for teacher-student communication and learning based on the development of digital technology. Teachers and students can communicate and learn in cloud class, and even complete classroom teaching. Through cloud based classes, teachers can create classes and courses, push teaching materials such as courseware, videos, images, and text to students, and students can also respond in cloud based classes. The launch of this modern interactive teaching platform has brought more possibilities for art teaching. In the process of practice and exploration in the use of cloud classes, teachers have changed the teaching state, no longer instilling knowledge into students, but teaching students how to use modern technology to obtain real and effective information, how to improve the interaction of learning in the process of learning, and how to conduct active inquiry learning methods [10]. How to make this technological means play a significant advantage in art classroom and extracurricular teaching and learning, making the use of mobile devices such as mobile phones in students' hands undergo powerful changes, turning them into powerful learning tools, and stimulating students' interest in using mobile phones for self-directed learning. Making these tools better serve art appreciation teaching is worth exploring and researching strategies for teachers and students to interact in real-time using mobile phones [11].

By using this interactive platform in autonomous learning, students can choose learning content according to their own needs, the depth of learning content according to their own ability, and the learning content according to their own needs, whether in class or at any free time after class. Teachers can track and feedback students' learning situation in time, so as to achieve effective learning. The appropriate combination of the positive role of fuzzy control can effectively improve the teaching effect of art appreciation.

5.2   Sampling Point Optimization Strategy Based on Fuzzy Control

In the process of art appreciation, it is necessary to combine fuzzy control method to control the image intelligently, and resample the image by setting discrete sampling points to simulate the deformation caused by the transformation of viewing angle. Because discrete sampling cannot guarantee the optimal matching of the sampled image, this paper uses Nelder-Mead method [12] as an optimization tool based on ASIFT algorithm, and introduces fuzzy control according to the characteristics of ASIFT sampling space to realize the adaptive adjustment of simplex parameters, in order to make the sampling points converge towards the optimal matching direction.

5.2.1 Affine Imaging Model

ASIFT algorithm simulates the deformation of target in different angles by means of affine image sampling. Through Singular Value Decomposition (SVD), the algorithm verifies that any positive definite affine transformation A can be decomposed into:

$$A = \lambda R_\psi \begin{pmatrix} t & 0 \\ 0 & 1 \end{pmatrix} R_\phi = \lambda \begin{pmatrix} \cos\psi & -\sin\psi \\ \sin\psi & \cos\psi \end{pmatrix} \begin{pmatrix} t & 0 \\ 0 & 1 \end{pmatrix} \begin{pmatrix} \cos\phi & -\sin\phi \\ \sin\phi & \cos\phi \end{pmatrix} \quad (5.1)$$

Among them, $\lambda > 0$, $\varphi \in [0, 180]$, $t \geq 1$, R_ψ and R_φ are rotation matrices corresponding to camera orientations. Figure 5.1 depicts the geometric meaning of λ, ψ, φ in Eq. (5.1). Among them, λ represents the scale change, $\varphi = \arccos(\frac{1}{t})$, and ψ is the camera rotation angle. In the sampling process, the image to be matched is placed in the center of XOY plane, and the transformed image can be resampled according to the camera orientation and angle.

Because SIFT (Scale-Invariant Feature Transform) operator is invariant to rotation and scale, ASIFT only samples t and l in Eq. (5.1). The sampled image can be obtained by the following transformation matrix, see Eq. (5.2):

$$I_{t,\phi} = \begin{pmatrix} t & 0 \\ 0 & 1 \end{pmatrix} R_\phi(I) \quad (5.2)$$

Figure 5.1 depicts the ASIFT sampling point setting with respect to t and φ, where the black dots indicate where the camera is placed.

After the sampled images are generated, all images are extracted and matched by SIFT features. In order to speed up the algorithm, ASIFT adopts dual-resolution strategy. In the first stage of the algorithm, the image to be matched is sampled by 3 × 3 to reduce the resolution of the image, so as to speed up SIFT feature extraction and matching, and save the five transformation models with the most matching. Re-transform and SIFT feature extraction in high-resolution images to improve the robustness of the algorithm to affine transformation.
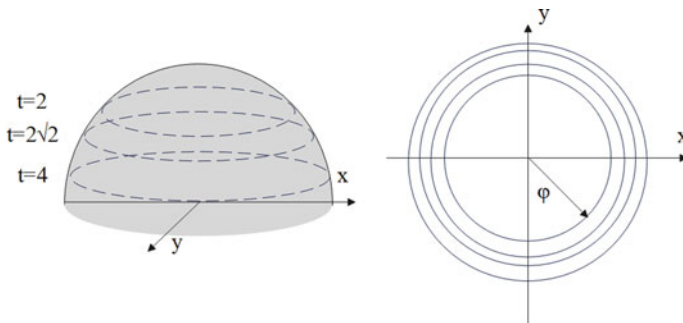
Fig. 5.1 Sampling point settings of t and φ

Although ASIFT algorithm has strong robustness to the change of viewing angle, the sampling points of ASIFT algorithm are discrete, which cannot guarantee the maximum matching of the obtained images in continuous space. As shown in Fig. 5.2a, b, there is deformation between the two images. By affine sampling of two images and calculating SIFT feature matching number, the matching point function corresponding to rotation angle is shown in Fig. 5.2c. It can be seen that the matching feature is a multimodal problem. Obviously, the matching number obtained by ASIFT finite discrete sampling points cannot guarantee global optimality. Because the sampling points of ASIFT algorithm are dense and the optimal matching is generally not far from the global optimum, this paper introduces Nelder-Mead algorithm, which takes the approximate optimal transformation model found by ASIFT algorithm as the initial point, and uses Nelder-Mead algorithm's ability to climb mountains quickly to find the optimal transformation model. In addition, according to the characteristics of image sampling set, this paper also introduces fuzzy control strategy to realize the adaptive adjustment of simplex parameters, so that simplex algorithm can better converge to the extreme point of matching function.

5.2.2   Fuzzy Control Strategy with Pure Shape Parameters

In Nelder-Mead method, γ, β and ρ are the key parameters, which determine the search range and convergence rate of simplex. Generally, we take $\gamma = 1$, $\beta = 0.5$, and $\rho = 0.5$. In the observation of ASIFT, we find that its parameter space and objective function have the following characteristics (see Fig. 5.3).

(1) The objective function changes little (flat) near the peak value. This is because the traditional SIFT algorithm itself has a certain view invariance, and changing the sampling parameters in a small range will not affect the SIFT matching value. Therefore, even if the search range is enlarged near the optimal value, the convergence property of the algorithm is generally not affected;

(2) The objective function shows a step in the non-peak region. Especially, in the process of climbing to the "peak", the objective function changes dramatically, so the search range should be reduced to ensure the convergence stability of the algorithm.

In view of the above characteristics, this paper introduces fuzzy control strategy into Nelder-Mead simplex method. The purpose is to make the optimization algorithm adaptively adjust the parameters according to the current matching value, so as to improve the search efficiency. Because ASIFT only samples two rotation angles, simplex consists of three vectors in two-dimensional parameter space. If the three vectors are assumed to be a_0, a_1 and a_2 respectively, the difference between the three vectors can be expressed by the following Eq. (5.3):

Fig. 5.2 Image deformation
and multimodal cost function

(a)

(b)
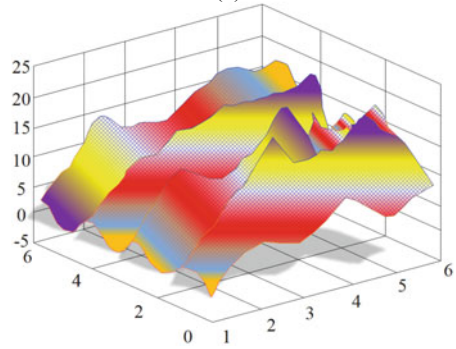
(c)

$$E = \frac{1}{3N} \sum_{i=0}^{2} E(a_i) \qquad (5.3)$$

$$\mathrm{Var} = \frac{1}{3N} \sum_{i=0}^{2} (E(a_i) - E(\overline{a}))^2 \qquad (5.4)$$

Fig. 5.3 Basic operation of Nelder-Mead algorithm
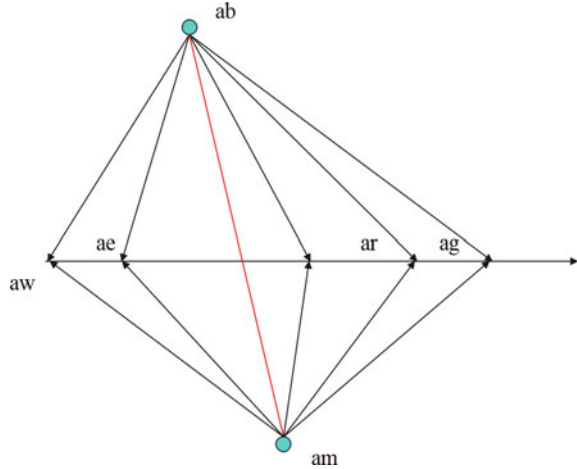
Among them, $\overline{a}$ represents the mean of three vectors, $E(a_i)$ represents the number of matches corresponding to the i-th vector, and N represents the number of feature matches of the optimal vector.

5.2.3   Fuzzy Control Model of Art Appreciation Class

Combined with fuzzy control algorithm, this paper puts forward the idea of using paintings to improve visual literacy, analyzes paintings and students as the main factors affecting the improvement of visual literacy, and puts forward specific improvement methods. Finally, the solutions are applied to specific teaching practices. Moreover, this paper gets teaching feedback from students' classroom participation and homework completion, and explores effective resources suitable for improving students' visual literacy, as shown in Fig. 5.4.

Under the background of computational thinking teaching, based on the virtual teaching model of "input-virtualization-output", this study recombs the relationship between users and systems in virtualization from the perspective of embodied cognition, that is, the relationship between students, learning tools, and teachers. Specifically, students form a perceptual motor cycle by controlling the feedback of learning tools and perceptual learning tools, while teachers need to support students' interaction with tools (as shown in Fig. 5.5). The introduction of cognitive perspective enables this model to explain more deeply how students learn computational thinking in the interaction between body and environment, and the role played by teachers in it.

Fig. 5.4 Teaching modulus of art appreciation class combined with fuzzy control algorithm
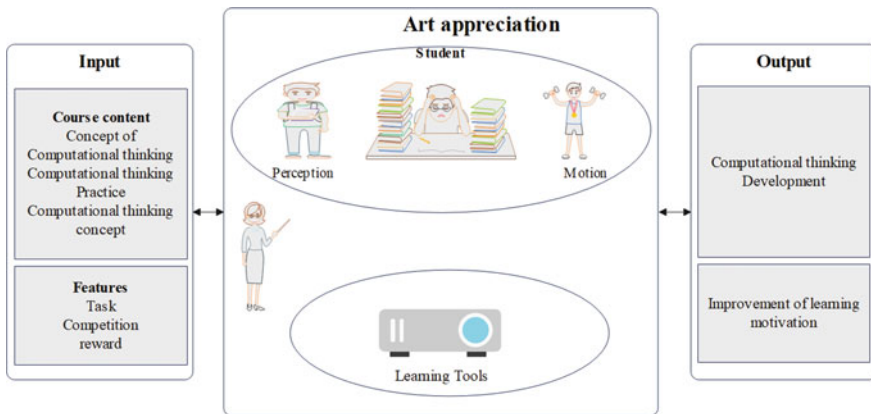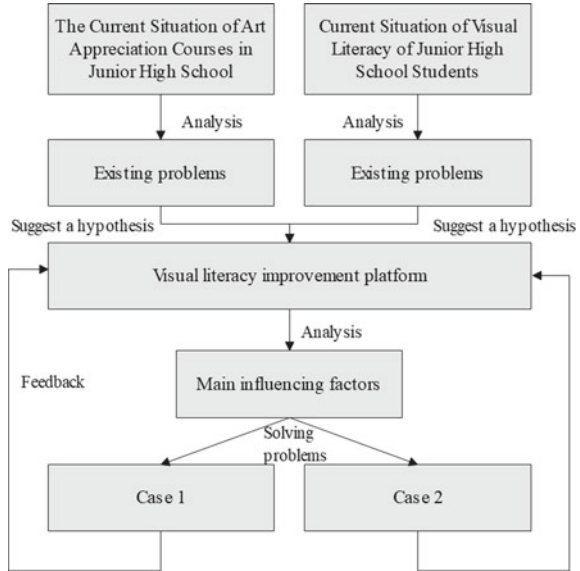
Fig. 5.5 Virtual teaching model of computational thinking in art appreciation class

5.3　Verification of the Function of "Fuzzy Control" in Art Appreciation

The "fuzziness" in painting creation does not mean the real confusion or pure fuzziness in its connotation. It is relative to the clear concept of rational abstraction, relative to the accuracy of science and relative to the essential law of abstraction. It refers to the richness, polysemy and uncertainty of sensibility, which has no strict scientific logic, but has a moving emotional rationality with strong subjective color.

Moreover, emotional factors undoubtedly run through the whole process of painting creation, and it is the rich emotional experience that urges painters to pick up brushes. The artist's inspiration imagination is the irresistible passion of emotion, and it is the strong artistic impulse of not spitting out unhappiness that has the motive force of continuous innovation and development of painting art. There is no doubt that finding our attitude towards life-unique emotional experience is the first step into creation.

Art works have the basic characteristics of modeling, visibility, static, and materiality. Therefore, art image has naturally become an ideal terminal form for artists to realize in art works. The purpose of a work of art is to express basic or remarkable features, which are more complete and clearer than physical objects. Artists first form a concept of basic features, and then change physical objects according to the concept. After such changes, the objects are "consistent with the artist's concept", that is to say, they become "ideal". Although it also belongs to objective existence, it is different from the objective reality in our lives. The so-called "art originates from life and is higher than life". This shows that the concepts instilled by artists in their works also have "undetermined" "fuzzy levels".

In art appreciation, students often play a "rational" bystander and an object of appreciation, describing artistic emotions in a stylized way, such as "embodying the wisdom and strength of the working people", "expressing the lofty ideals of the author", "reflecting the darkness and cruelty of feudal society", etc., without their own true emotional imagination at all, they are completely passive in appreciation.

Constructivism theory holds that learning is a process in which learners actively construct knowledge, rather than a process in which textbooks and teachers' knowledge are simply loaded into students' minds. Art appreciation can't be a process in which teachers instill a single certain related knowledge into students, and students can't be bystanders and recipients of appreciation.

Based on the "fuzzy level" of art works, we should create a certain situation, encourage students to boldly imagine emotions and feel artistic images from multiple angles, and don't let teachers' aesthetic expression become the only aesthetic standard.

The "fuzzy level" in art works leaves readers with broad thinking space and room for emotional association, and each reader's personality is different. Teachers can make full use of this, explore each student's perception potential, and give students more opportunities to take the initiative to participate, which is very beneficial to the development of students' aesthetic personality.

Build a simulation experimental environment by combining hardware and software environments. The hardware environment is divided into five parts, namely: output device, input device, central processing unit, motherboard, and memory. The specific hardware device environment settings are shown in Table 5.1

Under the guidance of the above ideas, this paper verifies the effect of fuzzy control algorithm in art appreciation.

Figure 5.6 shows an appreciation case of hazy art works. In this paper, the fuzzy control algorithm proposed in this paper is used to analyze art works in a variety of ways, so as to improve the diversity of art works and facilitate students to appreciate

Table 5.1 Simulation experimental environment

Type	Model
Display	DELL Ultra Sharp3008 WFP
Central processing unit	Intel Core i9 -3970X
Memory storage	ADATA XPG DDR3-1600 4 GB*4GIGABYTE GA-X79-UD7
Motherboard	Cinema series
Scanner	Guide 600/i700 Series
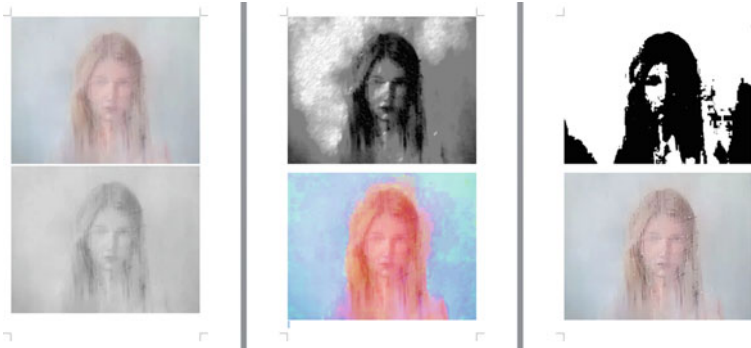
Fig. 5.6 A case of fuzzy appreciation of art works

art works from multiple angles. On this basis, we verify the effect of art appreciation system based on fuzzy control, count the practical effect of this model in art appreciation class, and get the verification results shown in Table 5.2 and Fig. 5.7.

As shown in Table 5.2 and Fig. 5.7, the fuzzy control model proposed in this paper has good performance in art appreciation, with evaluation scores distributed directly in [77,87]. Based on this, the method proposed in this paper is compared with the fuzzy control method proposed in Ref. [12] to analyze its effectiveness in art appreciation. Reference [12] developed an optimized driven deep learning technique for image forgery detection. Local GaborXOR patterns and Texton features were extracted from the partition, and deep neural fuzzy networks were used to detect forgery. Similarly, a scoring method is used for comparison, and the results shown in Table 5.3 are obtained.

From the above analysis, it can be seen that the fuzzy control method proposed in this article has good effects on art appreciation and has certain advantages compared to traditional algorithms.

From the above research results, we can see that the fuzzy control algorithm proposed in this paper can effectively improve the appreciation effect of art works, facilitate the development of students' creative thinking, and contribute to the innovation and improvement of the follow-up art appreciation course.

Table 5.2   Effect evaluation of art appreciation system based on fuzzy control

Number	Fuzzy control evaluation	Number	Fuzzy control evaluation	Number	Fuzzy control evaluation
1	79.83	13	83.61	25	78.36
2	77.29	14	78.96	26	83.70
3	80.18	15	80.17	27	83.89
4	77.66	16	79.63	28	80.18
5	83.79	17	80.47	29	80.04
6	82.46	18	83.48	30	79.15
7	80.18	19	82.55	31	83.96
8	83.43	20	79.30	32	79.72
9	84.06	21	83.21	33	84.19
10	85.02	22	85.69	34	78.12
11	81.72	23	78.06	35	78.71
12	84.95	24	85.99	36	80.12
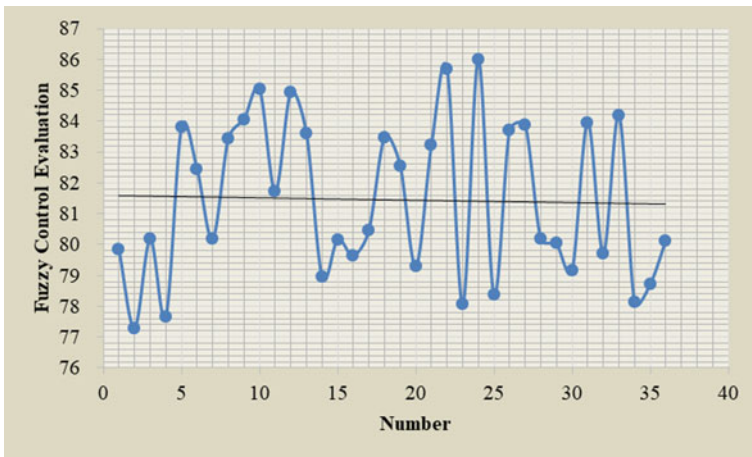
Fig. 5.7   Statistical diagram of system evaluation data

Table 5.3   Comparison test results

	Method of this article	Method of Ref. [12]
1	85.23	79.52
2	84.32	78.24
3	84.63	80.11
4	84.35	79.32
5	85.21	79.56
6	85.33	80.11

5.4   Conclusion

Today's education is vigorously advocating the cultivation of students' innovative thinking and practical ability. The art discipline aims at cultivating students' aesthetic ability and aesthetic quality, which can only be reflected in real life. "Lifelong education" has been deeply rooted in people's hearts, and art education is not the accumulation of art works, but the comprehension of the inner meaning of artistic images, so as to hone their thinking habits and emotional imagination.

In the process of art appreciation, we need to combine fuzzy control method to control the image intelligently, and resample the image by setting discrete sampling points to simulate the deformation caused by the transformation of visual angle. This paper gives a teaching model of art appreciation course combined with fuzzy control, and verifies the effect of the teaching model by combining cases with teaching evaluation. The research shows that the fuzzy control algorithm proposed in this paper can effectively improve the appreciation effect of art works, facilitate the development of students' creative thinking, and contribute to the innovation and improvement of the follow-up art appreciation course.

References

1. Wan, Q., Song, S.S., Li, X.H., Zhang, Q., Yang, X., Zhang, Y.C., et al.: The visual perception of the cardboard product using eye-tracking technology. Wood Res. **63**(1), 165–178 (2018)
2. McCartney, N., Tynan, J.: Fashioning contemporary art: a new interdisciplinary aesthetics in art-design collaborations. J. Vis. Art Pract. **20**(1–2), 143–162 (2021)
3. Lockheart, J.: The importance of writing as a material practice for art and design students: a contemporary rereading of the Coldstream Reports. Art Des. Commun. High. Educ. **17**(2), 151–175 (2018)
4. Sachdev, G.: Engaging with plants in an urban environment through street art and design. Plants People Planet **1**(3), 271–289 (2019)
5. Andreeva, Y.M., Luong, V.C., Lutoshina, D.S., Medvedev, O.S., Mikhailovskii, V.Y., Moskvin, M.K., Veiko, V.P., et al.: Laser coloration of metals in visual art and design. Opt. Mater. Express **9**(3), 1310–1319 (2019)
6. Nebessayeva, Z., Bekbolatova, K., Mussakulov, K., Zhanbirshiyev, S., Tulepov, L.: Promotion of entrepreneurship development by art and design by pedagogy. Opción **34**(85–2), 729–751 (2018)
7. Mourtzis, D.: Simulation in the design and operation of manufacturing systems: state of the art and new trends. Int. J. Prod. Res. **58**(7), 1927–1949 (2020)
8. Klockars, K.W., Yau, N.E., Tardy, B.L., Majoinen, J., Kämäräinen, T., Miettunen, K., Rojas, O.J., et al.: Asymmetrical coffee rings from cellulose nanocrystals and prospects in art and design. Cellulose **26**(1), 491–506 (2019)
9. Maras, K.: A realist account of critical agency in art criticism in art and design education. Int. J. Art Des. Educ. **37**(4), 599–610 (2018)
10. Ravelomanantsoa, M.S., Ducq, Y., Vallespir, B.: A state of the art and comparison of approaches for performance measurement systems definition and design. Int. J. Prod. Res. **57**(15–16), 5026–5046 (2019)

11. Tsai, K.C.: Teacher-student relationships, satisfaction, and achievement among art and design college students in Macau. J. Educ. Pract.Pract. **8**(6), 12–16 (2017)
12. Mariappan, G., Reddy, P.V.B., Satish, A.R., et al.: Adaptive partitioning-based copy-move image forgery detection using optimal enabled deep neuro-fuzzy network. Comput. Intell.. Intell. **38**(2), 586–609 (2022)

Chapter 6
Discussion on the Establishment and Application of Intelligent Design Platform for Concrete Proportioning

Zhengguang Zhang and Jing Chen

Abstract More than 3 billion m^3 of ready-mixed concrete was produced nationally in 2021, the largest structural engineering materials for transportation and urban construction. The key to ensuring project quality and cost optimization is the design of the concrete mix ratio. The system shares the massive concrete raw material, mix ratio, compressive strength, and real-time testing data deposited by concrete producers to the cloud (Ali cloud) through the concrete mix ratio intelligent design and sharing platform. It provides real-time feedback to guide the adjustment and optimization of the mix ratio through the machine learning algorithm deployed in the cloud, integrating expert knowledge, deep neural network, and Monte Carlo algorithm. It also carries out 28-day concrete compressive strength prediction. The platform and terminal equipment realize the digitization and sharing of data related to concrete ratio design, which is an important carrier for the industrialization of concrete mix data and is of great significance to cost reduction and efficiency of engineering construction, as well as having great potential commercial value. For the application scenario of slab ballastless track, a test device for intelligent testing of key properties of self-compacting concrete (SCC) is designed and produced, relying on the intelligent design and sharing platform to realize the collection, storage, analysis, and application of SCC data.

6.1 Introduction

Machine learning is capable of mining laws and knowledge from complex data through various computational models and algorithms. It has become one of the core technologies in contemporary artificial intelligence. Deep neural networks, with the

Z. Zhang (✉) · J. Chen
School of Materials Science and Engineering, Chongqing JiaoTong University, Chongqing, China
e-mail: 786002916@qq.com

J. Chen
Chongqing Construction Building Materials and Logistics Company, Chongqing, China

advantage of fitting nonlinear problems, have been used to predict the key properties of concrete and mix ratio design [1]. It has been shown that the use of deep learning techniques for concrete proportion design is an effective way to address the design of concrete proportions for complex components.

Ren et al. introduced a new approach to optimize the proportion design of high-performance concrete (HPC) for multiple objectives, including compressive strength, production cost, and carbon emissions, using artificial intelligence algorithms and metaheuristic search techniques [2]. The effectiveness and superiority of this method have been successfully demonstrated through its application in a specific engineering project [3]. Zhao discussed potential issues that may arise when integrating the concrete industry with the artificial intelligence industry. It is important to note that effective communication between the concrete and artificial intelligence industries requires individuals with relevant knowledge to act as intermediaries, and the cultivation of such personnel is necessary [4]. For the two core requirements of intelligent concrete mix design and accurate prediction of concrete properties, four technical aspects are described in this paper. Firstly, hardware, basic network construction, computer hardware, and equipment intelligent transformation are carried out; then data collection system deployment and development are carried out; then the intelligent design and sharing platform of the mix ratio is established; finally, big data mining and analysis of the platform are carried out and developed and applied.

Based on the intelligent design and sharing platform of concrete ratio, a special concrete performance testing device is designed for the rheological properties, construction performance, and forming quality of CRTSIII SCC application scenarios, which builds a physical platform for data collection of the same type of concrete and establishes a data foundation for intelligent design of this type of concrete.

6.2   Platform Architecture

A necessary prerequisite for intelligent concrete mix design is the acquisition, processing, and application of raw material, mix, and performance data obtained from existing concrete business operations. In pursuit of this objective, a series of technological advancements have been pursued to optimize data utilization and enhance the intelligence of concrete mix design. As shown in Fig. 6.1, we virtualized the data in the host, storage, network, and other infrastructure to form a pool of resources such as computing resources, storage resources, and network resources. This allows us to flexibly adjust the resource allocation to meet the needs of different application scenarios.

In the specific implementation process, we relied on Chongqing Construction Industry Building Materials Logistics Co., Ltd. to establish a database covering raw materials, mixing ratios, and performance data. This database includes various key data generated in the production process of the enterprise, such as cement type, aggregate grade, admixture content, etc. By analyzing these data in detail, we can
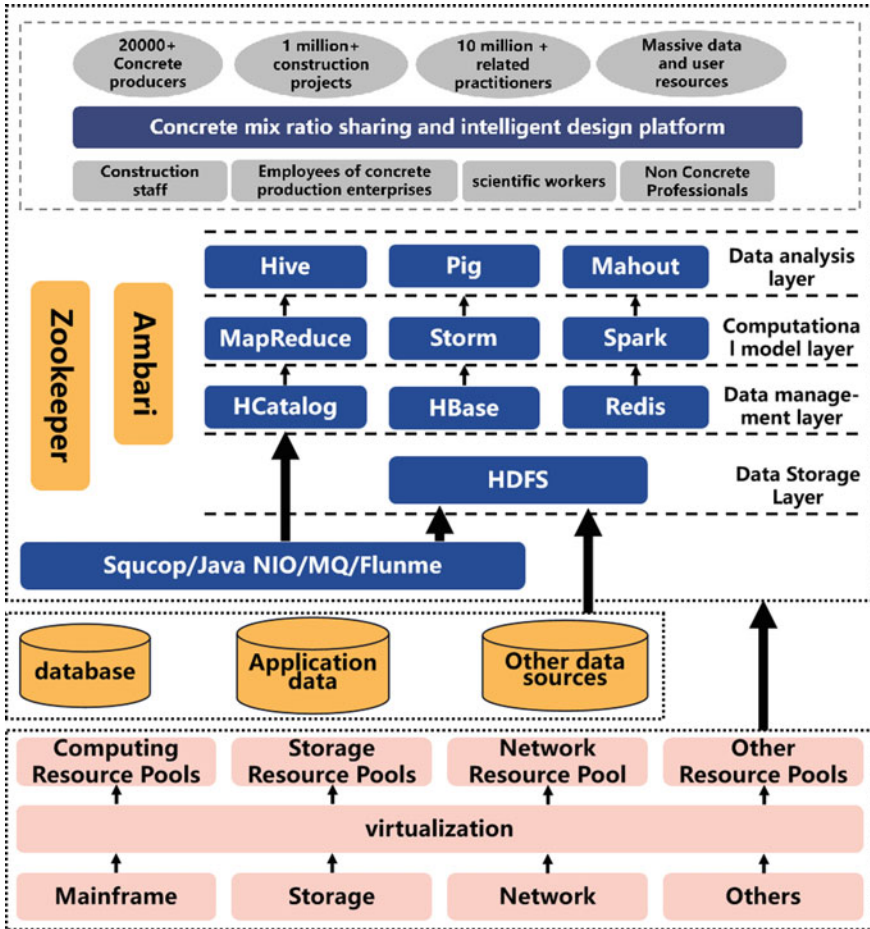
Fig. 6.1 Overall architecture of the intelligent design and sharing platform for concrete mix ratio

gain a more comprehensive understanding of the various variables in the concrete production process and provide a basis for intelligent design.

To further enrich the database, we also intend to use other infrastructures to collect specific data for specific application scenarios. For example, special equipment was developed to measure and upload the performance of key indicators of self-compacting concrete (SCC) for ballastless track, and a special database was created. This data will not only help us to better understand the concrete performance requirements in these specific scenarios, but will also provide additional reference information for our intelligent design.

6.3 Design Scheme

The platform proposes a prediction model for 28-day compressive strength of concrete based on integrated learning, considering that the prediction ability of multiple models is stronger than that of a single model. Subsequently, considering that deep learning has a more mature framework and can adapt to the real-time required for production, by weighing the advantages of deep learning and integrated learning, a deep learning-based intelligent concrete mix ratio design model is proposed, which selects the mix ratio by establishing an expert knowledge base, adjusts the mix ratio with Monte Carlo random scoring, and uses a deep learning-based concrete performance prediction method. Finally, the cost of concrete mix ratio is used as the optimization target to find the optimal value.

6.3.1 Record Extraction and Cost Optimization

On the application terminal, the user enters the technical requirements of the desired target concrete and the varieties of raw materials and their performance indexes through the intelligent design page, and then searches, matches, and scores a large number of records in the cloud concrete database through the matching rule table summarized from the expert experience, and the 10 records with the highest scores are used as the results of the initial screening and transmitted in the form of an alternative set to the intelligent design model. Then, based on the records matched by the database, the intelligent design model integrates expert knowledge, deep neural network, and raw material prices, and uses Monte Carlo search algorithm to find a set of optimal mix ratio design solutions in the domain knowledge space. Finally, this solution and the 10 historical records matched by the database are put back to the intelligent design page as the final result [5, 6].

The ultimate goal of the intelligent design is to minimize the unit cost of the concrete while satisfying the target concrete performance requirements and proportional constraints. According to this objective, the mathematical expression of optimal cost model is shown in Fig. 6.2. After determining the optimization target, the concrete mix fine-tuning specific steps are shown in Fig. 6.2: the user needs to filter out the concrete production mix with the highest rating in the database as the benchmark mix through the scoring rules, calculate the production cost of the mix as the preset optimal mix unit production cost Cost_min, set d to 0, set the maximum effective number of counts d_{max} to 50,000 times, carry out Iterative calculation, and finally achieve the purpose of cost reduction. "d" refers to the number of iterations of the process.
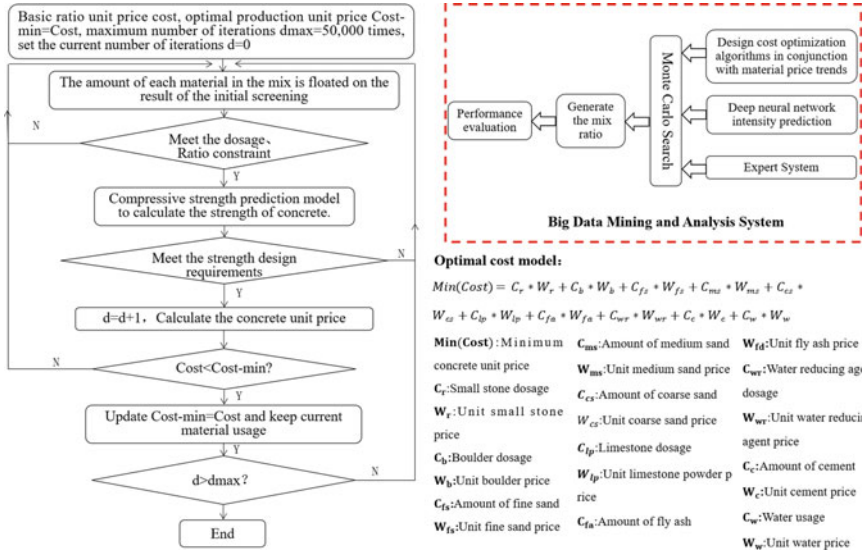
Fig. 6.2 Cost optimization model

6.3.2 Compressive Strength Prediction Model

The prediction model framework for the 28-day compressive strength of concrete is shown in Fig. 6.3. The model mainly consists of four components: data preprocessing, feature engineering, ADARF (AdaBoost Method Based on Random Forests) regression model, and performance evaluation criteria. Because of manual data collection, data entry, and other factors, the provided concrete data have problems with missing data and noise. Therefore, we need to perform data preprocessing on historical data, which mainly includes eliminating outliers, removing duplicate data, and missing value filling. After data preprocessing, this paper analyzes the heat map, consults industry experts for feature selection and fusion, and finally selects common regression evaluation indexes to evaluate the performance of the model, as shown in Fig. 6.3.

The concrete mix production dataset provided by Chongqing Construction Group contains 11 attributes, covering 9,500 production data from January to December 2018. Of these, 3 attributes are related to concrete mix production, while 28 attributes are related to concrete production conditions and performance testing. The dataset has been preprocessed and cleaned, including removing missing values, deleting duplicate data, removing outliers, and filling in missing values. Pearson correlation coefficients and consultations with concrete experts were used for feature selection and combination. For the first type of attribute, missing values were replaced with 0 to indicate that the material was not used. For the second type of attribute, missing values were filled in with the median value to obtain the best predictive performance. The second type of attribute related to concrete production conditions was encoded
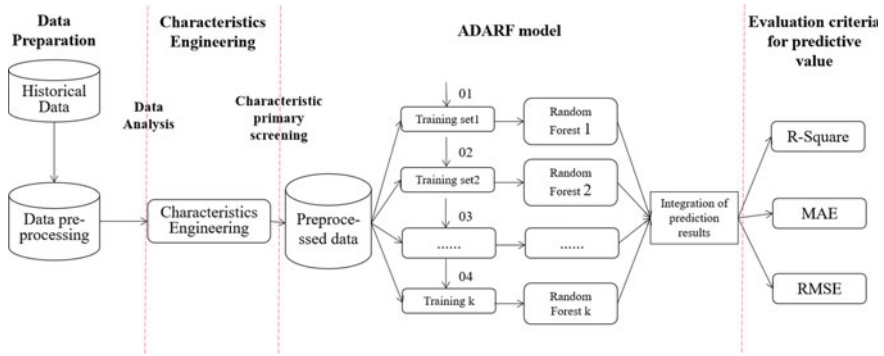
Fig. 6.3 Prediction model for 28-day compressive strength of concrete
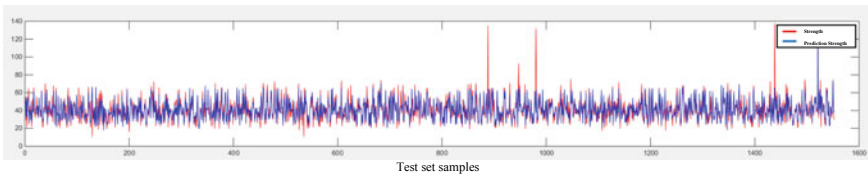
Fig. 6.4 Actual compressive strength versus model-predicted compressive strength

using ordered numbers for better performance. Overall, the dataset contains rich information, and after preprocessing and feature selection, it can be used to establish a concrete compressive strength prediction model [7].

The actual compressive strength of concrete on the test set at the same time and the model-predicted compressive strength are shown in Fig. 6.4, with red representing the actual compressive strength and blue representing the predicted compressive strength. As can be seen from the figure, the neural network operation results match well with the actual compressive strength and their regression values with good accuracy. Only three groups of ultra high compressive strength concrete predicted values can be seen as significant errors, because they exceed the predicted threshold. The online capability of the built BP neural network is strong through experimental testing, which can adapt to the high real-time requirement of the concrete intelligent proportioning design model.

6.3.3 Performance Testing Device of CRTSIII SCC

CRTSIII SCC is a type of concrete with high fluidity, resistance to segregation, and gap passage properties. Before construction, the SCC must be subjected to a process test—the uncovering test. The uncovering test is mainly to observe the working performance of concrete during the filling process, to uncover the slab 24 h after

filling, and to judge the forming quality of SCC by inspecting the air bubbles on the joint surface and section of concrete. The ratio will then be empirically adjusted in conjunction with the ambient temperature and humidity conditions. This test is tedious, time-consuming, and labor-intensive, and the empirical judgment by visual inspection is less efficient and accurate. It cannot form a systematic method for adjusting the mix ratio. The uncovering test has specific requirements for the site, which cannot be met by ordinary R&D laboratories. At the same time, concrete is highly sensitive to materials and environment, and a small change in the mix ratio will have a large impact on the concrete performance. Therefore, we have designed a device that can standardize the performance testing of the same type of SCC, taking into account the actual needs. The device is small enough to be used in the scenarios of laboratory and mixing plant, and can be used to standardize the recording, performance data, and conditions, then store them. The application of this device is an attempt to the concrete intelligent design platform in the design of special concrete mixes.

In order to meet the special performance inspection requirements of CRTSIII SCC [8], our design scheme is as follows: the test storage device is an inverted quadrilateral cone-shaped feeding cylinder that can control the concrete filling volume and characterize the concrete viscosity by detecting the concrete outflow time; the length of the device chute is set to 4.2 m according to the distance from the track slab to the filling port in engineering applications, and the discharge port is designed For observation; In order to release the concrete after hardening, the concrete chute cross-section is designed as inverted trapezoid, and handrails are set around;In order to clearly observe the concrete flow state, the chute cover is designed as acrylic transparent material, and at the same time, a sheet pressure detection module is installed on the chute cover to measure the jacking force after the concrete filling is completed;Spacers were set at four equal parts of the chute to simulate distribution of reinforcement, with the aim of testing its gap passage performance. The model drawing is shown in Fig. 6.5.

6.4 Technical Architecture and Application

The system forms a complete technical architecture by establishing an intelligent design and sharing platform for concrete, designing an intelligent design scheme for the mix ratio, constructing a pre-integrated prediction model for the 28-day compressive strength of concrete, and inventing an intelligent data collection terminal such as performance testing device of CRTSIII SCC, which can realize data collection in various ways, mix ratio design for various needs, data extraction, optimization and prediction.

The system has a wide range of application scenarios. For professional concrete production enterprises, the production process requires a large number of concrete ratio design work. There is a large amount of raw materials, ratio, and performance data, which can supplement and improve the database. For non-professional units
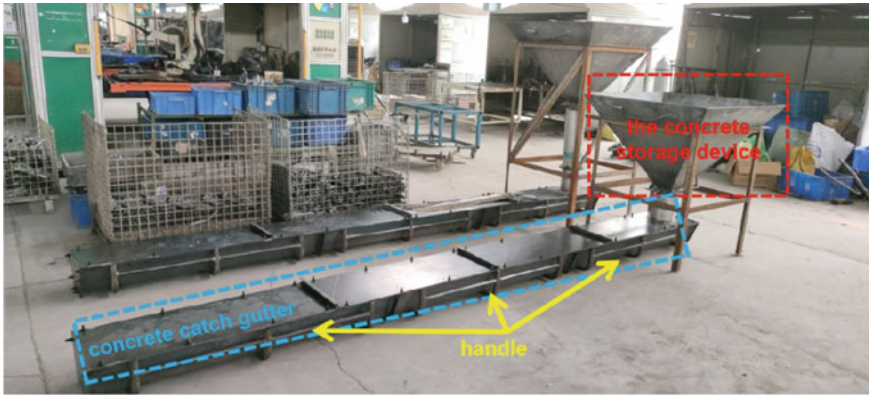
(a)Performance testing device of CRTSⅢ SCC

(b)Acrylic cover plate   (c)Pressure detection device
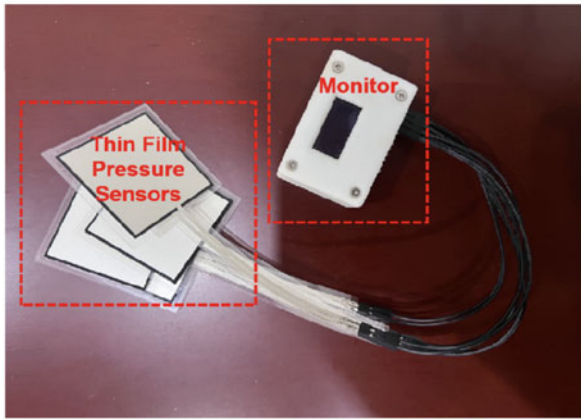
Fig. 6.5 Performance Testing Device for CRTSIII SCC

and on-site mixing stations, it can lower the threshold of the industry and improve the efficiency and accuracy of the mix design. For universities and research institutions, it provides new ways for data collection and analysis. For special concrete projects, it provides a data interface for concrete with special performance requirements, and realizes data collection, storage, analysis, and application. The technical architecture and application are shown in Fig. 6.6.

Based on this, relevant tests were conducted in this study. Firstly, the target mix design parameters were determined as follows: compressive strength grade C30, variety: ordinary concrete, slump: 200 mm, expansion: 500 mm, impermeability grade: P6. The source material information was as follows: cement from Chongqing Xiaonanhai Cement Plant, variety grade: P·O42.5R; fine aggregate 1: fine sand, fine
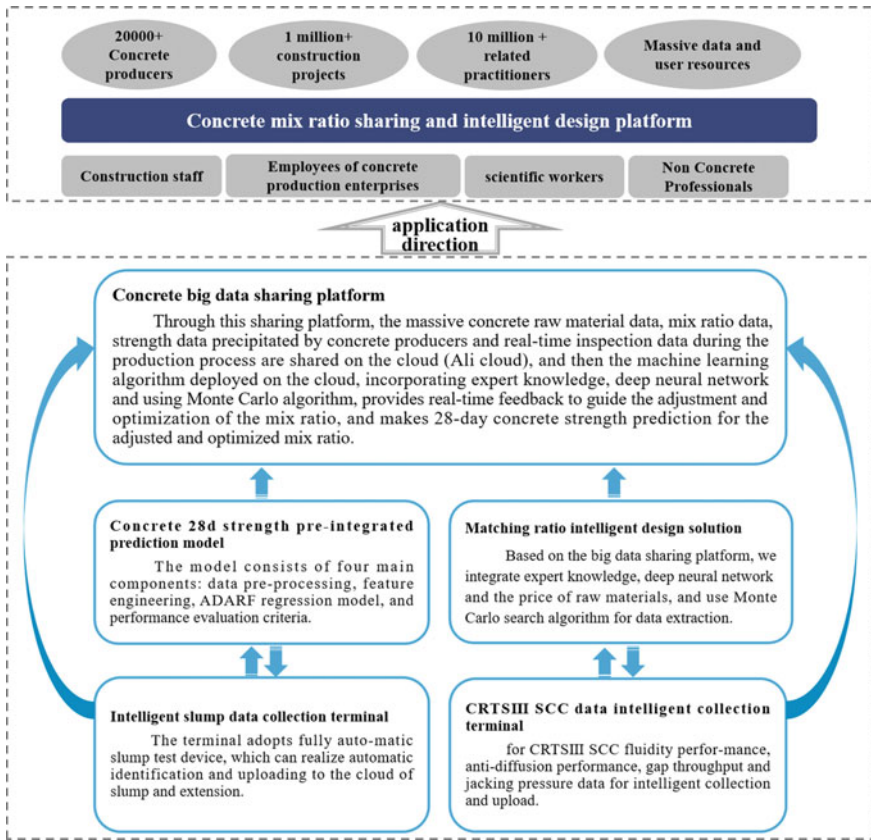
Fig. 6.6 Technical architecture and application direction

aggregate 2: medium sand; coarse aggregate 1: 5–10 mm, coarse aggregate 2: 10–20 mm; water reducing agent variety: PCA-l polycarboxylic acid high-performance water reducing agent; water reducing rate: 30%.

Finally, the target concrete mix design was developed, with the dosage per cubic meter (kg) of cement, coarse aggregate 1, coarse aggregate 2, fine aggregate 1, fine aggregate 2, water, and water reducing agent being 315, 375, 709, 12, 804, 160, and 6.53, respectively. The calculated density of the concrete was 2382 kg/m^3, and the compressive strength prediction model yielded a compressive strength of 45.3 MPa at 28 days, which met the design requirements.

6.5   Conclusion

Concrete mix ratio intelligent design and sharing platform is the product of the combination of traditional concrete producers and digital technology, which has significantly improved the accuracy and efficiency of concrete mix ratio design and saved engineering costs. The platform has been developed into a SaaS product and is now open to a wider range of construction workers, concrete producers, scientists, and non-concrete professionals, greatly improving the intelligence of concrete mix design, improving the efficiency and accuracy of design, lowering the technical threshold of relevant practitioners, and providing a new solution to problems related to the design of special concrete mixes.

References

1. Ziolkowski, P., Niedostatkiewicz, M.: Machine learning techniques in concrete mix design. Materials **12**(8), 1256 (2019)
2. Jiang, Z.W., Xu, C.P., Zhang, S.: Multi-objective performance-based optimization design method for C50 concrete mix proportion. J. Build. Mater. **22**(4), 499–505, 522 (2019)
3. Ren, Q., Li, W., Li, M., Yang, L., Zhang, M., Shen, Y.: Multi-objective intelligent optimization design and analysis method for high-performance concrete mix proportion in hydraulic engineering. J. Hydraul. Eng.Hydraul. Eng. **53**(01), 98–108 (2022)
4. Zhao, F.: A preliminary exploration of technological modeling and intelligent prospect of cement-based material mix design-several issues on modeling and industry docking. Concrete **08**, 60–63 (2021)
5. Naderpour, H., Rafiean, A.H., Fakharian, P., et al.: Compressive strength prediction of environmentally friendly concrete using artificial neural networks. J. Build. Eng. **16**, 213–219 (2018)
6. Cao, X.L., Wang, Q.C., Bao, X.Y.: Concrete mix ratio design and strength prediction. J. Silic. Bull. **03**, 55–59 (2015)
7. Lv, Y.X., Shi, X.Y., Ran, L.Y., et al.: Random forest-based ensemble estimator for concrete compressive strength prediction via AdaBoost method. In: The International Conference on Natural Computation, Fuzzy Systems and Knowledge Discovery, pp. 557–565. Springer, Cham (2019)
8. Lv, M., An, X.H., Li, P.F., Zhang, J.B., Bai, H.: Research progress on the whole-process intelligent production of self-compacting concrete. J. Tsinghua Univ. (Natural Science Edition), 1–11 (2022)

Chapter 7
Locally Adaptive Processing of Color Tensor Images Represented as Vector Fields

Lakhmi C. Jain, Roumen K. Kountchev, and Roumiana A. Kountcheva

Abstract A new approach for locally-adaptive processing of color RGB images represented as tensors of size M × N × 3, is offered in this work. Unlike the famous similar methods of the kind, the processing here is executed on a single matrix only, which comprises the modules of the vectors, corresponding to the image pixels' colors. A group of related basic algorithms for locally-adaptive processing is presented, which have lower computational complexity than that of the algorithms, applied individually on each of the RGB components. As it is known, in the famous color RGB transform models of the kind YCrCb, HSV, HSI, Lab, KLT, etc., the processing is applied on the most powerful transformed color component only, and after inverse operation, the original RGB model is restored. In contrast, the idea for locally-adaptive processing does not need direct and inverse transform of the color model. Together with this, the brightness and the color hue of the processed image pixels, are retained. The characteristics of the proposed basic algorithms for contrast enhancement, linear and non-linear sharpness filtration, noise suppression, and texture segmentation, are defined. Some examples for locally-adaptive processing of color medical images are given, which illustrate the related algorithms. The presented approach could be also used for other kinds of color images, where the visibility of their local structure is of high importance.

L. C. Jain
KES International, Selby, UK

R. K. Kountchev
Technical University of Sofia, Sofia 1000, Bulgaria

R. A. Kountcheva (✉)
TK Engineering, Sofia 1582, Bulgaria
e-mail: kountcheva_r@yahoo.com

7.1 Introduction

The initial form for color image representation is a tensor of size M × N × 3, which has three sections—the matrices R,G,B each of size $M \times N$, whose pixels have $m = 2^b$ intensity levels in the range (0 to $m - 1$), coded through 24 bpp, for $b = 8$. The objective of this work is to present and analyze some basic algorithms for locally-adaptive processing of color tensor images represented as vector fields, and to evaluate the advantages in some basic operations for various applications, such as: contrast enhancement, noise filtration, contours extraction, areas segmentation, etc. In many publications [1–6] related to color images processing, used the approach in which the RGB color model is transformed by using some other models: YCrCb, HSV, HSI, Lab, KLT, etc. [7]. In these cases, the chosen operations are applied on the most powerful component of the new model, after which the original RGB model is inversely restored. Such approach implies the use of direct and inverse transform of the color model, which increases significantly the computational complexity of the processing. In [8], a method is described to improve the quality of RGB images through saturation increase and retaining the hue, but without brightness preserving.

In this work, a new approach is offered for locally-adaptive processing of color images, represented as matrices of the modules of the color vectors, framed by a sliding window. This approach is highly efficient and adaptive, which opens wide abilities in various application areas. The proposed algorithms do not need direct and inverse transform of the color model and ensure hue and brightness preservation in the processed image. These properties of the introduced algorithms are based on the new form for color tensor image presentation, i.e.—the vector field, which comprises the colors of all pixels. The paper is structured as follows: in Sect. 7.2, the tensor image representation as a vector field is explained; in Sect. 7.3—the essence of the proposed new approach is given; in Sect. 7.4, the image color vectors' modules are defined through 2D-DFT; in Sect. 7.5, the local histograms of color vectors' modules are calculated; Sect. 7.6 is about the local cumulative histograms application; in Sect. 7.7 are given the details of the locally-adaptive filtering for tensor images, represented as vector fields; and the conclusions are in Sect. 7.8.

7.2 Color Image Tensor Representation as a Vector Field

7.2.1 Color Vectors Presentation in Orthogonal Coordinate System Framed by a RGB Cube

In Fig. 7.1a, an RGB cube is shown, into which are defined the color vectors $\mathbf{C}_{k,i}$ for the pixels (k,i) of the color tensor image of size $M \times N \times 3$, 24 bpp. One example vector placed in the color cube is shown, denoted as $\mathbf{C}_0$. The color vector $\mathbf{C}_{k,i}$ in the orthogonal RGB coordinate system, is defined by the relation:
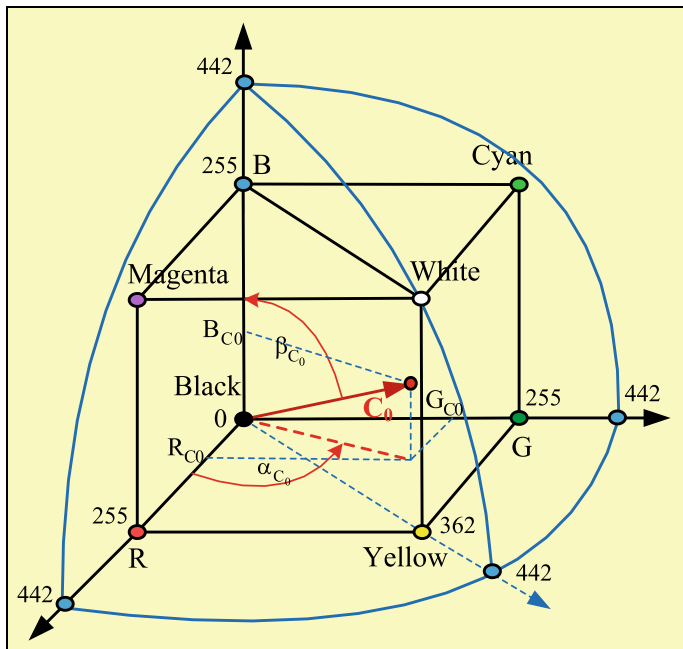
Fig. 7.1 RGB cube in a sphere with a radius MC = 442 and the color vector

$$\mathbf{C}_{k,i} = [R_{k,i}, G_{k,i}, B_{k,i}]^T \text{ for } k/i = 0, 1, 2, \ldots, (M-1)/(N-1). \tag{7.1}$$

7.2.2 RGB Image Representation as a 2D Vector Field

The tensor RGB image representation as a 2D vector field in the 3D spherical coordinate system, is defined by the modules and the phase angles of the color vectors, $\mathbf{C}_{k,i}$.

The color vector $\mathbf{C}_{k,i}$ (denoted as $\mathbf{C}_0$ on Fig. 7.1) could be represented in the spherical polar coordinate system, in accordance with the relation below:

$$\mathbf{C}_{k,i} = [M_C(k, i), a_C(k, i), b_C(k, i)]^T \text{ for } M_C(i, j) = 0, 1, 2, \ldots, 255\sqrt{3}, \tag{7.2}$$

where $(255\sqrt{3} \approx 441.6 \approx 442)$ and $0 \leq \alpha_C(k,i) \leq \pi/2; 0 \leq \beta_C(k,i) \leq \pi/2$.

$\mathbf{C}_0 = [R_{C0}, G_{C0}, B_{C0}]^T$, colored in red (in the RGB cube).

The module, and the orientation angles of the color vector $\mathbf{C}_{k,i}$, are defined by the relations:

$$M_C(k, i) = \|\mathbf{C}_{k,i}\| = \sqrt{R_{k,i}^2 + G_{k,i}^2 + B_{k,i}^2} \tag{7.3}$$

$$\alpha_C(k, i) = \arcsin[B_C(k, i)/M_C(k, i)] \tag{7.4}$$

$$\beta_C(k, i) = \arcsin\{G_C(k, i)/\sqrt{[R_C(k, i)]^2 + [G_C(k, i)]^2}\} \tag{7.5}$$

As a result, the matrices $[R(k, i)], [G(k, i)]$, and $[B(k, i)]$, each of size $M \times N$, are replaced by two matrices: of the modules $[M_C(k, i)]$, and of the color vectors' angles $[\theta_C(k,i)] = [\alpha_C(k), \beta_C(i)]$, both of size $M \times N$. The relationship between the orthogonal and the spherical coordinate systems (R, G, B) and (M_C, α_C, β_C), is:

$$R_C = M_C \cos \alpha \sin \beta; \ G_C = M_C \cos \alpha \cos \beta; \ B_C = M_C \sin \alpha; \tag{7.6}$$

$$M_C = \sqrt{R_C^2 + G_C^2 + B_C^2}; \ \alpha_C = \arccos(R_C/\sqrt{R_C^2 + G_C^2}); \ \beta_C = \arcsin(B_C/M_C). \tag{7.7}$$

Then, the color vector could be represented as follows:

$$\mathbf{C}_{k,i} = M_C(k, i)e^{j\,\theta_C(k,i)} = M_C(k, i)e^{j\,[\alpha_C(k), \beta_C(i)]}$$

7.3 The Essence of the New Approach

The new approach is based on the replacement of the three matrices of the tensor image RGB components by a single matrix, which comprises the modules of the color vectors of the pixels. The locally-adaptive processing is applied on the module of the vector, corresponding to the pixel placed in the center of a sliding window. The processing is based on the well-known algorithms used for halftone matrix images, which are the particular case of the color tensor images, when the vertices of all color vectors are placed on the diagonal between the black and white areas in the RGB cube. For such vectors, the three components are equal, i.e. $R = G = B, = \alpha\beta = \pi/4$, and their modules are in the range from 0 up to $(m - 1)\sqrt{3}$ (here m denotes the number of values for each component R, G, and B). Depending on the processing algorithm used, the magnitudes of part of the so calculated color vectors could get too large values, and as a result, their ends will be placed out of the RGB cube: this happens if at least one of the R, G, B components is larger than $(m - 1)$. The colors of the corresponding image pixels could not be reproduced accurately, and produced noticeable color distortions. To solve the problem, the largest color component should be corrected, so as to get a new value, equal to $(m - 1)$. Then, to avoid additional color distortions in the restored image, all color vectors placed in and out of the cube, should be corrected accordingly. As a result, the brightness is changed too. To retain the pixel brightness, additional correction is needed (which

follows the color correction). Both corrections (color and brightness) are needed only in case that the number of vectors placed out of the color cube is higher than a pre-defined threshold. In the text below are given the specific features of the basic algorithms for locally-adaptive processing of color images, applied on the matrices of the color vectors' modules, framed by the sliding window.

7.4 Definition of the Image Color Vectors' Modules Through 2D-DFT

To define the image color vectors' modules, forward 2D Discrete Fourier Transform (2D-DFT) is executed for the modules $M_C(k.i)$ of the color vectors $\mathbf{C}_{k,i}$, in correspondence with the relation:

$$\mathbf{s}_C(q, p) = \frac{1}{M \times N} \sum_{k=0}^{M-1} \sum_{i=0}^{N-1} M_C(k, i) e^{-2\pi j\left(\frac{qk}{M} + \frac{pi}{N}\right)} \tag{7.8}$$

$$\text{for } q/p = 0, 1, .., (M-1)/(N-1).$$

Here, $\mathbf{s}_C(q, p)$ is the spectrum color coefficient. The inverse 2D-DFT is defined by the relation:

$$M_C(k, i) = \sum_{q=0}^{M-1} \sum_{p=0}^{N-1} \mathbf{s}_C(q, p) e^{2\pi j\left(\frac{qk}{M} + \frac{pi}{N}\right)} \text{ fork/i} = 0, 1, .., (M-1)/(N-1). \tag{7.9}$$

Each spectrum coefficient $\mathbf{s}_C(q, p)$ is represented as a vector in the complex space:

$$\mathbf{s}_C(q, p) = \text{Re}(\mathbf{s}_C(p, q)) + j\text{Im}(\mathbf{s}_C(p, q)) = \|\mathbf{s}_C(p, q)\| e^{j\phi(p,q)} \tag{7.10}$$

where $\|s_C(p, q)\| = \sqrt{\text{Re}^2(\mathbf{s}_C(p, q)) + \text{Im}^2(\mathbf{s}_C(p, q))}$ is the amplitude 2D spectrum, and $\phi(p, q) = arctg\left[\frac{\text{Im}(\mathbf{s}_C(p,q))}{\text{Re}(\mathbf{s}_C(p,q))}\right]$ is the phase 2D spectrum of the matrix $[M_C(k, i)]$, which comprises the color vectors' modules.

In general, the 2D-DFT in a sliding window could be used for homomorphic locally-adaptive filtering of the existing multiplicative or convolutional noises in the color image, retaining the saturation transitions. To accelerate the 2D-DFT calculation, the well-known algorithm for 2D fast Fourier transform (2D-FFT) is used [9].
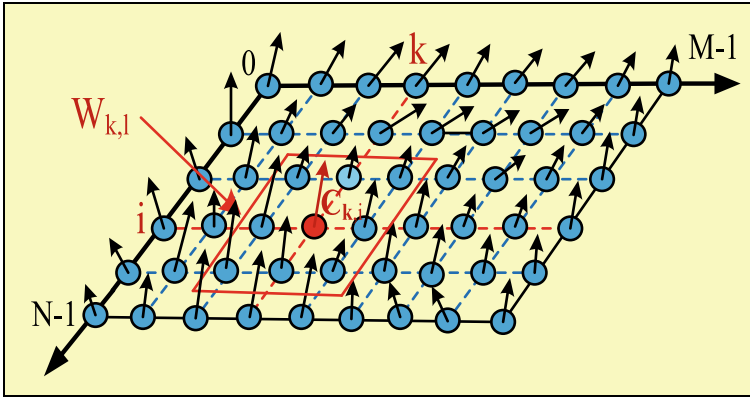
Fig. 7.2 The vector field Ck,i for the pixels of the color tensor image of size $M \times N \times 3$, and the sliding window $W_{k,i}$, used for the local processing

7.5 Calculation of the Local Histograms of Color Vectors' Modules

7.5.1 Local Histogram

The local histogram of the modules of image color vectors $\mathbf{C}_{k,i}$ in the sliding window $W_{k,i}$ of size $(2b + 1) \times (2b + 1)$ (framed in red on Fig. 7.2 for the case $b = 1$), is defined by the relation:

$$h_{k,i}(r) = \frac{N_{M_C}^{k,i}(r)}{(2b + 1)^2} \text{ for} r = 0, 1, 2, \dots, \tag{7.11}$$

where $m'' = \left\lfloor 255\sqrt{3} + 0.5 \right\rfloor = 442$, when $m - 1 = 255$; $\lfloor \bullet \rfloor$ denotes the "rounding" operator; $N_{M_C}^{k,i}(r)$ is the number of pixels, for which the value of the module $M_C(k, i)$ for the corresponding color vector $\mathbf{C}_{k,i}$, is equal to r.

7.5.2 Local Modified Histogram

The local modified histogram of the modules of color vectors $\mathbf{C}_{k,i}$ of the tensor RGB image framed by the sliding window $W_{k,l}$, is defined as follows:

– the adaptive threshold $CL_{k,i}$ is calculated, which limits the local histogram, $h_{k,i}(r)$. The area of the histogram, which is above this limiting value, is represented as a rectangle of same area, which has one side of length $m' = \left\lfloor m\sqrt{3} + 0.5 \right\rfloor$. The

so calculated rectangle area is added to the part placed under the threshold and is obtained from the so-called "modified local histogram", $h_{k,i}^M(r)$. The equalization of this modified histogram is much more accurate than that of the initial local histogram, $h_{k,i}(r)$. The value $(CL_{k,i})$ is automatically calculated following the conditions to equalize the histogram areas placed above, and below the threshold [10], i.e.:

$$\sum_{r=0}^{m''} h'_{k,i}(r) = \sum_{r=0}^{m''} h''_{k,i}(r) = 0.5 \text{ for } h'_{k,i}(r) + h''_{k,i}(r) = h_{k,i}(r). \quad (7.12)$$

Accordingly, the parts of the histogram $h_{k,i}(r)$, which are above and below the threshold value, are defined by the relations:

$$
\begin{aligned}
h'_{k,i}(r) &= \begin{cases} h_{k,i}(r) - CL_{k,i} & \text{for } h_{k,i}(r) \geq CL_{k,i}; \\ 0 & \text{for } h_{k,i}(r) < CL_{k,i}; \end{cases} \\
h''_{k,i}(r) &= \begin{cases} CL_{k,i} & \text{for } h_{k,i}(r) \geq CL_{k,i}, \\ h_{k,i}(r) & \text{for } h_{k,i}(r) < CL_{k,i} \end{cases}
\end{aligned}
\quad (7.13)
$$

To calculate $CL_{k,i}$ in accordance with Eq. (7.12), the following iterative algorithm is proposed [10]:

Let $CL_{k,i} = x$, with initial values $x = 0$, and $= \delta 0.01$(experimentally set).
Step 1.$x = x + \delta$;.
Step 2.$D(x) = \sum_{r=0}^{m''} [h_{k,i}(r) - x]$ for $h_{k,i}(r) \geq x$;
Step 3.If $D(x) \begin{cases} > 0.5 & \text{return in step 1,} \\ < 0.5, \text{ then } x = x - \delta \text{ and return in step 2, } . \\ \approx 0.5 & \text{go to step 4;} \end{cases}$
Step 4. Stop and set $CL_{k,i} = x$..

- to accelerate the calculation of $CL_{k,i}$, the image is divided into square sub-blocks. For each sub-block are calculated the local histogram $h_{k,i}(r)$ of the color vectors' modules and the adaptive threshold $CL_{k,i}$, regarding the corresponding central element, $M_C(k, i)$. For each of the remaining matrix elements $[M_C(k, i)]$, an individual threshold is calculated through bilinear interpolation, by using the thresholds calculated for the central elements of the neighbor sub-blocks in horizontal and vertical directions.
- after the threshold $CL_{k,i}$ is calculated, the modified local histogram is defined, in accordance with the relation:

$$h_{k,i}^M(r) = (1/m') \sum_{i=0}^{m''} h'_{k,i}(i) + h''_{k,i}(r) \quad (7.14)$$

where $m' = \left\lfloor 256\sqrt{3} + 0.5 \right\rfloor = 443$, for $m = 256$.

7.5.3 Local Cumulative Histogram

The local cumulative histogram of the vectors' modules $\mathbf{C}_{k,i}$ framed by the window, is calculated:

$$
\begin{aligned}
H^{k,i}_{M_C}(r) &= \sum_{l=0}^{r} h^M_{k,i}(l) = [(r+1)/m'] \sum_{l=0}^{m''} h'_{k,i}(l) \\
&+ \sum_{l=0}^{r} h''_{k,i}(l) = \begin{cases} (r+1)/m' \text{ for } h_{k,i}(r) \geq CL_{k,i}; \\ \sum_{l=0}^{r} h_{k,i}(l) \text{ for } h_{k,i}(r) < CL_{k,i}; \end{cases}
\end{aligned}
\tag{7.15}
$$

for $r = 0,1,2,\ldots, m''$

From the above relation, it follows that the local cumulative histogram $H^{k,i}_{M_C}(r)$ is a linear function of the current value of r. This is why, for the above-threshold area, full equalization of the modified local histogram $h^M_{k,i}(r)$ is achieved, which does not depend on its distribution. In the sub-threshold area, however, the equalization of $h^M_{k,i}(r)$ depends on the histogram $h_{k,i}(r)$ and sometimes it is not full.

7.5.4 Computational Cost

The computational cost [10] of the operations, needed to define the cumulative histogram $H^{k,i}_{M_C}(r)$, is reduced through recursive calculation of $h^M_{k,i}(r)$:

$$
h^M_{k+1,i}(r) = h^M_{k,i}(r) - h^M_{k-d,i}(r) + h^M_{k+d+1,i}(r) \text{ for r} = 0, 1, 2, ..,
\tag{7.16}
$$

After summing up for both sides of Eq. (7.16), is obtained:

$$
H^{k+1,i}_{M_C}(r) = H^{k,i}_{M_C}(r) - H^{k-d,i}_{M_C}(r) + H^{k+d+1,i}_{M_C}(r)
\tag{7.17}
$$

7.6 Applications of the Local Cumulative Histograms

7.6.1 Local Contrast Enhancement

The local contrast of the color image is enhanced by using the local cumulative histogram $H^{k,i}_{M_C}(r)$, in correspondence with the relation:

$$g_r(k, i) = \begin{cases} 442 \text{ for } \left\lfloor 442\ H_{Mc}^{k,i}(r) + 0.5 \right\rfloor > 442; \\ \left\lfloor 442\ H_{MC}^{k,i}(r) + 0.5 \right\rfloor \text{ - in all other cases,} \end{cases} \tag{7.18}$$

for $r = 0,1,\ldots,442$, when $m = 256$.

Here $g_r(k, i)$ is the new value for the element (k,i), which replaces the original value r.

To avoid false contours appearance in the processed image, it is supposed here to increase the number of bits used for image elements' coding: for example, if the values r of the elements $M_C(k,i)$ in the original matrix were coded with 10 bits, after the processing, 12-bits coding for the new elements, $z_r(k,i)$ is supposed to be used:

$$z_r(k, i) = \left\lfloor m'' \times H_{MC}^{k,i}(r) + 0.5 \right\rfloor$$
$$\text{for } r = 0, 1, 2, \ldots, m''; \ \left(m'' = \lfloor 1.73(m - 1) + 0.5 \rfloor \right) \tag{7.19}$$

In this case, the number of levels $m = 2^{12} = 4096$ and $m'' = \lfloor 1.73.4095 + 0.5 \rfloor = 7086$, correspondingly.

7.6.2 Calculation of the RGB Vectors of the Enhanced Image

For this, the following relation is used:

$$C_{\kappa,i}^E = \left[R_{\kappa,i}^E, G_{\kappa,i}^E, B_{\kappa,i}^E \right]^T \text{ for k/i = 1, 2, \ldots, M/N} \tag{7.20}$$

where $R_{\kappa,i}^E = \frac{z_r(k,i)}{M_C(k,i)} R_{k,i}$; $G_{\kappa,i}^E = \frac{z_r(k,i)}{M_C(k,i)} G_{k.}$; $B_{\kappa,i}^E = \frac{z_r(k,i)}{M_C(k,i)} B_{k,i}$,
for $r = 0,1,\ldots, m''$

7.6.3 Adaptive Color Correction

The adaptive color correction of vectors $C_{k,i}^E$ is done on the basis of the vectors, whose ends are out of the RGB cube. For this, the following steps are performed:

Step 1. For all $C_{\kappa,i}^E$ vectors is checked if their ends are out of the RGB cube, and if there is at least one of their components, whose magnitude is larger than the maximum value, $m - 1$. After that is checked if the condition $N_C \geq \delta$ is satisfied, in which N_C is the number of color vectors $C_{\kappa,i}^E$ which are out of the RGB cube, and δ is the pre-selected threshold. If these two conditions are satisfied simultaneously, the vector $C_{\kappa0,i0}^E = [R_{k0,i0}^E, G_{k0,i0}^E, B_{k0,i0}^E]^T$ is detected, which has at least one component larger than all other components.

Step 2. In case, that the component $R^E_{k_0,i_0}$ of the vector $\mathbf{C}^E_{\kappa_0,i_0}$ is larger than the maximum value, then $R^E_{k_0,i_0} = \max(R^E_{k,i}, G^E_{k,i}, B^E_{k,i}) > m - 1$ for $k/i = 0, 1, 2,$ ..., $(M-1)/(N-1)$. For the components of this vector, the following correction is done:

$$R^E_{k_0,i_0}(cor) = m - 1,\ G^E_{k_0,i_0}(cor) = G^E_{k_0,i_0}/(R^E_{k_0,i_0}/m - 1),$$
$$B^E_{k_0,i_0}(cor) = B^E_{k_0,i_0}/(R^E_{k_0,i_0}/m - 1). \tag{7.21}$$

The brightness of the pixel (k_0,i_0), in which color vector $\mathbf{C}^E_{k_0,i_0}(cor)$ is corrected, is defined by the relation:

$$Y^E_{i_0,j_0}(cor) = 0.21 \times (m-1) + 0.72(m-1)(G^E_{i_0,j_0}/R^E_{i_0,j_0})$$
$$+ 0.07(m-1)(B^E_{i_0,j_0}/R^E_{i_0,j_0}) \tag{7.22}$$

Taking into account that (in accordance with [10, 11]), the brightness of the pixel (k_0,i_0) in the original image is defined by the relation: $Y_{k_0,i_0} = 0.21\,R_{k_0,i_0} + 0.72\,G_{k_0,i_0} + 0.07\,B_{k_0,i_0}$, to retain the brightness of this pixel in the improved image, must satisfy the equation:

$$Y_{k_0,i_0} = Y^E_{k_0,i_0}(cor) = 0.21 R^E_{k_0,i_0}(cor) + 0.72 G^E_{k_0,i_0}(cor) + 0.07 B^E_{k_0,i_0}(cor), \tag{7.23}$$

from which follow the relations:

$$R^E_{k_0,i_0}(cor) = m - 1, G^E_{k_0,i_0}(cor) = (m-1)(G^E_{k_0,i_0}/R^E_{k_0,i_0}),$$
$$B^E_{k_0,i_0}(cor) = (m-1)(B^E_{k_0,i_0}/R^E_{k_0,i_0}). \tag{7.24}$$

For the remaining vectors $\mathbf{C}^E_{k,i} = [R^E_{k,i}, G^E_{k,i}, B^E_{k,i}]^T$, to retain the brightness of their pixels (k,i) for $k/i = 0,1,2,..,(M-1)/(N-1)$, the components of the corresponding corrected vectors $\mathbf{C}^E_{k,i}(cor)$ must be calculated accordingly:

$$R^E_{k,i}(cor) = (m-1)(R^E_{k,i}/R^E_{k_0,i_0}),\ G^E_{k,i}(cor)$$
$$= (m-1)(G^E_{k,i}/R^E_{k_0,i_0}),\ B^E_{k,i}(cor) = (m-1)(B^E_{k,i}/R^E_{k_0,i_0}). \tag{7.25}$$

Step 3. In case, that the maximum value of one of the components $G^E_{k_0,i_0}$ or $B^E_{k_0,i_0}$ is higher than $m - 1$, it should be corrected in a way, similar to the correction done for the maximum component, $R^E_{k_0,i_0} > m - 1$. The correction of the components of the remaining color vectors $\mathbf{C}^E_{k,i}$ is done by analogy with Eq. (7.25).

To illustrate the presented algorithm, in Fig. 7.3a are shown the original medical tensor R, G, B images, and in Fig. 7.3b—same images, after local contrast enhancement with a sliding window of size 33×33 (experimentally set).
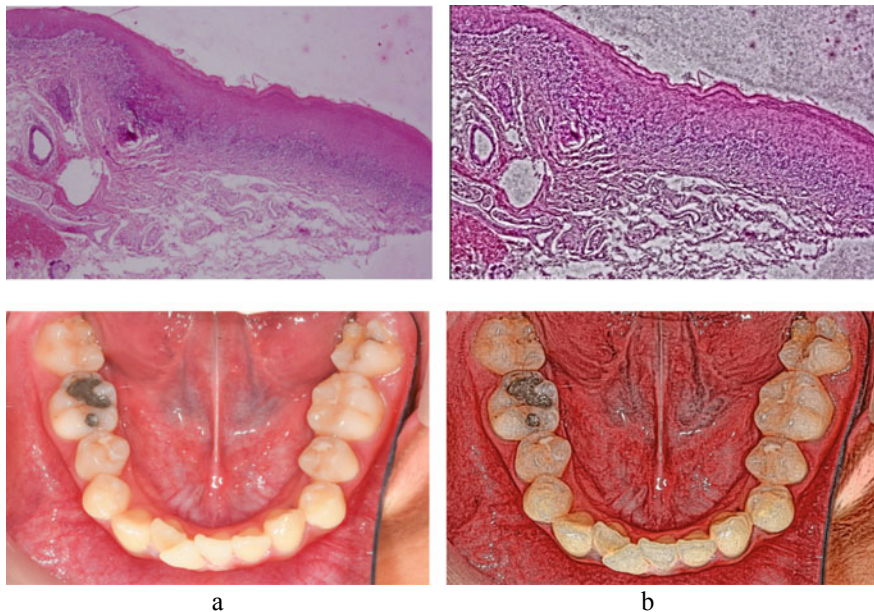
Fig. 7.3 Medical R, G, B images: **a** originals; **b** after local contrast enhancement with a sliding window $W_{k,i}$ of size 33×33

7.7 Locally-Adaptive Filtering for Tensor Images, Represented as Vector Fields

In this section, some of the well-known algorithms [1–6, 9, 12–14] for locally-adaptive linear and non-linear filtering are investigated for the case, when they are applied on the matrix $[M_C(k, i)]$ of size $M \times N$, if its elements are quantized at m' levels.

7.7.1 Linear 2D Filtering

The linear 2D filtering of color tensor image is represented through the modules of the color vectors framed by the sliding window $W_{k,l}$, of size $(2b + 1) \times (2h + 1)$:

$$F_C(k, i) = M_C(k, i) * f(k, i) = \sum_{s=-b}^{b} \sum_{l=-h}^{h} M_C(k + s, i + l) f(s, l) \qquad (7.26)$$

for $k/i = 0,1,…, (M − 1)/(N − 1)$, where $f(s,k)$ denotes the kernel of the 2D filter, defined in the window $W_{k,i}$; $F_C(k, i)$ is the filtered value of the elements $M_C(k, i)$,

framed by the window, and "$*$" denotes the operator for 2D convolution of $M_C(k, i)$ and $f(s,k)$. The kind and the size of the kernel $f(s,k)$ determine the filtration result.

- To achieve higher sharpness (saturation changes) in the image, is used the algorithm, based on the Laplacian operator. The following assumptions are set.

Let:

$$F_C(k, i) = (1 + 4\alpha)M_C(k, i) - \alpha\,[M_C(k - 1, i) \\ + M_C(k + 1, i) + M_C(k, i - 1) + M_C(k, i + 1)], \tag{7.27}$$

where the window $W_{k,i}$ is of size 3×3 (for $b = h = 1$). If $= \alpha 1$ is set, the filter kernel is defined by the corresponding matrix,

$$[f_\alpha(k, i)] = \begin{bmatrix} 0 & -\alpha & 0 \\ -\alpha & (1 + 4\alpha) & -\alpha \\ 0 & -\alpha & 0 \end{bmatrix} = \begin{bmatrix} 0 & -1 & 0 \\ -1 & 5 & -1 \\ 0 & -1 & 0 \end{bmatrix}.$$

In the general case, the sharpness increase is achieved through the algorithm for adaptive unsharp masking, in accordance with which:

$$F_C(k, i) = \begin{cases} F_C'(k, i) & \text{for}\,|M_C(k, i) - \overline{M_C(k, i)}| \geq \delta, \\ M_C(k, i) & \text{in other cases,} \end{cases} \tag{7.28}$$

where $F_C'(k, i) = (1 + \alpha)M_C(k, i) - \alpha\overline{M_C(k, i)}$; $0 < \alpha \leq 1$; δ is the threshold value, and $\overline{M_C(k, i)}$ is the mean value of the elements, framed by the sliding window $W_{k,i}$ of size $(2h + 1)(2b + 1)$:

$$\overline{M_C(k, i)} = \frac{1}{\beta} \sum_{s=-b}^{b} \sum_{l=-h}^{h} M_C(k + s, i + l) \text{ for } \beta = (2h + 1)(2b + 1) \tag{7.29}$$

The algorithm, described above, is illustrated by Fig. 7.4: in Fig. 7.4a is shown the original image, and in Fig. 7.4b—the result of the local sharpness enhancement with a sliding window of size 3×3.

To accelerate the calculation of $\overline{M_C(k, i)}$, two-dimensional recursion is used, based on the relation:

$$\overline{M_C(k, i)} = \overline{M_C(k - 1, i)} + \overline{M_C(k, i - 1)} \\ - \overline{M_C(k - 1, i - 1)} + (1/\beta)[M_C(k + b, i + h) \\ - M_C(k + b, i - h - 1) - M_C(k - b - 1, i + h) \\ + M_C(k - b - 1, i - h - 1)]. \tag{7.30}$$

As a result, the mean value $\overline{M_C(k, i)}$ is recursively calculated by only 7 operations instead of adding all pixels in the sliding window. In the last case, the number of
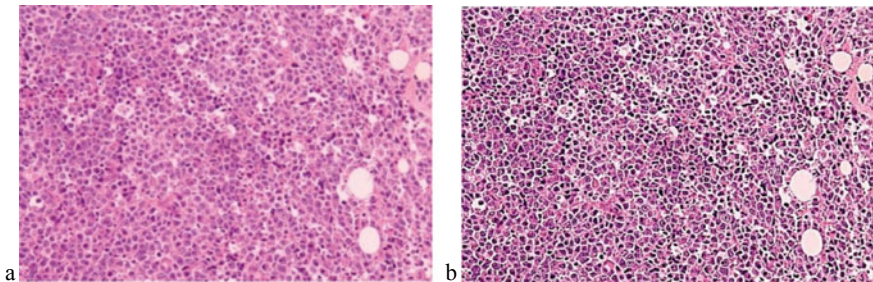
Fig. 7.4 Medical R,G,B image: **a** original; **b** same image, after local sharpness enhancement for a filter kernel of size 3×3

needed operations is $(2b + 1) \times (2h + 1) - 1$ (for example, if $b = h = 5$, we get $(2b + 1) \times (2h + 1) - 1 = 120$, and then the acceleration of the calculations $\overline{M_C(k, i)}$ is $120/7 = 17.14$ times).

The recursive calculation of $F'_C(k.i)$ in the relation (7.28) for the unsharp masking, is executed in correspondence with the equation:

$$
\begin{aligned}
F'_C(k.i) &= (1 + \alpha)M_C(k, i) - \alpha[\overline{M_C(k - 1, i)} \\
&+ \overline{M_C(k, i - 1)} - \overline{M_C(k - 1, i - 1)}] - (\alpha/\beta)[M_C(k + b, i + h) \\
&- M_C(k + b, i - h - 1) - M_C(k - b - 1, i + h) \\
&+ M_C(k - b - 1, i - h - 1)].
\end{aligned}
\tag{7.31}
$$

- The locally-adaptive image filtering aimed at the additive Gaussian noise reduction, is performed in accordance with the relation:

$$
F^f_C(k, i) =
\begin{cases}
\overline{M_C(k, i)} + \dfrac{\sigma^2_{M_C}(k,i) - v^2}{\sigma^2_{M_C}(k,i)}[M_C(k, i) - \overline{M_C(k, i)}] & \text{for } \sigma^2_{M_C}(k, i) \geq v^2; \\
\overline{M_C(k, i)} & \text{for } \sigma^2_{M_C}(k, i) < v^2,
\end{cases}
\tag{7.32}
$$

where: $F^f_C(k, i)$ is the filtered element $M_C(k, i)$; $\overline{M_C(k, i)}$ denotes the mean value of the element $M_C(k, i)$ in the sliding window $W_{k,i}$ of size $(2b + 1) \times (2h + 1)$; $\sigma^2_{M_C}(k, i) = [(1/\beta)\sum_{s=-b}^{b}\sum_{l=-h}^{h} M^2_C(k + s, i + l)] - \overline{M_C(k, i)}$ is the local variance of the element $M_C(k, i)$ in the sliding window $W_{k,i}$; $v^2 = (1/M \times N)\sum_{i=1}^{M}\sum_{j=1}^{N}\sigma^2_{M_C}(k, i)$ is the mean noise variance in the input matrix $[M_C(k, i)]$. To accelerate the calculation of the mean value $\overline{M_C(k, i)}$ for all elements, except those on the first row and first column of the input matrix $[M_C(k, i)]$, recursive relation is used in accordance with Eq. (7.30). When compared to the well-known adaptive Wiener filter [12], the main advantage of the new filter is, that it is adaptive to the relation of the local variation to the global one, in result of which the transitions in the image are retained, and the noise is suppressed.

7.7.2   Weighted Median Filtering

The weighted median filtering of pulse noises in the color tensor image, represented through the matrix $[M_C(k, i)]$ of the color vectors' modules, framed by the sliding window $W_{k,l}$ of size $(2b + 1) \times (2h + 1)$, is executed in accordance with the relation:

$$F_C^{WM}(k, i) = Med_W M_C(k, i) = Med\ [t(s, l) \times M_C(k + s, i + l) : s, l \in W_{k,i}], \tag{7.33}$$

where s $=$ - b, - b + 1,.., 0,..,b − 1,b; l $=$ - h, - h + 1,.., 0,..,h − 1,h. The coefficients $t(s,l)$ show how many times appears the corresponding element $M_C(k + s, i + l)$ in the monotonic increasing sequence x_p for $p = 1,2,…,P$, from which is defined the weighted median function, x_{WM}:

$$x_1 \leq x_2 \leq … \leq x_{WM} \leq …x_{P-1} \leq x_P \quad \text{for} P = (2b + 1)'(2h + 1). \tag{7.34}$$

The filtered element (k,i) corresponds to the weighted median $F_C^{WM}(k, i) = x_{WM}$. In accordance with Eq. (7.33), the sum of all elements $t(s,l)$ is an odd number, and the elements x_p in Eq. (7.34) are defined by the modules $M_C(k + s, i + l)$ framed by the window $W_{k,l}$, after rearrangement into an increasing monotonic sequence. The size of the window is defined so as to frame the noise elements of average size, which should be filtered.

The algorithm is illustrated in Fig. 7.5: in Fig. 7.5a is shown the noise image, and in Fig. 7.5b—the filtered image.

a   b
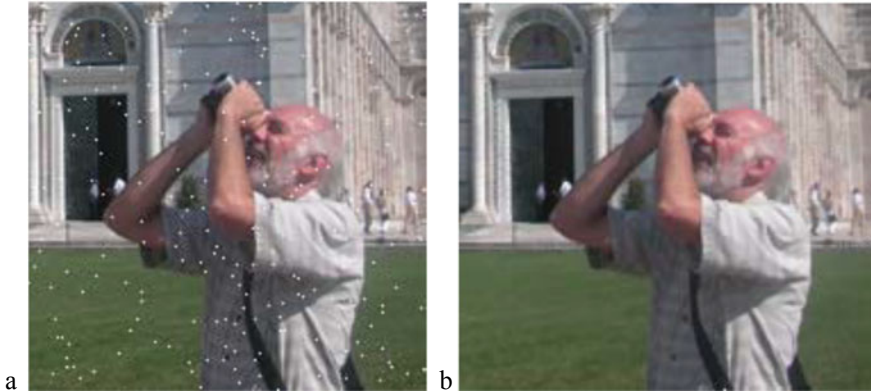
Fig. 7.5 Test R, G, B image: **a** The image with 1% additive pulse noise; **b** same image, after weighted median filtering by using a window of size 3 × 3 (for $b = h = 1$)

7.7.3 Suppression of Additive Pulse and Gaussian Noises

To suppress the additive pulse and Gaussian noises in a color image, and to retain the existing transitions, the algorithm for vector median filtering is used [13]. For this, from the color vectors placed in the sliding window $W_{k,l}$ (Fig. 7.1), the sequence $\mathbf{C}_1, \mathbf{C}_2, .., \mathbf{C}_p, .., \mathbf{C}_{P-1}, \mathbf{C}_P$ is composed. For each vector from the sequence $\mathbf{C}_p = [R_p, G_p, B_p]^T$ are calculated the distances D_p to all remaining vectors, $\mathbf{C}_j = [R_j, G_j, B_j]^T$, framed by the window $W_{k,l}$, i.e.:

$$D_p = \sum_{j=1}^{P} \sqrt{(R_p - R_j)^2 + (G_p - G_j)^2 + (B_p - B_j)^2} \text{ for p} \neq \text{j and p/j} = 1, 2, .., \text{P.}$$

(7.35)

The so calculated distances D_p are arranged as an increasing monotonic sequence, $D_1 \leq D_2 \leq \ldots \leq D_P$. The index p_0 of the filtered color vector $\mathbf{C}_{p_0} = [R_{p_0}, G_{p_0}, B_{p_0}]^T$, which replaces the vector $\mathbf{C}_{k,i}$ in the center (k,i) of window, is defined by the condition:

$$D_{p_0} = \min\{D_j\} \text{ for j} = 1, 2, .., \text{P.}$$

(7.36)

7.7.4 Morphological Filtration

For the morphological filtration of the color image A (represented as the matrix $[M_C(k, i)]$), is used the "flat" structuring element B with components $b(s,l)$, defined in a sliding window of size $(2b + 1) \times (2h + 1)$. The filtration is executed by using the following basic morphologic operators [6, 14]:

- morphological dilatation and erosion:

$$D(A, B) = \max [M_C(k - s, i - l) + b(s, l)] = A \oplus B$$

(7.37)

$$E(A, B) = \min [M_C(k + s, i - +l) - b(s, l)] = A \ominus B$$

(7.38)

where $s = -b, -b + 1, .., 0, .., b - 1, b; \; l = -h, -h + 1, .., 0, .., h - 1, h.$

- morphological opening and closing:

$$OP(A, B) = (A \ominus B) \oplus B = AoB = D\{E(QA, B), B\}$$

(7.39)

$$CL(A, B) = (A \oplus B) \ominus B = A \cdot B = E\{D(QA, B), B\}$$

(7.40)

7.7.4.1 Operator for Morphological Noise Suppression

The operator for morphological noise suppression is represented as:

$$F_{sm} = Morph \ Smooth \ (A, B) = CL\{OP(A, B), B\} = (AoB) \cdot B \quad (7.41)$$

7.7.4.2 Morphological Gradient Operators for the Outer and Inner Contours

The morphological gradient operators for detection of the outer and inner contours of the objects are represented as follows:

$$F_{ext} = DG(A) = D(A, B) - A; \ and \ F_{int} = EG(A) = A - E(A, B). \quad (7.42)$$

7.7.4.3 Morphological Gradient Operators of Laplace, Bother, Li^1 and Li^2

The morphological gradient operators of Laplace, Bother, Li^1, and Li^2 for contours detection are represented as follows:

$$F_{Lap} = DG(A) - EG(A); \ F_{Both} = DG(A) + EG(A); \quad (7.43)$$

$$F_{Li}^1 = \min[DG(A), EG(A)]; \ F_{Li}^2 = \max[DG(A), EG(A)]. \quad (7.44)$$

7.7.4.4 Morphological Operators Top Hat and Bot Hat

The morphological operators Top Hat and Bot Hat for detection of dark/light objects on an irregular background, are defined as given below:

$$Top \ Hat \ (A, B) = CL(A, B) - A; \ Bot \ Hat \ (A, B) = A - OP(A, B). \quad (7.45)$$

7.7.4.5 Morphological Operator for Sharpness Enhancement

The morphological operator for sharpness enhancement and for contrast enhancement of the small details in the color image, respectively, is defined by the relation below:

$$F_{ms} = Morph\ Sharpness\ (A, B) = A + [A - (AoB)] - [(A \cdot B) - A].$$
$$(7.46)$$

7.7.4.6   Segmentation of Color Textures

The segmentation of color texture images is based on morphological filtration. The following assumptions are set:

Let the color image A, represented by the matrix $[M_C(k, i)]$ contains two different textures, each built by repetitive elements of different average sizes. To detect the border, the following three steps are performed:

$$Step\ 1 :\ S_1^n = E(A, nB_1) = (((A \ominus B_1) \ominus B_1)....) \ominus B_1 = A \ominus nB_1 \qquad (7.47)$$

where n denotes the number of erosions, and B_1 is the structuring element. Its shape is chosen so that after the n-th erosion, the elements of one of the two textures disappear, merging into a homogenous area, i.e.:

$$Step\ 2 :\ S_2^m = D(S_1^m, mB_2) = (((S_1^m \oplus B_2) \oplus B_2)....) \oplus B_2 = S_1^m \oplus mB_2, \qquad (7.48)$$

where m denotes the number of dilatations, and B_2 is the structuring element. Its shape is chosen so that after dilatations, the elements of the second texture disappear, merging into a homogenous area, i.e.:

$$Step\ 3 :\ S = S_2^m - (S_2^m \ominus B_1), \qquad (7.49)$$

where S is a color image, which contains the border between both textures, of width one pixel only.

The shape and the size of the structuring elements B_1 and B_2 conform to the mean values of the corresponding elements in the first and second textures. In this way, the number of erosions and dilatations needed to execute steps 1 and 2, is reduced. In particular, if $B_1 = B_2 = B$, the values of n and m increase, but the operations needed for steps 1 and 2, are simpler.

In case that the color image contains more than two different textures, the presented morphological algorithm for detecting the border between neighbor textures is applied repeatedly, depending on the number of textures.

After each dilatation, needed for the morphological filtration or segmentation, should be evaluated the number of color vectors, whose ends are out of the color cube. In case that this number is higher than the preset threshold, color and brightness correction of the vector field is needed, similar to that from Sect. 7.6 (the algorithm for local contrast enhancement).

The algorithm for morphological filtration is illustrated in Fig. 7.6, where in Fig. 7.6a is shown the original color image. It contains two textures with similar
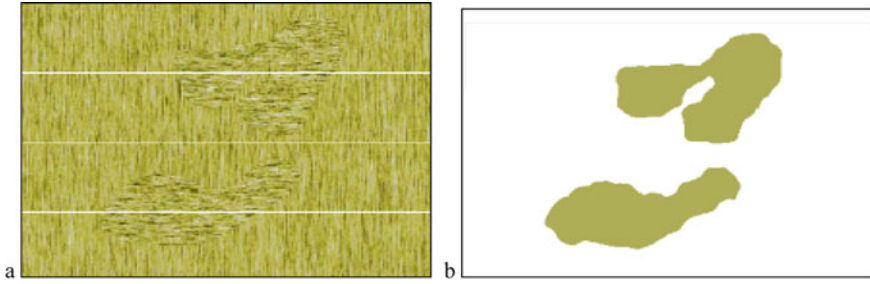
Fig. 7.6 Color texture image: **a** original; **b** after morphological segmentation by using a flat structuring element B, shaped as a horizontal/vertical line and placed in a window of size 9 × 9

color characteristics, but with different orientations of their elements (horizontal and vertical). In Fig. 7.6b is shown the result obtained after a morphological segmentation with a flat structuring element B, whose shape is a line (horizontal/vertical), defined in a window of size 9 × 9. As a result of the segmentation, the elements of both textures merge into two homogenous areas. If the color image contains two textures, which comprise similar elements, distinguished by their hue, similar algorithm could be used. However, in this case, the algorithm for morphological segmentation should be applied on the matrix $[\theta_C(k,i)]$ of the angles (orientation) of the color vectors $\mathbf{C}_{k,i}$ instead of the matrix $[M_C(k, i)]$, composed by the modules of these vectors.

7.8 Conclusions

The objective of this work is to formulate one new approach for locally-adaptive processing of color third-order tensor RGB images represented in a vector form, and to analyze the characteristics of the corresponding basic algorithms so that to exploit efficiently the spatial and inter-channel correlation. These algorithms need only operations executed on a single matrix image, which comprises the modules of the corresponding color vectors. As a result, triple reduction of the computational complexity is achieved, compared to algorithms executed on each color component individually. Together with the reduced computations, the hue and the brightness of the original image are retained.

The presented locally-adaptive algorithms are extremely efficient in the processing of medical images, which have variable color characteristics (brightness, saturation and hue). The new approach will be further investigated and extended, aiming at applications in various multidisciplinary areas. The future development of the locally-adaptive algorithms will be mainly aimed at the integration with deep neural networks with different architectures, so as to achieve higher flexibility in the adaptive processing of color images.

References

1. Thyagarajan, K.: Digital Image Processing with Application to Digital Cinema. Focal Press, Elsevier (2006)
2. Celebi, M., Lecca, M., Smolka, B. (eds.): Color Image and Video Enhancement. Springer, Heidelberg (2015)
3. Jain, A.: Fundamentals of Digital Image Processing. Prentice Hall, Englewood Cliffs, NJ (2018)
4. Gomez-Agis, J., Kober, V.: Local adaptive image processing in a sliding transform domain. In: Proc. SPIE 6696, Applications of Digital Image Processing, 669623, 24 (2007). https://doi.org/10.1117/12.735044
5. Pratt, W.: Digital Image Processing. John Wiley & Sons Inc., Publication (2007)
6. Gonzales, R., Woods, R.: Digital Image Processing, 4th edn, Pearson Education (2019)
7. Renhard, E., Ward, G., Pattanaik, S., Devebec, P., Heidrich, W., Myszkowski, K.: High Dynamic Range Imaging: Acquisition, Display, and Image-based Lighting. Morgan Kaufmann Publications, Elsevier (2010)
8. Inoue, K., Jiang, M., Hara, K.: Hue-preserving saturation improvement in RGB color cube. J Imaging **7**, 150 (2021). https://doi.org/10.3390/jimaging7080150
9. Rao, K., Kim, D., Hwang, J.: Fast Fourier transform: algorithms and applications. Springer (2010)
10. Kountchev R, Bekiarsky A, Mironov R, Bekiarska S.A.: Method for local contrast enhancement of endoscopic images based on color tensor transformation into a matrix of color vectors' modules using a sliding window. MDPI Symmetry **6**, 14(12), 2582, Open access. https://doi.org/10.3390/sym14122582
11. Recommendation ITU-R BT.709-5 (04/2002): Parameter values for the HDTV standards for production and international programme exchange. BT Series Broadcasting service (television). https://www.itu.int/pub/R-REC/en
12. Jin, F., Fieguth, P., Winger, L., Jernigan, E.: Adaptive wiener filtering of noisy images and image sequences. In: Proceedings of the International Conference on Image Processing, 14–17 Sept. 2003, Barcelona, Spain, https://doi.org/10.1109/ICIP.2003.1247253
13. Lukas, R., Smolka, B.: Application of the adaptive center-weighted vector median framework for the enhancement of cdna microarray images. Int. J. Appl. Math. Comput. Sci. **13**(3), 369–383 (2003)
14. Dougherty E. (Ed.) Mathematical morphology in image processing. CRC Press (2018)

Chapter 8
Energy Efficient VgSOT-MTJ Based 1 Bit Subtractor

Payal Jangra and **Manoj Duhan**

Abstract To harness the potential of VgSOT MRAM in digital signal processing circuits, this study presents a 1-bit full subtraction circuit based on voltage gated Spin–Orbit Torque Magnetic Tunnel Junction (MTJ) technology. The circuit design adopts a dual-track structure that seamlessly integrates CMOS and MTJ components. By precisely controlling the timing of reading and writing operations, the circuit achieves the desired full subtraction functionality. This integrated structure enables the seamless integration of MTJ memory devices into the full subtractor circuit while significantly reducing overall power consumption by minimizing the frequency of MTJ writing operations. This paper has implemented VgSOT, SOT, and STT based subtractor and borrow circuit for performance evaluation. Performance parameters like average delay, energy consumption, and Average power consumption have been analyzed in this paper. With VgSOT MTJ based subtractor, performance improvement of 93% and 97% is seen in terms of energy/Average power consumption over SOT and STT based implementations. In terms of average delay. VgSOT MTJ based subtractor performs 47% and 69% better over SOT and STT based implementations.

8.1   Introduction

In the realm of advanced technologies, the continuous scaling down of CMOS (Complementary Mosfet) technology [1, 2] to lower nodes has led to an upsurge in leakage current, which contributes significantly to the overall dynamic power consumption, accounting for approximately 40% [3]. As a consequence, the demand for low-power devices becomes paramount for achieving high-performance in deep sub-micrometer technology. To overcome these challenges, researchers in academia and industry have shifted their focus towards nanoscaled technologies [4, 5], with magnetic tunnel junctions (MTJs) [6–8] emerging as a prominent contender. MTJs have garnered considerable attention due to their remarkable attributes,

P. Jangra (✉) · M. Duhan
Department of Electronics and Communication, DCRUST, Murthal, India
e-mail: 18001903007payal@dcrustm.org

including non-volatility [9], high speed, minimal leakage [10]/power consumption, and compatibility with semiconductor devices [11, 12]. These spintronic devices [13–15] leverage both the charge and spin properties of electrons and are composed of two ferromagnetic layers separated by a dielectric layer. The pinned layer or reference layer remains firmly magnetized, while the free layer's magnetization direction can be altered. MTJs exhibit two distinct states: the parallel state (R_P) with low resistance and the anti-parallel state (R_{AP}) with high-resistance.

The unique characteristics of MTJs have positioned them as a promising candidate for various applications, particularly in the field of memory technology [16]. The ability to switch between low resistance parallel and high resistance anti-parallel states offers the foundation for reliable data storage and retrieval. Furthermore, the compatibility of MTJs with existing semiconductor technologies facilitates seamless integration into conventional CMOS circuits, enabling the development of hybrid systems that leverage the strengths of both spintronic and traditional electronic components. This opens up exciting possibilities for the design of advanced memory architectures, such as spin-transfer torque magnetic random-access memory (STT-MRAM) [17, 18] and spin–orbit torque magnetic random-access memory (SOT-MRAM) [19, 20], that offers enhanced performance, reduced power consumption, and improved scalability. With ongoing research and development efforts, the potential of MTJs in revolutionizing memory technologies is being realized, paving the way for future advancements in data storage and processing.

The emergence of voltage-controlled spin–orbit torque (VgSOT) MTJs (leveraging the voltage-controlled magnetic anisotropy effect [21]) [22] has revolutionized the field of memory design. VgSOT MTJs provide an additional degree of freedom in spintronic device design, enabling precise control over the magnetic states of the MTJ through the application of voltage pulses. This unique feature has led to significant advancements in data storage and processing capabilities. By utilizing VgSOT MTJs in memory architectures, it becomes possible to achieve lower-power, higher-speed, and trustworthy operations. The ability to dynamically control the magnetic states of the MTJs allows for efficient data storage, retrieval, and manipulation, thereby opening up new possibilities for memory applications in various domains. The continued exploration and utilization of VgSOT MTJs in memory designs will undoubtedly lead to exciting developments and transformative improvements in data storage and processing capabilities.

This research paper presents the design of a functional circuit for digital signal processing systems. The circuit focuses on implementing a full subtractor utilizing a VgSOT MTJ device. The circuit ensures efficient utilization of resources while maintaining the desired functionality of the full subtractor, showcasing its potential for low-power digital signal processing applications. Section 8.2 presents the subtractor and borrow circuits implemented using VgSOT, SOT, and STT MTJ respectively. Simulation results have been presented in Sect. 8.3 while performance analysis in terms of energy, delay has been done in Sect. 8.4. Section 8.5 concludes the research work on VgSOT performance compared to SOT and STT and Sect. 8.6 presents the future scope for VgSOT based devices.

8.2 VgSOT MTJ Based Full Subtractor

The hybrid functional circuit [23] designed for MTJ device applications is depicted in Fig. 8.1. This circuit comprises three essential components: the MOSFET circuit, the pre-charge Sense Amplifier (PCSA) [24], and the MTJ device. The PCSA component facilitates the reading of the memory content stored in the MTJ device, while the MOSFET circuit is specifically designed to execute the necessary logic functions required by the circuit. The MTJ device serves as the storage element, storing the necessary circuit information (logic "0" or "1" based on the states of the MTJs) to perform the desired circuit function. The circuit structure provides numerous advantages such as fast readout speed, high readout accuracy, and lower power consumption during the readout process.

Figures 8.2 and 8.3 present the VgSOT MTJ based subtractor and the borrow circuit. Within each part, two non-volatile MTJ devices are employed to create a Non-volatile circuit, where the VgSOT devices store complementing information. The circuit arrangement includes a set of output terminals that are complementary to each other, which generate the subtraction—Sub and $\overline{\text{Sub}}$ and borrow variables—borrow and $\overline{\text{borrow}}$.

The subtractor circuit works in the writing and the reading/calculating modes of operation. The transition between these modes is controlled by the clock signal. During the low phase of the clock, transistors MP1 and MP2 are activated, allowing Sub and $\overline{\text{Sub}}$ being set to a logic Vdd. During the reading operation, the stored information from the VgSOT MTJ is retrieved through the pre-charge sense amplifier (PCSA).

The logical functions of the full subtraction circuit depicted in Figs. 8.2 and 8.3 are expressed by Eqs. (8.1) and (8.2), representing the operations of subtraction and borrowing, respectively. The circuit corresponding to these equations is divided into two parts, each responsible for implementing the subtraction and borrow functions. Each part of the circuit in the figure consists of two tracks, with MTJs utilized in
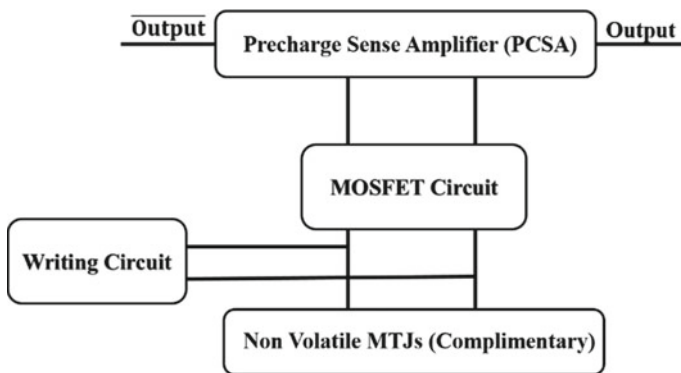
Fig. 8.1 Hybrid MTJ/CMOS circuit [23]

Fig. 8.2 VgSOT MTJ based
subtractor circuit
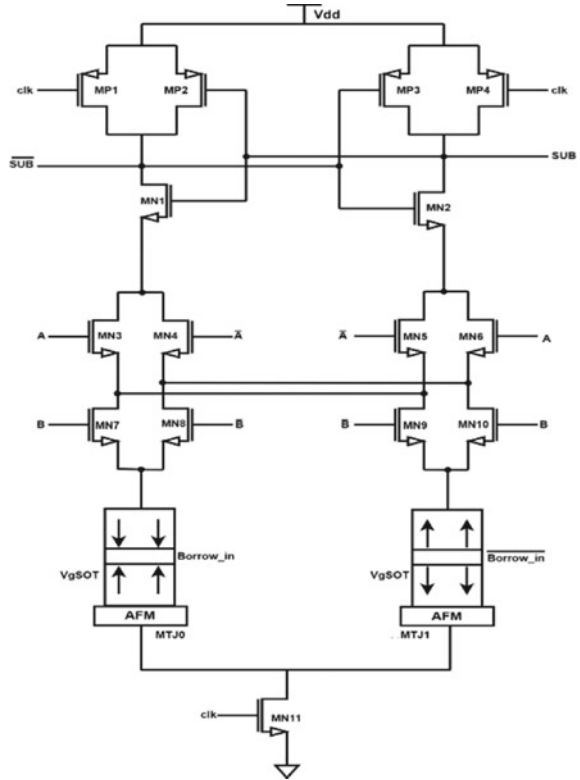
both tracks.

$$Sub = A \oplus B \oplus Borrow\_in$$

$$= A.B.Borrow\_in + A.\overline{B}.\overline{Borrow\_in} + \overline{A}.B.\overline{Borrow\_in} + \overline{A}\,\overline{B}\,Borrow\_in$$

$$(8.1)$$

$$Borrow = \overline{A}.\overline{B}.Borrow\_in + \overline{A}.B.\overline{Borrow\_in}$$
$$+ \ \overline{A}.B.Borrow\_in + A.B.Borrow\_in \qquad (8.2)$$

The subtractor and borrow circuit, during the writing operation, MP1 and MP4 transistors get enabled, causing the potentials of Sub, $\overline{\text{Sub}}$, Borrow, and $\overline{\text{Borrow}}$ being pulled to a logic high level. Concurrently, MN5 and MN6 transistors are closed, allowing for the writing operation of the MTJ storage content.

Fig. 8.3 VSOT MTJ based borrow circuit
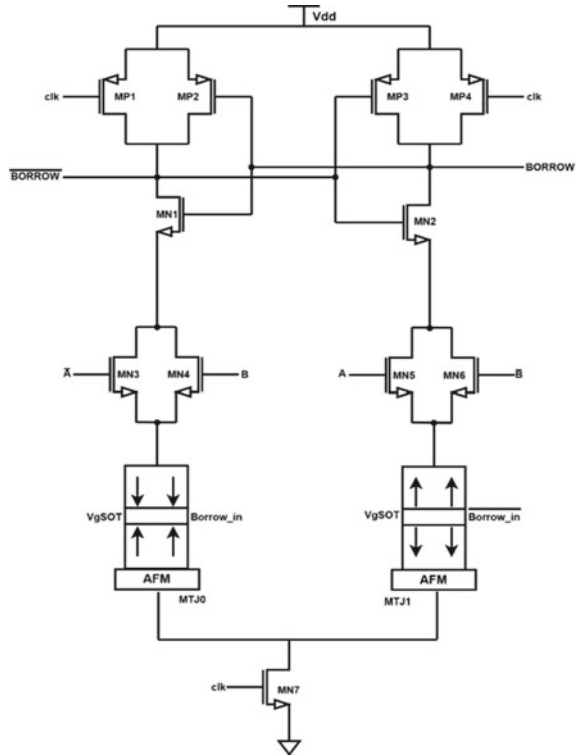
During the calculating/reading mode, the transistors MP1 and MP4 are closed, while MN5 and MN6 are open. This configuration enables the reading of the MTJ storage content. Additionally, based on the input signals A, B, and Borrow_in, the outputs of Sub and Borrow can be obtained, thereby achieving the full subtraction function of the circuit.

Consider the scenario where the inputs B = 0 and A = 0, and the stored state of VgSOT MTJ0 in Figs. 8.2 and 8.3 is logical "0," representing Borrow_in = 0. Correspondingly, MTJ1 stores the content "1" indicating $\overline{Borrow}$ = 1. In the writing mode, the signals Sub, $\overline{Sub}$, Borrow, and $\overline{Borrow}$ are set to logic 1 level. When CLK signal is also logic 1, MN5 is turned on, establishing conducive paths in: MN4-MN84-MTJ0-MN11 and MN6-MN10-MTJ1-MN11. However, since the stored state of MTJ1 is "1," it exhibits a lower resistance state, causing a large current to flow through path MN6-MN10-MTJ1-MN11. As a result, the output Sub transitions between lower and high state values, achieving the difference function when Sub = 0. Simultaneously, MN6 is activated, creating a conductive path in path 5: MN3-MTJ0-MN7 and path 8: MN6-MTJ1-MN7 in borrow circuit. As the stored state of MTJ1 is "1," it also presents a low resistance state, leading to a large current in path 8. Consequently, the Borrow terminal reaches a low level first, followed by

Table 8.1 Subtractor truth-table

Borrow_in	B	A	Sub	Borrow
0	0	0	0	0
0	0	1	1	0
0	1	0	1	1
0	1	1	0	0
1	0	0	1	1
1	0	1	0	0
1	1	0	0	1
1	1	1	1	1

the later transition of $\overline{\text{Borrow}}$ to a high level. This condition corresponds to Borrow = 0, accomplishing the borrowing function.

For various combinations of inputs B, A, and Borrow_in in the MTJ device, Sub and Borrow are determined following the same operating principle. These values align with the truth table of the VgSOT based subtractor circuit, as shown in Table 8.1. The truth table presents the correlation between the input variables and the corresponding output values of the full subtractor circuit.

Similarly, we have implemented the SOT and STT based subtractor and borrow circuits, as seen in Figs. 8.4, 8.5, 8.6, and 8.7, respectively. The functionality of subtractor remains the same for SOT and STT based implementations similar to VgSOT MTJ subtractor. VgSOT employs Antiferromagnetic layer (AFM) as compared to Heavy Metal (HM) layer in SOT.

8.3 Simulation Results and Modulation Parameters

The simulation of the Vg-SOT based Full subtractor has been conducted using CADENCE VIRTUOSO 16.6 software on a 45 nm technology node, with a supply voltage (VDD) of 1.2 V. Vg-SOT MRAM, SOT MRAM, and STT MRAM Verilog-models are employed in this paper. Table 8.2 shows the Vg-SOT, SOT, and STT device parameters used in circuit simulations.

Fig. 8.4 SOT MTJ based
subtractor circuit
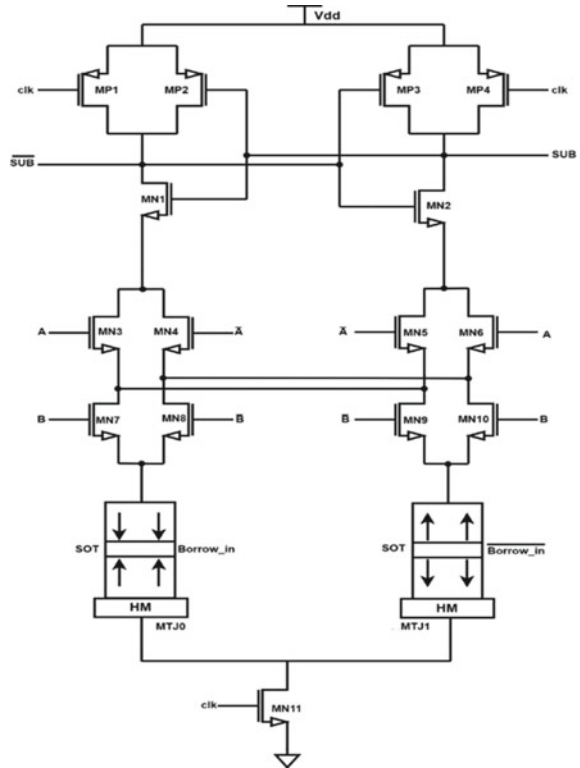
As per subtractor truth table, inputs A, B, and Borrow_in are configured. The
transient analysis of VgSOT MTJ based subtractor, depicted in Fig. 8.8, confirms
the validity of the circuit. During the "writing" mode, when CLK is set to 0, the
VgSOT MTJ undergoes a "writing" process. Specifically, the stored content in MTJ0
transitions from "0" to "1", while the content in MTJ1 transitions from "1" to "0".
Conversely, when CLK is set to 0, the stored content in MTJ0 switches from "1" to
"0", and the content in MTJ1 switches from "0" to "1".

By analyzing the simulation results in Fig. 8.8, it is evident that the circuit operates
in accordance with subtractor functional truth table. For each combination of A, B,
and Borrow_in, the corresponding values of Sub and Borrow align precisely with
the expected outcomes. The simulated behavior of the circuit matches the predicted
functionality, thereby validating the accurate operation of the full subtractor circuit.

Fig. 8.5 SOT MTJ based
borrow circuit
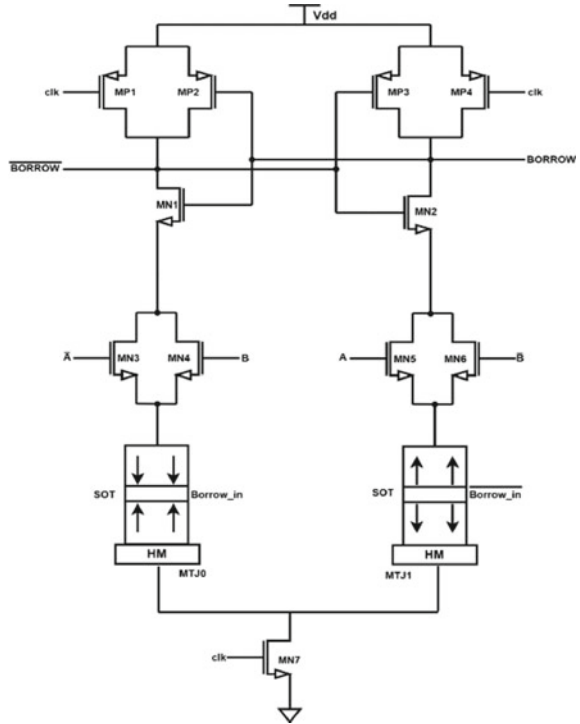
Similarly, Figs. 8.9 and 8.10 show the transient response of SOT and STT-MTJ based subtractor respectively.

8.4 Performance Evaluation

Table 8.3 presents the comparison between different performance parameters such as Energy consumption (fJ), Delay (ns), and Average power consumption (μW) among VgSOT, SOT, and STT MTJ based subtractor implementation respectively.

From Table 8.3, it is seen that in terms of Energy consumption, VgSOT MTJ based subtractor performs 93% and 97% better as compared to SOT and STT-based subtractor implementations. In terms of average delay, VgSOT MTJ based implementation perform 45% and 69% better as compared to SOT and STT-based implementations, respectively. In terms of Average power consumption, performance improvement of 93% and 97% is seen over SOT and STT based subtractor.

Fig. 8.6 STT MTJ based
subtractor circuit
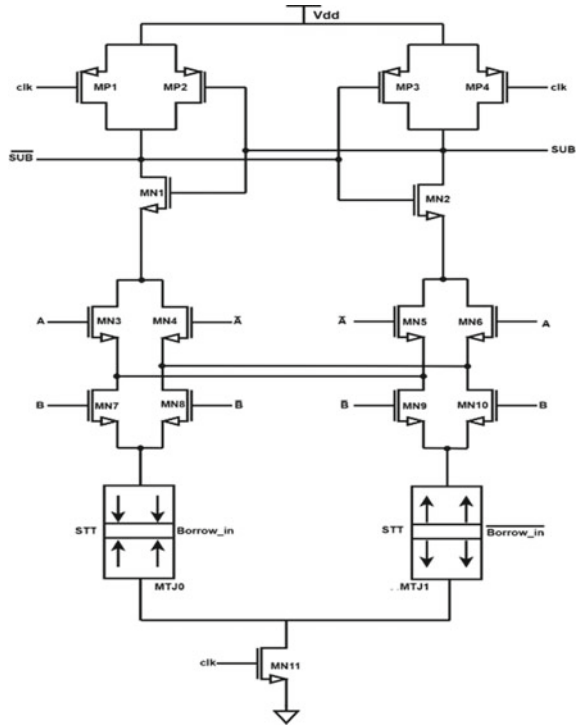
Figures 8.11, 8.12, and 8.13 show the graphical representation of performance
parameters comparison between different design implementations of subtractor as
shown in Table 8.3.

Fig. 8.7 STT MTJ based
borrow circuit
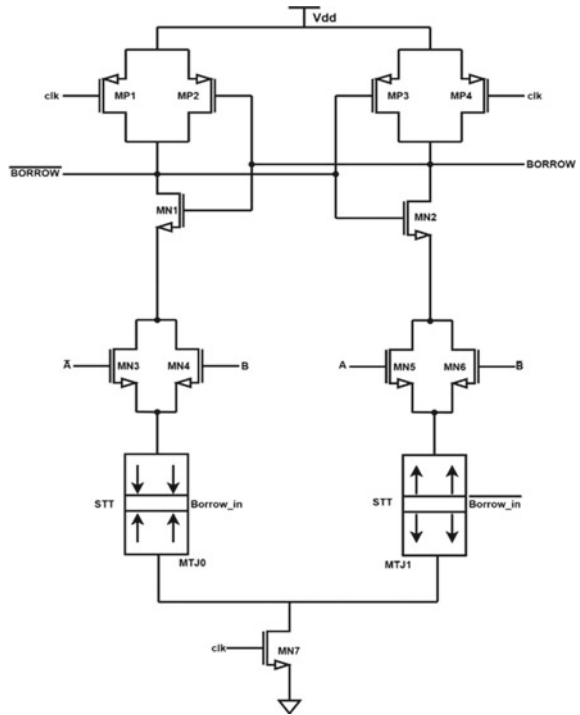
Table 8.2 Device parameters

Parameters	Vg-SOT [25]	SOT [26]	STT [27]
Write voltage (V)	1.2	1.2	1.2
CMOS technology (nm)	45	45	45
Tunnel magnetoresistance ratio (TMR) (%)	100	120	200
MTJ surface area (nm * nm)	50 * 50	40 * 40	40 * 40
Oxide barrier thickness (nm)	1.4	0.85	0.85
Free layer thickness (nm)	1.1	0.7	1.3
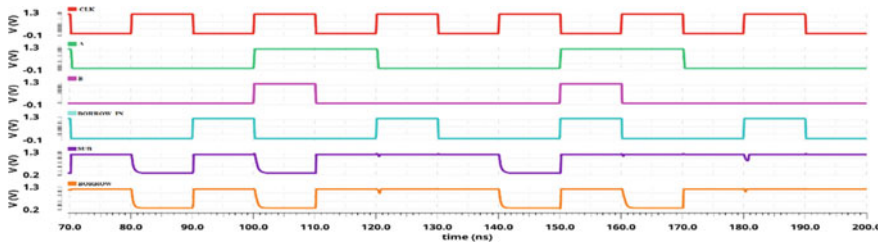
Fig. 8.8 Transient analysis of VgSOT MTJ based subtractor and borrow circuit
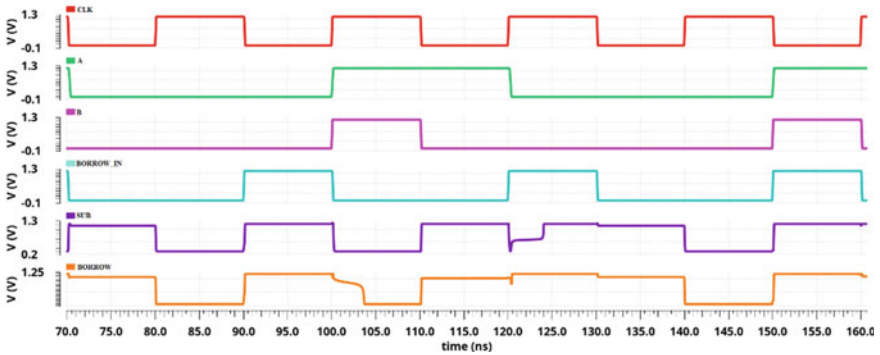
Fig. 8.9 Transient analysis of SOT MTJ based subtractor and borrow circuit
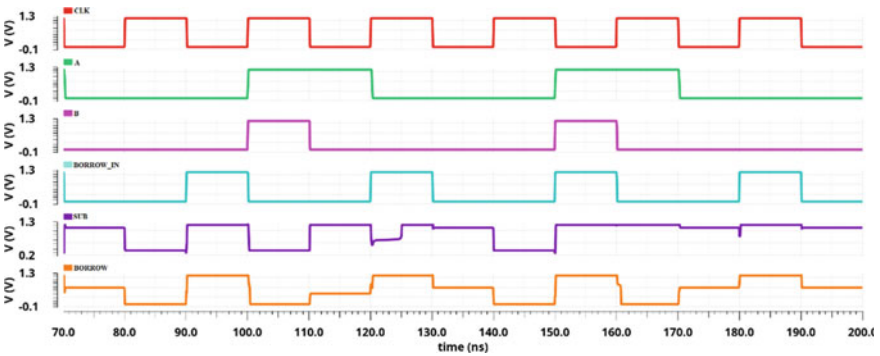
Fig. 8.10 Transient analysis of STT MTJ based subtractor and borrow circuit

Table 8.3 Performance parameters comparison between different designs

Design	Energy consumption (fJ)	Delay (ns)	Average power consumption (μW)
VgSOT MTJ subtractor	19.4	1.26	0.986
SOT MTJ subtractor	310	2.3	14.81
STT MTJ subtractor	691	4.11	35.22

Energy Consumption (fJ) Variation
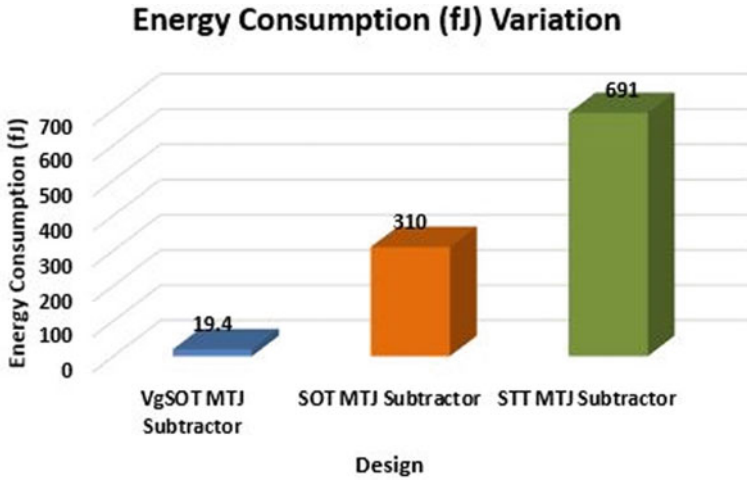
Fig. 8.11 Energy consumption variation for different design
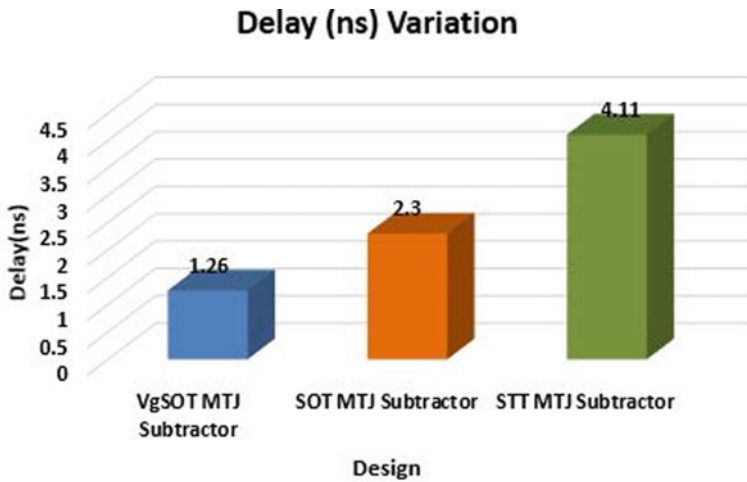
Delay (ns) Variation

Fig. 8.12 Delay consumption variation for different design
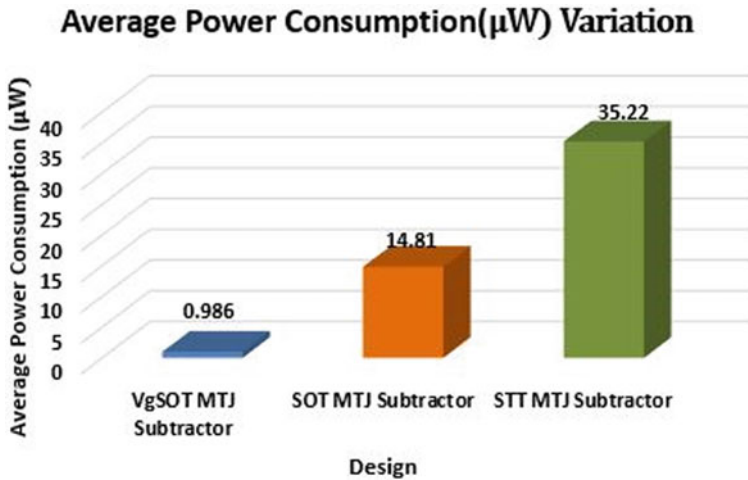
Fig. 8.13 Average power consumption variation for different design

8.5   Conclusion

In conclusion, the VgSOT-based 1-bit subtractor circuit presents a novel approach for digital signal processing. By utilizing the VgSOT effect in conjunction with vertical MTJs, this circuit offers an efficient solution for performing subtraction operations with reduced power consumption. Simulation results demonstrate the successful implementation of the subtraction circuit, validating the outputs sub and borrow as per truth table. From performance parameters comparison, With VgSOT MTJ based subtractor, performance improvement of 93 and 97% is achieved in terms of energy/Average power consumption as compared to SOT and STT based implementations. In terms of average delay. VgSOT MTJ based subtractor performs 47 and 69% better over SOT and STT based implementations. With its low-power characteristics and reliable functionality, the VgSOT-based 1-bit subtractor circuit holds significant promise for enhancing digital signal processing systems in the domain of performance and energy efficiency.

Furthermore, VgSOT MTJ 1-bit subtractor circuit opens up possibilities for broader applications in the field of digital signal processing. Its successful implementation serves as a foundation for the development of more complex arithmetic units and computational circuits. By leveraging the advantages of VgSOT and MTJ technology, it is feasible to explore the design of higher-order subtractor, multi-bit subtraction circuits, and even more advanced computational modules for low-power and high-speed processors.

Additionally, the integration of VgSOT-based circuits with existing digital systems holds potential for enhancing overall system performance and efficiency. The reduced power consumption and high-speed operation offered by the VgSOT-based 1-bit subtractor circuit make it an attractive choice for various applications, such as in

portable devices, Internet of Things (IoT) systems, and embedded systems. The compact size and compatibility with semiconductor devices further contribute to its versatility and integration capabilities.

8.6 Future Scope

The successful implementation of VgSOT-based circuits in the 1-bit subtractor has opened up exciting possibilities for their application in various fields. Moving forward, there are several potential areas of future research and development for VgSOT-based applications:

Advanced Computing Systems: VgSOT-based circuits can be further explored and optimized for advanced computing systems, such as high-performance processors and data centers. Their unique characteristics, including non-volatility, low-power consumption, and high speed, make them attractive candidates for improving overall system performance and energy efficiency.

Non-Volatile Storage Solutions: The integration of VgSOT with memory technologies holds great potential for the development of non-volatile storage solutions. By leveraging the advantages of VgSOT, such as low write energy and high endurance, researchers can explore the design of next-generation non-volatile memory devices, such as MRAM, that offer fast access times, high density, and reliable data retention.

Neuromorphic Computing: VgSOT-based circuits can play a significant role in the advancement of neuromorphic computing systems. With their ability to emulate the behavior of biological synapses, VgSOT-based circuits can enable the development of energy efficient and high-performance neuromorphic systems for applications in artificial intelligence, machine learning, and pattern recognition.

Integration with IoT Devices: As the Internet of Things (IoT) continues to expand, there is a need for low-power and compact devices. VgSOT-based circuits have the potential to meet these requirements by enabling the design of energy efficient IoT devices with enhanced computational capabilities and non-volatile memory storage, contributing to the growth of smart homes, wearable devices, and industrial IoT applications.

Emerging Technologies and Applications: VgSOT-based circuits can be explored in emerging technologies and applications. For example, their compatibility with semiconductor devices makes them suitable for integration in flexible electronics and sensor systems, where low-power and high-density circuitry is essential. Additionally, their ability to operate at cryogenic temperatures makes them attractive for quantum computing and quantum information processing.

System-level Integration: Future research can focus on the system-level integration of VgSOT-based circuits into complex electronic systems. This includes exploring their compatibility with existing semiconductor processes, optimizing their performance in mixed-signal environments, and designing efficient interconnects for seamless integration with other functional blocks.

In summary, the future of VgSOT-based applications holds tremendous potential for advancing computing systems, non-volatile storage solutions, neuromorphic computing, IoT devices, emerging technologies, and system-level integration. Continued research and development in these areas will drive innovation and unlock new opportunities for VgSOT-based technologies in various domains.

References

1. Hoppe, B., Neuendorf, G., Schmitt-Landsiedel, D., Specks, W.: Optimization of high-speed CMOS logic circuits with analytical models for signal delay, chip area, and dynamic power dissipation. IEEE Trans. Comput. Des. Integr. Circuits Syst. **9**(3), 236–247 (1990)
2. Chen, C.: Overcoming research challenges for CMOS scaling: industry directions. In: Proceedings of the 2006 8th International Conference on Solid-State and Integrated-Circuit Technology, ICSICT-2006, pp. 4–7 (2006)
3. Kim, N.S.: Leakage current: Moore's law meets static power. Computer (Long. Beach. Calif) **36**(12), 68–75 (2003). https://doi.org/10.1109/MC.2003.1250885
4. Wei, L., Chen, Z., Roy, K., Johnson, M.C., Ye, Y., De, V.K.: Design and optimization of dual-threshold circuits for low-voltage low-power applications. IEEE Trans. Very Large Scale Integr. Syst. **7**(1), 16–24 (1999). https://doi.org/10.1109/92.748196
5. Taur, Y., Buchanan, D.A., Chen, W.: CMOS scaling into the nanometer regime. Proc. IEEE **85**(4), 486–503 (1997). https://doi.org/10.1109/5.573737
6. Kok, K.Y., Ng, I.K.: Giant magnetoresistance (GMR): spinning from research to advanced technology. ASEAN J. Sci. Technol. Dev. **19**(2), 33–43 (2017). https://doi.org/10.29037/AJSTD.336
7. Black, W.C., Das, B.: Programmable logic using giant-magnetoresistance and spin-dependent tunneling devices. J. Appl. Phys. **87**(9), 6674–6679 (2000). https://doi.org/10.1063/1.372806
8. Moodera, J.S., Kinder, L.R., Wong, T.M., Meservey, R.: Large magnetoresistance at room temperature in ferromagnetic thin film tunnel junctions. Phys. Rev. Lett. **74**(16), 3273–3276 (1995). https://doi.org/10.1103/PHYSREVLETT.74.3273
9. Jangra, P., Duhan, M.: Performance-based comparative study of existing and emerging non-volatile memories: a review. J. Opt. 1–15 (2022). https://doi.org/10.1007/S12596-022-01058-W/METRICS
10. Lin, H.Y., Lin, C.S., Chiou, L.Y., Da Liu, B.: Leakage current reduction in CMOS logic circuits. In: IEEE Asia-Pacific Conference on Circuits and Systems, APCCAS, vol. 1, pp. 349–352 (2004). https://doi.org/10.1109/APCCAS.2004.1412767
11. Engel, B.N. et al.: A 4-Mb toggle MRAM based on a novel bit and switching method. IEEE Trans. Mag. **41**(1) I, 132–136 (2005). https://doi.org/10.1109/TMAG.2004.840847
12. Kawahara, T., Takemura, R.: 2Mb spin-transfer torque RAM (SPRAM) with bit-by-bit bidirectional current write and parallelizing-direction current read. In: IEEE International Solid-State Circuits Conference Digest of Technical Papers (2007). https://doi.org/10.1109/ISSCC.2007.373503
13. Jangra, P., Duhan, M.: A review on emerging spintronic devices: CMOS counterparts. In: 7th International Conference on Communication and Electronics Systems, ICCES 2022 – Proceedings, pp. 90–99 (2022). https://doi.org/10.1109/ICCES54183.2022.9835778
14. Jangra, P., Duhan, M.: Comparative analysis of devices working on optical and spintronic based principle. J. Opt. 1–21 (2023). https://doi.org/10.1007/S12596-023-01181-2/METRICS
15. Wolf, S.A., et al.: Spintronics: a spin-based electronics vision for the future. Science **294**(5546), 1488–1495 (2001). https://doi.org/10.1126/SCIENCE.1065389
16. Guo, Z., Yin, J.: Spintronics for energy-efficient computing: an overview and outlook. Proc. IEEE **109**(8), 1398–1417 (2021). https://doi.org/10.1109/JPROC.2021.3084997

17. Fong, X., Kim, Y, Yogendra, K.: Spin-transfer torque devices for logic and memory: prospects and perspectives. IEEE Trans. Comput. Des. Integr. Circuits Syst. **35**(1), 1–22 (2016). https://doi.org/10.1109/TCAD.2015.2481793

18. Koike, H., Tanigawa, T.: Review of STT-MRAM circuit design strategies, and a 40-nm 1T-1MTJ 128Mb STT-MRAM design practice. In: 2020 IEEE 31st Magnetic Recording Conference TMRC (2020). https://doi.org/10.1109/TMRC49521.2020.9366711

19. Cubukcu, M., Boulle, O.: Spin-orbit torque magnetization switching of a three-terminal perpendicular magnetic tunnel junction. Appl. Phys. Lett. **104**(4), 042406 (2014). https://doi.org/10.1063/1.4863407

20. Brataas, A., Hals, K.M.D., Brataas, Hals, K.M.D.: Spin-orbit torques in action. NatNa **9**(2), 86–88 (2014). https://doi.org/10.1038/NNANO.2014.8

21. Jangra, P., Duhan, M.: Performance analysis of voltage-controlled magnetic anisotropy MRAM-based logic gates and full adder. ECS J. Solid State Sci. Technol. **12**(5), 051001 (2023). https://doi.org/10.1149/2162-8777/ACD1B1

22. Sarkar, M.R., Bappy, M.M.A., Azmir, M.M., Rashid, D.M., Hasan, S.I.: VG-SOT MRAM design and performance analysis. In: IEEE 12th Annual Information Technology, Electronics and Mobile Communication Conference, IEMCON, pp. 715–719 (2021). https://doi.org/10.1109/IEMCON53756.2021.9623147

23. Dikshit, S.N., Nisar, A., Dhull, S., Bindal, N., Kaushik, B.K.: Hybrid spintronics/CMOS logic circuits using all-optical-enabled magnetic tunnel junction. IEEE Open J. Nanotechnol. **3**, 85–93 (2022). https://doi.org/10.1109/OJNANO.2022.3188768

24. Upadhyaya, Y.K., Hasan, M.: Energy efficient robust pre-charge sense amplifier. In: Proceedings of the International Conference on Advances in Electrical and Computer Engineering, UPCON 2019, pp. 1–5 (2019). https://doi.org/10.1109/UPCON47278.2019.8980146

25. Kaili, Z.: Compact Modeling and Analysis of Voltage-Gated Spin-Orbit Torque Magnetic Tunnel Junction. IEEE (2020). https://ieeexplore.ieee.org/stamp/stamp.jsp?arnumber=9032097

26. Kazemi, M., Rowlands, G.E., Ipek, E., Buhrman, R.A., Friedman, E.G.: Compact model for spin-orbit magnetic tunnel junctions. IEEE Trans. Electron Dev. **63**(2), 848–855 (2016). https://doi.org/10.1109/TED.2015.2510543

27. Wang, Y., Zhang, Y., Deng, E.Y., Klein, J.O., Naviner, L.A.B., Zhao, W.S.: Compact model of magnetic tunnel junction with stochastic spin transfer torque switching for reliability analyses. Microelectron. Reliab. **54**(9–10), 1774–1778 (2014). https://doi.org/10.1016/J.MICROREL.2014.07.019

Chapter 9
Hybrid Prediction Model for Mechanical Properties of Low Alloy Steel Based on SVR-MLP

Ci Song

Abstract As research into alloyed materials continues to advance there are different types of low-alloy steel with different chemical compositions and organisations, so there is a need for more efficient methods of predicting the mechanical properties of low-alloy steels compared to experimental studies. In this paper, three data-driven regression models are developed to predict the mechanical properties of different types of low-alloyed steels. The first model, Support Vector Regression (SVR), achieves good results for the prediction of nominal yield strength and tensile strength, but not for elongation and cross-sectional shrinkage; the second model is a multilayer perceptron regression model, which is similar to but worse than SVR for the prediction of the four mechanical properties; finally, it is a hybrid model that combines SVR and Multilayer Perceptron (MLP) through a linear model, and its prediction accuracy is very The final model is a hybrid model fusing SVR and MLP with high prediction accuracy, which is significantly better than the single prediction model, confirming the usefulness of the model fusion strategy in predicting the mechanical properties of low-alloy steel.

9.1 Introduction

The mechanical properties are the various mechanical behaviours of the material when subjected to various applied loads under different circumstances, and its good or bad determines whether the material fails or fractures in its working condition. Low-alloy steel is a typical class of special steel materials, which can be used in the manufacture of grinding wheel shafts, gears, piston parts etc. It is widely used in machinery, automobiles, aircraft and other fields, so the study of mechanical properties of low-alloy steel deserves attention [1]. With the increasing computing power of computers and theoretical advances in data science, machine learning and

C. Song (✉)
School of Resources and Materials, Northeastern University at Qinhuangdao, Hebei, China
e-mail: 202016108@stu.neu.edu.cn

deep learning have made breakthroughs and taken a dominant position in the field of artificial intelligence. The discipline of mechanics has accumulated a large amount of numerical simulation data, experimental measurement data and field monitoring data in the past decades, and these large-scale, high-dimensional data contain rich physical characteristics, but it is difficult to analyse these data and summarise the physical laws by traditional mathematical tools alone. Machine learning can be used to learn and mine the data for features, and eventually discriminate, predict and generate new data [2]. Its powerful non-linear fitting capability makes it an important contribution to the field of regression prediction, but it is computationally expensive due to the large number of samples required for learning and its tendency to reach local optima. As each model has its own strengths and weaknesses, this paper first uses the SVR and MLP (Multilayer Perceptron) regression models to independently predict the mechanical properties of low-alloy steel. After analysing and comparing their predictions, the paper will then use a hybrid model that linearly combines the outputs of the two models to make predictions again and compare the differences with the single model.

9.2 Data Sets

The data used in this study, "MatNavi Mechanical properties of low-alloy steels", was obtained from MatNavi [3] and collected on the Kaggle platform [4]. This dataset contains the alloy code, chemical composition (C, Si, Mn, P, S, Ni, Cr, Mo, Cu, V, Al, N, Nb + Ta), carbon equivalent, alloy temperature, stress value (nominal yield strength) $\sigma_{r0.2}$ at 0.2% plastic strain, tensile strength Rm, elongation δ and cross-sectional shrinkage ψ. After data cleaning, the sample size of the data is 951, a total of 15 items of chemical composition, carbon equivalent and alloy temperature were selected as features, and a total of 4 items of nominal yield limit, tensile strength, elongation and cross-sectional shrinkage were selected as labels to divide the data into a training set and a test set in a ratio of 8:2.

9.3 Support Vector Regression (SVR)

Unlike ordinary regression models, in SVR no loss is calculated as long as the data is within the interval band. The loss function is calculated when and only when the Euclidean distance between the curve function $f(x)$ is fitted and the label y is greater than the error tolerance threshold ϵ. Then maximising the interval L (minimising $\frac{\|w\|^2}{2}$) while minimising the loss function becomes the ultimate optimisation task [5].

$$\underset{w,b}{\text{minimize}} \frac{\|\overrightarrow{w}\|^2}{2} + C \sum_{i=1}^{n} \mathcal{L}_{\epsilon}(f(x_i) - y_i) \tag{9.1}$$

where C is the penalty parameter and $\uparrow_\epsilon$ is the ϵ-insensitive loss function, defined as follows.

$$\uparrow_\epsilon(x) = \begin{cases} 0, |x| < \epsilon \\ |x| - \epsilon, \, Other \end{cases} \tag{9.2}$$

9.3.1 Kernel Functions

The goal of a support vector (regression) machine is to find a hyperplane using linear regression. However, almost most of the problems encountered in practical applications are non-linear, and the function of the kernel function is to map data points that cannot currently be separated or represented by linear equations to a higher dimensional space under which SVR can find a hyperplane using linear regression [6]. The kernel function used in this paper is the Gaussian radial kernel function, which is defined as follows.

$$K\left(x_i, x_j\right) = exp\left\{-\frac{\|x_i - x_j\|^2}{2\sigma^2}\right\} \tag{9.3}$$

9.3.2 Model Training

For good or bad prediction results, this paper uses the R^2 coefficient, which is defined as follows.

$$R^2 = 1 - \frac{\sum_{i=1}^n (y_i - f^*(x_i))^2}{\sum_{i=1}^n (y_i - \overline{y})^2} \in (0, 1) \tag{9.4}$$

The closer R^2 is to 1, the better the model fits the curve, and the closer it is to 0, the closer the model's prediction results are to the average, and the less it serves the function of prediction. From the above analysis, it can be seen that for the establishment of the SVR, the main parameters to be set are the penalty parameter C, the error tolerance threshold ϵ, and the kernel function exponential term coefficient $= \frac{1}{2\sigma^2}$. Due to the small sample size, this paper uses the violent search method for the selection of parameters. For the penalty parameter C, the output is the number of R^2 obtained when the value is taken over the interval $(100, 3000)$ in steps of 100. For the error tolerance threshold ϵ, the output is the R^2 number obtained when the value is taken over the interval $(1, 10)$ using 1 as the step size. For the kernel function coefficient γ, the output is the R^2 number obtained when the value is taken over the interval $(1, 10)$ in steps of 1. The value with the highest score is set as the parameter

Table 9.1 R^2 achieved by SVR on the test set

Performance indicators	$\sigma_{r0.2}$ (MPa)	Rm (MPa)	δ (%)	ψ (%)
C	1000	2000	300	100
γ	3	3	5	4
ϵ	0.02	0.02	0.02	0.02
R^2	0.9537	0.9746	0.7642	0.8892

by selecting R^2. As the SVR is a single output model, it needs to be modelled for each label and the optimal combination of parameters obtained and the R^2 obtained on the test set are shown in the following Table 9.1.

9.4 Multilayer Perceptron

A multilayer perceptron (MLP) is an artificial neural network for forward propagation of information, consisting of multiple layers of nodes, each fully connected to the next. In addition to the input node, each node is a neuron (or processing unit) with a non-linear activation function. The network is usually trained using error back propagation to obtain the gradients of the parameters to be tuned for optimisation by a gradient descent type of optimisation algorithm.

9.4.1 Model Building

For the establishment of the MLP model, the main parameters set are: the number of neurons in the input layer, corresponding to the number of features 15; the number of intermediate hidden layers and the number of neurons in each layer, which determines the complexity of the model: the more hidden layers and neurons in each layer, the more complex the model, the stronger the non-linear approximation ability but also more prone to overfitting. In this paper, the number of hidden layers is 4, each layer contains 96 neurons and uses an l_2 regular term of size 0.01 to prevent overfitting; the number of neurons in the output layer corresponds to the number of labels 4. In order to obtain the non-linear fitting ability, the activation function needs to be added to the neurons in the MLP, and the activation function used in this paper is ReLU, which is defined as follows.

$$g(x) = \max(0, x) \tag{9.5}$$

For the loss function, this paper uses huberloss, defined as follows.
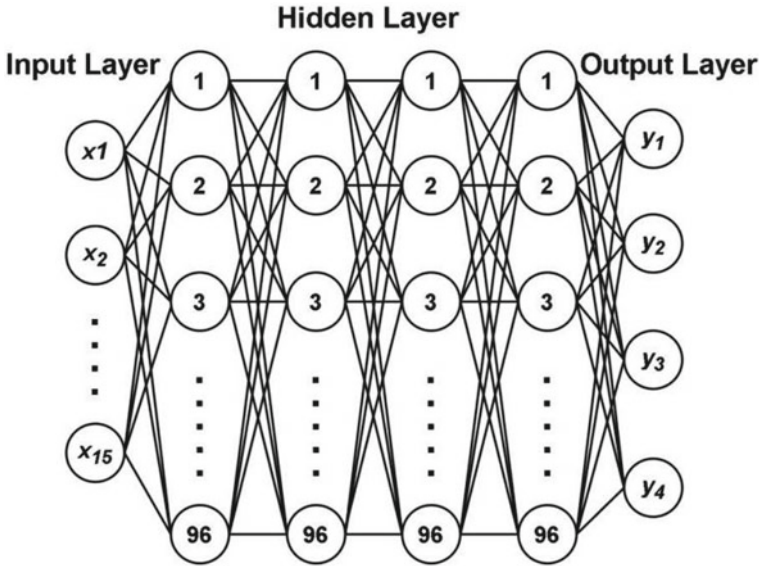
Fig. 9.1 Visualisation of the MLP network structure

$$L(y, f(x)) = \begin{cases} \frac{1}{2}(y - f(x)), |y - f(x)| \leq \varphi \\ \varphi \cdot (|y - f(x)| - \frac{1}{2}\varphi), other \end{cases} \tag{9.6}$$

This loss function penalises outliers to a lesser extent than the MSE, improving the robustness of the model. In addition, the mean absolute error (MAE) is used for the evaluation without affecting the training process:

$$MAE = \frac{1}{n} \sum_{i=1}^{n} |y_i - f(x_i)| \in [0, +\infty) \tag{9.7}$$

The MLP network structure is shown in the following Fig. 9.1.

9.4.2 The Adam Optimisation Algorithm

The optimiser of the training model is also an important parameter. The essence of the optimiser is the gradient descent algorithm, but because of the complex structure of the neural network, the general gradient descent algorithm is not effective, so there are many improved optimisers, AdaGrad (Adaptive gradient method) proposed by John Duchi, by continuously adjusting the learning rate during the training process let it show good performance in dealing with sparse gradients [7]. RMSProp (Root Mean Square prop) was developed from AdaGrad and is suitable for handling non-smooth

objectives [8, 9]. Finally, the Adam optimisation algorithm used in this paper, which combines the advantages of RMSProp and AdaGrad, is the most popular gradient descent algorithm today. The iteration formula in Adam is.

$$\theta_{i+1} = \theta_i - \frac{\alpha}{\sqrt{\hat{n}_i} + \epsilon} \hat{m}_i \tag{9.8}$$

Of which:

$$\begin{cases} \hat{m}_i = \frac{m_i}{1-\mu^t} \\ m_i = \mu \cdot m_{i-1} + (1 - \mu) \cdot g_i \end{cases} \tag{9.9}$$

$$\begin{cases} \hat{n}_i = \frac{n_i}{1-v^i} \\ n_i = v \cdot n_{i-1} + (1 - v) \cdot g_i^2 \end{cases} \tag{9.10}$$

In the above equation θ_i is α parameter to be adjusted in the neural network, α is the learning rate and g_i is the current gradient. The definition shows that $\hat{m}_t$ takes into account the historical information of the gradient using weighted moving average and recursive method to correct the current gradient, and $\hat{n}_t$ takes the same approach to adjust the magnitude of the learning rate. In this paper, the Adam parameters are set as follows: $\alpha = 0.001$, $\mu = 0.9$, $v = 0.999$.

9.4.3   Model Training

The MLP model was trained 2000 times and 256 data were crawled for each training session, using the test set as the validation set. The training process took a total of 78 s. The variation of the loss function and model accuracy on the training and validation sets during the training process is shown in the following Fig. 9.2.

The loss functions and MAE curves of the training and validation set almost overlap, demonstrating that no overfitting occurs and that the model has good generalisation capability. The R^2 obtained by the model on the test set is shown in the following Table 9.2.

A comparison of the results achieved with the SVR shows that the MLP was slightly inferior to the SVR in this prediction task.

9.5   Hybrid Models

Both SVR and MLP failed to achieve satisfactory results in the prediction of elongation and section shrinkage. In this paper, a simple SVR-MLP hybrid model was attempted to obtain higher accuracy, and the fusion strategy was as follows [10].
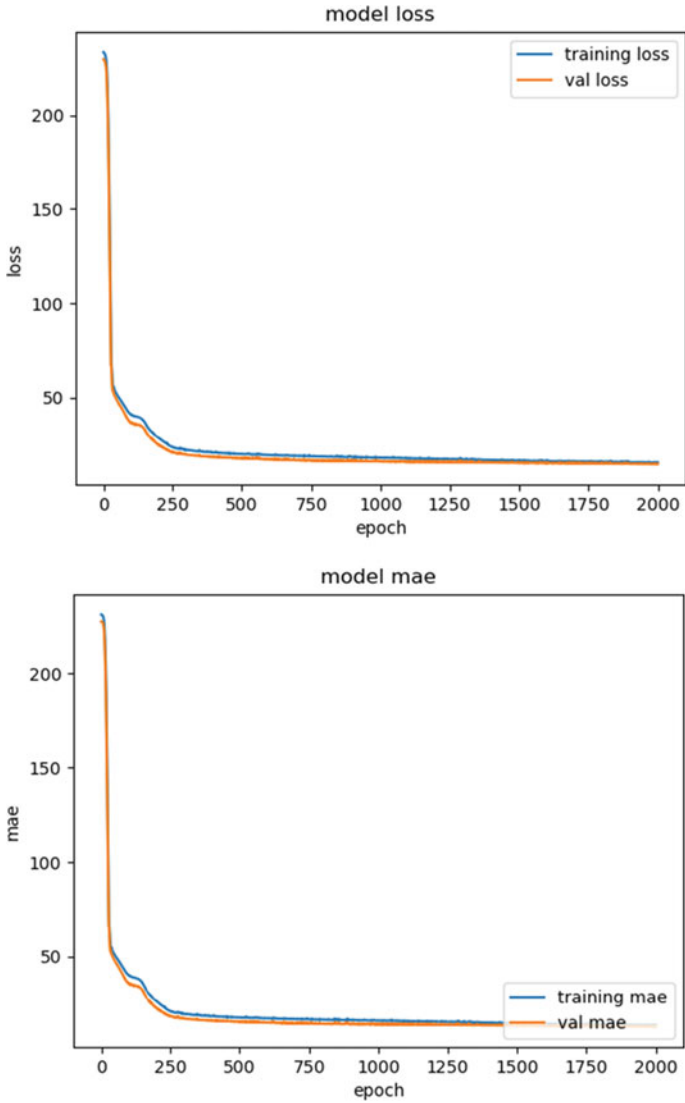
Fig. 9.2 Visualisation of huberloss and MAE training process changes

Table 9.2 R^2 obtained by MLP on the test set

Performance indicators	$\sigma_{r0.2}$ (MPa)	Rm (MPa)	δ (%)	ψ (%)
R^2	0.9403	0.9577	0.7593	0.7831

(1) The mechanical properties of all samples are predicted using the trained SVR and MLP regression models, respectively, and the results are noted as $Y_{svr} = [\sigma_{r0.2,svr}, Rm_{svr}, \delta_{svr}, \psi_{svr}]$ and $Y_{mlp} = [\sigma_{r0.2,mlp}, Rm_{mlp}, \delta_{mlp}, \psi_{mlp}]$.

(2) Noting that the final output is $Y_{out} = [\sigma_{r0.2}, Rm, \delta, \psi]^T$, build the following multiple linear regression model.

$$Y_{out} = \alpha Y_{svr} + \beta Y_{mlp} + C \tag{9.11}$$

or

$$\begin{bmatrix} \sigma_{r0.2} \\ Rm \\ \delta \\ \psi \end{bmatrix} = \begin{bmatrix} \alpha_1 \\ \alpha_2 \\ \alpha_3 \\ \alpha_3 \end{bmatrix} \begin{bmatrix} \sigma_{r0.2,svr} \\ Rm_{svr} \\ \delta_{svr} \\ \psi_{svr} \end{bmatrix}^T + \begin{bmatrix} \beta_1 \\ \beta_2 \\ \beta_3 \\ \beta_3 \end{bmatrix} \begin{bmatrix} \sigma_{r0.2,mlp} \\ Rm_{mlp} \\ \delta_{mlp} \\ \psi_{mlp} \end{bmatrix}^T + \begin{bmatrix} C_1 \\ C_2 \\ C_3 \\ C_4 \end{bmatrix} \tag{9.12}$$

(3) The linear regression model was solved using least squares and then predicted on the test set using R^2 to assess the effectiveness of the model (Fig. 9.3).

The R^2 numbers obtained by the hybrid model on the test set for the predictions of nominal yield limit, tensile strength, elongation and section shrinkage are shown in the Table 9.3.

The above table shows that the hybrid model used in this paper achieves significantly better predictions than the single model, especially for elongation and section shrinkage which are not well predicted by SVR and MLP, the hybrid model performs very well.
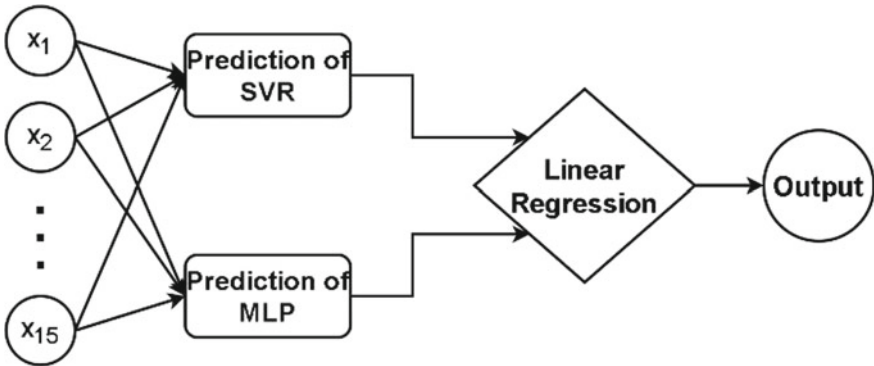
Fig. 9.3 Hybrid model structure

Table 9.3 R^2 obtained for the hybrid model on the test set

Performance indicators	$\sigma_{r0.2}$(MPa)	Rm (MPa)	δ (%)	ψ (%)
R^2	0.9877	0.9731	0.9617	0.9653

9.6 Conclusion

In this paper, the nominal yield strength, tensile strength, elongation, and section shrinkage of low-alloy steel were predicted by building a regression model with SVR and MLP and a hybrid model using linear regression to integrate the two. However, the prediction accuracy of the multiple linear regression model using their outputs as inputs was high for each mechanical property index after training, which proved that the hybrid model has obvious advantages over the single prediction model.

9.7 Discussion

There is a direct mapping relationship between the features and labels in this data, so the polynomial fusion strategy established in this paper may not be applicable in other prediction tasks encountered, and a hybrid model with a more complex fusion structure is needed. Future research can explore and delve into the following aspects.

1. Model optimisation: parameter tuning of the SVR-MLP model is crucial to its prediction accuracy and performance. Future research can explore more efficient parameter optimisation algorithms to further improve the prediction accuracy and stability of the model.
2. Data mining: The mechanical properties of low-alloy steel are influenced by a variety of factors, including chemical composition, heat treatment process, metallographic organisation, etc. Future research can explore more efficient parameter optimisation algorithms to further improve the prediction accuracy and stability of the model. Future research can explore the influence of these factors on the mechanical properties of low-alloy steel through large-scale data mining and analysis to provide more comprehensive and accurate data support for the model.
3. Model integration: In addition to the SVR-MLP model, there are many other machine learning algorithms, such as decision trees, support vector machines, neural networks, etc., which can also be used for the prediction of mechanical properties of low-alloy steels. Future research can integrate these algorithms with the SVR-MLP model to build a more powerful and comprehensive hybrid prediction model for the mechanical properties of low-alloy steel.
4. Application areas: Low-alloy steels are widely used in many fields such as aviation, automotive, and construction, and the prediction of their mechanical properties has wide application prospects in industrial production and scientific research. Future research can further expand the application area of the model to more complex and diverse low-alloy steel materials and engineering problems.

References

1. Zhao, T. X., Cui, H. J., Sun, Y. B., Huang, T. H.: Quantitative testing and uncertainty assessment of low-content elements in low-alloy steel. Phys. Chem. Test.-Phys. **58**(11), 25 (2022)
2. Saeid, P., Donehower, L. A., Katsonis, P., Teng-Kuei, H., Jenniferk, A., Kwanghyuk, L., et al.: Epimutestr: a nearest neighbor machine learning approach to predict cancer driver genes from the evolutionary action of coding variants. Nucl. Acids Res. (12), 12 (2022)
3. MatNavi: https://mits.nims.go.jp/en/2022-12-01 Last accessed on 2022-12-02
4. Kaggle: https://www.kaggle.com/2022-12-01 Last accessed on 2022-12-02
5. Duchi, J., Hazan, E., Singer, Y.: Adaptive subgradient methods for online learning and stochastic optimization. J. Mach. Learn. Res. **12**(7) (2011)
6. Karimipour, A., Abad, J.M.N., Fasihihour, N.: Predicting the load-carrying capacity of GFRP-reinforced concrete columns using ANN and evolutionary strategy. Compos. Struct. **275**, 114470 (2021)
7. Tieleman, T., Hinton, G.: Lecture 6.5-rmsprop: Divide the gradient by a running average of its recent magnitude. COURSERA: Neural Netw. Mach. Learn. **4**(2), 26–31(2012)
8. Kingma, D. P., Ba, J.: Adam: A method for stochastic optimization. arXiv preprint arXiv:1412. 6980 (2014)
9. Xu, Z. W., Liu, X. M., Zhang, K.: Mechanical properties prediction for hot rolled alloy steel using convolutional neural network. IEEE Access **7**, 47068–47078 (2019)
10. Liu, W., Yan, L., Zhang, X., Gao, D., Peng, J.: A Denoising SVR-MLP Method for Remaining Useful Life Prediction of Lithium-ion Battery. In: 2019 IEEE Energy Conversion Congress and Exposition (ECCE), IEEE (2019)

Chapter 10
A Human-Inspired Semantic SLAM Based on Parking-Slot Number for Autonomous Valet Parking

Zhenquan Shen, Zhan Song, Zhenzhong Xiao, and Xiang Chen

Abstract With the rapid development of automatic driving field, automatic parking has become increasingly concerned commercially. SLAM (Simultaneous Localization and Mapping) as an important technology is applied to autonomous valet parking (AVP) in recent years. However, it is difficult to take full advantage of the data from vision sensors owing to abundant similar elements in the parking lot. In this paper, a semantic SLAM based on slot number in parking lot is proposed. The system recognizes the slot number as semantic markers by a CNN (Convolution Neural Network) and classifies the slot according to the semantic markers. Then a semantic ICP (Iterative Closest Point) algorithm is used for mapping and localization modules. The results of the experiments on our simulation dataset show that this method performs well and has a better accuracy than traditional ICP. This work may have a promotion for autonomous valet parking and be applied to commercial products one day.

10.1 Introduction

In recent years, automatic driving has developed rapidly as traffic requires a safer and more efficient way [1]. As an important part of automatic driving, automatic parking technology has received more and more attention. It can help drivers automatically drive the car in constrained environments where much attention and experience is required. An automatic parking approach should consist of state inputs, environment build, digital signal processor and output [2]. In detail, digital signal processor include detection, localization, path planning and tracking.

Z. Shen (✉) · Z. Song
Shenzhen Institutes of Advanced Technology, Chinese Academy of Sciences, Shenzhen 518055, China
e-mail: shenzhenquan@pku.org.cn

Z. Shen · Z. Xiao · X. Chen
Orbbec Inc., Shenzhen 518062, China

SLAM is a technology which can build an environment and localize it according to the input data from sensors. Nowadays, SLAM is used in increasing fields with the era of artificial intelligence coming. Automatic driving is a representation of these fields. SLAM can play an important role in the automatic parking system, the results of which will help the other part of the system achieve path planning and control.

Although there are some works focus on SLAM in the situation of parking lot, there is still a significant problem that remains to be solved. Parking lot has many similar elements such as slot which is difficult to distinguish one from another even for a human. This leads to being hard to take full advantage of the data from vision sensors.

In this paper, we propose a semantic SLAM based on slot number in parking lot to overcome the defect that vision sensors cannot make full use of their advantages under the situation with many similar elements. We are inspired by humans who do the same task by cognizing the semantic marks.

10.2   Literature Review

Grimmett, et al. developed an automatic parking system in V-Charge project [3]. This approach builds a metric map meanwhile a semantic map is built. The semantic map can generate road net through algorithm and in addition, a velocity map is given according to the probability with which space is occupied by barrier. However, calculating the probability will consume much computing resource. Schwesinger, et al. replaced calculating the probability with ultraphonic sensors and binocular cameras also in the V-Charge project [4]. It will consume less computing resource but extra sensors are needed.

Hu, et al. choose seven semantic classes through semantic segmentation of the IPM (Inverse Perspective Mapping) [5]. Corresponding pixels are mapped to generate point cloud. Point cloud fused to obtain local map with the pose from odometry and IMU (Inertial Measurement Unit). Localization is accomplished by ICP algorithm. Qin, et al. following this way propose the AVP-SLAM [6]. However, all the parking slots are classified as the same category, which cannot perform well in the situation with similar elements such as parking lot.

Shao, et al. use DeepPS net to detect parking slot and minimize the loss function consisting of IMU error, visual error and IPM error [7]. This method needs some priori knowledge about parking slots. Fang, et al. give a SLAM based on fiducial markers for autonomous valet parking [8]. This method relies on markers and it is unsuitable for most scenarios. A semantic SLAM framework that leverages the hybrid edge information on bird's-eye view images is presented. Xiang, et al. extract useful edges from the synthesized bird's- eye view image and the free-space contours for the SLAM task [9]. But edges are not high-level semantic feature. Tripathi, et al. come up with a trained trajectory parking scheme for frequently parking in a persistent map [10]. This method relies on trained trajectory and cannot work for the first time entering the parking lot.

10.3 Methodology

The pipeline of the whole SLAM proposed by this paper is shown in Fig. 10.1. First of all, vehicle-mounted four fish-eye cameras, IMU and wheel encoder sensors are used to acquire data from environment. Additionally, data from sensors are preprocessed according to their types and structures. The above two steps are called perception module that is receiving environment message with the help of sensors and algorithms. Later, the processed data are fed into mapping module and localization module simultaneously. Mapping module can build environment map with perception message and localization module can obtain vehicle pose in the map which means the relationship between the vehicle and environment.

10.3.1 Preprocessing

Preprocessing has two parts: images from fish-eye cameras part and signals from IMU and wheel encoder part. Signals from IMU and wheel encoder can refer to Forster, et al. and Zunaidi, et al. for details [11, 12]. They are converted to the pose of the vehicle. Images from fish-eye cameras are processed by the following steps.

10.3.2 IPM Image

Four surround-view cameras are a common setup for the high-configuration commercial cars. One camera is in the front, one camera is in the rear, and two cameras are on the left and right separately. These cameras are equipped with fish-eye lens and look downward [6].

The intrinsic and extrinsic parameters of each camera are calibrated offline. Each pixel is projected into the ground plane under the vehicle center coordinate, which is also called IPM. After the inverse perspective projection, we synthesize points from four images into a big one. The details of these operations can refer to the paper published by Qin, et al. in 2020 [6].

10.3.3 Feature Detection

We adopt the CNN for semantic feature detection. There are several networks that can accomplish the semantic segmentation such as FCN [13], SegNet [14], PSPNet [15], DeepLab [16] and U-Net [17]. In this paper, we choose the U-Net described by Ronneberger et al. [17] to segment images into different categories.
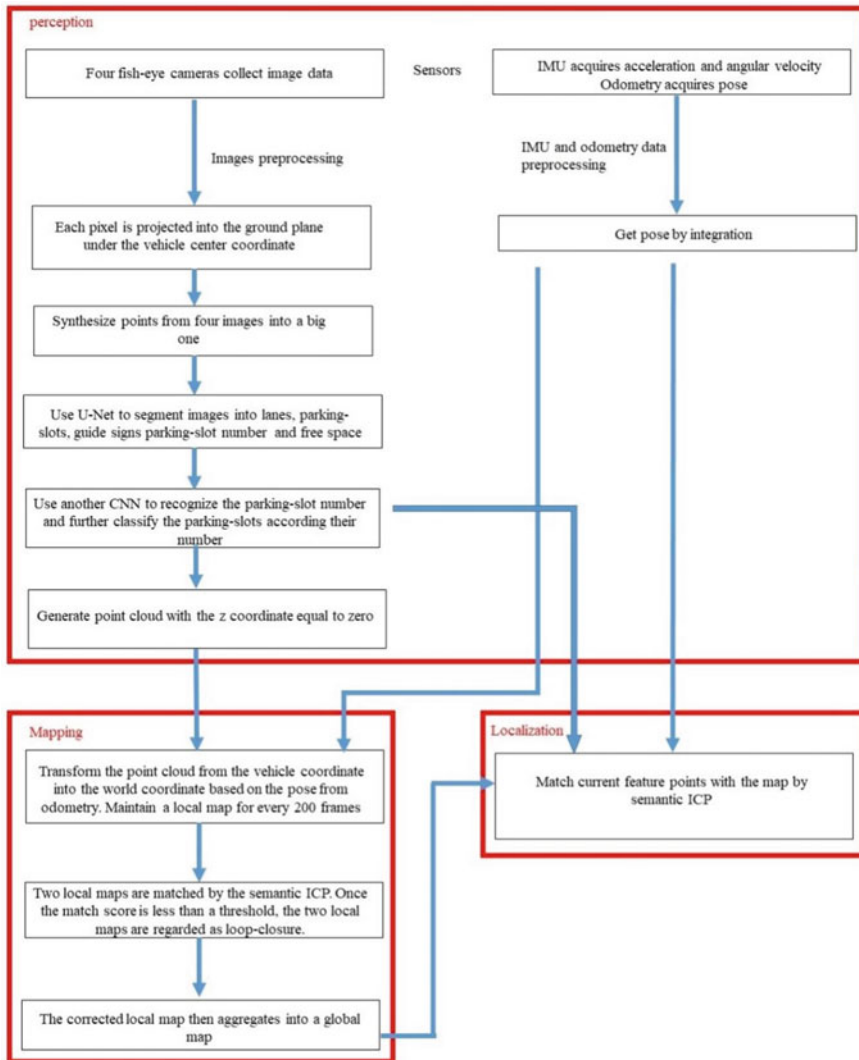
Fig. 10.1 This is the pipeline of the whole SLAM system. There are three modules in this system including perception, mapping and localization

The network architecture consists of a contracting path and an expansive path. The contracting path consists of the repeated application of two 3×3 convolutions, each followed by a rectified linear unit (ReLU) and a 2×2 max pooling operation with stride 2 for downsampling. At each downsampling step, we double the number of feature channels. Every step in the expansive path consists of an upsampling of the feature map followed by a 2×2 convolution ("up-convolution") that halves the number of feature channels, a concatenation with the correspondingly cropped

Fig. 10.2 This is a point cloud frame which is generated by feature detection with CNN for IPM and coordinate transformation through camera parameters
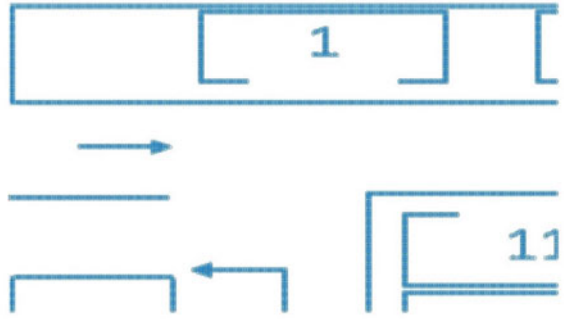
feature map from the contracting path, and two 3×3 convolutions, each followed by a ReLU. At the final layer, a 1×1 convolution is used to map each 64-component feature vector to the desired number of classes. In total, the network has 23 convolutional layers. This network classifies pixels into lanes, parking slots, guide signs on the floor, parking slot number on the floor and free space.

After semantic segmentation, we use another CNN [18] to recognize the parking slot number and further classify the parking slots according to their number, each one for a different category. The network models consist of multiple convolution layers and a fully connected layer at the end. In each convolution layer, a 2D convolution is performed, followed by a 2D batch normalization and ReLU activation. The number of channels is increased after each layer in order to account for the reduction in feature map size. Once the feature map size becomes small enough, a fully connected layer connects the feature map to the final output. A 1D batch normalization is used at the fully connected layer, while dropout is not used. We use three different networks and combine the results from these networks. The networks differ only in the kernel sizes of the convolution layers: 3×3, 5×5, and 7×7. The first network uses 10 convolution layers with $16(i + 1)$ channels in ith convolution layer. The feature map becomes 8×8 with 176 channels after the 10th layer. The second network uses 5 convolution layers with 32i channels in ith convolution layer. The feature map becomes 8×8 with 160 channels after the 5th layer. The third network uses 4 convolution layers with 48i channels in ith convolution layer. The feature map becomes 4×4 with 192 channels after the 4th layer. After detection, these feature pixels are extracted from the IPM and generate a point cloud for each IPM with the z coordinate equal to zero. The results are shown in Fig. 10.2.

10.3.4 Mapping

As shown in Fig. 10.1, the point cloud attained from feature detection will be transformed from the vehicle coordinate into the world coordinate based on the pose from odometry measurements of the IMU and wheel encoder. The equation is below,

$$\begin{bmatrix} x^w \\ y^w \\ z^w \end{bmatrix} = R_0 \begin{bmatrix} x^v \\ y^v \\ 0 \end{bmatrix} + t_0. \tag{10.1}$$

where R_0 and t_0 are separately rotation and translation from odometry, index w and v respectively represent coordinate in the world and coordinate in vehicle. Point clouds aggregate into a local map with a point cloud filter method [19]. Point clouds derived from sequential frames are accumulated to generate a local map and a voxel filter is applied to this local map to guarantee points in a voxel not too much. We maintain a local map for every 200 frames.

Since odometry drifts as time goes on, a loop detection is needed to correct the pose. For the latest local map, we compare it with other local maps. Two local maps are matched by the semantic ICP method which is described in detail in Sect. 3.6. Once the match score given by semantic ICP is less than a threshold, the two local maps are regarded as loop-closure. The pose from the odometry is updated by the constraint of the loop-closure obtained from semantic ICP. The corrected local map then aggregates into a global map with the same point cloud filter method mentioned above.

10.3.5   Localization

The pose of the vehicle is finally decided by semantic ICP correct. Moreover, the vehicle can be localized when it comes to this parking lot again based on the semantic map which has been built previously. Similar to the mapping procedure, surround-view images are synthesized into one IPM image. Semantic features are detected on the IPM image and lifted into the vehicle coordinate. Then the current pose of the vehicle is estimated by matching current feature points with the map. The estimation adopts the semantic ICP method, which is described in detail in Sect. 3.6.

10.3.6   Semantic ICP

The whole algorithm of semantic ICP is shown in Table 10.1. We refer to the work published by Parkison et al. in 2018 [20] and modify this method to gain a better performance. The main modification is that the influence of a category of points is considered only if the amount of this category of points is larger than a threshold. This operation can reduce errors caused by noisy data.

Step 1. The initial relative pose transformation T^{init}, the source point cloud χ_s, the target point cloud χ_t, and the semantic category corresponding to each point in the point cloud is used as the input of the algorithm. Generally, T^{init} is given by the pose of odometry measurement from the IMU and wheel encoder. The source point

Table 10.1 The whole algorithm procedure of semantic ICP

Require: initial transformation T^{init}, source point cloud χ_s, target point cloud χ_t, the semantic category;

$T^* = T^{init}$;

while not converged **do**:

    $T^{old} = T^*$;

    For each category **in** χ_s:

      If the amount of points of this category in $\chi_s > \alpha$:

        If there is the same category in χ_t:

          $x_k^s = T^*(x_k^s)$;

          For each x_k^s:

          Find N matches though nearest neighbor search;

            For each match:

              Join $\rho_\alpha\left(w_k\|x_k^t - T(x_k^s)\|_{C_k}^2\right)$ into loss function;

            End for

          End for

        End if

      End if

    End for

    $T^* = arg \max\limits_{T\epsilon SE(3)} \sum_{k=1}^{n\times N} \rho_\alpha\left(w_k\|x_k^t - T(x_k^s)\|_{C_k}^2\right)$;

    If $d_{SE(3)}\left(T^{old}, T^*\right) < \varepsilon$:

      Converged is true;

End while

Return T^*

cloud is the point cloud of the current frame or the current local map, the target point cloud is the stored local maps or global map. The semantic category of each point in the point cloud has been given after feature detection.

Step 2. Assign the initial relative pose transformation T^{init} to the current pose T^*.

Step 3. Store the current pose T^* in T^{old}.

Step 4. Select each semantic category in the source point cloud χ_s in turn. For each semantic category, if the number of points in the category is greater than a certain threshold α and the semantic category exists in the target point cloud χ_t, then all points of this category in the source point cloud χ_s performs coordinate transformation with current pose T^*.

Step 5. For each point of the last step, find the N nearest neighbor points through the nearest neighbor search in the target point cloud with the same semantic category.

Step 6. If the distance between searched point and source point is smaller than a threshold, then the effect of this match $\rho_\alpha\left(w_k\|x_k^t - T\left(x_k^s\right)\|_{C_k}^2\right)$ is added to the loss function. Where $\rho_\alpha(\bullet)$ is Cauchy kernel, weight w_k equals to $\frac{1}{N}$, $\|\bullet\|_{C_k}^2$ means taking the 2-norm, x_k^t and x_k^s are respectively the points in χ_t and χ_s.

Step 7. Minimize the loss function and find the new T^*.

$$T^* = \arg\max_{T \in SE(3)} \sum_{k=1}^{n \times N} \rho_\alpha \left(w_k \| x_k^t - T(x_k^s) \|_{C_k}^2 \right). \qquad (10.2)$$

Step 8. If the difference between T^* and T^{old} on the $SE(3)$ manifold is less than a certain threshold ε, then the result is deemed to convergence and the current pose T^* is output; otherwise, return to step 3.

10.4 Experimental Results

We validate our method on the simulation dataset made by ourselves. The point clouds obtained from the IPMs are recorded at 30 Hz. Wheel encoders and IMU provide odometry measurements at a frequency of 100 Hz. All the results of the experiment in this paper are taken at the average values of three times.

10.4.1 Mapping Metric Evaluation

Since this method is created to solve the problem that vision sensors cannot take full advantage of their abilities under the situation where many similar elements exist, the most important part of this method is semantic ICP based on parking-slot number recognition. For mapping metric evaluation, we compared our method called 'SICP' to other methods consisting of odometry only and traditional ICP. We also provide the ground truth to evaluate the performance of these methods.

As shown in Fig. 10.3a, a local map is built with odometry only during SLAM process. It can be seen that the map has double images marked by red. It is caused by the odometry measurements drift with errors accumulated along time development. Traditional ICP has no help in correcting the error. On the contrary, it makes things worse as exhibited in Fig. 10.3b. The main reason is that there are too many similar elements between the source and target point clouds to match correctly for traditional ICP. Miss matches lead to the map having a strange shape.

Figure 10.3c is the map built by SICP. It is clear that the map is very close to the ground truth drawn in Fig. 10.3d. It indicates that SICP helps to correct the pose given by the odometry and has a good performance during the mapping module.

10.4.2 Localization Accuracy

Besides mapping, localization accuracy is another significant index to evaluate the properties of a SLAM system. The vehicle runs around the simulated parking lot with the length 82 m and width 40 m. The results of the experiments are displayed
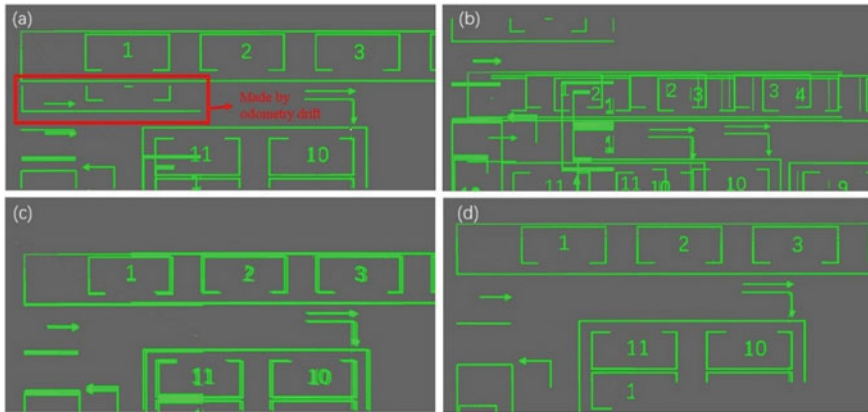
Fig. 10.3 Local maps are built by different methods consisting of **a** odometry only, **b** ICP, **c** SICP and **d** ground truth

in Fig. 10.4 with (a), (b), (c) and (d) according to odometry only, traditional ICP, SICP and the ground truth respectively. Table 10.2 gives out the values of absolute trajectory error (ATE) and percentage error of these methods.

Comparing the trajectories in Fig. 10.4a–c with d, we can find the three trajectories all deviate from the ground truth with the error being accumulated before the loop-closure is detected. Odometry only in Fig. 10.4a has no correction from a loop-closure detection so that the ATE in the end reaches 4.156 m, while ICP and SICP
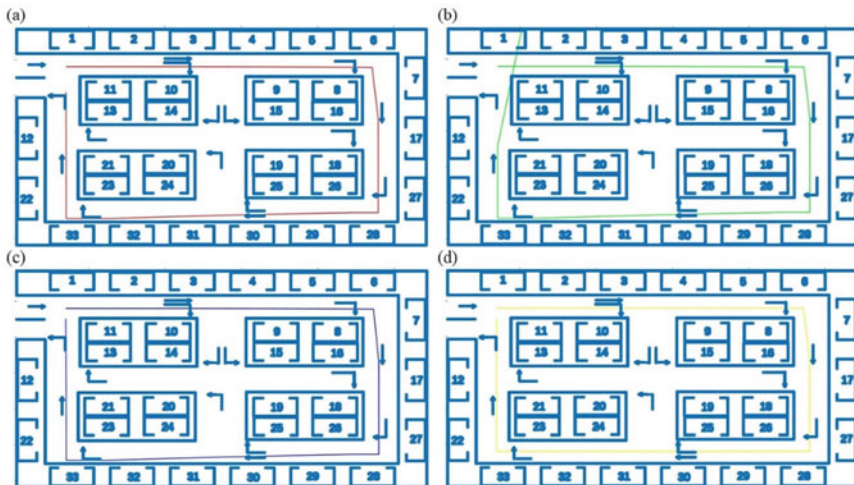
Fig. 10.4 The trajectories around the simulated parking lot are generated from different method consisting of **a** odometry only, **b** ICP, **c** SICP and **d** ground truth

Table 10.2 Values of
absolute trajectory error
(ATE) and percentage error

	ATE (m)	Percentage error (%)
Odometry only	4.156	1.7
ICP	14.135	5.79
SICP	1.221	0.5

can detect a loop-closure at the end of the trajectory separately. Although a loop-closure is detected, ICP even makes the ATE bigger reaching 14.135 m because of mismatch. It demonstrates that the traditional ICP fails under the parking lot situation where many similar elements exist. Different from traditional ICP, SICP has a good performance during correcting the accumulated error of the odometry and the ATE reduces to 1.221 m. The accuracy improves a lot than odometry only and traditional ICP. It illustrates that SICP based on parking-slot number recognition can improve the localization accuracy in a parking lot while traditional ICP cannot do the same task as well.

10.5 Conclusion

This paper puts forward a semantic SLAM based on parking-slot number for autonomous valet parking. It takes the signals acquired from the vehicle-mounted four fish-eye cameras, IMU and wheel encoder as input data. Raw data are processed by preprocessing module to get the odometry measurements and point clouds, the points of which are classified by parking-slot number. Then point clouds and odometry measurements are sent to mapping and localization modules. Point clouds are accumulated to generate a local map and further a global map through the poses from the odometry and the corrected poses from loop-closure performed by semantic ICP. Experiments are conducted on our simulation dataset. And the results demonstrate this method has a good performance on mapping and localization. Moreover, the semantic ICP can improve the accuracy better than traditional ICP under the situation where many similar elements exist.

References

1. Tang, F., Gao, F., Wang, Z.: Driving capability-based transition strategy for cooperative driving: from manual to automatic. IEEE Access **8**, 139013–139022 (2020). https://doi.org/10.1109/ACCESS.2020.3012671

2. Hsu, T.H., Liu, J.F., Yu, P.-N., Lee, W.S., Hsu, J.S.: Development of an automatic parking system for vehicle. In: IEEE Vehicle Power and Propulsion Conference, pp. 1–6. IEEE (Nov. 2008)

3. Grimmett, H., Buerki, M., Paz, L., Pinies, P., Furgale, P., Posner, I., Newman, P.: Integrating metric and semantic maps for vision-only automated parking. In: IEEE International Conference on Robotics and Automation (ICRA), pp. 2159–2166. IEEE (May 2015)

4. Schwesinger, U., Bürki, M., Timpner, J., Rottmann, S., Wolf, L., Paz, L.M., Grimmett, H., Posner, I., Newman, P., Häne, C.: Automated valet parking and charging for e-mobility. In: IEEE Intelligent Vehicles Symposium (IV), pp. 157–164. IEEE (Aug. 2016)

5. Hu, J., Yang, M., Xu, H., He, Y., Wang, C.: Mapping and localization using semantic road marking with centimeter-level accuracy in indoor parking lots. In: IEEE Intelligent Transportation Systems Conference (ITSC), pp. 4068–4073. IEEE (Oct. 2019)

6. Qin, T., Chen, T., Chen, Y., Su, Q.: Avp-slam: Semantic visual mapping and localization for autonomous vehicles in the parking lot. In: IEEE/RSJ International Conference on Intelligent Robots and Systems (IROS), pp. 5939–5945. IEEE (Jul. 2020)

7. Shao, X., Zhang, L., Zhang, T., Shen, Y., Li, H., Zhou, Y.: A tightly-coupled semantic SLAM system with visual, inertial and surround-view sensors for autonomous indoor parking. In: Proceedings of the 28th ACM International Conference on Multimedia, pp. 2691–2699 (Oct. 2020)

8. Fang, Z., Chen, Y., Zhou, M., Lu, C., Rottmann, N., Bruder, R., Xue, H., Schweikard, A., Rueckert, E., Nabati, R.: Marker-based mapping and localization for autonomous valet parking. In: IEEE/RSJ International Conference on Intelligent Robots and Systems WS (IROSWS) (Oct. 2020)

9. Xiang, Z., Bao, A., Su, J.: Hybrid bird's-eye edge based semantic visual SLAM for automated valet parking. In: IEEE International Conference on Robotics and Automation (ICRA), pp. 11546–11552. IEEE (2021)

10. Tripathi, N., Yogamani, S.: Trained Trajectory based Automated Parking System using Visual SLAM on Surround View Cameras (Jan. 2020). arXiv:2001.02161

11. Forster, C., Carlone, L., Dellaert, F., Scaramuzza, D.: On-manifold preintegration for real-time visual–inertial odometry. IEEE Trans. Robot. **33**(1), 1–21 (2016). https://doi.org/10.1109/TRO.2016.2597321

12. Zunaidi, I., Kato, N., Nomura, Y., Matsui, H.: Positioning system for 4-wheel mobile robot: encoder, gyro and accelerometer data fusion with error model method. CMU. Journal **5**(1), 1 (2013). https://doi.org/10.1007/978-3-642-39244-3_14

13. Long, J., Shelhamer, E., Darrell, T.: Fully convolutional networks for semantic segmentation. In: Proceedings of the IEEE Conference on Computer Vision and Pattern Recognition, pp. 3431–3440 (2015). https://doi.org/10.1109/cvpr.2015.7298965

14. Badrinarayanan, V., Kendall, A., Cipolla, R.: Segnet: A deep convolutional encoder-decoder architecture for image segmentation. IEEE Trans. Pattern Anal. Mach. Intell. **39**(12), 2481–2495 (2017). https://doi.org/10.1109/TPAMI.2016.2644615

15. Zhao, H., Shi, J., Qi, X., Wang, X., Jia, J.: Pyramid scene parsing network. In: Proceedings of the IEEE Conference on Computer Vision and Pattern Recognition, pp. 2881–2890 (Dec. 2016)

16. Chen, L.C., Papandreou, G., Kokkinos, I., Murphy, K., Yuille, A.L.: Semantic image segmentation with deep convolutional nets and fully connected CRFs. (Jun. 2016). arXiv:1412.7062

17. Ronneberger, O., Fischer, P., Brox, T.: U-net: convolutional networks for biomedical image segmentation. In: International Conference on Medical Image Computing and Computer-Assisted Intervention, pp. 234–241. Springer (2015). https://doi.org/10.1007/978-3-319-24574-4_28

18. An, S., Lee, M., Park, S., Yang, H., So, J.: An ensemble of simple convolutional neural network models for MNIST digit recognition (2020). arXiv:2008.10400, https://doi.org/10.48550/arXiv.2008.10400

19. Han, X.F., Jin, J.S., Wang, M.J., Jiang, W., Gao, L., Xiao, L.: A review of algorithms for filtering the 3D point cloud. Signal Process.: Image Commun. **57**, 103–112 (2017). https://doi.org/10.1016/j.image.2017.05.009
20. Parkison, S.A., Gan, L., Jadidi, M.G., Eustice, R.M.: Semantic Iterative Closest Point through Expectation-Maximization. BMVC, p. 280 (2018)

Chapter 11
Review of the Security Risks and Practical Concerns with Current and Future (6G) Communications Technology

Parvinder Singh, Pardeep Kumar, and Audithan Sivaraman

Abstract Gradually, the 6th Generation cellular network standard is being adopted (6G). Due to the creative and distinctive features of 6G, such as the capacity to deliver connection even in space and underwater, governments, corporations, and academics are investing a substantial amount of time, money, and effort in this subject. The next generation technology will be effective around the year 2030–2035. The next generation will be able to provide strong connectivity between machines and mobile devices. The speed can reach 1 Gbps in the downlink and 500 Mbps in the uplink. Edge computing, blockchain, advanced IoT and Li-Fi (Light Fidelity) technologies, as well as Artificial Intelligence (AI), are believed to provide the foundation for forthcoming innovations. Further research into the fundamental architecture of 6G is necessary to pinpoint these areas for development. We have examined a variety of concerns that might arise while employing next generation communication technologies, such as security and practical concerns. All of the physical layer's facts, which are crucial for implementation, were taken into account during the study. The conclusion of the study includes all the pertinent information and arguments that researchers might take into account while they work on next generation communication technologies.

11.1 Introduction

6G or Next Generation (nG) is the successor of the 5th generation (5G) communication technology. NG will definitely use higher frequency bands to provide higher speeds than 5th generation communication systems. Speed is inversely proportional

P. Singh (✉) · P. Kumar
Department of CSE, DCRUST, Murthal, India
e-mail: parvindersingh.cse@dcrustm.org

A. Sivaraman
Department of IT, NSUT, New Delhi, India
e-mail: audithan.sivaraman@nsut.ac.in

to latency, so as speed improves latency will decrease. The researchers hypothesize that nG will support a microsecond latency communication which is much lower than that of 5th generation cellular networks. Which is 1000 times faster than a ms throughput or we can say it is 1/1000th latency of a μs throughput [1]. The next generation will provide hyper-connectivity between machines and mobile devices. NG speeds can reach 1 Tbps in the downlink (according to Dr. Mahayar Shirvani-moghaddam, Senior Lecturer at the University of Sydney) and around 100 Gbps in the uplink. Moreover, it is observed that in the next generation mobile and communication technologies will reach the level that the earlier generations could not reach. The next generation is being seen as the basis for edge computing, advanced IoT, and Li-Fi (Light Fidelity) technologies. Therefore, nowadays many futuristic vendors are investing in NG wireless standards and specifications such as 6G will be a network that will be around for years.

This paper is divided into 5 sections:

Section 11.2: Evolution of mobile cellular networks.

Section 11.3: Benefits of nG over 5G.

Section 11.4: The security issues perceived in 1G–5G.

Section 11.5: Vision for nG Architecture and Challenges while implementing next generation.

Section 11.6: Challenges while implementing next generation technology.
Here we are moving forward toward Sect. 11.1.

11.2   Evolution of Mobile Cellular Networks

We have improved the wireless communication system and expanded its capabilities to make it more powerful and robust. We have all experienced several generations.
Let's discuss each one separately [1–4].

11.2.1   0th Generation

- The pre-cell phones were the radio cell phones that were being used in vehicles before the arrival of mobile cell phones.
- Communication was limited to voice only.
- These cell phones were typically placed in vehicles.

11.2.2   1st Generation

- Calling facility was introduced in this generation.
- Analog signals were used for the communication.
- The Frequency Division Duplexing (FDD) was used for the channel allocation.
- Each channel was of 25 MHz.
- It only provided spotty coverage.
- There is no support for roaming between operators.
- Audio quality was not good.
- Speedy: 2.4 kbps.

11.2.3   2nd Generation

- Transitioning from analog to digital signals.
- SMS and voice both were supported.
- Support for the: Mobile Data, PCS, Wireless LAN, and Digital Cellular segments.
- The 2G WLAN provided a significant data rate and broad coverage.
- The rate is 64 kbps.

11.2.4   2.5th Generation

- 2.5G followed 2G, which made use of the GPRS concept.
- Furthermore, mail and streaming services were introduced.

11.2.5   2.75th Generation

- The 2.5G was replaced by 2.75G, also referred to as EDGE, which provided services more swiftly.
- Internet speeds of up to 128 kbps were offered, and an edge connection was also used.

11.2.6   3rd Generation

- The infrastructure of the Internet was improved.
- Better system and capability.
- Provides quick Wi-Fi internet.
- It was connected using WCMA and UMTS.
- The data rate was 2 Mbps.

11.2.7   4th Generation

- Based upon the IP protocol.
- LTE (Long-term evaluation), mainly focused on the internet. [Application-based mobile system]
- Vo-LTE, often known as voice over LTE, is used for both internet and voice.
- Any desired service may be selected with freedom and flexibility, and with an appropriate QoS.
- Higher usability.
- Affordable multimedia service with transmission capabilities.
- Streaming in HD resolution.
- Speed: -100 Mbps.

11.2.8   5th Generation (Moving Generation)

This generation has already started coming into existence in many countries, and it will soon do so in many more countries. Here are some important details about this generation [3, 5].

- Higher data rates as compared to 4G (4th Generation).
- Significantly lower data latency will result in faster and more secure connectivity.
- Enormous network capacity.
- It is 30 times faster than 4G.
- The flexibility of the network would rise.

11.3   Benefits of 6G (nG) Over 5th Generation Cellular Networks

11.3.1   Use of Different Spectrum

As we know that each generation of cellular communication networks uses a different spectrum which is increasing with respect to generations. So, we can say that the 5G network is working on 6–24 GHz frequency band then nG communication systems will have a spectrum from 95 GHz to 3 Thz. This will surely increase the diversity of the network in many aspects [3, 6, 7].

11.3.2 Faster Than 5G Technology

As discussed earlier, 6G (nG) will operate over a much larger frequency band, so it will provide data rates of 1 terabit per second in the downlink (theoretically) and latency between 1 ms and 1 μs. The speed of the next generation will be 100 times faster than 5G [3, 6, 8].

11.3.3 IoT Booming After 5G

IoT is an emerging field nowadays. IoT (Internet of Things) was launched in the era of fourth-generation communication technologies, but due to some constraints, a large number of devices were not supported by 4G (compared to 5G), the existence of IPv4 (Internet Protocol version 4) due to which large number of global IPs were not available. But as 5G is launched in conjunction with IPv6, IoT is going to become more popular with the birth of 5G. Now we are trying to move on to another generation (6G) which will be 100 times better than 5G so it will definitely accelerate the popularity of IoT [3, 6, 8].

11.3.4 Low Latency/Delay

The time taken by an information packet to be transmitted over a single frequency channel is called latency or delay. It was observed that the latency of the 5th generation was around 50 ms which was 10 times less than the 4th generation networks. As per the study, 6G (nG) is giving latency between 1 ms and 1 μs which is 5 times less than the 5th generation communication network, which means that nG will provide a better data rate per second than 5G [3, 6, 8].

11.4 Security Issues Perceived During 1st to 5th Generations

11.4.1 1G

The first generation was introduced in the 1980s. This generation offered telephonic communication services for the first time. This generation was entirely based on analog signals. Many issues were observed during the first generation, such as semi-reliable, hands-off issues, data security, etc. The main issue was security in fact this generation transferred data in a non-encrypted form so data was insecure during transmission. Therefore, users were not sure about data privacy and administrators

Table 11.1 Security issues in mobile communication generations

Security issues in mobile communication generations				
1G	2G	3G	4G	5G
Data Transfer was in Plain Text (**No Encryption**)	One Way Authentication was there. **Base Station to UE**	IP Vulnerabilities and OA Attacks	New device threats, MAC Layer Issues, and OA Attacks	Cloud Threats

did not feel secure about the network. The data can be accessed by intruders and unauthorized users [9–11].

11.4.2 2G

The second generation saw a transition from analog to digital communication. This generation was based on Time Division Multiple Access (TDMA) which provides voice data transmission and a short message service (SMS) facility. This generation is often referred to as GSM which provides all the services like authentication, and data privacy for both the users and the network. Network providers check the authenticity of users with the help of a random challenge and response approach. Data encryption has also been introduced in this generation. The SIM (Subscriber Identity Module) encrypts the data with the keys and transfers the data over the channel. Sadly, after the security improvements in the first generation, the second generation also lacks one-way authentication. It means the network can authenticate users by this one-way authentication but the user was not able to authenticate to the network. Therefore, base stations can act as legitimate members to steal users' private data and information. This was a huge threat in the second generation [9–11] (see Table 11.1).

11.4.3 3G

The third-generation communication system was introduced in 2000 capable of providing data rates up to 2 Mbps. Such speeds were not achieved by previous generations. This generation enabled advanced services like video streaming, high-speed internet access, and IP calls which were not possible in previous generations. This generation addressed many of the security weaknesses of the second generation. Here Two-way authentication was introduced which provides the ability for authentication between the user and the network or vice versa. Another authentication was also introduced in this generation known as Authentication and Key Agreement with open-air security which protects the data while traveling through radio waves in the open air. The third-generation was the release of the third-generation partnership project which gives this generation additional capabilities such as secure tracing, user tracking, and

user identification. Internet Protocol (IP) vulnerabilities, end-to-end communication wireless attacks such as integrity attacks, unauthorized access, denial of service, etc. are considered threats in third-generation communication systems [9–11].

11.4.4   4G

The fourth-generation was introduced in release 5 of 3GPP. 4G was launched under the name LTE (Long-Term Evolution) which emphasizes internet service and Vo-LTE (Voice over Long-Term Evolution) which emphasizes internet as well as voice communication. 4G was providing asynchronous data rates in both downlink (1 Gbps) and uplink (500 Mbps). OFDMA (Orthogonal Frequency Division Multiple Access) and SC-FDMA (Single Channel Frequency Division Multiple Access) were implemented for downlink and uplink, respectively. 4G provides a latency of 1 ms so it was able to handle all complex applications like high-definition TV broadcasts and high-definition video broadcasts. The threats observed in this generation are related to wireless radio communication such as data tampering, data theft, data modification, denial of service (DoS), and unauthorized access. Hence, the large number of user participation in the network makes it more vulnerable to security than older generations. Medium Access Control (MAC) layer vulnerabilities are also there [9–11].

11.4.5   5G

The 5th generation communication technology was introduced in 2020. 5G has been launched in some countries and telecommunication companies are planning to launch 5G in other countries soon. The 5G is launched with 3 different applications:

1. eMBB (enhanced Mobile Broadband).
2. URLLC (Ultra-reliable low latency communication.
3. MTC (Machine Type Communication).

The 5G provides 1 Tbps speed in downlink (theoretically) and 1 Gbps speed in uplink (theoretically).

As 5th generation is able to connect a large number of devices with good quality of service index across the network. Security and privacy issues can be identified by examining the network architecture. There are 3 parts to 5G network architecture, namely access network, backhaul network, and core network. Each network and its devices have different security and privacy issues. For example, the handover process between different networks or different devices can lead to privacy issues or attacks. The backhaul network is sandwiched between the access network and the core network, and the backhaul's connectivity with both is via microwave, wireless channels, and satellite links. Because the backhaul network has the least security

issues as compared to the other two. Security issues are delivered to the core network by moving backhaul sensors i.e., 2022, 22, etc. to the data plane using SDN and NFV technologies. Enhanced mobile broadband applications provide higher data rates as well as various security and privacy concerns.

To overcome these problems, 2 mechanisms have been developed so far. The first mechanism provides data communication between devices using basic authentication and key management technology. On the other hand, the second mechanism uses a protocol to group the devices with the help of the AKA-based Grouping Protocol. 5G deals with a large number of devices as it uses MIMO extensively. These multiple input and output streams also lead to a lot of privacy and security concerns. Additionally, the nature of 5G networks is an open architecture so the network as well as private information about users may be accessible to intruders or attackers. Therefore, these addressed security issues must be resolved to make it a more secure network in the future. The following Figs. 11.1 and 11.2 show the architecture and security issues of the 1st to 6th/next generation of 5G respectively [3, 9–11].
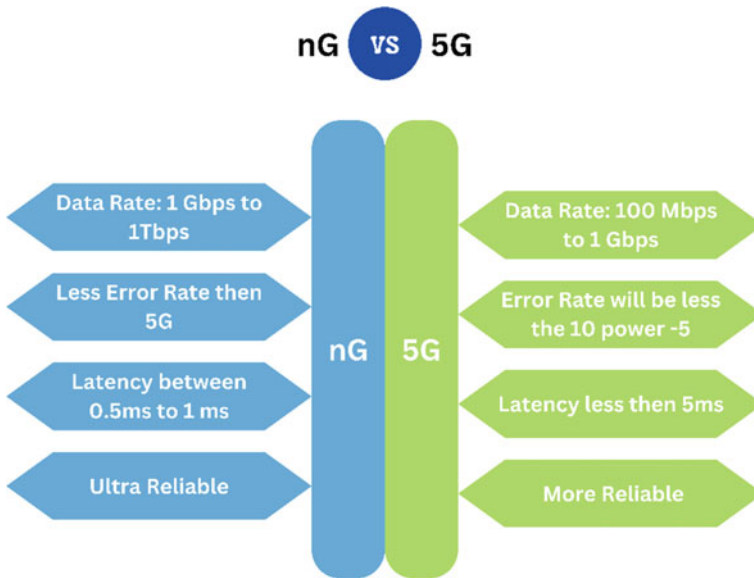
Fig. 11.1 Comparison among features of nG and 5G
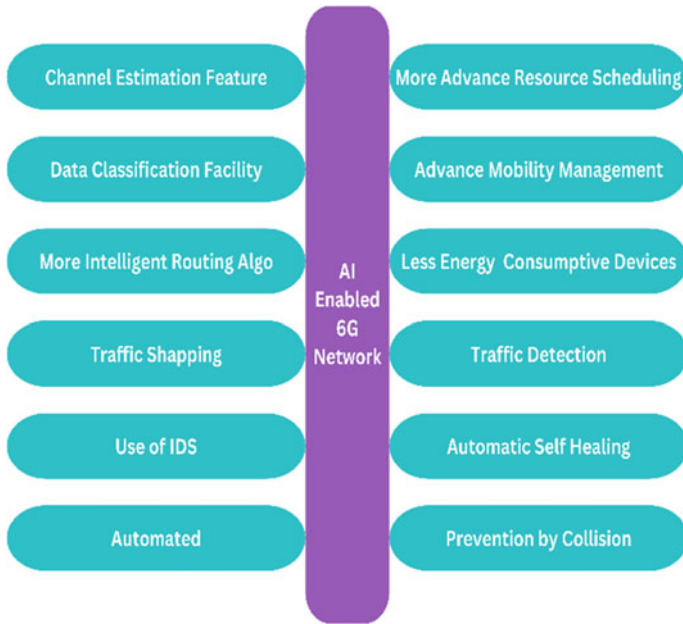
Fig. 11.2 AI-based network benefits

11.5 Vision for nG Architecture and Challenges While Implementing Next Generation

Figure 11.3 shows the detailed architecture of 5th generation communication networks. There are 6 core modules namely AMF, SMF, UFP, UDM, PCF, and Data Network which play a complete role in providing 5G Internet/Cellular connectivity to the users. The 6th generation (NG) architecture, on the other hand, will look like this: There's no doubt that we'll be seeing much faster speeds and higher-power signals that will entice customers of NG services. But what will be the architecture of ng and modules that will cover the whole realistic and robust future network? NG connectivity, power, and speed will serve as the backbone for the further development of networks and technologies that were predicted earlier. Certainly, the successor always overcomes the shortcomings of the predecessor, so NG will overcome the shortcomings of the existing networks in terms of network connectivity, better infrastructure, stronger connectivity, massive data rates, lower latency, and much more. Advanced IoT, Li-Fi, advanced AI, and edge computing will take advantage of the fast speed of NG to coordinate with complex systems and powerful connectivity [12].
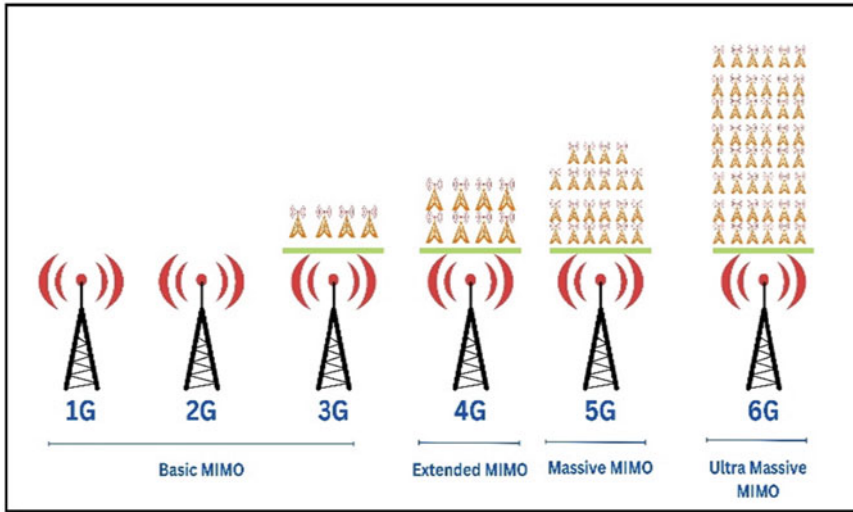
. 11.3 Use of ultra massive MIMO

11.6 Challenges While Implementing Next Generation Technology

- Possibility of pure coverage.
- High-frequency range communication.
- AI-based network.
- Pure use of frequency bands.
- Security of the data and network.
- Flexible Network and Self-healing capability.
- Energy Saving Networks.
- Moving toward the possibility of certainty.
- Transparency (Openness) and Customizable.

11.6.1 Possibility of Pure Coverage

Mobile phones have made our lives very easy as we can talk to anyone at any time and can access the internet facility. But in this era, around 3 billion people are not able to avail the communication services. This is because of the non-deployment of the base stations/service providers in the remote area due to many hurdles like cost, unreachability, geographic conditions, etc. The next generation can work on space-earth integration. That integration can provide satellite internet and a communication system through which the remote and distinct areas can have access to the communication system [11, 13, 14].

11.6.2   High-Frequency Range Communication

As we know the next generation (6G) will work on the Tera Hertz frequency. Which may cover from 95 GHz to 3 THz. If it uses this frequency, it means the nG will exploit with no limitations. But the use of higher frequency will lead to some issues like [11, 13, 14]:

- Less coverage distance.
- Very high cost of deployment.
- Premature ecosystem of terminals.
- Environmental issues.
- Less penetration power.

11.6.3   AI-Based Network

Nowadays Artificial Intelligence has already been applied in many sectors of the industries like Image detection, voice recognition, and other types of automation. With the development of the advanced network low latency, high data rates, stability, and reliability are very important factors. We are working to achieve these factors but in a large network, the satisfaction of these factors is a very tedious task. So, our researchers are working on the improvement of these factors by implementing AI to automate the network and to provide robust and powerful network services [11, 13–15].

To overcome these leading issues all the telecommunication researchers and companies have to work together.

11.6.4   Pure Use of Frequency Spectrum

The communication technology is based upon the Spectrum. So, the sharing of the dynamic spectrum is being studied for the next generation like many different sectors namely AI, Blockchain and other applications will use the spectrum. Now the allocation unit has to emphasize each and every factor while distributing the spectrum for every type of application. That will provide a stable and robust nG network. The Massive MIMO was used in the 5G era but an ultra-massive MIMO technique must be used to provide a fair use of spectrum and user satisfaction [11, 13, 14, 16].

11.6.5 Security of the Data and Network

The digital network is playing a very important role in this era. But when we are moving forward with digitization the factor of security must be considered. The benefits of 5G nowadays include low latency, outstanding dependability, large bandwidth, and especially network security. In the next generation networks, the PQC (Post-quantum Cryptography), QKD (Quantum Key Distribution), and other techniques are being implemented to provide a better and more secure network [11, 13, 14].

11.6.6 Flexible Network and Self-healing Capability

The network must be intelligent enough to provide a resilient and self-healing capability. Because these facts are too specific to be obtained without any automatic network. The network should be automated which will calculate all the necessary things through which it can decide whether the users are experiencing the fair facility of the network or not. If a problem occurs in the network, the network should be intelligent enough to detect the problem and fix the problem automatically. This can be achieved by implementing AI in the network (as discussed earlier) [11, 13, 14].

11.6.7 Energy Saving Networks

Nowadays there is a drastic increase in the number of users in the network (human beings and machines (IoT)). To satisfy the needs of each and every user the deployment of the base stations is also increasing. As the number of users are increasing the system resource consumption is also increasing in parallel. Therefore, the devices must be less energy consumptive which will help us to save our precious resources and to save our ecosystem as well [11, 13, 14].

11.6.8 Moving Toward Possibility of Certainty

The services provided by mobile internet in the past were fraught with ambiguities and instability. In the 4G era, these services may easily satisfy customers. After all, a small amount of packet loss and network latency won't prevent users from watching movies and making purchases online. However, the delivery of low latency and high dependability is required for the spread of the 5G and 6G networks across all sectors and device types. In order to deliver end-to-end network service capabilities, the concept of slicing and MEC is associated with 5G. Network services are expected

to be more dependable and better equipped to adapt to a range of scenarios across a wide range of enterprises in the 6G era [11, 13, 14].

11.6.9 Transparency (Openness) and Customizability

We all know about the two internet pillars—sharing and transparency—help it to develop. As we enter the 5G era, mobile networks should actively motivate the combination of Communication Technology and Information Technology. This will make it possible for numerous industries to join the digital revolution. The pillars of transparency and customizability will grow in the next generation by providing flexible and responsive services with a good interface which will help the industries to adapt the networks and customized applications [11, 13, 14].

11.7 Conclusion

In this paper, we have studied real life and all the challenges related to network security through various resources. These challenges are very effective for next generation technologies. Therefore, the researchers have to emphasize these challenges to build a reliable, scalable, robust, flexible, secure, automated, and effective network.

References

1. Gawas, A.: An overview on evolution of mobile wireless communication networks: 1G–6G. Int. J. Recent. Innov. Trends Comput. Commun. **3**(5), 3130–3133 (2015)
2. Garg, K., Mishra, A.: 5G Network Advanced techniques: a literature review. Int. J. Eng. Tech. Res. (IJETR) (2018)
3. Kumar, A., Gupta, M.: A review on activities of fifth generation mobile communication system. Alex. Eng. J. (Elsevier) (2017)
4. Hakeem, S., Hussein, H., Kim, H: Security requirements and challenges of 6G technologies and applications. Sensors (2022)
5. Femenias, G., Riera-Palou, F., Mestre, A., Olmos, J.: Downlink scheduling and resource allocation for 5G MIMO-multicarrier: OFDM vs FBMC/OQAM. IEEE Access (2017)
6. de Alwis, C., Kalla, A., Pham, Q.V., Kumar, P., Dev, K., Hwang, W.J., Liyanage, M.: Survey on 6G frontiers: trends, applications, requirements, technologies and future research. IEEE Open J. Commun. Soc., 1–1 (2021)
7. https://www.rantcell.com/how-is-6g-mobile-network-different-from-5g.html. Accessed 18 Mar. 2023
8. https://www.techtarget.com/searchnetworking/definition/6G. Accessed 15 Mar. 2023
9. Nawaz. F., Ibrahim, J., Junaid, M., Kousar, S., Parveen, T., Ali, M.: A review of vision and challenges of 6g technology. Int. J. Adv. Comput. Sci. Appl. 11, 643–649 (2020)
10. Gui, G., Liu, M., Tang, F., Kato, N., Adachi, F.: 6G: opening newhorizons for integration of comfort, security and intelligence. IEEE Wirel. Commun. (2020)

11. Wang, M., Zhu, T., Zhang, T., Zhang, J., Yu, S., Zhou, W.: Security and privacy in 6G networks: new areas and new challenges. Digit. Commun. Netw. **6**(3), 281–291 (2020)
12. A White Paper on 5G Architecture. 5GPPP Architecture Working Group, Version-2, pp. 1–140 (2017)
13. Porambage, P., Gur. G., Osorio, D., Liyanage, M., Ylianttila, M: 6G Security Challenges and Potential Solutions, Proceeding 2021 Joint European Conference on Networks and Communications (EuCNC) & 6G Summit (2021)
14. https://www.iplook.com/info/top-10-challenges-for-6g-i00096i1.html. Accessed 24 Mar. 2023
15. Ismail, L., Buyya, R.: Artificial intelligence applications and self-learning 6G networks for smart cities digital ecosystems: taxonomy, challenges, and future directions. Sensors, 1–30 (2022)
16. https://www.ni.com/en-in/shop/wireless-design-test/what-is-the-mimo-prototyping-system/5g-massive-mimo-testbed--from-theory-to-reality--.html. Accessed 01 Apr. 2023
17. ENISA: Artificial intelligence cyber security challenges. ENISA, Technical Report (Dec. 2020)
18. OFDM: httpsmorse.colorado.edu~tlen5510textclasswebch8.html. Accessed 12 Mar. 2023

Chapter 12
Effect of Rehabilitation Robot Training on Cognitive Function in Stroke Patients: A Systematic Review and Meta-analysis

Wenzhan Xie, Jiaqian Yan, Mingxun Zhang, and Yihan Chen

Abstract Objective: Post-stroke cognitive impairment is one of the major dysfunctions after stroke, which can lead to a variety of negative health outcomes. This study aims to evaluate the effects of rehabilitation robotic therapy in post-stroke cognitive impairment patients. Methods: As of December 2022, PubMed, Embase, Web of Science, Cochrane Library, and China National Knowledge Infrastructure were searched through electronic databases. Eligibility criteria RCTs evaluate RCTs of rehabilitation robots on treatment events in patients with cognitive impairment after stroke, compared to control groups. Results: Eight studies were included (n = 431). When combined with routine cognitive training efficacy, rehabilitation robot intervention observably reduced MOCA scores, MBI scores, and FMA scores. Furthermore, the FIM scores and MMSE scores were also better than the control groups. Rehabilitation robot training can improve the cognitive function of stroke patients and is an effective means of stroke rehabilitation.

W. Xie (✉) · J. Yan · Y. Chen
School of Rehabilitation Medicine, Shandong University of Traditional Chinese Medicine, Jinan, China
e-mail: z577741395@163.com

J. Yan
e-mail: 19859026699@163.com

Y. Chen
e-mail: 13676371605@163.com

M. Zhang
College of Chinese Medicine, Shandong University of Traditional Chinese Medicine, Jinan, China
e-mail: zmx181080@163.com

159

12.1 Introduction

Post-stroke cognitive impairment is a clinical syndrome characterized by cognitive impairment that occurs after stroke and lasts for 3–6 months. It is one of the major functional disorders after stroke. Statistically, three quarters of stroke survivors show cognitive impairment, with an incidence of up to 80% [1]. Cognitive dysfunction includes executive force, memory, visual-spatial, and emotional defects associated with depressive/anxiety issues. Post-stroke cognitive impairment makes patients unable to well cooperate with rehabilitation training, hinders the progress of functional recovery, affects the ability of daily life activities, reduces the living quality and survival time of patients, significantly adds the pressure of family and social and economic burden of, and has a negative impact on rehabilitation strategies.

Traditional rehabilitation therapy only carries out routine cognitive training, which consumes a considerable amount of manpower and material resources, and the training process is relatively simple and lacks interest. It relies on the skills and professional knowledge of therapists, and has few active participation of patients, which makes the effect of rehabilitation training not ideal. Currently, increasing evidence highlights the possible impact of robotic rehabilitation on functional recovery in neurology patients. At present, the rehabilitation robot has been gradually applied in clinical rehabilitation, studies have shown that rehabilitation robots can combine task orientation and virtual reality technology, with high intensity, high repetition, and rich environment stimulation characteristics, and can provide personalized auxiliary support, to ensure that the patients in the right way to complete the task needed to keep power, is an important supplement of cognitive rehabilitation training. Previous meta-analysis studies have involved only rehabilitation robots being useful in improving motor function and daily living ability, but no clear study suggests its role in enhancing cognitive skills. Therefore, we strictly included the experiment by standardized screening and demonstrated the conclusion by comparing the scores of five aspects. This article aimed to assess the impact of rehabilitation robot therapy in post-stroke cognitive impairment patients by meta-analysis.

12.2 Methods

In accordance with the comments contained in the Cochrane Interventions System Review Manual, we performed detailed operational definition instructions before starting the search [2], as shown in Fig. 12.1.

Study	Participant characteristics (N, diagnosis, average age, % male)	Setting	Intervention initiation (post-stroke cognitive impairment)	Intervention and control description	Frequency and duration	Outcome measures
SU Lili et al CHINA	n=65 (33 intervention) subacute stroke with cognitive impairment Age range 60-71 years Male 46.7%	Wenzhou Medical University, the First Affiliated Hospital	3weeks-6weeks	Intervention:Upper limb rehabilitation robot training Control:routine cognitive training	Frequency: 1×per day Session length:20 min Duration: 4weeks	Baseline and at 4weeks: • MOCA • MMSE • FMA-UE • MBI
Zhao Defu et al CHINA	n=59 (39 intervention) mild to moderate cognitive impairment after stroke Age range 40-87 years Male 49.2%	unclear	unclear	Intervention:rTMS therapy and upper limb robot virtual scenario training Control:conventional cognitive training and therapy	Frequency: 1×per day Session length:20 min Duration: 20days	Baseline and at 6weeks: • MOCA • MBI
Alfredo Manuli et al Italy	n=60 (30 intervention) mild to moderate cognitive impairment after stroke Age range 32-55 years Male 55.6%	unclear	>6 months	Intervention: Robotic Rehabilitation Control: conventional physical and cognitive therapy	Frequency: 5×per week Session length: 60 min Duration: 8weeks	Baseline and at 16weeks: • FAB BDI FIM COGN MOT TOT MOCA TOT MH TMT VS WEIGL
Irene Aprile et al Italy	n=100 (51intervention) post-stroke anxiety neurosis Age range 35-85 years Male unclear	unclear	>6months	Intervention:three robots (Motore, Amadeo, and Diego) and one sensor-based device(Pablo) Control: routine cognitive training	Frequency: 5×per week Session length: 45 min Duration:6 weeks	Baseline and at 4weeks: • several cognitive tests • Fugl-Meyer • Motricity • Index MBI
Sahel Taravati et al Italy	n=37 (17intervention) Stroke hemiplegia Age range 33-68 years Male 75.7 %	unclear	4-30months	Intervention: robotic rehabilitation Control: conventional rehabilitation	Frequency: 5×per week Session length: 30-45 min Duration: 4weeks	Baseline and at 8weeks: • MAS • FIM • NEADL • FMA • SS-QOL• MoCA • CES-D
Gi-Wook KIM et al Korea	n=30(15 intervention) chronic stroke patients with hemi plegia Age range 20-85 years Male73.3 %	Department of Rehabilitation Medicine of Chonbuk University Hospital	>6months	Intervention:performed upper extremity training with the Neuro-X® Control:conventional rehabilitation	Frequency:3×per week Session length: 40 min Duration:6 weeks	Baseline and at 4weeks: • FMA • HFT • MAS • K-MMSE
Derya Zengin Metli et al Turkey	n=35 (20 intervention) Stroke patients Age range 51-67 years Male 60%	Ankara Physical Medicine and Rehabilitation Training and Research Hospital	6 - 24 weeks	Intervention: robotic rehabilitation Control:conventional rehabilitation program	Frequency:3×per week Session length:30 min Duration:5 weeks	Baseline and at weeks: • MMT • MI • FMA • FIM • SF-36
SU Lili et al CHINA	n= 60(30intervention) Stroke and hemiplegia were complicated with cognitive dysfunction Age range 61-70 years Male 46.7%	Department of Rehabilitation Medicine, the First Affiliated Hospital of Wenzhou Medical University	unclear	Intervention:Virtual scene task-oriented training of the upper limb robot Control:routine cognitive training	Frequency: 5×per week Session length:40 min Duration: 4weeks	Baseline and at 4weeks: • MOCA • MMSE • MBI

Fig. 12.1 Summary characteristics of studies

12.2.1 Selection Criteria

We included studies evaluating adults (>18 years old) with mild to moderate cognitive impairment after stroke (ischemic or hemorrhagic) according to the WHO definition. Randomized controlled trials involving only evaluating the outcome of rehabilitation robotic interventions and compared with conventional cognitive training and routine rehabilitation training interventions. Different experiments adopt different rehabilitation training systems, but all of them can combine task orientation with virtual reality technology, have the characteristics of high intensity, high repetition, and rich environmental stimulation, and can achieve the purpose of training patients' cognitive function. Only studies reporting the MBI, MoCA, FMA, FIM, and MMSE were included.

12.2.2 Search Strategy

As of December 2022, the electronic databases are retrieved. Combine the selected medical topic titles with free-text terms such as robotics (e.g., remote operation, telerobotics, soft robotics) and stroke (e.g., cerebrovascular accident, cerebral infarction) to create a final search strategy. This can be used in other databases by using the appropriate Boolean operators and search symbols. And the Chinese translation is also used in the Chinese database. Our study does not extend to the grey literature field.

12.2.3 Study Selection and Data Extraction

The authors independently extracted the data into a predesigned spreadsheet including the study background and timeframe, the participants' demographics, the intervention of their descriptors, and outcome measures. Collect data required for meta-analysis including relevant SD and mean difference between baseline and postintervention to assess outcomes. Differences in data extraction or study selection were discussed by two reviewers and commented on and judged by a third reviewer.

12.2.4 Quality Assessment

The reviewers estimated the risk of error in all research that accorded with the selection standard by identifying the bias attributable to randomization, attrition bias, blinding, and reporting through the checklist. The overall high risk was for research with a high risk of bias under different fields, while the moderate risk was for studies with ambiguous information in any domain. Low risk criteria in each domain apply to studies. Grade measures (recommendation, evaluation, progress, and assessment levels) methods were also used for assessing the quality of each outcome and measuring evidence for the tabulated data (MoCA, MBI, FIM, MMSE, and FMA). The initial "high quality" rating of the RCT fell by one level due to serious concern (or a very serious problem on two levels), involving the risk of bias, indirect, inconsistency, or publication bias associated with associated evidence for each result.

12.2.5 Data Analysis

The study characteristics were qualitatively integrated. The mean difference and SD of mean difference were used in the meta-analysis of continuous variables (MoCA,

MBI, FIM, MMSE, FMA). Not all research has stated the numerical values of SDs before and after using the robots. Under these circumstances, the direct contact study's authors requested missing data and, if not, we estimated the missing values by an indirect approach. We deal with heterogeneity by using a random effects model caused by the expected population (post-stroke cognitive impairment) and robotic interventions.

12.3   Results

Based on the search strategy of this research, 1325 articles were identified after removing duplicates; 16 full-text articles (Fig. 12.2) were retrieved from them. After exclusion, they were systematically reviewed and meta-analyzed in eight retained RCTs involving a total of 431 patients. Relatively low risk of bias in four research, two research moderate, and one research relatively high (Fig. 12.3). The ratings of the quality of evidence scores for each meta-analysis result ranged from medium to very low.

12.4   Quantitative Synthesis (Meta-analysis)

12.4.1   MBI Score

MBI data from three studies [3–5], including 184 patients (intervention n = 102, showed that rehabilitation robots improved MBI scores more significantly (MD = 19.93, 95%, CI = 17.94 to 21.91, P < 0.00001, I^2 = 99%, Fig. 12.4). We found that heterogeneity comes from Zhao (2020) through a susceptivity analysis. Heterogeneity was significantly lowered when this research was eliminated (MD = 8.67, 95%, CI = 6.13 to 11.21, P < 0.00001, I^2 = 0%).

12.4.2   FMA Score

Two RCTs measured the FMA scores, representing 72 patients (n = 37), as compared to the control groups [6, 7]. From the summary data of these two studies, rehabilitation robots significantly reduced the FMA scores (MD = 3.04, 95%, CI = 1.42 to 4.66, P = 0.0002, I^2 = 0%, Fig. 12.5).
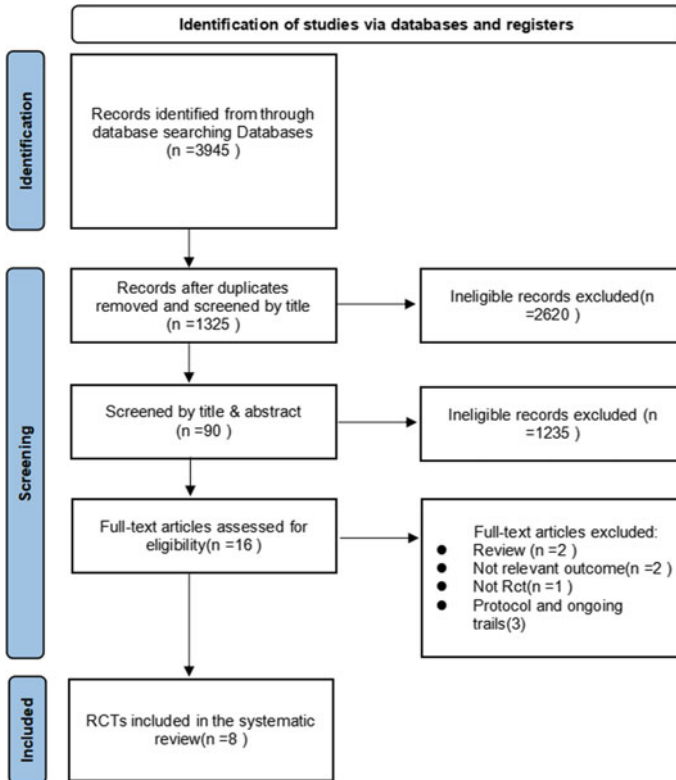
Fig. 12.2 Flow chart for research selection process

12.4.3 MOCA Score

The MOCA data came from five studies [3–5, 7, 8], including 281 patients (intervention n = 149), the intervention group significantly improved the MOCA scores when compared with the conventional cognitive training groups (MD = 5.86, 95%, CI = 5.60 to 6.11, and P < 0.00001, I^2 = 99%, Fig. 6a). We found that heterogeneity comes from Zhao (2020) and Alfredo (2020) through a susceptivity analysis. Therefore, the heterogeneity was recalibrated and found to be reduced (MD = 2.27, 95%, CI = 1.77 to 2.77, P < 0.00001, I^2 = 0%).

12.4.4 MMSE Score

Rehabilitation robots were associated with improved MMSE scores (MD = 3.07, 95%, CI = 2.63 to 3.51, P < 0.00001, I^2 = 0%, Fig. 6b), involving two randomized
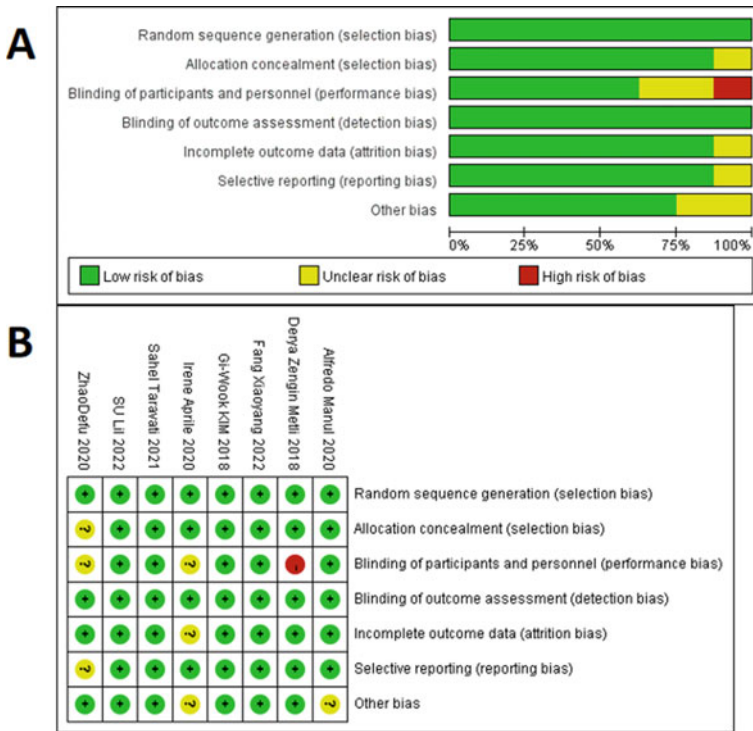
Fig. 12.3 **a** Risk of bias: review writers' estimates of the involved research on the percentage of items in each risk of bias; **b** Risk of bias summary: inspect the writers' estimates on the items expressed in each risk of bias in the involved research
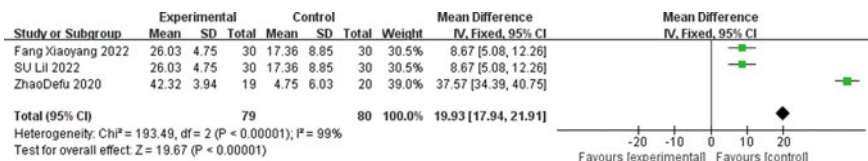
Fig. 12.4 Forest plot of MBI scores induced by rehabilitation robots and control intervention
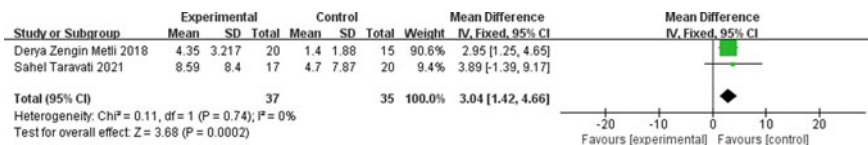
Fig. 12.5 Forest plot of FMA score induced by rehabilitation robots and control intervention
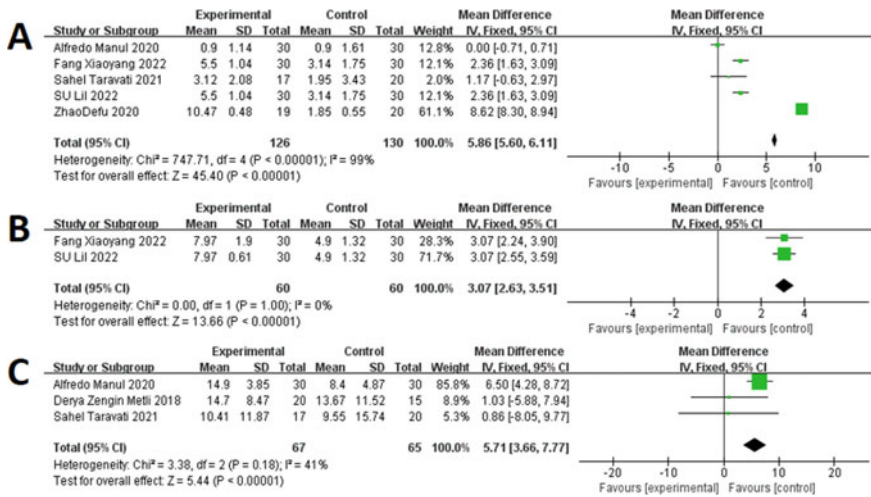
Fig. 12.6 Forest plot of **a** MOCA scores, **b** MMSE scores, **c** FIM induced by rehabilitation robots and control intervention

controlled trials including 125 patients (n = 63) [3, 5]. Because very few studies were included, it was impossible to find a source of heterogeneity.

12.4.5 FIM Score

Three RCTs represented 132 patients (intervention n = 67), in comparison with the control group [6–8]. Summary data from these three experiments showed better treatment outcomes in rehabilitation robot groups (MD = 5.71, 95%, CI = 3.66 to 7.77, P < 0.00001, I^2 = 41%, Fig. 12.6c).

12.4.6 Adverse Events

Only one patient in the eight RCTs had an adverse event, developed scalp tingling at the start of the treatment, which disappeared after 1 day of rest, and continued participation in therapy.

12.5 Discussion

Post-stroke cognitive impairment is one of the major dysfunctions after stroke [9]. The advantage of this study is the introduction of multiple outcome scores, including five aspects: MOCA, MBI, FIM, MMSE, and FMA, which can show practical improvements in subfields including attention, memory, and executive function, making the findings more comprehensive and credible. We addressed studies with less heterogeneity by using fixed-effects models and sensitivity analyses. The MOCA, MBI, FIM, MMSE, and FMA scores in the rehabilitation robot groups were all dramatically improved compared with the conventional cognitive training groups. At the same time, after the intervention, the scores of both groups were dramatically improved compared with those before the intervention. It suggests that routine homework training, whether combined with conventional cognitive training or rehabilitation robot training, can improve the cognitive function of stroke patients and improve their ability to live in their daily activities. However, the training effect of rehabilitation robot training combined with conventional operation therapy is more significant. This result did not significantly differ in cognitive function in patients with different cultural levels. The results are identical to the conclusions of several scholars [6, 10]. Cognitive impairment is mainly manifested as structural and visual-spatial function, memory, execution force, timing and orientation force, attention disorder, etc., and patients can have one or more symptoms. Patients with cognitive dysfunction are often difficult to pay attention to, training is missing the point, unable to well understand and implement the goals and treatment plans set by the therapist, and unable to apply the sports skills learned to daily life. The virtual scene training of the rehabilitation robot makes the patients get rid of the boredom of the routine operation treatment, mobilizes the enthusiasm of the patients, and makes the patients more actively participate in the daily training. It can give patients rich sound and light dynamic stimulation, attract patients' attention, and the computer system can also compare the patient training effect immediately [11]. Through repetitive training, it can effectively enhance sensory and motor information input, improve attention, increase patients' training interest and enthusiasm, accelerate the recovery of damaged brain function and, promote the recovery of cognitive function. It can effectively promote the improvement of attention in the cognitive function of PSCI patients, so as to improve their cognitive function and promote the improvement of ADL.

In the past few years, robotic therapy has aimed to improve exercise performance and ADL, although cognitive disorder is usually overlooked or its treatment is independent of exercise injuries [12]. Cognitive therapy is critical in subjects with frequent concurrent cognitive and exercise disorders, such as stroke patients. Indeed, as observed in several studies [13], the limited shift in limb motor improvement of limb mobility, such as ADL, may be because of a lack of attention to coexisting cognitive impairment. Aprile et al. (2020) show that rehabilitation robot training has made tremendous strides in multiple domains of cognitive dysfunction after stroke [14]. In addition, the visual feedback, auditory feedback, situational feedback, and

reward and punishment feedback generated during the training process of the rehabilitation robot form a rich environmental stimulus. Abundant environmental stimuli can activate gene expression associated with cellular remodeling, promote axonal elongation and the establishment of new synaptic connections, and increase neuroplasticity. Dendritic spines are an important region for synaptic remodeling. Studies in rats show that enriched environmental stimuli can increase the number of dendritic spines and synapses, increase the number of neuronal stem cells and neuroblasts in rats, and promote the migration of proliferating cells to the area of cerebral infarction. Rich environmental stimulation can promote the regeneration of neurons and processes in rats, accelerate the remodeling of neural network, transfer functional brain regions, and promote the reorganization of brain function.

Furthermore, our study currently has the following limitations. First, the study time is not long, and its long-term efficacy needs to be improved in subsequent studies. For future studies, studies planning more participants and long-term follow-up to draw conclusions are probably appropriate. Second, the virtual scene training is not immersive, and the training effect is not ideal. If further improvement can be achieved, it is not only more conducive to functional improvement, but also has a better patient training experience. Furthermore, future experiments should improve the standardized reporting of robot-assisted rehabilitation, encourage randomized controlled trials to follow the STRICTA guidelines, and rigorously design large-scale RCTs to fully meet the standard for reporting interventions included in the guidelines for clinical trials of rehabilitation robots.

12.6   Conclusion

Based on our study, rehabilitation robot training can improve the cognitive function of stroke patients and promote the improvement of daily living ability, which is an effective means of stroke rehabilitation.

References

1. Lo, J.W., et al.: Profile of and risk factors for poststroke cognitive impairment in diverse ethnoregional groups. Neurology **93**(24), e2257–e2271 (2019)
2. Moher, D., Liberati, A., Tetzlaff, J., Altman, D.: Preferred reporting items for systematic reviews and meta-analyses: the PRISMA statement. PLoS Med. **6**(7), e1000097 (2009)
3. Su, L.L., et al.: Effects of upper limb robot-assisted training on cognition and upper limb motor function for subacute stroke patients. Chin. J. Rehabil. Theory Pract. **28**(05), 508–514 (2022)
4. Zhao, D.F., et al.: Repetitive transcranial magnetic stimulation combined with upper limb robot virtual scenario training for stroke patients with cognitive impairment. Chin. J. Rehabil. **35**(06), 295–298 (2020)
5. Lili, S., et al.: Virtual situational task-oriented training of upper limb robot for stroke study the influence of cognitive function in patients. Chin. J. Rehabil. **37**(02), 101–104 (2022)

6. Zengin-Metli, D., et al.: Effects of robot assistive upper extremity rehabilitation on motor and cognitive recovery, the quality of life, and activities of daily living in stroke patients. J. Back Musculoskelet. Rehabil. **31**(6), 1059–1064 (2018)

7. Taravati, S., et al.: Evaluation of an upper limb robotic rehabilitation program on motor functions, quality of life, cognition, and emotional status in patients with stroke: a randomized controlled study. Neurol. Sci. **43**(2), 1177–1188 (2022)

8. Manuli, A., Psy, M., Psy, D.L., Msc, A.C., Balletta, P.T., Luca, R.D., et al.: Can robotic gait rehabilitation plus virtual reality affect cognitive and behavioural outcomes in patients with chronic stroke? A randomized controlled trial involving three different protocols. J. Stroke Cerebrovasc. Dis. **29**(8), 104994 (2020)

9. Kim, G.W., Won, Y.H., Seo, J.H., Ko, M.H.: Effects of newly developed compact robot-aided upper extremity training system (Neuro-X®) in patients with stroke: a pilot study. J. Rehabil. Med. **50**(7), 607–612 (2018)

10. Mehrholz, J., et al.: Electromechanical and robot-assisted arm training for improving activities of daily living, arm function, and arm muscle strength after stroke. Cochrane Database Syst. Rev. **9**(9), Cd006876 (2018)

11. McDowd, J.M., Filion, D.L., Pohl, P.S., Richards, L.G., Stiers, W., et al.: Attentional abilities and functional outcomes following stroke. J. Gerontol. Ser. B Psychol. Sci. Soc. Sci. **58**(1), P45–53 (2003)

12. Zinn, S., Dudley, T.K., Bosworth, H.B., Hoenig, H.M., Duncan, P.W., Horner, R.D.: The effect of poststroke cognitive impairment on rehabilitation process and functional outcome. Arch. Phys. Med. Rehabil. **85**(7), 1084–1090 (2004)

13. Hsieh, Y.W., Wu, C.Y., Lin, K.C., Yao, G., Wu, K.Y., Chang, Y.J.: Dose-response relationship of robot-assisted stroke motor rehabilitation: the impact of initial motor status. Stroke **43**(10), 2729–2734 (2012)

14. Aprile, I., et al.: Robotic rehabilitation: an opportunity to improve cognitive functions in subjects with stroke. An explorative study. Front. Neurol. **11**, 588285 (2020)

Chapter 13
The Application Value of Virtual Reality Navigation Combined with Rapid On-Site Evaluation in CT-Guided Lung Biopsy

Ning Chen, Zixi Yang, Benli Ye, Huiqiao Guo, Feng Wang, Chenxi Zhang, and Dongxu Wang

Abstract The purpose is to evaluate the value of Virtual Reality (VR) navigation system-assisted CT-guided percutaneous aspiration biopsy combined with Rapid on-site Evaluation (ROSE) in the accurate diagnosis of pulmonary nodules and pulmonary infections. This study retrospectively analyzed the medical records of CT-guided percutaneous transthoracic needle biopsy (CT-PTNB) patients at the Second Hospital of Qiqihar Medical College from March 2018 to December 2021. The 158 eligible patients who underwent lung aspiration biopsy were divided into an experimental group (81 patients) and a control group (77 patients). In the experimental group, a VR navigation system was used to assist CT-guided percutaneous aspiration biopsy combined with ROSE, and in the control group, patients underwent plain CT-guided pulmonary aspiration biopsy. Basic clinical information including gender, age, lesion location, and puncture length was recorded for all patients. The occurrence of intraoperative complications of lung puncture biopsy and secondary postoperative biopsies between the two groups of patients were also compared. There was no statistically significant difference between the two groups of patients in terms of clinical base information (all $P > 0.05$). Meanwhile, the incidence of bleeding [13.58% (11/81) vs. 27.27% (21/77), $\chi 2 = 4.582$, $P = 0.032$] and pneumothorax [6.17% (5/81) vs. 15.58% (12/77), $\chi 2 = 4.916$, $P = 0.027$] were significantly lower in the experimental group than in the control patients. In contrast, there was no statistically significant difference in the rate of secondary biopsy between the two groups [0.00%

N. Chen · Z. Yang · B. Ye · H. Guo · F. Wang
Medical Technology School, Qiqihar Medical University, Qiqihar 161006, Heilongjiang, China

C. Zhang
Basic Medicine School, Qiqihar Medical University, Qiqihar 161006, Heilongjiang, China

D. Wang (✉)
Medical Imaging Center, Second Affiliated Hospital of Qiqihar Medical University, Qiqihar 161006, Heilongjiang, China
e-mail: wangdongxu19840312@163.com

(0/81) vs. 3.90% (3/77), χ2 = 3.217, *P* = 0.073]. VR navigation system-assisted CT-guided pulmonary aspiration biopsy combined with rapid on-site evaluation (ROSE) is significantly better than conventional CT-guided pulmonary aspiration biopsy in terms of safety and reduction of secondary biopsy rate in patients and has high clinical application value.

13.1 Introduction

In recent years, with the development of society, due to the decline of air quality or some bad habits of people, lung diseases are increasing year by year, and the incidence and death rate of lung cancer tops the list [1]. CT-PTNB is a relatively simple, minimally invasive procedure in which the location of the lesion is determined by a CT scan, and aspiration or biopsy is performed under CT guidance to obtain a pathologic diagnosis [2]. However, conventional CT-guided needle biopsy (CTNB) is highly susceptible to factors such as the experience and skill level of the patient, resulting in the patient obtaining additional puncture injury, radiation damage, and even elevating the complication rate of the puncture procedure.

For this reason, many experimental studies have been conducted to improve the accuracy and safety of puncture operations by applying various methods for positioning and navigating the puncture needle, such as optical navigation systems, electromagnetic navigation systems, virtual reality (VR) navigation systems, and robotic navigation systems. Cheng et al. [3] showed that the application of electromagnetic navigation system to CT-PTNB in pulmonary nodule surgery could reduce complications, reduce patient turnaround, and save total time. Wang et al. [4] showed that optical positioning technology assisted puncture could improve puncture accuracy and shorten puncture procedure time within a certain range. VR navigation systems can assist in intraoperative positioning and real-time tracking of the puncture needle tip to provide precise, objective, and real-time interactive guidance for lung puncture biopsy during surgical operations to reduce injury to the organs. However, the application of VR navigation has hardly been reported.

Rapid on-site evaluation (ROSE) is a rapid cytology interpretation technique that accompanies the sampling process in real-time. When the target site is sampled, a portion of the sampled material is blotted onto a slide with essentially no loss of tissue specimen to make a cytological film base that is rapidly stained and immediately interpreted with a special microscope synthesizing clinical information. ROSE is more frequently used in bronchoscope biopsies to reduce the insufficiency of bronchoscope biopsy pathology specimens, and Izumo et al. [5] showed that ROSE can reduce the number of EBUS (Endobronchial Ultrasonography) punctures and improve the accuracy of pathology results. In contrast, few reports have applied ROSE to CT-PTNB.

VR navigation systems can not only reduce the risk of lung biopsy but also improve medical safety, diagnosis and treatment effects. ROSE not only ensures sufficient materials but also improves the accuracy of diagnosis and significantly reduces the

rate of the second biopsy. At present, there are few reports on the application of VR navigation system-assisted CT-guided percutaneous biopsy combined with ROSE in the accurate diagnosis of pulmonary nodules and lung infections. Therefore, this study evaluates its application value.

13.2 Materials and Methods

13.2.1 Study Population

This study was authorized by the Ethics Committee of Qiqihar Medical College (Qiqihar, China; protocol number: 2021–193). All the data showed in this study were anonymous, therefore, informed consent was waived for this study in compliance with the Declaration of Helsinki. This study retrospectively analyzed the patients' medical records who have PTNB in the Second Affiliated Hospital of Qiqihar Medical College from March 2018 to December 2021. Inclusion criteria: patients who underwent PTNB and were able to provide images and reports. Exclusion criteria: lesions located in non-pulmonary parenchyma such as pleura and mediastinum. A total of 158 patients (age 18–86 years; 83 males and 75 females) were involved; patients were partitioned into two groups by random number table (Fig. 13.1). There were 81 patients in the experimental group (VR navigation combined with ROSE), 42 males and 39 females; 77 patients in the control group (traditional CT-PTNB), 41 males and 36 females; the gender, age, lesion location, comparison of the size of the body part affected by the diseases (measured by the long diameter of the mediastinal window lesion) and puncture length (the length of the coaxial needle entering the body during puncture). They all have no statistical significance ($P > 0.05$), as shown in Table 13.1.

13.2.2 Operation Steps

All patients signed an informed consent form for PTNB before the procedure. Patients did not receive aspirin for more than 7 days and their blood counts and coagulation were within interventional radiology guidelines [6]. Guided by 64 rows of spiral CT scans, an 18G semi-automatic biopsy needle and a 17G coaxial needle were used. During the operation, the VR navigation system was used to assist CT-guided positioning, and the patient breathed calmly for CT scanning, and the scanned data was transmitted to the navigation system synchronously to identify the marked points of the CT image and determine the target area. After correcting the image, the fused image showed a real-time VR fusion navigation mode (Fig. 13.2), and then the best needle route was determined to avoid the interlobar pleura, nerves, blood vessels, and pulmonary vesicles. Under 3D guidance, a 17G coaxial needle was inserted into
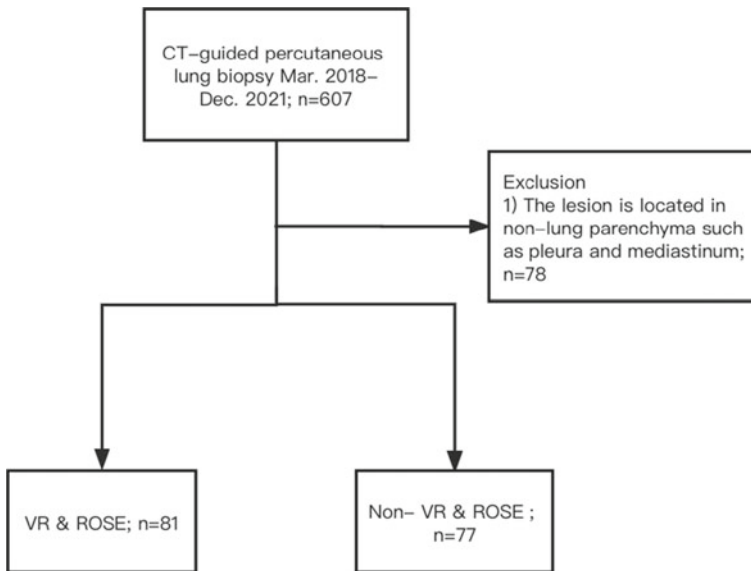
Fig. 13.1 Flow chart of patients enrolled in the present study. (n, number of samples participating in the experiment. VR, virtual reality navigation systems. ROSE, rapid on-site evaluation)

Table 13.1 Demographics and baseline values of the two groups

	Sex, male/female	Age[a] (years)	Nodule distribution		Nodule size[a] (cm)	Distance from nodule to pleura[a] (cm)
			Upper lung	Lower lung		
VR & ROSE	41/36	62.71 ± 10.83	43	34	31.10 ± 18.44	18.59 ± 9.93
Non-VR & ROSE	42/39	63.67 ± 10.56	53	28	32.19 ± 16.95	17.31 ± 10.41
χ2- or t-value	0.031[b]	−0.559[c]	4.476[b]		−0.400[c]	0.795[c]
P-value	0.816	0.577	0.345		0.690	0.428

a. Data are expressed as the mean ± standard deviation; b. t-value; c. χ2-value

the border of the lesion, and the 18G semi-automatic biopsy needle was replaced for biopsy. On the premise of no loss of tissue specimens, part of the imprints was applied on the glass sheet, fixed in 95% ethanol solution, and stained with rapid hematoxylin–eosin (Hematoxylin–eosin, HE). If the nuclear heterogeneous cells are observed under the microscope (Fig. 13.3), stop the operation, otherwise re-biopsy through the coaxial needle, until qualified, the comprehensive clinical information will be read immediately. The tissue was put into a formalin-fixed solution and sent to the pathology department for pathological diagnosis.
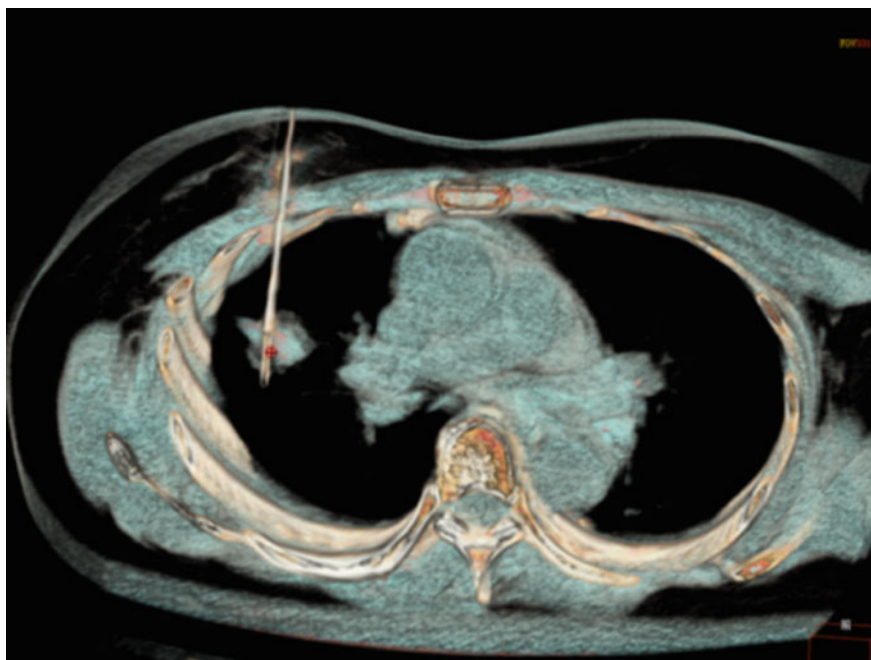
Fig. 13.2 VR navigation system assists in real-time puncture image, and the red dot is the target marking position

Fig. 13.3 Microscopic observation of nuclear heterogeneous cells
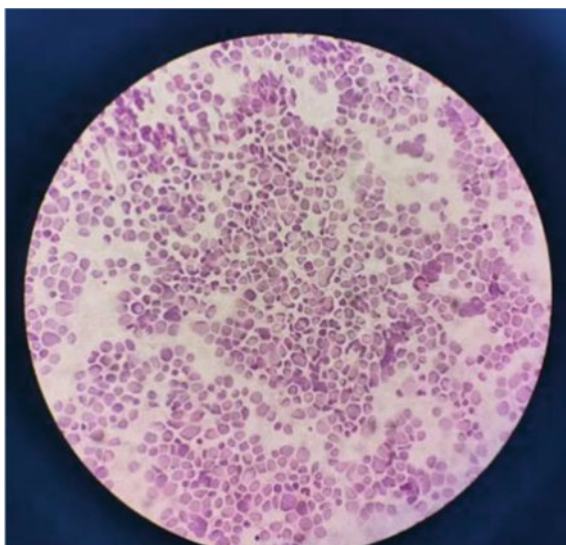
13.2.3 Statistical Methods

The measurement data of normal distribution are processed by SPSS25.0 statistical software, and the mean ± standard deviation ($\bar{x} \pm s$) table is used. The counting data is expressed in the number of examples. The age, lesion diameter (upper and middle lobe of the upper lung, the lower lobe of the lower lung), and puncture length between groups were compared by independent sample t-test. The sex, location of focus, and incidence of complications between the two groups were compared by chi-square test, $P < 0.05$ was regarded as a statistically significant difference.

13.3 Results

In this study, there were no major complications in both groups, including bleeding in control group'21 patients and 11 in the experimental group, pneumothorax in 12 participants in the control group, and 5 patients in the magnetic conductivity group. The incidence of bleeding [13.58% (11/81) vs. 27.27% (21/77), $\chi 2 = 4.582$, $P = 0.032$] and pneumothorax [6.17% (5/81) vs. 15.58% (12/77), $\chi 2 = 4.916$, $P = 0.027$] was significantly reduced in all patients in the experimental group in comparison with the control group, as shown in Table 13.2. At the same time, the bleeding in both groups can be stopped and pneumothorax can be absorbed by itself, and there are no follow-up hospitalized patients due to puncture complications.

In this study, there were no serious symptoms like air embolism. In this study, 3 patients in the control group needed secondary biopsies, while no patients in the experimental group underwent secondary biopsies. The secondary biopsy rate of the control group was 3.90% (3/77), and that of the experimental group was 0% (0/81). There were no statistical differences in the second biopsy between the two groups ($\chi 2 = 3.217$, $P = 0.073$), as shown in Table 13.2.

Table 13.2 Comparison of complications and the rate of secondary biopsy between the two groups of patients

	Complications		The rate of secondary biopsy
	Hemoptysis	Pneumothorax	
VR & ROSE	21 (27.27)	12 (15.58)	3 (3.90)
Non-VR & ROSE	11 (13.58)	5 (6.17)	0
$\chi 2$-value	4.582	4.916	3.217
P-value	0.032	0.027	0.073

VR, virtual reality navigation systems. ROSE, rapid on-site evaluation

13.4   Discussion

CT-guided percutaneous lung aspiration biopsy has been widely applied in clinical diagnosis of lung diseases, however, as a blinded operation, CTNB has many drawbacks. The smaller the lesion, the deeper the location, and the more complex the anatomy, all result in more frequent needle tract adjustments. However, repeated lung punctures can lead to various complications, and there is also a certain probability that a second biopsy will be required due to insufficient samples obtained from the puncture, causing extra injury to the patient. To reduce the adverse effects of blind puncture, the image navigation-assisted positioning puncture system comes into being, which mainly composed of spatial positioning systems, computing and corresponding data processing, and image processing software [7]. Puncture surgery navigation systems are mainly used in fields like head, neurosurgery, orthopedics, and more. Because the thoracic surgery navigation technology is still in the early research stage with electromagnetic navigation, it has technical shortcomings such as the puncture needle end wire affecting the operation, a bit long preparation time, and may be subject to magnetic interference. Electromagnetic navigation still cannot provide accurate depth and real-time monitoring of the lung puncture path information, nor can it send feedback on the margin of error caused by the needle tip entering the lung tissue and cannot resolve the margin of error when puncturing on account of patient's respiratory motion [7]. The key to accurate lung puncture lies in quickly tracking organ displacement, and deformation during lung puncture and finding the best time to puncture.

Virtual Reality (VR) is an advanced computer human–computer interface that has been developed in recent years and is characterized by conceptualization, interactivity and immersion. VR technology has been widely used in the modern biomedical field and has had a huge and far-reaching impact on the development of medical care. With the combination of VR technology and recently developed surgical technologies (imaging, navigation, etc.), VR technology is playing an increasingly important role in disease diagnosis, surgery, and medical teaching. In this study, VR navigation technology was used to monitor the puncture procedure in real-time, combined with spatial positioning, to accurately grasp the spatial alignment between the surgical site and the puncture needle, to determine its anatomical structure, and to adjust the depth and angle of the needle based on the patient's respiratory motion, to facilitate the precise operation of the lung lesion. This approach not only ensures a high degree of accuracy, but also avoids electromagnetic interference and can be used in all areas of biopsy guidance.

The VR navigation system includes 2 main key functional modules: (1) image acquisition and reconstruction: image acquisition and multi-directional reconstruction according to the standard scanning method, forming a three-dimensional data field, which is used as a data source to simulate the implementation of the navigation interface in the CT surgical navigation system during surgery. In addition, the original acquisition image and the 3D image can be used to plan the puncture according to the surgical plan and mark the target area to ensure the efficacy and

safety of the surgery. (2) location: the system is used to monitor the position of the surgical tool relative to the human body, including the direction and depth of puncturing, and to match the actual coordinate system of the patient with the spatial scale of the preoperative scan image, and to guide the doctor's puncture operation through the virtual 3D VR image. The VR technology inputs the patient's preoperative imaging data (e.g., CT, MRI) into the working system for processing, analyzing, and integrating to form objective and detailed 3D simulated images, and the fitted 3D images can be highly compatible with the actual anatomical position during surgery or even completely overlapped [8]. In summary, CT scan is performed during the surgery when the patient is breathing calmly, and the acquired scan trapped image data is input into VR navigation computer system to reconstruct and form 3D visualized images, which can outline the tumor shape and size, and observe the spatial location relationship between the tumor and adjacent important structures such as nerves, blood vessels, intestinal tubes, etc., design the surgical planning and needle route according to the images, pay attention to the puncture route to avoid important tissues. Design the surgical planning and needle route according to the image, pay attention to the puncture route to avoid the important tissues, identify the marker points of CT image, determine the target area, and fuse the image after correction to appear the real-time VR fusion navigation.

With the help of a VR real-time accurate lung puncture navigation system, we can plan the accurate and safe puncture path, calculate the position error caused by the patient's breathing in real-time, predict the puncture risk of lung biopsy, and accurately simulate the needle tip position on the image in real-time during the puncture process, effectively improve the accuracy of the puncture needle to reach the target point of the lesion, thus to avoid important blood vessels and organs, and to reduce the occurrence of surgical complications. It also greatly shortens the puncture time, reduces the radiation dose suffered by patients and doctors, and improves the efficiency of imaging equipment use.

CTNB being an invasive operation, obtaining a qualified and enough histological specimen is essential to puncture biopsy. In general, the more specimens, the higher the positive rate. But complications may also increase, so quality assessment after obtaining the specimen is especially important. ROSE is an immediate diagnostic pathology procedure that allows a rapid evaluation of the adequacy and accuracy of material obtained during bronchoscopy within 2–3 min using rapid staining of smears, studies written by Wang et al. [9] show that in pulmonary nodule punctures ≤2 cm in diameter, the application of ROSE can reduce both the drawbacks due to the inadequacy of biopsy pathology specimens and the number of puncture biopsies. Meanwhile, the accuracy of the pathology results will be improved.

Because percutaneous lung aspiration biopsy is an invasive procedure, postoperative complications are inevitable. According to studies, hemorrhage and pneumothorax are the most frequent complications of percutaneous lung biopsy, but the reports on its incidence are inconsistent, ranging from 7 to 30% for bleeding [10] and about 20% for pneumothorax [11]. In this study, the puncture was successful in both groups, and the incidence of hemorrhage and pneumothorax in the VR navigation group was significantly lower than that in the control group, and there were no severe

complications such as air embolism. However, further analysis showed that most of these symptoms such as bleeding or pneumothorax were mild, and only in rare cases did they require further special treatment such as thoracentesis and drainage, and in most cases, no special treatment was needed after surgery until the patient coughed up the bleeding mass or absorbed it on his own. Therefore, although there is a significant difference in the overall complication rate between the two, the impact of the difference in clinical practice is limited. There was no need for a second biopsy in the VR group, and 3 patients in the control group had a second biopsy following the first puncture because the specimen was too small to be diagnosed. However, there was no significant difference in the secondary puncture rate between the two groups, which may be due to the small total sample size in this study.

There are some limitations in this study. First, this is a retrospective study, and some data might not be complete. Secondly, there is insufficient sample size, and it is necessary to conduct multi-dose clinical studies with large samples in the event of a bias.

In conclusion, VR navigation system-assisted CT-guided puncture biopsy combined with ROSE is significantly better than conventional CT-guided lung puncture biopsy in terms of safety and the degree of harm to patients by reducing the incidence of complications, improving the diagnostic rate, some reduction in secondary biopsy rate, lessening the number of CT scans while cutting down the cost and the harm caused to patients by radiation. With the update and diversification of VR technology, its use will become more convenient and accessible. Therefore, as a new technology, VR navigation has a vast prospect for lung nodule localization, biopsy, and minimally invasive interventional procedures.

References

1. Bray, F., Ferlay, J., Soerjomataram, I., Siegel, R.L., Torre, L.A., Jemal, A.: Global cancer statistics 2018: GLOBOCAN estimates of incidence and mortality worldwide for 36 cancers in 185 coun-tries. CA: A Cancer J. Clin. **68**, 394–424 (2018)
2. Zhang, L., Luo, Z.M., Zhang, W., Zhou, Y.T., Li, Y.B.: Clinical application of multilayer CT-guided percutaneous lung aspiration biopsy. China Med. J. **51**(12), 18–21 (2016)
3. Cheng, Z., Mei, P.Y., Wang, L., Jiang, K.: Clinical effectiveness and safety of electromagnetic navigation-guided localization and CT-guided percutaneous localization for pulmonary nodules: a systematic review and meta-analysis. Chin. J. Clin. Thorac. Cardiovasc. Surg. **29**(01), 23–29 (2022)
4. Wang, J., Li, W.H., Ge, Y.: Computer-aided puncture navigation system based on optical positioning. Chin. J. Med. Phys. **33**(02), 162–166 (2016)
5. Takehiro, I., Yuji, M., Shinji, S., Christine, C., Toshiyuki, N., Takaaki, T.: Utility of rapid on-site cytologic evaluation during endobronchial ultrasound with a guide sheath for peripheral pulmonary lesions. Jpn. J. Clin. Oncol. **47**(3), 221–225 (2017)

6. Patel, I.J., Davidson, J.C., Nikolic, B., Salazar, G.M., Schwartzberg, M.S., Walker, T.G., Saad, W.A., et al.: Consensus guidelines for peri-procedural management of coagulation status and hemostasis risk in percutaneous image-guided interventions. J. Vasc. Interv. Radiol. Jvir. **23**(6), 727–736 (2012)
7. Zhang, Z.W., Shao, G.L.: Application of image-guidance-assisted localization puncture system in minimally invasive interventional therapy. J. Interv. Radiol. **26**(10), 948–951 (2017)
8. Roitberg, B.Z., Kania, P., Luciano, C., Dharmavaram, N., Banerjee, P.: Evaluation of sensory and motor skills in neurosurgery applicants using a virtual reality neurosurgical simulator: the sensory-motor quotien. J. Surg. Educ. **72**(6), 1165–1171 (2015)
9. Wang, D., Zhang, Q., Wang, Y., Dou, W., Ding, G., Wen, Q., Han, Y., Du, Y., Li, B.: Application of rapid on-site evaluation in computed tomography-guided percutaneous transthoracic needle biopsy of pulmonary nodules of ≤2.0 cm in diameter. Exp. Ther. Med. **24**(5), 663 (2022)
10. Ohno, Y., Hatabu, H., Takenaka, D., et al.: CT-guided transthoracic needle aspiration biopsy of small (≤ 20 mm) solitary pulmonary nodules. Ajr. Am. J. Roentgenol. **180**, 1665–1669 (2003)
11. Hirasawa, S., Hirasawa, H., Taketomi-Takahashi, A., Morita, H., Tsushima, Y., Endo, A.K., et al.: Air embolism detected during computed tomography fluoroscopically guided transthoracic needle biopsy. Cardiovasc. Intervent. Radiol. **31**, 219–221 (2008)

Chapter 14
Gray and White Matters Segmentation in Brain CT Images Using Multi-task Learning from Paired CT and MR Images

Taohai Han and Hongkai Wang

Abstract   Computer tomography (CT) has been routinely used for decades in clinical neuroimaging. Compared to Magnetic resonance imaging (MR), CT is more readily available and more cost-effective, but the soft-tissue contrast is much lower. In brain CT images, the unclear soft-tissue boundaries and the high noise level hamper accurate segmentation of the gray and white matter, leaving obstacles for the subsequent geometrical quantification of brain structures. To address this challenge, this paper specifically acquires same-patient CT and MR image pairs and proposes a multi-task learning model for simultaneous tissue segmentation and modality transfer. We aim to use the modality transfer task to learn corresponding MR and CT features which assists the segmentation task to achieve more accurate results than single modality learning. Moreover, we add a Shannon entropy loss function to the training loss to further combat the high noise influence and reduce the fragmentation problem of the segmentation results. Experimental results proved that our multi-task framework achieves more accurate segmentation than the single segmentation task, and the Shannon entropy loss results in much fewer broken brain regions than the state-of-the-art (SOTA) U-net method. Our study provides a useful tool for clinical neural CT image analysis.

T. Han
School of Biomedical Engineering, Faculty of Medicine, Dalian University of Technology, Dalian, Liaoning, China

H. Wang (✉)
Liaoning Key Laboratory of Integrated Circuit and Biomedical Electronic System, Dalian University of Technology, Dalian, Liaoning, China
e-mail: wang.hongkai@dlut.edu.cn

14.1 Introduction

With the aging of the population and the growing number of age-related mental diseases, craniocerebral examinations have become more and more important for early disease prevention and diagnosis. Brain CT, especially high-resolution brain CT, is a commonly used tool for brain disease screening. Compared with cranial MR images, brain CT has the advantage of easy access and a large inventory [1], but the soft-tissue contrast and signal-to-noise ratio are relatively lower. The popularity of brain CT results in a large number of high-resolution brain CT images for clinical examination and diagnosis, which increases the burden of the human reviewer [2]. To perform computer-aided diagnosis based on the brain CT images, automated segmentation of brain regions is a prerequisite step. Since CT doesn't have good soft-tissue contrast as MR, it is almost infeasible to segment sub-cortical brain regions from CT images. Therefore, the segmentation of entire gray and white matters becomes a practical clinical need.

Despite the rapid development of computer-assisted medical image segmentation technology, especially deep learning technology in the last decade, there is still no ideal algorithm for gray and white matter segmentation from CT images. The reason is that the contrast between gray and white matter in brain CT images is particularly low thus the boundary is very blurred [3, 4], which we can see in Fig. 14.1. Besides, the high noise level makes it even more difficult to achieve accurate segmentation results. Due to these problems, even experienced physicians have difficulty in manually labeling white and gray matter from CT images. Therefore, the labeling required for deep learning training is difficult to produce, hampering the implementation of deep learning methods in this task.

Unlike CT-based segmentation, gray and white matter segmentation from MR images is already a well-solved problem, there are many existing solutions for MR-based brain region segmentation, such as FreeSurfer [5], SPM [6], BrainSuite [7], etc. Nevertheless, there are still a few studies based on CT images. Li et al. concluded that the continuous improvement of CT scanning quality leads to increasing feasibility for soft-tissue segmentation from CT [8]. Qian et al. [9] used the active contour model for cerebrospinal fluid segmentation of brain CT images. And Manniesing [10] proposed

Fig. 14.1 Comparison of brain CT image and brain MR image. **a** The brain CT image. **b** The brain MR image

(a)   (b)
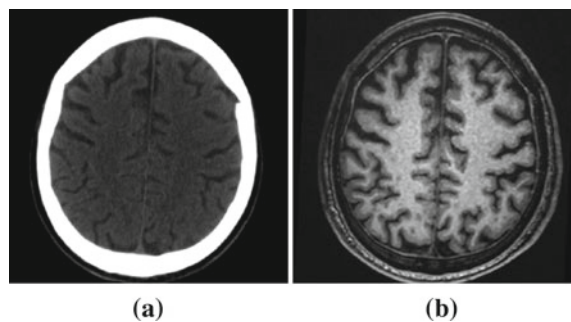
a CT-based segmentation method with a post-correction process. Yahiaoui et al. [11] targeted the segmentation of ischemic stroke regions on brain CT, and Li et al. [12] studied the segmentation of hemorrhagic lesions. In summary, most of the existing studies on brain region segmentation algorithms are based on MR images, while most of the segmentation algorithms for brain CT focus on specific diseases, rather than gray and white matter regions.

Considering the large amounts of daily acquired brain CT images and the clinical need for white and gray matter segmentation, it is highly demanding to develop automated algorithms for CT-based gray and white matter segmentation. Although the low soft-tissue contrast and high noise level impose difficulties for accurate segmentation, the recent progress in multi-task deep learning shed light on novel solutions to this problem. Multi-task learning puts several tasks requiring similar data features together for simultaneous deep network training so that different tasks help each to achieve better performance than any single task alone. For medical image segmentation, a series of studies have shown that multi-task learning effectively promotes inter-task cooperation and improves overall segmentation accuracy [13–15].

In this study, we take advantage of the multi-task learning strategy to overcome the low soft-tissue contrast and high noise interference and improve the segmentation accuracy of gray and white matter from brain CT images. Through simultaneous learning of CT segmentation and CT-to-MR modality transfer, the network learns the corresponding latent features between the two modalities, therefore exceeding the performance of learning from a single modality (CT). Our study has the following main contributions:

(i)   Unlike many existing unpaired domain adaption methods, our study especially acquired 27 pairs of same-patient CT and MR images. In this way, pixel-level strong inter-modality feature correspondence is established, so that the network learns the corresponding high-contrast MR features to promote the segmentation accuracy of CT images.

(ii) The acquisition of paired MR and CT images solves the labeling difficulty of CT images. We used the well-recognized FreeSurfer software to segment the MR images and map the tissue labels into CT image space via inter-modality registration. Therefore, the training labels for the CT segmentation network are obtained.

(iii) We overcome the high noise interference in the CT images by adding the Shannon entropy loss which encourages the high confidence network. As a result, the low confidence segmentation caused by the noise is removed and the segmentation result becomes more compact.

14.2   Method

14.2.1   Image Dataset

The dataset for this study was specially acquired pairs of brain CT and MR images of 27 normal subjects, i.e., each of the samples have corresponding CT and MR images of the same patient. First, we used FreeSurfer to segment the brain regions of the MR images to obtain the white and gray matter labels. Then, using rigid registration, the MR images are aligned to the corresponding CT images, and the segmentation labels are mapped into CT image space via the rigid transformation resulting from the registration. This study focuses on 2D image segmentation thus 2260 2D slices are exacted from the 27 image series, each containing one brain CT slice, one label map, and one MR slice aligned to the CT space. The size of each slice image is 512 × 512. We use the CT image as the input of the multi-task network, the white matter, and gray matter labels to supervise the segmentation task, and the aligned MR image to supervise the modality transfer task. Figure 14.2 shows the flow chart for making brain CT image segmentation labels.
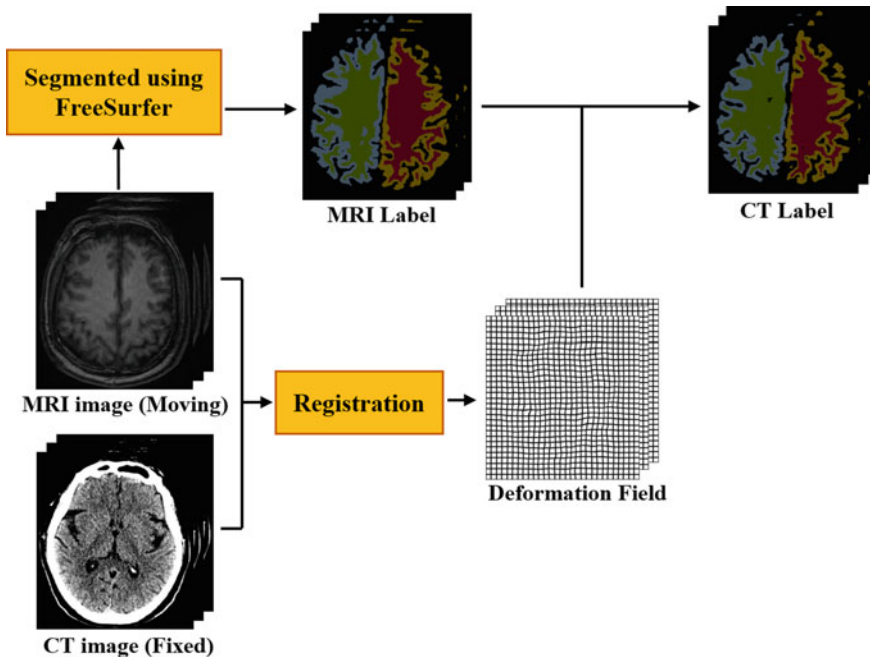

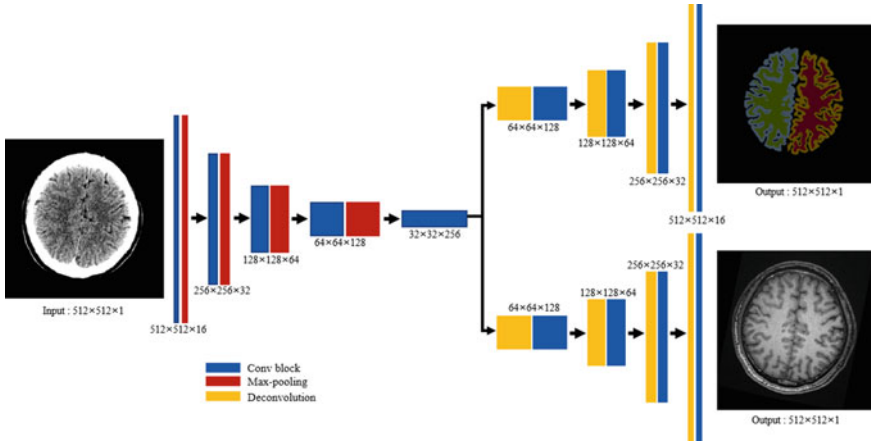**Fig. 14.2**   Workflow of the proposed method for making brain CT labels

Fig. 14.3 The architecture of the proposed multi-task learning network model

14.2.2   Network Architecture

Our end-to-end multi-task network architecture is shown in Fig. 14.3. The network contains one encoder part and two decoder branches for the segmentation task and the modality conversion task, respectively. The two tasks share the same encoder containing four down-sampling layers, such a structure fully acquires multi-scale information for feature extraction of the brain CT. The two tasks have their independent decoders, and both contain four up-sampling layers. The image segmentation and modality transfer tasks, in turn, drive the encoder to extract the common features required for both tasks, thus improving the performance of each task by learning relative features from the other task.

14.2.3   Loss Function

For the segmentation task, we use a hybrid loss function, including a cross-entropy loss term [16] and a Shannon entropy loss [17] term, respectively.

The cross-entropy loss function is a commonly used loss function for image segmentation, which calculates the cross-entropy between the network prediction probability and the ground truth label:

$$L_{ce} = -\sum_{c=1}^{M} y_c \log(p_c) \tag{14.1}$$

where M represents the number of segmentation classes, y_c represents the one-hot encoding of the corresponding pixel labels, and p_c represents the prediction probability of the neural network that the pixel belongs to that species. For the whole image, the cross-entropy loss of all the pixels is averaged.

In addition to the conventional cross-entropy loss, this paper introduces the Shannon entropy loss function to enhance the prediction confidence of the segmentation task:

$$L_{se} = -\sum_{c=1}^{M} p_c \log(p_c) \tag{14.2}$$

where p_c represents the prediction probability of the neural network for the pixel belonging to each class. For the whole image, the Shannon entropy loss of all the pixels is averaged. We adopt the Shannon entropy loss to encourage networks to make more confident predictions, and to combat the low prediction confidence caused by the high CT noise.

The overall segmentation loss function is the weighted sum of the cross-entropy loss and the Shannon entropy loss:

$$L_{seg} = \alpha L_{ce} + (1 - \alpha)L_{se} \tag{14.3}$$

where α is the factor that adjusts the ratio of the two loss functions.

For the modality transfer task, the SSIM (Structural Similarity) loss function [18] is used in this paper. The SSIM index is often used to measure the structural similarity between two images. The SSIM index is sensitive to the perception of local details:

$$SSIM(p, g) = \frac{(2\mu_p\mu_g + c_1)(2\sigma_{pg} + c_2)}{(\mu_p^2 + \mu_g^2 + c_1)(\sigma_p^2 + \sigma_g^2 + c_2)} \tag{14.4}$$

where μ_p and μ_g represent the pixel means of the predicted and labeled images, respectively. σ_p and σ_g represent the standard deviations of the predicted and labeled images, respectively. σ_{pg} represents the covariance of the predicted and labeled images. c_1 and c_2 are constant terms preventing the divisor from being zero.

The corresponding SSIM loss function is then defined as

$$L_{trans} = 1 - SSIM \tag{14.5}$$

The overall loss function of the model is defined by the following equation:

$$L_{mix} = \beta L_{seg} + (1 - \beta)L_{trans} \tag{14.6}$$

where β is the factor that adjusts the ratio of the two loss functions.

14.2.4 Model Training

In this study, the brain CT images input to the network are intercepted with grayscale between [20,60] and the MR images aligned with the CT images are intercepted with grayscale between [100,500] and normalized respectively. We take 0.5 for both α and β in the loss function. We randomly select 2000 2D slices from the dataset as the training set and the remaining 260 slices as the test set. The model training process uses Adam optimizer to optimize the parameters of the model, and the learning rate is set to 1×10^{-4}, and the learning rate decay with multiple steps is also set. The model was trained on two 3090Ti graphics cards manufactured by NVIDIA and built using PyTorch 1.9.

14.3 Result and Analysis

For evaluation, we compared the proposed method with the state-of-the-art (SOTA) U-Net model [19] based on the 260 test slices. To verify the contribution of the modality transfer task and the Shannon entropy loss function, we also conducted ablation studies to compare our method with the multi-task learning without Shannon entropy loss, and the single task segmentation with the Shannon entropy.

We chose the Dice coefficient [20] to evaluate the segmentation accuracy, which is defined as

$$Dice = 2\frac{|R_r \cap R_s|}{|R_r| + |R_s|} \tag{14.7}$$

where R_r is the brain area obtained by network prediction and R_s is the label obtained by mapping the FreeSurfer segmentation of MR image into the CT space. A dice coefficient close to 1 indicates an accurate segmentation and 0 indicates completely inaccurate segmentation.

Table 14.1 reveals that our method obtains the overall highest Dice in comparison with the other three methods. Compared with the U-Net network, we achieved a Dice improvement of 0.03 and 0.02 for white matter and gray matter, respectively. Ablation studies removing either the modality transfer task or the Shannon entropy loss resulted in a drop in the Dice coefficient. It is interesting to see that the Shannon entropy loss contributes slightly more than the modality transfer task, but this should be further validated with more test data in the future study.

Figure 14.4 shows the segmentation results of the four methods at different anatomical positions. We demonstrate the registered MR and the FreeSurfer labels (the ground truth) along with the input CT images. It can be seen that our method produces visually closer results to the ground truth. Compared to the original U-Net result, the addition of Shannon entropy loss results in fewer broken regions, while the multi-task learning also helps to produce more accurate segmentation, especially for the complex-shaped white matter region.

Table 14.1 Comparison table of dice coefficients

Method	White matter	Gray matter
U-Net	0.71 ± 0.05	0.65 ± 0.04
U-Net + Shannon entropy loss	0.74 ± 0.04	0.67 ± 0.04
U-Net + modality transfer	0.73 ± 0.04	0.66 ± 0.04
Our method	**0.74 ± 0.03**	**0.67 ± 0.04**
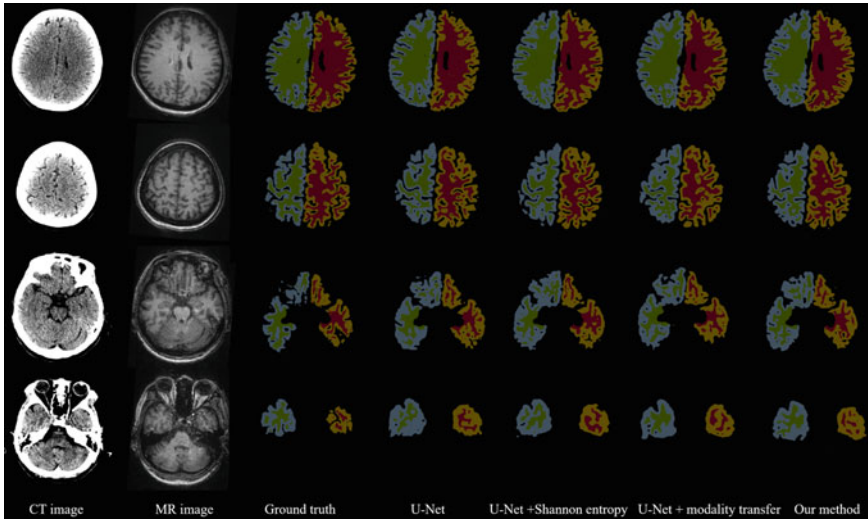
Fig. 14.4 Comparison of our method with the other three methods

14.4   Conclusion

This study addresses the difficult CT-based gray and white matter segmentation problem using multi-task learning based on specially acquired CT-MR image pairs of the same patients. Using the CT-to-MR modality transfer as an auxiliary task, the corresponding MR image feature is learned by the network to promote the segmentation of the CT image. We also added the Shannon entropy to the loss function to overcome the high noise interference. This work has potential value for improving the data analysis ability for clinical brain CT images.

References

1. Fawzi, A., Achuthan, A., Belaton, B.: Brain image segmentation in recent years: a narrative review. Brain Sci. **11**(8), 1055 (2021). https://doi.org/10.3390/brainsci11081055

2. Irimia, A., Maher, A.S., Rostowsky, K.A., Chowdhury, N.F., Hwang, D.H., Law, E.M.: Brain segmentation from computed tomography of healthy aging and geriatric concussion at variable spatial resolutions. Front. Neuroinform. **13**, 9 (2019). https://doi.org/10.3389/fninf.2019.00009.

3. Gupta, V., et al.: Automatic segmentation of cerebrospinal fluid, white and gray matter in unenhanced computed tomography images. Acad. Radiol. **17**(11), 1350–1358 (2010). https://doi.org/10.1016/j.acra.2010.06.005

4. Zhao, C., Carass, A., Lee, J., He, Y., Prince, J.L.: Whole brain segmentation and labeling from CT using synthetic MR images. In: Machine Learning in Medical Imaging, pp. 291–298. Springer International Publishing (2017). https://doi.org/10.1007/978-3-319-67389-9_34.

5. Greve, D.N., et al.: Different partial volume correction methods lead to different conclusions: an 18F-FDG-PET study of aging. Neuroimage **132**, 334–343 (2016). https://doi.org/10.1016/j.neuroimage.2016.02.042

6. Ashburner, J., Friston, K.J.: Unified segmentation. NeuroImage **26**(3), 839–851 (2005). https://doi.org/10.1016/j.neuroimage.2005.02.018.

7. Shattuck, D.W., Leahy, R.M.: BrainSuite: an automated cortical surface identification tool. In: Medical Image Computing and Computer-Assisted Intervention–MICCAI 2000, pp. 50–61. Springer Berlin Heidelberg (2000). https://doi.org/10.1007/978-3-540-40899-4_6.

8. Li, Z., et al.: Improvement of image quality and radiation dose of CT perfusion of the brain by means of low-tube voltage (70 KV). Eur Radiol. **24**(8), 1906–1913 (2014). https://doi.org/10.1007/s00330-014-3247-1.

9. Qian, X., Wang, J., Guo, S., Li, Q.: An active contour model for medical image segmentation with application to brain CT image: an active contour model for medical image segmentation. Med. Phys. **40**(2), 021911 (2013). https://doi.org/10.1118/1.4774359.

10. Manniesing, R., et al.: White matter and gray matter segmentation in 4D computed tomography. Sci Rep. **7**(1), 119 (2017). https://doi.org/10.1038/s41598-017-00239-z

11. Yahiaoui, A.F.Z., Bessaid, A.: Segmentation of ischemic stroke area from CT brain images. In: 2016 International Symposium on Signal, Image, Video and Communications (ISIVC), pp. 13–17. Tunis, Tunisia (2016). https://doi.org/10.1109/ISIVC.2016.7893954.

12. Li, L., et al.: Deep Learning for Hemorrhagic Lesion Detection and Segmentation on Brain CT Images. IEEE J. Biomed. Health Inform. **25**(5), 1646–1659 (2021). https://doi.org/10.1109/JBHI.2020.3028243.

13. Murugesan, B., Sarveswaran, K., Shankaranarayana, S.M., Ram, K., Joseph, J., Sivaprakasam, M.: Conv-MCD: a plug-and-play multi-task module for medical image segmentation. In: Machine Learning in Medical Imaging, pp. 292–300. Springer International Publishing (2019). https://doi.org/10.1007/978-3-030-32692-0_34.

14. Tan, C., Zhao, L., Yan, Z., Li, K., Metaxas, D., Zhan, Y.: Deep multi-task and task-specific feature learning network for robust shape preserved organ segmentation. In: 2018 IEEE 15th International Symposium on Biomedical Imaging (ISBI 2018), pp. 1221–1224. Washington, DC (2018). https://doi.org/10.1109/ISBI.2018.8363791.

15. Murugesan, B., Sarveswaran, K., Shankaranarayana, S.M., Ram, K., Joseph, J., Sivaprakasam, M.: Psi-Net: shape and boundary aware joint multi-task deep network for medical image segmentation. In: 2019 41st Annual International Conference of the IEEE Engineering in Medicine and Biology Society (EMBC), pp. 7223–7226. Berlin, Germany (2019). https://doi.org/10.1109/EMBC.2019.8857339.

16. Zhang, Z., Sabuncu, M.R.: Generalized cross entropy loss for training deep neural networks with noisy labels. arXiv, Nov. 29, 2018. Accessed 07 Jan 2023. [Online]. Available: http://arxiv.org/abs/1805.07836

17. Liu, B., Desrosiers, C., Ben Ayed, I., Dolz, J.: Segmentation with mixed supervision: confidence maximization helps knowledge distillation. Med. Image Anal. **83**, 102670 (2023). https://doi.org/10.1016/j.media.2022.102670.
18. Zhao, H., Gallo, O., Frosio, I., Kautz, J.: Loss functions for image restoration with neural networks. IEEE Trans. Comput. Imaging. **3**(1), 47–57 (2017). https://doi.org/10.1109/TCI.2016.2644865.
19. Ronneberger, O., Fischer, P., Brox, T.: U-Net: convolutional networks for biomedical image segmentation. In: Medical Image Computing and Computer-Assisted Intervention–MICCAI 2015, pp. 234–241. Springer International Publishing (2015). https://doi.org/10.1007/978-3-319-24574-4_28.
20. Zou, K. H., et al.: Statistical validation of image segmentation quality based on a spatial overlap index1. Acad. Radiol. **11**(2), 78–189 (2004). https://doi.org/10.1016/S1076-6332(03)00671-8.

Chapter 15
Wearable Long-Term Graph Learning for Non-invasive Mental Health Evaluation

Daili Yang, Bin Gao, Liwei Huang, Boyu Chen, and Yaozong Chen

Abstract Long-term non-invasive mental health monitoring based on wearable devices has received increasing attention. In the study, a wearable sensing device that can collect wearer's audio, behavior, and environmental sensing data in real-time without infringing on the wearer's privacy is designed. Using this system, we have conducted a 4-week physical and mental health experiment for college students. For audio features, we use full connection and nearest neighbor connection to construct individual graphs, and then develop graph convolutional networks to identify autism. We have also developed an explanatory model to extract subgraphs of individual graphs. The results show that the afternoon or evening time period has a greater impact on high-scoring autistic people.

15.1 Introduction

Non-interventional monitoring of physical and mental health is an urgent global research issue. According to the relevant reports, there are about 450 million people suffering from serious mental illness in the world, which has caused a serious burden on individuals and society [1]. Effective symptom prediction, tracking, and personalized intervention can help to improve the mental health of various groups of people. However, traditional clinical methods are usually insufficient in real-time monitoring of symptoms. In addition, traditional mental health diagnosis methods obtain clinical data by looking, smelling, asking, cutting, and questionnaires. According to the analysis of the mental health scale and clinical diagnosis, data based on the experience of medical staff, the personality characteristics, and mental state of the diagnosed persons are assessed. Traditional mental health monitoring methods may affect the accuracy of the evaluation results, and often medical staff cannot obtain the patient's intervention effect in time. With the continuous prosperity of artificial

D. Yang (✉) · B. Gao · L. Huang · B. Chen · Y. Chen
School of Automation Engineering, University of Electronic Science and Technology of China, UESTC, Chengdu, China
e-mail: 382033019@qq.com

intelligence and the Internet of Things, sensing technology can solve these problems by fine-tracking voice, physiological, and behavioral signals related to mental health.

Due to the continuous innovation of sensor technology, wearable devices have been widely used in emotion recognition, mental health monitoring and evaluation, and emotional feedback and regulation. In [2], an electronic badge was developed to automatically detect speech and nonverbal information, such as physical proximity to others, conversation time, the number of face-to-face interactions, and physical activity levels. Motion Logger [3], a product of AMI (Ambulatory Monitoring, Inc.), could evaluate sleep quality by collecting light levels and physical activity. A new wearable ring sensor was designed to continuously measure activity and physiological information. The experiences of volunteers in different emotional states verified the effectiveness of the devices [4]. In [5], physiological and social signals were continuously and naturally measured by wearable wristbands E4. Then, machine learning technology was used to predict the severity of depression. Perez et al. [6] used an optical sensor on a smart watch to detect irregular pulses to identify atrial fibrillation, and used an irregular pulse notification algorithm to identify possible atrial fibrillation to assist medical visits. Maritsch et al. utilized smart watches to monitor heartrate variability (HRV) in daily life to obtain users' responses to physical exercise, psychophysiological stress, and heart disease. Continuous monitoring of HRV helped to determine and predict health and psychological health issues [7]. Costa et al. [8] designed an EmotionCheck that could produce unobtrusive vibrations on the user's wrist to change the user's perception for his heartrate. It is beneficial for users relieve anxiety through false feedback on slowing down the heart rhythm. In [9], the author proposed BoostMeUp, a smart watch intervention that provided personalized tactile feedback that simulated different heart rates. BoostMeUp intervention could lead to positive cognition, thus balancing the emotional state.

In our study, wearable sensing devices embedded in audio, acceleration and gyroscope, light, humidity, and body temperature sensors are developed and it can continuously collect multimodal sensor data. In order to protect privacy, audio features can be extracted in real-time on wearable sensing devices. Using this wearable sensing device, we have carried out a 4-week long-term mental health monitoring experiment among 16 students. In the analysis of audio features, we have developed the model of a graph convolutional network to assess the levels of autism, and developed the algorithm for machine learning explainer to explain and analyze individual graphs, and to reveal which time period has the greatest impact on autistic people during one day.

15.2   Methodology

The overall framework of the proposed platform is presented in Fig. 15.1. Firstly, we have separately assessed the emotional and psychological status of subjects in the form of questionnaires. According to the scores of the questionnaires, 16 subjects who met the experimental conditions were selected and their demographic information
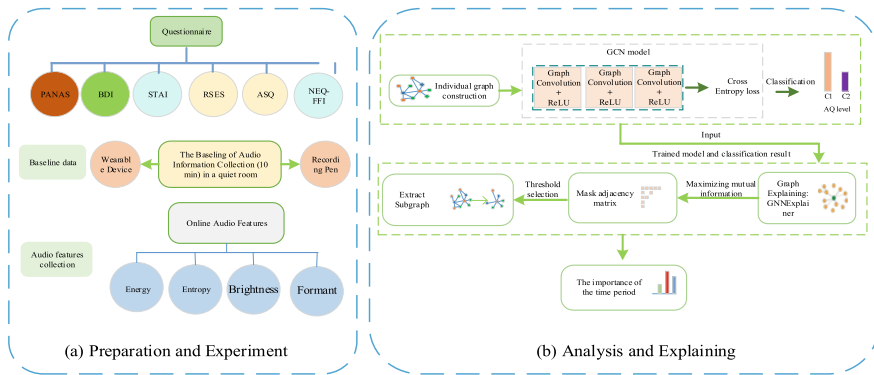
Fig. 15.1 Proposed graph assessment platform

was recorded. Subsequently, baseline audio signals of subjects are collected through a recording pen and wearable devices. In the preparation and experiment stage, subjects wear wearable sensing devices every day to record audio, and activity signals. The recording period of each subject is a month. Considering the computing power of the devices and the wearer' privacy problem, only 4 audio features are calculated online and real-time on wearable sensing devices and original audio files will not be stored. Finally, we construct audio features into a graph structure, and a graph convolutional network (GCN) model is developed to learn graph data and evaluate levels of autism. Subsequently, GNNExplainer is applied to obtain a subgraph of each individual graph to investigate time period for one day that affects the subject's tendency to autism [10].

15.2.1 Wearable Sensing Devices

Wearable sensing devices have been designed to long-term and non-invasively collect audio, behavior, and physiological information related to physical and mental health. Figure 15.2 shows the overall architecture of the wearable devices. The wearable device mainly includes two MEMS silicon microphones, an audio code acquisition chip WM8978, three-axis accelerometer and three-axis gyroscope composed of behavior sensor MPU6050, light sensor BH1750, environmental sensor BMP180, physical sign sensor SI7021. Considering the real-time computing capabilities, we have selected the main controller STM32F405G based on the arm-cortex4 kernel and embedded DSP module. In addition, it also includes an OLED display for human–computer interaction, an SD memory card for data storage, a USB fast charge interface, a Debug port, a power management module, and a 2200mAh rechargeable lithium battery for long-term monitoring.

Fig. 15.2 Structure block
diagram of a wearable
sensing device
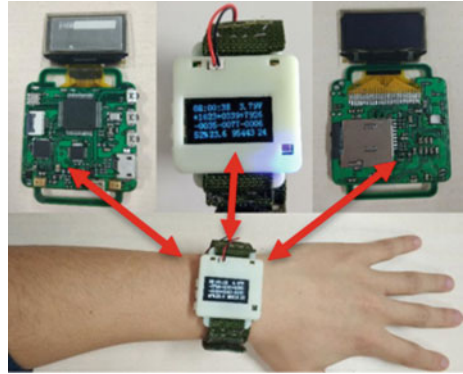
15.2.2 Software Architecture of Wearable Devices

In Fig. 15.3, a real-time operating system (RT-Thread) is used to improve the computing efficiency of the CPU. The multiple tasks of the system are divided into multiple independent threads to run. In the Audio-Thread, MEMS dual microphones are used to collect raw audio data. The microphones are analog microphones. The audio decoder unit WM8978 with code conversion function is used to process analog audio signals. The chip integrates the audio signal filtering function, and the built-in filter parameters can be adjusted through programming. The frequency of audio data collection is 8000 Hz. In Calculate-Thread, Because of the large volume of the original audio signal file, the key feature of the audio signal is extracted in the calculation thread. The computing thread processes audio data every 10 min, and in order to ensure the synchronization of audio signal collection, a double buffering strategy is adopted for audio collection. In order to protect the privacy of users, the original audio information should not be saved. When the feature extraction is completed, the original audio data is automatically deleted. In the File-Thread, when activity sensors, and environmental sensors collect a certain amount of data, they will notify the file thread to save these data through the signal mechanism, and the extracted audio features are also saved through the file thread. In addition, the activity data of device users is obtained by the acceleration and gyro sensors in the Activity-Thread. After the data is collected, the data will be formatted to facilitate the storage and transmission of the data. The data collection frequency of this thread is 100 Hz. In the Environment-Thread, the humidity, temperature, and light signals are acquired and converted. The power values and obtained sensor data will be displayed on the OLED in real-time.
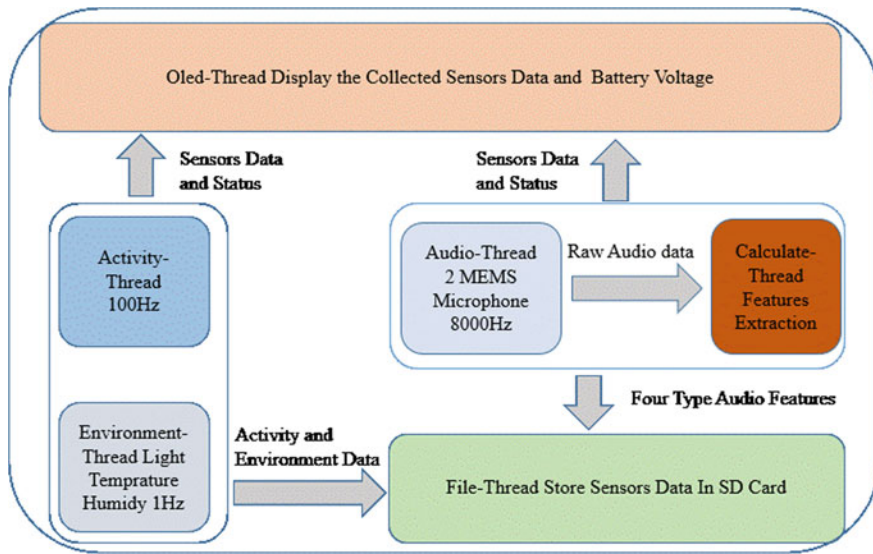
Fig. 15.3 Software architecture of wearable sensing devices

15.2.3   Audio Features Calculation

The audio data processing flow is presented in Fig. 15.4. Considering the privacy problem for the wearers, the wearable sensing devices use a digital signal processing module inside the main controller to process the collected digital signals in time and frequency signals, and then calculate the audio features inside the microcontroller. The original audio signal is deleted immediately after the feature extraction calculation is completed. Due to the limited computing power of the microcontroller, a total of 4 audio features related to mental health are calculated in the smart wearable device, including short-term energy, formant, brightness, and spectral entropy. The audio features calculated online can not only ensure the privacy of the wearer's daily life, but also compress the original audio data, which greatly reduces the storage space for long-term monitoring data.

The statistical features of 4 audio features extracted in real-time and online on the wearable sensing devices have been calculated to find more perceptual information of audio signals. These audio features chiefly contain the minimum value, maximum value, standard deviation, amplitude statistics, sum values, average value of short-term energy, spectral entropy, brightness, and formant. At the same time, we also extract the audio activity feature. Finally, we have obtained 105 audio features.

Online processing on wearable devices

Preprocessing

Framing

Pre-emphasis

Windowing

Feature calculation

Time domain
Energy

Frequency domain
Formant
Brightness
Entropy

Raw audio
data

Statistical feature
calculation
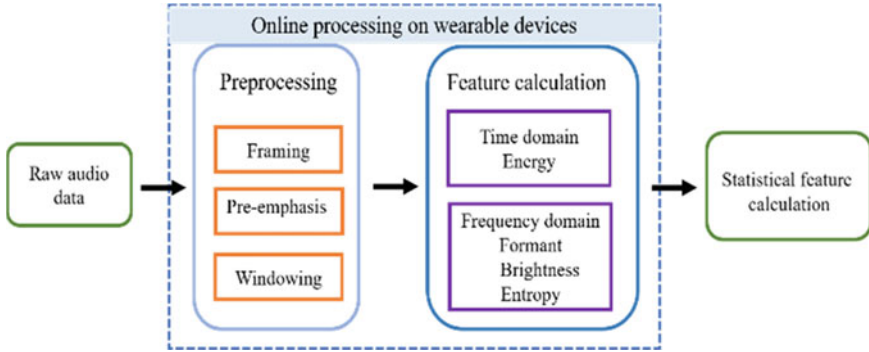
Fig. 15.4 The calculation process of audio features

15.2.4 Correlation Analysis

In order to explore the connection between audio signals collected by wearable devices and autism, we have applied a Pearson correlation method. The calculation formula is expressed as follows.

$$\rho_{X,Y} = \frac{cov(X,Y)}{\sigma_X \sigma_Y} = \frac{E[(X - \mu_X)(Y - \mu_Y)]}{\sigma_X \sigma_Y} \tag{15.1}$$

where cov represents the covariance of sample X and Y, σ_X and σ_Y are the standard deviation of sample X and Y, μ_X and μ_Y are the average values of sample X and Y, and E is the expectation of the samples. In this paper, we have analyzed the correlation between audio features and 5 types of questionnaires.

15.2.5 Graph Learning and Interpreter

Individual Graph Construction

According to the characteristics of audio data collected by wearable sensing devices, we have constructed undirected graphs $G_{IG} := (V, E, H)$ where V, E and H respectively represent a set of audio nodes, a set of edges among audio nodes, and a feature set of audio nodes. The connections among nodes of a graph G_{IG} are determined by the adjacency matrix $A \in R^{|V| \times |V|}$, where $A_{i,j} = 1$ if $e_{ij} \in E$ else $A_{i,j} = 0$.

For audio features collected by wearable devices, it is expected to find out the time period of the day that most influences the subjects with autism tendency. We use half-day audio feature data as a node, and then one week of audio feature data is constructed into an individual graph. For the connection among nodes, we have

analyzed two connection methods, including full connection, and nearest neighbor connection.

Individual graph learning

For individual graphs built by the audio nodes, the objective is to judge the subject's levels of autism scores. Graph networks must consider both nodes information and connection relationships among nodes. Graph Convolutional Network (GCN) [11, 12] can automatically learn both the features of nodes and the connection relationships among nodes. Therefore, a GCN model is developed to classify individual graphs. Given a GCN model, to obtain the feature expression of the node, a total of three steps are as follows:

1. Information transfer with its neighbor nodes:

$$m_{ij}^{l} = MSG\left(h_i^{l-1}, h_j^{l-1}, r_{ij}\right) \tag{15.2}$$

2. Aggregates neighbor node information:

$$\mathrm{M}_i^{l} = AGG\left(m_{ij}^{l} | v_j \in N_{vi}\right) \tag{15.3}$$

3. Combine with the upper-level expression of its own node to generate the local-level node expression:

$$h_i^{l} = Update\left(M_i^{l}, h_i^{l-1}\right) \tag{15.4}$$

where, v_j represents the nodes of the graph, h_i^{l-1} and h_j^{l-1} is representations of nodes v_i and v_j in the previous layer, r_{ij} is the relation between nodes, m_{ij}^{l} represents that the message for node pair (v_i, v_j) is a function MSG of v_i's and v_j's representations h_i^{l-1} and h_j^{l-1} in the previous layer, N_{vi} is a neighborhood of node v_i, M_i^{l} is an aggregated message via an aggregation method AGG.

In this study, we have developed an autism assessment model, which is composed of three GCN modules. The feature dimension of input variable for the first GCN layer is 8, the dimension of middle layer is 20, the dimension of the third GCN layer is determined as 20, and finally, the last layer of the evaluation model is the full connection layer. In addition, each layer of the evaluation model uses the Rectified Linear Unit (ReLU) as the activation function. The evaluation error between autism levels of the subjects and predicting labels is optimized by minimizing cross-entropy loss.

Individual graph interpreter

GNNExplainer is a model-independent interpreter of the Graph Neural Network (GNN) model. GNNExplainer can extract key components from graph network structures and node attributes to explain the trained GNN model. For GNNExplainer, the

essence of learning task is to maximize mutual information (MI), thereby the prominent subgraph structures and subsets of node attributes are obtained to explain GNN models and the important influence factors of graph structure data.

We have applied GNNExplainer model to generate an explanation for each individual graph. These explanations can evaluate the levels of autism scores of relevance of black-box graph neural network reasoning. Moreover, we analyze the interpretation of those individual graphs to find out the time period that most affect autism.

15.2.6 Experiment

Subjects and Settings

In this study, a total of 16 students were recruited from the University of Electronic Science and Technology of China. They are all right-handed, in good health, free of mental illness treatment, and drug or alcohol abuse. Under informed circumstances, they voluntarily participated in the long-term mental health monitoring experiment, and signed informed consent. In order to obtain the emotional state of subjects, all subjects filled out 5 types of questionnaires before the experiment, including autism spectrum (AQ), PANAS, State-Trait Anxiety Inventory (STAI), Beck Depression Inventory (BDI), and Rosenberg Self-Esteem Scale (RSES). A total of 16 subjects completed the long-term monitoring experiment. The average age of subjects is 22.16 ± 0.22 years, and there are 8 undergraduates and 8 postgraduates, but there is only one girl, because the proportion of boys is much higher than that of girls with autism. The studies have been approved by the Ethical Committee of the University of Electronic Science and Technology of China.

Procedures

The whole experiment has 4 steps. The first step is to screen candidate subjects through 5 types of questionnaires, and mainly select candidates with obvious autistic tendency and good mental health for long-term monitoring experiments. The second step is to collect data from the wearable device in a quiet and static state, and collect 5 min of self-introduction voice and behavior data from the subject through the voice recorder and the wearable device. The third step is to collect experimental data for long-term mental health monitoring. During the experiment, the subjects began to wear the wearable device every morning, stopped the device before going to bed at night, and try to ensure continuous monitoring for one day as much as possible. In the fourth step, the subjects refilled the State-Trait Anxiety Scale, Depression Questionnaire, Emotion Questionnaire, and Autism Scale every week. Each subject performed the experiment for one month.

15.3 Analysis and Evaluation

15.3.1 Threshold Selection of Audio Features

Wearable sensing devices are utilized to collect audio features data from long-term mental health experiments. In order to remove environmental noise, we also collect baseline audio data in a quiet environment. The short-term energy of audio is calculated and can reflect whether there is voice activity. According to calculation and analysis, the threshold for audio short-term energy is set to 4. Therefore, most of the external interference and noise in the audio signals will be excluded and it is conducive to correlation analysis and model establishment.

15.3.2 Correlation Analysis

The Pearson correlation analysis between 105 audio features and the mental health scales is carried out. In Table 15.1, the results of the correlation between audio features and 5 questionnaire scores are presented, where "numbers" represents the feature numbers and the absolute values of correlation coefficients exceed 0.5. We can conclude from Table 15.1 that the formants-related audio features and scores of various questionnaires show a moderate correlation, and this shows that the formant is very likely to have some connection with the mental state of the subjects in the long-term psychological monitoring experiments. Otherwise, any one of the four audio features embedded in smart wearable devices, namely short-term energy, spectral entropy, brightness, and formant, has a moderate correlation with at least one scale. This suggests that audio features computed online on wearable devices not only preserve privacy, but also correlate with mental health status. We can find that the absolute values of the correlation coefficient between AQ scores and four audio features are greater than 0.5, and they are sum_formant_50% (0.57), formant_mean5_50% (0.57), formant2_max (−0.57) and formant5_max (−0.53). Therefore, the results also show that audio formants are moderately correlated with AQ scale scores. It can also be known from the table that the number of features for the correlation between audio-related features and other questionnaires is not less than 3. Furthermore, this indirectly proves the effectiveness of the four features extracted by wearable devices in long-term mental health monitoring experiments.

Table 15.1 Correlation results of audio features and mental health scales

Questionnaires	|Correlation|	Numbers	Audio features (correlation value)
AQ	>0.5	4	Formant2_max (−0.57), formant_mean5_50% (−0.57), sum_formant_50% (0.56), formant5_max (−0.53)
Positive	>0.5	6	Sum_formant_mean (−0.65), energy_max (0.56), formant2_max (0.56), timeTable_75% (0.55), formant3_max (0.53), formant5_max (0.50)
Negative	>0.5	6	Formant_count_25% (−0.75), entropy_std (0.68), formant4_mean (−0.63), sum_formant_max (0.57), brightness_min (−0.53), formant3_75% (0.53)
SAI	>0.5	4	Formant4_25% (−0.57), formant1_std (−0.51), brightness_75% (−0.50), formant_count_25% (−0.56)
TAI	>0.5	19	Entropy_75% (0.52), timeTable_std (−0.59), formant1_max (−0.53)
RSES	>0.5	9	Formant1_75% (−0.57), formant2_75% (−0.60), formant3_75% (−0.50) formant4_75% (−0.54), energy_std (−0.58), formant_count_50% (0.58)
BDI	>0.5	3	TimeTable_75% (−0.53), timeTable_min (0.51), sum_formant_50% (0.69)

15.3.3 Classification and Analysis of Individual Graphs

Classification of Individual Graphs

In the long-term mental health monitoring experiment, each participant filled out the AQ questionnaires once a week, and a total of four questionnaires were filled in. Therefore, we can judge the AQ levels by the scores of four AQ questionnaires. The labels of AQ data are determined by dividing the range of AQ questionnaire scores. The AQ levels are presented in Table 15.2.

We have constructed individual graphs for each subject using audio features. Therefore, 52 individual graphs are obtained. In order to fully mine the connection relationships of graph structure data, a GCN model has been designed to assess AQ levels of the subjects. Besides, the learning rate and the number of iterations of the evaluation model are 0.001 and 1200. tenfold cross-validation is used to prevent over-fitting and fully utilize sample data. The results are presented in Table 15.3.

Table 15.2 Divide AQ levels

| AQ levels (Labels)	AQ scores
0	= < 25
1	> 25

Table 15.3 Individual graphs are classified

Individual graphs	Validation accuracy
Fully connection	0.70
Nearest neighbor connection	0.72

As shown in Table 15.3, the classification validation accuracy of full connection and nearest neighbor connection individual graphs are 0.70 and 0.72, respectively. Because the samples are small, the verification accuracy is not very high. At the same time, the results show the verification accuracy will also be affected when the linking relationship of nodes changes.

Analysis of Individual Graphs

In order to further explore the relationships among nodes, we have used a GNNex-plainer model to generate subgraphs of individual graphs. Combined with the trained GCN evaluation model, we can get the mask matrix of the individual graphs. Subsequently, the adjacency matrixes of the subgraphs are produced by selecting an appropriate threshold of the mask matrix. The numbers of nodes of a subgraph extracted from an individual graph are set to 6, so that it can more clearly reveal the internal relationships of individual graphs.

In Fig. 15.5, for fully connected individual graphs, the subgraphs are distributed around a central node. Through statistical analysis, most of the central nodes of the subgraphs of high-scoring autism are mainly in the afternoon or evening time period, but the central nodes of the subgraphs of low-scoring autism have no obvious time period bias. In Fig. 15.6, for the individual graphs of nearest neighbor connection, most of the subgraphs of the individual graphs of the high-scoring autistic persons are distributed around a node that is the time period node of the afternoon or evening, and there are no fixed shapes for the subgraphs of the individual graphs of the low-scoring autism. So, we can find that the time periods of afternoon and evening have a greater impact on people with high scores on autism, while for people with low scores on autism, we can't find obvious time periods that have a greater impact on them.
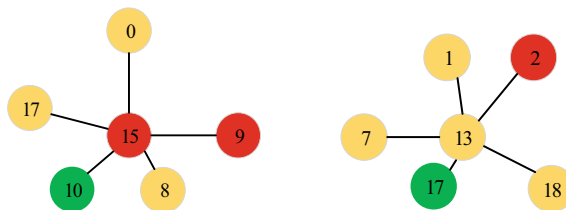
Fig. 15.5 Subgraphs of fully connected individual graphs of high-scoring autistic persons (Green, yellow, and red respectively represent morning nodes, afternoon nodes, and night nodes. The digits in the circles represent the node number and there is a total of 21 nodes in a week)

Fig. 15.6 a Subgraph of
high-scoring autistic
b Subgraph of low-scoring
autistic (Green, yellow, and
red respectively represent
morning nodes, afternoon
nodes, and night nodes)

(a)   (b)
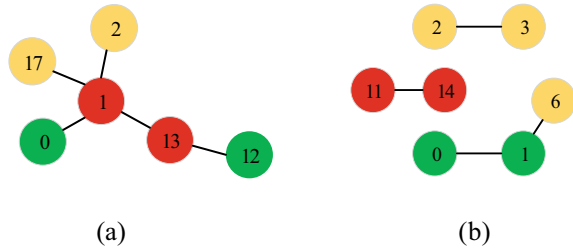
15.4 Conclusion

In the study, wearable sensing devices have been developed. The wearable devices
integrate audio, behavior, and environmental sensors. Using this system, we have
conducted a 4-week mental health experiment. For the collected audio features, we
carry out threshold analysis and correlation analysis. To explore the time period
that most affect people with high scores on autism, we further have developed a
GCN model to assess the levels of AQ. In addition, we have used the interpretability
algorithm of GCN models to investigate individual graphs. Through analysis, it can be
seen that the time periods of afternoon and evening have a greater impact on the high
scores of people with autism. In the future, more experiments will be carried out for
autistic patients to further verify our conclusions and further verify the effectiveness
of our proposed system.

References

1. Abdullah, S., Choudhury, T.: Sensing technologies for monitoring serious mental illnesses.
   IEEE Multimed. **25**(1), 61–75 (2018)
2. Olguin, D.O., Waber, B.N., Kim, T., Mohan, A., Ara, K., Pentland, A.: Sensible organizations:
   technology and methodology for automatically measuring organizational behavior. IEEE Trans.
   Syst. Man & Cybern. Part B Cybern. **1**(39), 43–55 (2009)
3. Sano, A., et al.: Prediction of happy-sad mood from daily behaviors and previous sleep history.
   In: 2015 37th Annual International Conference of the IEEE Engineering in Medicine and
   Biology Society (EMBC), pp. 6796–6799 (2015).
4. Mahmud, M.S., Wang, H., Hua, F.: SensoRing: an integrated wearable system for contin-
   uous measurement of physiological biomarkers. In: 2018 IEEE International Conference on
   Communications (ICC), pp. 1–7 (2018)
5. Ghandeharioun, A., Fedor, S., Sangermano, L., Ionescu, D., Picard, R.: Objective assessment
   of depressive symptoms with machine learning and wearable sensors data. In: 2017 Seventh
   International Conference on Affective Computing and Intelligent Interaction (ACII), pp. 325–
   332 (2017)
6. Perez, M.V., Mahaffey, K.W., Hedlin, H., Rumsfeld, J.S., Turakhia, M.P.: Large-scale assess-
   ment of a smartwatch to identify atrial fibrillation. N. Engl. J. Med. **20**(381), 1909–1917
   (2019)
7. Maritsch, M., Bérubé, C., Kraus, M., Lehmann, V., et al.: Improving heart rate variability
   measurements from consumer smartwatches with machine learning. ACM (2019)

8. Costa, J., Adams, A.T., Jung, M.F., Guimbretiere, F., Choudhury, T.: EmotionCheck: a wearable device to regulate anxiety through false heart rate feedback. Getmobile Mob. Comput. & Commun. **2**(21), 22–25 (2017)

9. Costa, J., Guimbretiere, F., Jung, M.F., Choudhury, T.: BoostMeUp: improving cognitive performance in the moment by unobtrusively regulating emotions with a smartwatch. Proc. ACM Interact. Mob. Wearable Ubiquitous Technol. **2**(3), 1–23 (2019).

10. Ying, R., Bourgeois, D., You, J., Zitnik, M., Leskovec, J.: GNNExplainer: generating explanations for graph neural networks. Adv. Neural Inf. Process. Syst. **32**, 9240–9251 (2019)

11. Kipf, T. N., Welling, M.: Semi-supervised classification with graph convolutional networks. arXiv(2017). https://doi.org/10.48550/arXiv.1609.02907

12. Zhou, J., Cui, G., Hu, S., Zhang, Z., Yang, C., Liu, Z., et al.:Graph neural networks: a review of methods and applications. AI Open. 57–81 (2020)

Chapter 16
Music Personalized Recommendation System Based on Deep Learning

Chaozhi Cheng

Abstract In the Internet age, these have brought great convenience for users to obtain personal preference information. Among them, personalized recommendation algorithm is a very key problem. The music personalized recommendation system studied in this paper combines DL (Deep learning) technology, uses CNN (Convolutional Neural Network) to predict the hidden features of music, and obtains the low-dimensional vector representation of music features. Combined with the hidden representation of user preferences, it learns the hidden layer output of auxiliary information through AE (Autoencoder) and then integrates it into the traditional personalized recommendation algorithm. Finally, a reasonable personalized recommendation is generated for relevant users. According to the experimental results, with the increase in the number of prediction scores, the value of MAE (Mean Absolute Error) decreases continuously. The MAE of this model is lower than other models, and it has a better recommendation effect. The reliability of the personalized music recommendation system established in this paper is verified.

16.1 Introduction

With the rapid rise of network technology and electronic information technology, technologies such as big data, cloud computing, robotics, artificial intelligence and DL (Deep learning) have also developed rapidly, which provide huge computing resources for the progress and development of the whole information age [1]. In the Internet age, these have brought great convenience for users to obtain personal preference information. In the recommendation system, the design of personalized recommendation algorithm is particularly important.

The music industry has gradually turned to online music. Faced with such a huge network user group, intelligent music recommendation has become an inevitable trend in the development of online music platforms. With the popularity of DL

C. Cheng (✉)
College of Music and Dance, Huaihua University, Huaihua, China
e-mail: ccz175@163.com

method in recent years, more and more personalized recommendation systems have begun to use DL method [2, 3]. Some studies have adopted LSTM (Long Short-Term Memory) network to recommend HashTag in Weibo [4]; Researchers put forward a way to extract features from audio signals by CNN (Convolutional Neural Network). Their main method is to get the feature vectors of music by matrix decomposition [5]. Similar music has similar feature vectors, so they can recommend similar music to users. Literature [6] proposes a hybrid recommendation system based on DL, which integrates external information about users and items into deep neural network by using embedding technology, thus alleviating the cold start problem.

Music is an ancient art that can bring happiness to human beings. However, in order to accurately find songs that meet users' requirements in a large number of music works, we must choose songs that meet users' preferences according to their preferences. On this basis, a new method of music personalized recommendation based on DL is proposed. The recommendation system can predict users' usage habits based on their usage habits and the characteristics of music data, and actively recommend music suitable for users [7, 8]. On this basis, this project plans to adopt the classic personalized recommendation method based on DL, and realize the effective mapping of users and songs through AE (Autoencoder) and CNN (Convolutional Neural Network). On this basis, according to different user preferences and different song content, the similarity analysis is carried out to get songs suitable for different songs.

16.2   Research Method

16.2.1   Recommend Algorithm Classification

Content-based Recommendation Algorithm

Based on the content-based recommendation method, the characteristics of users and objects are extracted, the user's preference model is constructed, and the matching degree between the characteristics of information to be selected and the user's preference model is calculated to produce recommendation results. The traditional content-based recommendation algorithm first obtains the items that have interacted with users, and then obtains the user's preference model through similar user active behaviors such as user's praise or rating of the items. Content-based recommendation mechanism uses items that have interacted with users, and obtain users' interest in different items through similar user behaviors such as praise, click, or rating. And collect similar items with high user interest, and then rearrange the recommendation degrees of these collected items and put them in the list to be recommended.

Collaborative Filtering Recommendation Method

Collaborative filtering recommendation is one of the most influential and widely used algorithms in industry. It is mainly divided into two categories: one is collaborative

filtering based on users, and the other is collaborative filtering based on items. There are similarities and great differences between them. The main idea of collaborative filtering based on items is to find items with high similarity and positive feedback in the user's historical behavior records by analyzing the user's historical records, and recommending them to the target users after sorting. Its underlying assumption is that if almost all users who like one item like another item, the two items have the greatest similarity; If a user's interest list includes two specific items, it has a high probability of belonging to a specific field, but if two items are included in most users' interest lists, it has a high probability of belonging to the same field.

Matrix Decomposition Recommendation Algorithm

In the scoring prediction scenario of recommendation system, blank records are filled by matrix decomposition, which alleviates the sparsity of data to some extent. In the matrix decomposition algorithm, the scoring matrix is decomposed into the form of multiplication of user feature matrix and item feature matrix, and the potential features of users and items are mined to predict the scoring of unrated items and reduce missing values. In many cases, the form of simple matrix decomposition and multiplication can not restore the scoring matrix well, and there are certain errors, which can be continuously reduced by combining gradient descent. When the user-item scoring matrix is very sparse, the gradient descent method is used to continuously reduce the error loss value, and at the same time, it is easy to produce the phenomenon of over-fitting, that is, the existing data is well fitted but the prediction effect of the missing value is not good.

16.2.2   Overall Design of Recommendation System

In the era of network information overload, how to maximize the information in the network has become the focus of attention. According to the keywords input by users, on this basis, a new recommendation method with wide application prospect is proposed. Although the information transmission mode between search engine and recommendation system is different, there are some differences between them. In the music industry, the earliest cooperative screening algorithms are based on clear feedback, that is, according to users' comments on a song or a singer. Aiming at the current recommendation system and different application scenarios, a common classification algorithm is given. When the information of a person or an object is used, it is considered as a content-based information recommendation. If the recommendation system uses interactive data generated by users and items, it is considered as a recommendation system based on collaborative filtering.

For music recommendation system, collaborative filtering algorithm has more practical experience. Because most users don't have the habit of evaluating music, users' rating data of music is sparse. The application of DL method in recommendation system is a new trend, which provides a new idea under the complicated situation

of music data processing [9]. Although most music systems or data sets have corresponding music tags, the problem of tag missing is still serious. The problem of missing music labels is quite common. When making music recommendation, it will face the challenge of completing or correcting labels. It is necessary to extract music features by using neural network model and label and classify music. For example, the "list" label under the "theme" standard has nothing to do with the characteristics of music itself, and this part of the label needs to be removed when the classification model is actually operated.

At present, CNN has been widely used in the fields of image and text recommendation. However, the key point of this topic is that, under the framework of CNN, it is fundamentally a composite recommendation model that integrates music content and users' historical behavior. The core idea is as follows: firstly, based on CNN, the hidden characteristics of songs are predicted and the low-dimensional vector expression of songs is obtained; Secondly, on this basis, based on AE learning, the implicit characteristics of songs are combined with the implicit characteristics of songs, and they are combined with classical song recommendation algorithms. In the training process, the tightly coupled model learns the parameters of AE and traditional personalized recommendation algorithm at the same time, and the two methods influence each other, so that the traditional personalized recommendation algorithm can provide prior knowledge when the hidden layer of AE learning features is output, and finally generate reasonable personalized recommendation for relevant users.

On the Internet, faced with a huge group of users, intelligent recommendation of music becomes more important, so that users can better find music that suits their preferences, and music services on the Internet become more attractive, thus increasing the profits of enterprises [10]. Through the research of this project, we can enrich the information of music recommendation, solve the problems of "cold start", "sparseness" and "scalability" in traditional music recommendation to some extent, and better meet the needs of users for personalized music. On this basis, this paper proposes a personalized music recommendation system based on DL (Fig. 16.1).

The system mainly includes user modeling module, music feature extraction module, and personalized recommendation algorithm module. The music feature extraction module is mainly used to preprocess audio content and extract spectral features, so as to prepare for training CNN to obtain the regression model of music potential feature prediction.

The realization of the whole system function mainly includes the following steps:

(1) Collect the historical behavior data of users in the system, and construct a hidden semantic model that can reflect the relationship between users and music according to a unified quantitative standard;
(2) Pre-processing the original music resource file, and extracting the spectrogram which can represent the music audio characteristics;
(3) Construct a convolutional neural network model, take the extracted spectrum as the input of the network model, and finally get the CNN regression model;

(4) When there are new music resources in the system, the audio feature map is also obtained first, and then the potential features of music are predicted by using the obtained CNN regression model. Combined with the user's preference model, the user's interest in music is calculated and sorted, and finally, the first new music resources of TopN are recommended to relevant users.

All data services of the system are exposed through the interface, and authorized calls can use the data services of the system service layer at will. The data service of the service layer interacts with the data layer through the persistence layer. The offline computing engine interacts with the data layer through the persistence layer and stores the offline computing results in the database. Recommend other music lovers who may be interested to users. In QQ music, song lists are created by users, and a user can create multiple song lists. Click on the user's details and the song list entries created by the user, as well as similar user recommendations based on the current viewing user.

16.2.3 Design of Personalized Music Recommendation Algorithm

Traditional recommendation algorithms have great limitations in the process of music recommendation. With the continuous development of DL, many music recommendation methods combining traditional recommendation algorithms with DL have emerged in the field of music recommendation. Most of them pay attention to the historical behavior data of users, but ignore the potential information. Because of the repetitive characteristics of historical behavior data, the recommended music is similar, and there are problems such as sparse data and cold start.

At present, mature commercial solutions are divided into two categories: search engine and recommendation system. Search engine is designed for users who have certain retrieval goals and needs. It can retrieve the information they need through keywords typed by users. On this basis, a new recommendation method with wide application prospect is proposed. There are two common characteristics in the applicable fields of recommendation system: first, there is a large amount of data in this field, and users do not have enough energy and time to contact and understand all items; Second, users have no clear demand for items in this field. Most of the fields that meet this feature are concentrated in the field of pan-entertainment, such as music, books, news, e-commerce, and so on. In the development of artificial intelligence, personalized recommendation algorithm combining DL and reinforcement learning emerged [11]. In the long river of recommendation system development, the traditional personalized recommendation algorithm played a key role in connecting the past with the future, and then the emerging personalized recommendation algorithms all improved and innovated on its basis.

At present, personalized recommendation technology has penetrated into every corner of the network, such as QQ music, which is closely related to users' browsing

records and personal information. Personalized recommendation system is based on a variety of information, analyzing users' preferences, thus judging the products that users may be interested in, and then displaying these products within the acceptable range of users, waiting for users to choose, which can be considered as a subjective behavior of personalized recommendation system. The conversion rate of push is also lower than that of personalized recommendation, and it will also cause users' disgust because of the deviation between the pushed content and users' preferences or the frequent push.

In this paper, we will introduce a personalized music recommendation algorithm based on CNN. CNN belongs to a feedforward neural network, which is different from multi-layer receptors in its connection mode. Among them, the connection mode of multi-layer perceptual network is a complete connection, and it is composed of convolution layer, pooling layer, and complete connection layer. CNN convolves multi-dimensional features, which can effectively extract more features, especially for images, voices, and other multi-dimensional features.

In the framework of CNN, there is a pool behind the convolution layer. The role of the pool is to compress the input data to a smaller scale, and then repeat the process, and then extract more data, and finally obtain a complete data. Based on the network structure of Le Net5, this paper studies the basic principles of CNN architecture as summarized above by drawing lessons from several other good convolutional neural networks. On this basis, a personalized music recommendation model based on 7-level network is proposed (Fig. 16.2).

The neural network consists of four convolution-pooling structures, in which two convolution-pooling structures cross each other to form two perfectly connected structures and a prediction output layer. In the input layer, each pixel size is $256 \times 256 \times 1$, which is the Mel spectrum extracted from the sound. This method uses the method of maximum pool and sets the size of the pool window as 2×2.
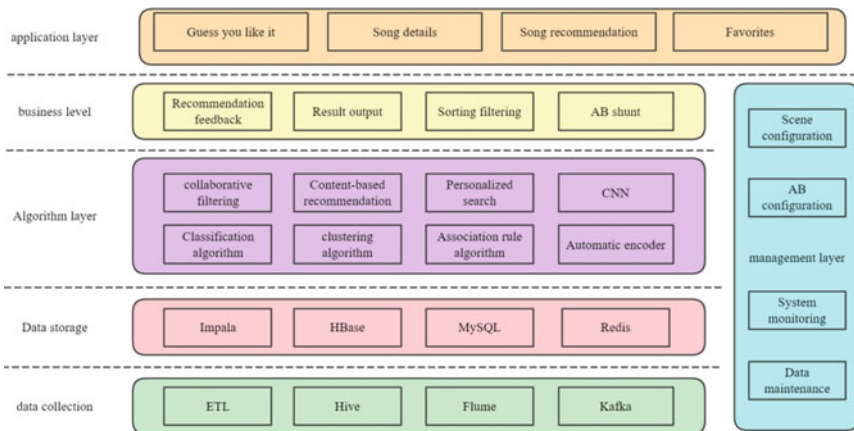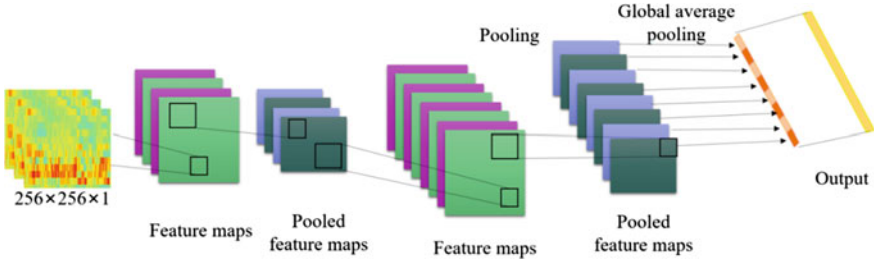

Fig. 16.1 Overall design block diagram of music personalized recommendation system

Fig. 16.2 CNN network model structure for personalized music recommendation

For a piece of music, descriptive information (music name, introduction, lyrics) and audio itself can represent its unique attributes. Among them, the feature of audio is the most unique and effective information representation of a piece of music. Through this feature, this paper can distinguish different music to the greatest extent. Converting sound signal into image representation can better use CNN to extract features [12].

Map Hertz frequency f to Mel frequency $mel(f)$, as shown in Formula (16.1):

$$mel(f) = 2595 \times \log_{10}\left(1 + \frac{f}{700}\right) \tag{16.1}$$

According to the Mel frequency obtained by Mel mapping formula, the perception of Mel frequency by human hearing is linear. When the Mel frequency of audio is doubled, the tone that human ears can perceive is also doubled. Mel spectrum uses human auditory perception characteristics to generate spectrum, and combining this characteristic with neural network can greatly improve the effect of automatic music classification.

AE is an unsupervised machine learning method based on coding and decoding. This method uses coding and decoding to reconstruct the input information and learn an implicit hierarchical expression from it. Acoustic emission consists of the following two steps:

Encoding process from input layer to hidden layer:

$$h = f(x) = \sigma\left(W'x + b\right) \tag{16.2}$$

Decoding process from hidden layer to output layer;

$$\tilde{x} = g(h) = \sigma\left(W^T h + b\right) \tag{16.3}$$

where W, b is the weight and bias term of the feature, $\sigma(\cdot)$ is the activation function, and AE aims to reconstruct the data in the input layer at the output layer, so its loss function combines different data forms.

Generally, the activation functions of artificial neural networks mainly include Sigmoid, Tanh, ReLU ELU, etc. The CNN model proposed in this paper chooses ReLU as its training activation function and Softmax as its output layer activation function.

ReLU, which is called rectifier linear element, is the mainstream activation function in the current network model. As shown in formula (16.4).

$$f(x) = relu(x) = \begin{cases} x, & x > 0 \\ 0, & other \end{cases} \quad (16.4)$$

ReLU has no negative value, it is hard saturated at $x < 0$, and its derivative is 1 at $x > 0$.

Softmax is often used for multi-classification and is used as the activation function of the prediction output layer in this model, as shown in Formula (16.5).

$$f(x)_j = \text{Softmax}(x)_j = \frac{e^{z_j}}{\sum_{i=1}^{k} e^{z_j}} \quad (16.5)$$

In order to ensure that the CNN network model will neither fail to fit nor over-fit, taking the gradient descent algorithm as an example, the parameter momentum update in the network can be expressed as follows:

$$\theta \leftarrow mu * \theta - \eta \frac{\partial L(\theta)}{\partial \theta} \quad (16.6)$$

In the formula, mu represents momentum, and the value of momentum coefficient is 0 ~ 1, and the commonly used values are 0.5, 0.9, 0.95, and 0.99. By adopting this parameter updating method, we can not only speed up the learning rate and increase the stability, but also have some ability to get rid of local optimization.

16.3   Experimental Analysis

The experimental data is a self-built QQ music data set, which contains user data, music data, singer data, song list data, and user music playing history data from QQ music. The physical environment of the experiment consists of Ubuntu as the operating system, Intel(R) Xeon(R) E5-2678 v3 as the processor, with a main frequency of 2.5GHZ and a turbo frequency of 3.1 GHz, and NVIDIA GeForce GTX 1080Ti as the graphics card. Adam is used to optimize the embedding dimension adjustment layer and recommendation model, and the learning rate is set to 0.0001 and 0.003 respectively. The dimension size of the fixed embedding vector is 8. The batch data size of the whole model during training is 500.
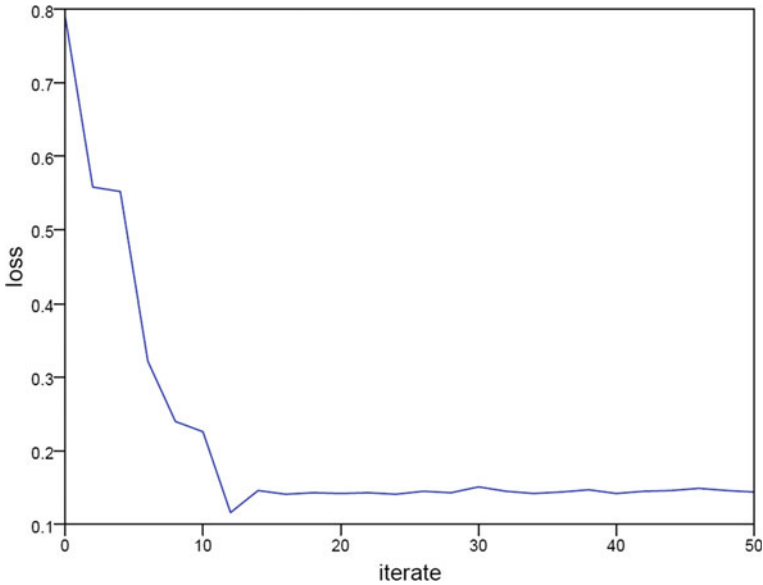
Fig. 16.3 Loss curve of training model

In this experiment, MSE (mean-squared error) is used as the loss function, and the CNN network model is trained by using the training set data. The training result is shown in Fig. 16.3.

We can see that with the increase of iterations, the loss error of the network model will decrease rapidly at first, and then it will decrease slowly. When the age reaches 12, the error will decrease to 0.116, the function will tend to converge, and the training process of the model will basically meet the expected requirements.

For the music recommendation model proposed in this paper, the scores of users' songs are predicted respectively, and the predicted scores of 10, 20, 30, 40, and 50 pieces of music are randomly selected to calculate MAE (Mean Absolute Error). The experimental results are shown in Fig. 16.4.

According to the experimental results, the MAE of this model is lower than the other two models, and it has a better recommendation effect. With the increase in the number of forecast scores, the value of MAE decreases continuously. The results show that the CNN combined with AE model proposed in this paper has the best model efficiency under MAE index, and also has the best anti-sparsity ability. The cold start problem of new items is solved, and the risk of over-fitting and falling into local minimum in the process of scoring matrix is reduced.
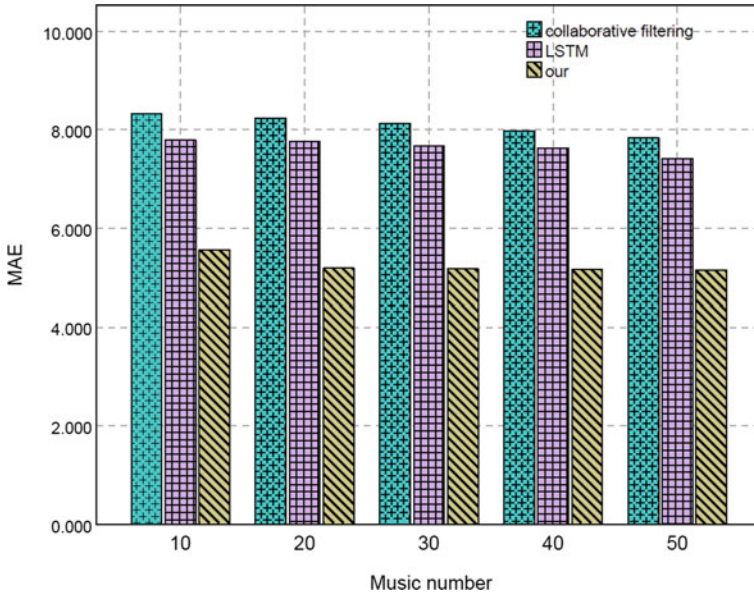
Fig. 16.4 The recommended model compares the experimental results

16.4 Conclusion

Personalized recommendation system plays a very important role in e-commerce system, audio and video playing platform, and news information software. How to predict users' interests based on their historical behavior data and other available information, so as to provide them with more accurate recommendations of products they are interested in, and thus improve their user experience, is the goal pursued by many scholars and application developers. The music industry has gradually turned to online music. Faced with this huge network user group, music intelligent recommendation has become a hot spot of online music service. On this basis, using AE, CNN, and other machine learning methods, a personalized music recommendation system based on DL is constructed to effectively mine information such as users and music. According to the experimental results, with the increase in the number of prediction scores, the value of MAE decreases continuously. The MAE of this model is lower than other models, and it has a better recommendation effect.

References

1. Zhang, J., Yang, Y., Tian. Q., Zhuo, L., Liu. X.: Personalized social image recommendation method based on user-image-tag model. IEEE Trans. Multimed. **19**(11) (2017)

2. Zhou, L., Wang, C.. Research on Recommendation of Personalized Exercises in English Learning Based on Data Mining. Scientific programming, Vol. 2021(14). pp.5042286.1–5042286.9(2021).
3. Wang, C.Y., Wang, Y.C., Chou, S.: A context and emotion aware system for personalized music recommendation. J. Internet Technol. **19**(3), 765–779 (2018)
4. Zhang, L., Tian, Z.: Research on the recommendation of aerobics music adaptation based on computer aided design software. J. Intell. Fuzzy Syst. **2**, 1–12 (2021)
5. Shi, J.: Music recommendation algorithm based on multidimensional time-series model analysis. Complexity **2021**(1), 1–11 (2021)
6. Li, M., Bao, X., Chang, L., et al.: Modeling personalized representation for within-basket recommendation based on deep learning. Expert. Syst. Appl. **192**(8), 116383 (2021)
7. Quintanilla, E., Rawat, Y. S., Sakryukin, A., et al.: Adversarial learning for personalized tag recommendation. IEEE Trans. Multimed. **23**, 1083–1094 (2020)
8. Yang, X., Zhou, Z., Xiao, Y.: Research on students' adaptive learning system based on deep learning model. Sci. Program. **2021**(Pt.13), 6593438.1–6593438.13 (2021)
9. Wang, M.: Applying Internet information technology combined with deep learning to tourism collaborative recommendation system. PLoS ONE **15**(12), 6 (2020)
10. Wang, X. Y., Chen, Q. Y.: Research on personalized recommendation system of libraries based on deep learning. Mod. Sci. Instrum. (6), 4.4–47 (2018)
11. Li, Q. N., Li, Ti. H.: Research progress of context-aware recommendation system based on deep learning. Comput. Syst. Appl. **29**(2), 8 (2020)
12. Shi, Y.Q., Liu, S.Y., Mao, C.: Research on object detection and content recommendation system in short video based on deep learning. Comput. Mod. **11**, 1 (2018)

Chapter 17
Handwritten Mathematic Expression Conversion to Docx

Bharti Sharma, Tripti Rathee, Minakshi Tomer, and Parvinder Singh

Abstract   This paper aims to embed Handwritten Mathematical Expressions (HME) directly into a Docx document. Writing Mathematical Expressions within a WYSIWYG (what you see is what you get) editor is a cumbersome task which requires a lot of manual effort, which this paper tries to automate. Methods: The task of Recognizing Mathematical Expression is bifurcated into two sub-tasks i.e. structural analysis and symbol recognition. This paper proposes to use deep learning techniques to do these sub-tasks using an end-to-end Densenet based encoder and Attention-Based decoder model, respectively. Findings: The model is trained on CROHME (Competition on Recognition of Online Handwritten Mathematical Expressions) dataset which consists of InkML files. These InkML files are initially processed to generate images and MathML from them. Novelty: We have been successful in creating docx from HME with accuracy trade-off of 1–2% by significantly reducing computational complexity than any other Web application based pre-existing techniques.

17.1   Introduction

Mathematics is called the "handmaiden of science", hence it plays a pivotal role in all scientific research done. Mathematics always presents itself in the form of equations, and Handwritten Mathematical expressions are the primary method of writing equations, which later is encoded in LaTeX or mathML for proper rendering on digital documents. However, automatically recognizing and converting them to

B. Sharma · T. Rathee (✉) · M. Tomer
Maharaja Surajmal Institute of Technology, New Delhi, India
e-mail: rathee.tripti@gmail.com

B. Sharma
e-mail: bhartisharma@msit.in

P. Singh
Deenbandhu Chhotu Ram University of Science and Technology, Murthal, India

an appropriate format remains a difficult task because of the nature of Handwritten Mathematical Expressions (HMEs). These problems include the two-dimensional nature of HMEs [1, 2] i.e. it tends to be related in a spatially.

Solving the HMEs problem can be broken down into two major stages, symbol recognition and structural analysis. Structural analysis may be done in two ways, which is sequentially and globally. Sequential analysis [3] first deals with symbol recognition and then proceeds to structural analysis. Whereas the global approach tends to deal with both of them at the same time. Sequential analysis and global analysis come with their own share of problems such as they require prior knowledge about the type of expressions to be generated for generating the parser. The complexity of the parser increases with increase in symbols dealt by the parser. They do not take into consideration the semantic context among associated symbols to deal with ambiguous symbols in case of sequential parsers.

In the last decade or so, encoder-decoder model have been utilized to solve the problem of HMEs because of its application in machine translation [4]. We propose a variation of encoder-decoder model which requires less time and has less complexity during the training phase. The model is trained to take as input images of HMEs and produce mathML strings which can be directly embedded within any word processor that accepts mathML. The overall goal of this is to generate document file such as .docx which a WYSIWYG text editor containing the mathematical expression since complex mathematical expressions are more often required within scientific documents and writing mathematical equations within the document with the present methods of manually adding expressions within the document is a hassle which we are trying to solve. MathML is a XML based document and since most text editors are XML based indirectly the conversion is a trivial task provided that the text editor supports that symbol and there exists a XLTS transformer that can convert MathML to a format used by the word processor.

The rest of the paper is organized as follows: Sect. 17.2 describes the related work summary. Section 17.3 describes the proposed methodology. Section 17.4 discusses the results and comparison, and finally Sect. 17.5 concludes this paper.

17.2 Related Work Summary

HMER consists of two elemental components that are symbol recognition and structural analysis. Provided the two dimensional nature of a mathematical expression for its structural analysis, many researchers prefer approaches based on predefined grammars as natural way to solve the problem. Several types of math grammars have been scrutinized. Chan and Yeung [5] have used definite clause grammars in their paper. However, their system works only on online mathematical expression; they have not demonstrated it on offline data set. The authors in [7] showed the fruitfulness of stochastic context-free grammars on various systems as they typically performed great in the CROHME competitions. Approaches based on probabilistic context-free grammars analyses the structure of mathematical expression and deals

with ambiguities in handwritten data, such an approach based on PCFG was proposed by [6, 8]. However, the proposed approach deals with only online maths expressions and in their future work they intend to apply it in offline mathematical expression recognition for both printed and hand written. The authors in [9] have proposed a novel neural network framework, namely encoder-decoder for sequence to sequence learning. The encoder decoder model has many applications including [10–12].

17.3 Methodology
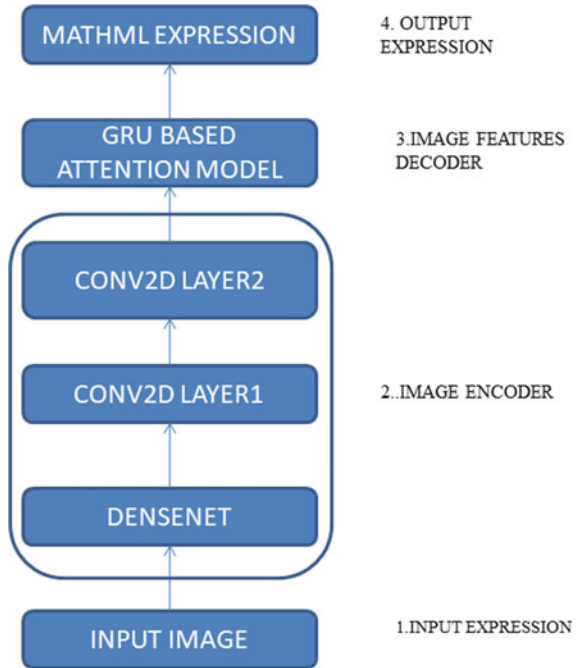
17.3.1 Overview

The encoder within our model is a pretrained Densenet [13] model with two subsequent Fully Convolutional Layer (FCN) [14] that results in encoded image features. The decoder is Recurrent neural network (RNN) [15] with gated recurrent units (GRU) [16] that converts the encoded image features into mathML string which is our desired output. The resultant model is (1) end-to-end trainable. (2) Produces expression based on data rather than predefined grammar (3) takes into account the semantic context of the symbol to choose the best symbol and position. The data used for the training and validations is CROHME dataset which consists of stroke metadata (pen-up, pen-down sequence) during generation of expression as well as the ground truth in the form of MathML. The flowchart of the proposed methodology is represented in Fig. 17.1.

17.3.2 Dataset Preprocessing

The handwritten expression are usually stored in images that can vary in quality and size, and image preprocessing is done to prepare images in specific format to feed into the encoder. The preprocessing includes image resizing image, center cropping and normalizing the image pixel values to keep values in range. The MathML corresponding to each image expression is stored separately with same name as image file. The MathML expression is consist of predefined tags, operator symbols, operand symbols following the pattern of one symbol at a between tags (opening and closing). MathML is a 2 dimensional representation of the input handwritten expression. The mathml expression is divided into tokens of tags, operator symbols, and operand symbols.

Fig. 17.1 Flowchart of
proposed model

MATHML EXPRESSION — 4. OUTPUT EXPRESSION

GRU BASED ATTENTION MODEL — 3.IMAGE FEATURES DECODER

CONV2D LAYER2

CONV2D LAYER1 — 2..IMAGE ENCODER

DENSENET

INPUT IMAGE — 1.INPUT EXPRESSION

17.3.3 Encoder

The Encoder takes transformed image to convert the 3 channel image to N channel feature matrix which is an intermediate form for decoder input. The encoder is consist of Densenet and convolution layers stacked over one another. The Densenet consist of denseblocks, in each denseblock the concatenation of the outputs of preceding layers is fed as input in succeeding layers. Let $\mathbf{H_l}(.)$ denote the convolution functionof the lth layer, then the output of layer l is represented as:

$$x_l = H_l\big([x_0; x_1; x_2; \ldots; x_{l-1}]\big) \qquad (17.1)$$

where x_0, x_1, …, x_l denote the output features produced in layers 0, 1, …, l, ";" denotes the concatenation operation of feature maps.

The connections established between layers enables Densenet to use features extracted in previous layers and easy gradient propagation to initial layers. Also, this mechanism strengthens features extraction in Densenet without implementing much deeper convolution layers.

In this paper, pre trained Densenet model provided by pytorch has been used. Using pre trained Densenet has its advances as it reduces the cost of training such complex and memory consuming architecture is easier to load. The output produced by Densenet is larger in size. CNN has been largely used to reduce the size of

representational *n*-dimensional matrix without affecting features represented by the *n*-dimensional matrix. Thus, the last layers of Densenet model are removed to make model work as a feature extractor instead of a classifier. Then two convolution layers are layered over output of Densenet to reduce the size of output to optimal feature representation. The proposed model takes as input a raw expression image and generates corresponding MathML sequence.

17.3.4   Decoder

The input block of the decoder provides one-hot encoding of the input word to the embedding layer. The embedding layer converts the one-hot encoding of input word to word embedding of hidden_size, H length vector. Word embedding is an efficient way to represent relation between words in a vocabulary. Embedding is a dense vector of floating points that represents a word's features and more importantly, these features can be learned via training of the embedding layer. The working of decoder has been shown in Fig. 17.2.

Let x_i be the one hot encoding of input word and O_{en} represent the encoder output. Then, O_e represent the output of embedding layer which takes as input a vector of vocabulary size and gives output vector of H size.

$$O_{emm} = W_{emm}x_i \tag{17.2}$$

The previous hidden state h_{t-1}, a vector of size H that corresponds to the last hidden state generated by the GRU.
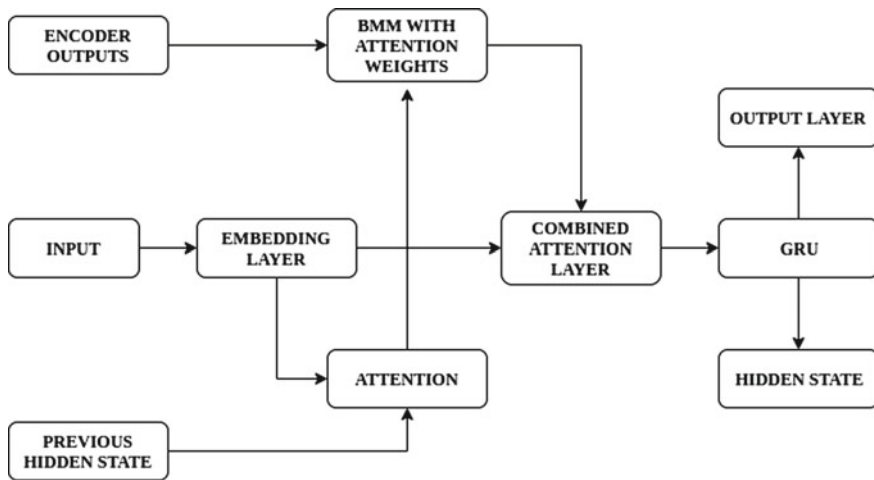

Fig. 17.2 Decoder

$$x_{\text{attn1}} = \{O_{\text{emm}}; h_{t-1}\} \tag{17.3}$$

Then, x_{attn1} is the concatenation of the embedding output and previous hidden state. Attention block which is a linear layer which takes input of size 2*H and gives output of size H is applied on x_{attn1}.

$$O_{\text{attn1}} = \text{softmax}(W_{\text{attn1}}x_{\text{attn1}} + b_{\text{attn1}}) \tag{17.4}$$

O_{attn1} represents the output of attention block which act as attention weights for the encoder output.

Softmax activation function is used to convert real values to probabilities so it can be applied on encoder output.

$$x_{\text{in}} = O_{\text{attn1}} \otimes O_{\text{en}} \tag{17.5}$$

x_{in} is the element-wise multiplication of attention weights and encoder output

$$x_{\text{out}} = \{O_{\text{emm}}; x_{\text{in}}\} \tag{17.6}$$

x_{out} represents the concatenation of embedding output and x_{in}, , which is input to second attention block called attention combined which is also a linear layer which takes input of size 2*H and gives output of size H.

$$O_{\text{attn2}} = \text{RELU}(W_{\text{attn2}}x_{\text{out}} + b_{\text{attn2}}) \tag{17.7}$$

The rectified linear activation function (RELU) is used as it is a piecewise linear function that will output the input directly if is positive; otherwise, it will output zero. O_{attn2} is the output of combined attention layer, and it is a vector of size H. O_{attn2} is the input to GRU block of the decoder.

$$x_t = O_{\text{attn2}} \tag{17.8}$$

GRU is an improved version of RNN which solves the problems of vanishing and exploding gradients. Let x_t be given input to GRU and the output h_t is computed as:

$$h_t = \text{GRU}(x_t, h_{t-1}) \tag{17.9}$$

Softmax activation function is applied on GRU output to generate vector of output probabilities, and argmax is applied to predict the output word.

17.3.5   Document

The predicted mathml is parsed to a tree structure and inserted into a word document using python libraries i.e. python-docx, xET.

17.4   Result and Comparison

This section describes the system settings for the experimentation purpose and the evaluation matrices used

17.4.1   Experimental Setup

The system is implemented on Intel(R) Core(TM) i5, 3.30 GHz CPU, 4 cores and 8 GB RAM. During training of the model the factors considered are loss and Validation.

The red line in Fig. 17.3 represents the value of Log loss, and the blue line represents validation loss.

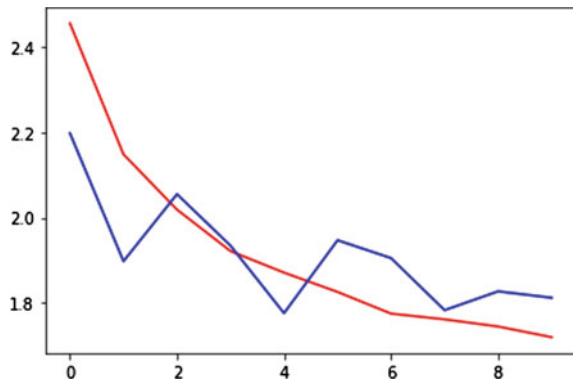Figure 17.4 shows decrease in loss in Red and increase in Bleu score on Test set in Blue curve with epochs.

Model comparison By Bleu Scores (see Table 17.1):

Initial predictions—<mrow><mi><mi></mi><mrow><mo><mi></mi>
<mrow><mi><mo></mi></mrow>

Original value—<mrow><mi> x</mi> <mrow> <mo> + </mo> <mi> y </mi></mrow></mrow>

The resultant output of Fig. 17.5 image comes out to be $x + y$.

Fig. 17.3 Loss and validation graph

Fig. 17.4 Loss and BLEU score
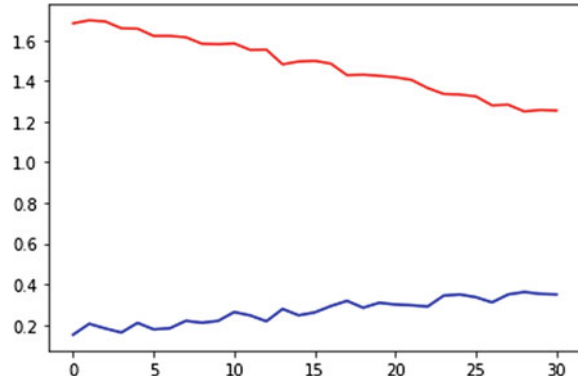
Table 17.1 Comparison results
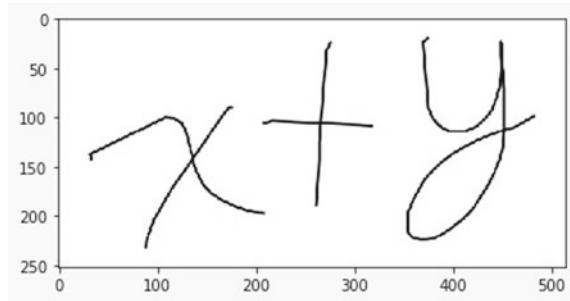
After epochs	Multi-scale model	Encoder-decoder model
10	0.36	0.32
20	0.43	0.47
30	0.55	0.56
40	0.59	0.62

Fig. 17.5 Input handwritten expression

17.5 Conclusion

In this paper, we concluded that using a pre-trained dense encoder model we can train an attention model with features to provide good accuracy. Densenet provides better image features than most of the state of the art models present for image segmentation and feature extraction. This reduces the computational cost significantly that is used to train a Densenet. Also, the MathML conversion of feature vectors provides a base for conversion to other standard formats of mathematical expressions. Also, the GRU based Architecture of Decoder is uniquely defined and experiments have been done regarding its effectiveness.

References

1. Anderson, R.H.: Syntax-directed recognition of hand-printed two-dimensional mathematics. In: Symposium on Interactive Systems for Experimental Applied Mathematics: Proceedings of the Association for Computing Machinery Inc. Symposium, pp. 436–459 (1967)
2. Belaid, A., Haton, J.P.: A syntactic approach for handwritten mathematical formula recognition. IEEE Trans. Pattern Anal. Mach. Intell. **1**, 105–111 (1984)
3. Zanibbi, R., Blostein, D., Cordy, J.R.: Recognizing mathematical expressions using tree transformation. IEEE Trans. Pattern Anal. Mach. Intell. **24**(11), 1455–1467 (2002)
4. Cho, K., Van Merriënboer, B., Gulcehre, C., Bahdanau, D., Bougares, F., Schwenk, H., Bengio, Y.: Learning phrase representations using RNN encoder-decoder for statistical machine translation (2014). arXiv:1406.1078
5. Chan, K.F., Yeung, D.Y.: Error detection, error correction and performance evaluation in on-line mathematical expression recognition. Pattern Recogn. **34**(8), 1671–1684 (2001)
6. Álvaro, F., Sánchez, J.A., Benedí, J.M.: An integrated grammar-based approach for mathematical expression recognition. Pattern Recogn. **51**, 135–147 (2016)
7. Sako, S., Nishimoto, T., Sagayama, S.: On-line recognition of handwritten mathematical expressions based on stroke-based stochastic context-free grammar. In: Tenth International Workshop on Frontiers in Handwriting Recognition. Suvisoft (2006)
8. MacLean, S., Labahn, G.: A new approach for recognizing handwritten mathematics using relational grammars and fuzzy sets. Int. J. Doc. Anal. Recognit. (IJDAR) **16**, 139–163 (2013)
9. Bahdanau, D., Cho, K., Bengio, Y.: Neural machine translation by jointly learning to align and translate (2014). arXiv:1409.0473
10. Bahdanau, D., Chorowski, J., Serdyuk, D., Brakel, P., Bengio, Y.: End-to-end attention-based large vocabulary speech recognition. In: 2016 IEEE International Conference on Acoustics, Speech and Signal Processing (ICASSP), pp. 4945–4949. IEEE (2016)
11. Chan, W., Jaitly, N., Le, Q.V., Vinyals, O.: Listen, attend and spell (2015). arXiv:1508.01211
12. Luong, M.T., Sutskever, I., Le, Q.V., Vinyals, O., Zaremba, W.: Addressing the rare word problem in neural machine translation (2014). arXiv:1410.8206
13. Iandola, F., Moskewicz, M., Karayev, S., Girshick, R., Darrell, T., Keutzer, K.: Densenet: implementing efficient convnet descriptor pyramids (2014). arXiv:1404.1869
14. Long, J., Shelhamer, E., Darrell, T.: Fully convolutional networks for semantic segmentation. In: Proceedings of the IEEE Conference on Computer Vision and Pattern Recognition, pp. 3431–3440 (2015)
15. Mikolov, T., Karafiát, M., Burget, L., Cernocký, J., Khudanpur, S.: Recurrent neural network based language model. In: Interspeech, vol. 2, no. 3, pp. 1045–1048 (2010)
16. Chung, J., Gulcehre, C., Cho, K., Bengio, Y.: Empirical evaluation of gated recurrent neural networks on sequence modeling (2014). arXiv:1412.3555

Chapter 18
Application of Image Processing in Air-Ground Combined Fire Fighting System

Min Wang, Jing Huang, Wentao Wang, Xiaoyan Xiang, and Kejun Lei

Abstract In modern fire rescue, the rise of UAV technology has brought unprecedented advantages for the air-ground joint fire fighting system to deal with emergencies such as fires. Image processing, a key component of drone technology, provides firefighters with real-time, high-definition images and data analysis that dramatically improves rescue efficiency and safety. This paper discusses in detail the methods and algorithms of fire detection and fire source location by image processing technology and expounds its potential in improving the accuracy and speed of fire detection. The function of image processing in fire emergency response is introduced. Through real-time monitoring and image analysis, it can help fire personnel to make decisions and take actions quickly. The results of fire detection and fire source location using image processing algorithms are shown by experiments, and the effectiveness and feasibility of these technologies are verified.

18.1 Introduction

In various natural disasters, the impact of fire on people is often huge. According to statistics, from 2012 to 2021, a total of 1.324 million residential fires occurred nationwide, resulting in 11,634 deaths, 6,738 injuries, and direct property losses of 7.77 billion Yuan [1]. It can be seen that once the fire occurs, it will pose a major threat to people's lives and property and national security. At present, the products for fire detection mainly use sensor technology, such as temperature sensor and smoke sensor. The temperature sensor can only detect the temperature change and may not provide accurate early warning in the early stage of the fire, resulting in slow response to the fire expansion. The smoke sensor is very sensitive to smoke, easily causes false alarms for smoke generated during cooking, and cannot detect smokeless fires. After extensive exploration, it is found that image processing technology can analyze a

M. Wang (✉) · J. Huang · W. Wang · X. Xiang · K. Lei
College of Communication and Electronic Engineering, Jishou University, Jishou 416000, Hunan, China
e-mail: 2950340589@qq.com

large amount of image data in a short period of time, quickly and accurately detect fire source and flame spread, provide real-time information to assist fire commanders to make smarter decisions and optimize rescue plans, and provide strong support for disaster response.

Drones can cover a large area, provide a high-altitude view and a view of hard-to-reach areas, help firefighters deploy at short notice, and play an important role in joint fire engine rescue activities. As an important part of UAV, image processing has injected new vitality and efficiency into fire rescue. Due to the rapid propagation of light, the camera can well simulate the human eye to find the fire in time, and the fire personnel can use the micro-processing system to compare and analyze the fire image, so as to quickly detect the fire and fire fighting linkage. This paper will discuss the application of image processing in the fire fighting system of UAVS, and reveal its important role in improving the efficiency of fire rescue and ensuring the safety of firefighters.

18.2   HSV Color Space

The RGB and BGR color spaces are color models based on the original red, green, and blue channels, consisting of red (R), green (G), and blue (B), used to describe combinations of various colors in color images. The values for each channel range from 0 to 255, representing the intensity of their respective colors. However, the RGB color space is dependent on devices and non-uniformities, making it less effective for image analysis [2]. Therefore, images in the RGB color space should be transformed through linear conversions into other color spaces. In contrast, HSV represents color attributes more intuitively in terms of hue, saturation, and brightness. Hence, this article will perform image processing on images in the HSV color space.

In this paper, the image of HSV color space will be processed. The HSV Color Space Diagram is shown in Fig. 18.1.

The HSV color space is a representation method that describes color as Hue, Saturation, and Value [3]. Hue is the basic property of color and refers to the position of the color in the spectrum. In the HSV color space, Hue is represented as an Angle that can be taken from 0° (red) to 360° (back to red again) [4]. Therefore, Hue determines the kinds of colors, such as red, green, blue, and so on. Saturation indicates the brightness or purity of a color. When Saturation is high, the color is more vivid and full; when the saturation is low, the color will become more gray, gradually approaching gray. Saturation values range from 0 to 100, where 0 indicates a gray color and 100 indicates a fully saturated color. Value refers to the brightness of the color. A higher Value indicates a brighter color, while a lower Value indicates a darker color. Brightness also ranges from 0 to 100, with 0 representing black and 100 representing white.

In HSV space, Hue, Saturation, and Value of colors can be adjusted independently, which is conducive to extracting color objects of ROI, eliminating background noise, maintaining color continuity when smoothing and filtering images, reducing the

Fig. 18.1 HSV Color Space Diagram
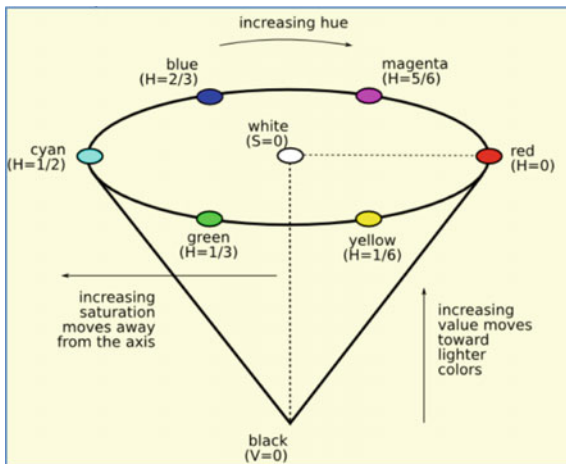
serrated effect of color boundaries, and facilitating color extraction and enhancement of images. It makes the image processing more intuitive.

18.3 Special Optical Treatment of Fire Detection Cameras

The stored procedure of an image in a computer covers key steps, including sampling, quantization, and digital representation.

Sampling is the process of spatially discretizing a continuous image. In this step, we represent the entire image by selecting some specific points in the image whose grayscale values represent the brightness information of the image at the corresponding location. The sampling interval is inversely proportional to the pixels of the image, which determines the detail rendering of the image. The selection of sampling intervals requires a balance between image quality and storage requirements. The following methods are usually used:

If we let the one-dimensional signal $y(x)$ be less than or equal to v, according to Eq. (18.1), the sampled values $y(iT)$ obtained by sampling the image data with spacing $T = 1/(2v)$ can completely recover $y(t)$ [5].

$$y(t) = \sum_{t=-\infty}^{\infty} y(iT)x(t - iT) \tag{18.1}$$

and

$$x(t) = \frac{\sin(2\pi vt)}{2\pi vt} \tag{18.2}$$

(a) Continuous Gray Scale   (b) Gray Quantization Value   (c) Gray-scale Quantization Effect
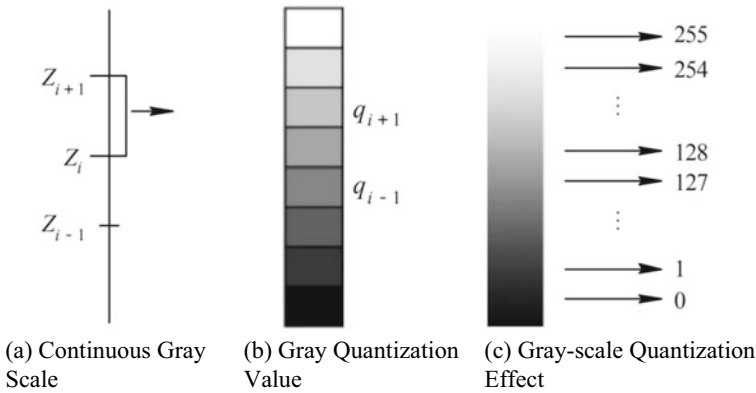
Fig. 18.2 Gray quantization diagram

Quantization is the process of converting the grayscale values of each sampled pixel from analog to discrete. It represents the grayscale values within a specific continuous range using integer values. Typically, it involves dividing the grayscale range of sampled values into equal intervals for quantization, as shown in Fig. 18.2. In this figure, (a) represents continuous numerical ranges for image grayscale levels as (Z_{i-1}, Z_i) and (Z_i, Z_{i+1}), , while (b) represents quantizing the continuous range (Z_i, Z_{i+1}) of grayscale values into different values as $q_{i-1}, q_i, q_{i+1}, \ldots$ (resulting in the effect shown in (c)).

Through sampling and quantization processing, continuous image data is converted into discrete digital matrices for processing and storage in digital computer systems. However, this color representation takes the form of interval quantization, that is, dividing continuous color values into a finite number of discrete intervals, which can lead to small differences in thresholds between different colors. This difference can have an impact on the accuracy of color recognition in extreme cases, especially in border color regions.

To overcome this problem, we employ a physics-based approach strategy to reduce recognition errors and enhance the robustness of image processing methods for flame detection. Specifically, we take advantage of the properties of combustion flames that produce large amounts of CO_2, which is evident in spectral analysis.

Since the combustion flame releases a large amount of CO_2, its spectral analysis shows that there is a significant peak value near 4.2 microns in the infrared band (as shown in Fig. 18.3), which is characterized by the spectral characteristics of the flame [6]. Based on this characteristic, we chose a special 4.2–4.5 micron narrow-band band-pass optical filter to enhance the capture of the flame signal.

In addition, we chose to manufacture the filter using germanium material to further optimize the acquisition and analysis of infrared bands. Germanium material has the characteristics of non-toxicity, moisture resistance, and good thermal conductivity, and its refractive index is relatively stable. Germanium material has excellent infrared transmission performance and small transmission loss and is easy to cut and polish
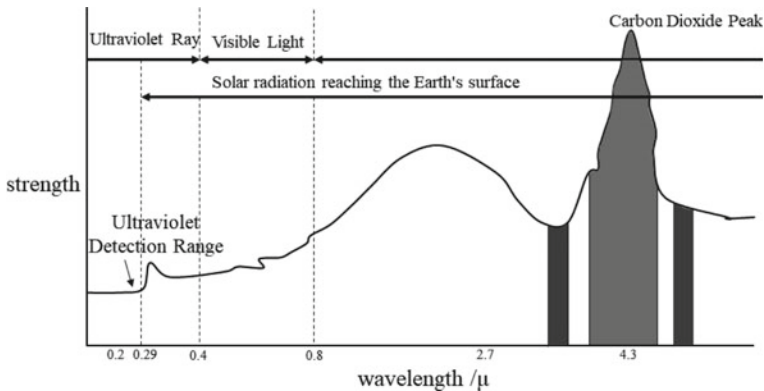
Fig. 18.3   Flame combustion spectrum

[7]. This filter helps to maximize the extraction of target infrared band information, thereby improving the accuracy and robustness of flame detection. By combining the advantages of physical materials with image processing methods, we are able to effectively reduce identification errors and thus enhance the reliability of flame detection.

18.4   Image Enhancement

In this paper, the high-performance CCD (Charge-Coupled Device) sensor combined with the computer vision library OpenCV was used for comprehensive acquisition and processing of the flame image. With the CCD sensor, we can convert the spectral information of the flame into an electrical signal to achieve efficient capture of the flame energy. Then, with the help of OpenCV, a powerful computer vision library, we carried out multi-level processing and analysis on the acquired image data to extract the key features of the flame. The processing steps are shown in Fig. 18.4.

18.4.1   Image Import and Enhancement

Image Import and Format Conversion

By using the function cv2.imread() of the OpenCV computer vision library, we are able to load the image from the drone's field of view and display it on the computer. By default, these images are formatted in blue, green, and red channels, known as BGR format. Then, we use the function cv2.cvtColor() provided by OpenCV to perform image format conversion, thereby enhancing the image [8], in order to better adapt to subsequent processing requirements.

Fig. 18.4 Image processing
flow chart
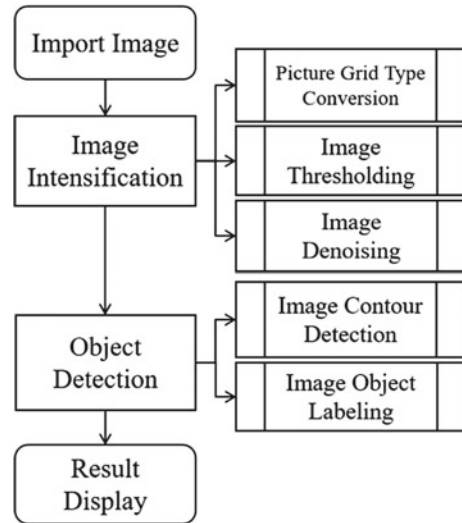
After the previous discussion, we have already learned about the advantages of the HSV color space. Next, we will show a comparative image of the HSV color channels with other image formats to gain a clearer understanding of the application of the HSV color space in the context of flame detection. Using the cv2.cvtColor() function, we convert the image to a grayscale format containing only a single luminance channel by selecting the flag cv2.COLOR_BGR2GRAY. We convert the image to the more conventional RGB format that matches human color perception by selecting the flag cv2.COLOR_BGR2RGB. Furthermore, we convert the image to the HSV format, which provides a more intuitive representation of image color attributes, by selecting the flag cv2.COLOR_BGR2HSV. Since the HSV color space demonstrates stronger resistance to interference compared to the RGB and BGR formats, to enhance the accuracy and robustness of flame detection, this article processes flame images using the HSV color space. Figure 18.5 presents a comparison of the effects after different format conversions:

Image Thresholding

In order to reduce the area of interest for flame identification, this paper extracts the area of specific color by setting an appropriate color threshold and splits the flame from the background. In order to meet the different changes of ambient illumination, we have obtained a more appropriate threshold range after several tests and then use the cv2.inRange() function for mask operation, with only the flame color part reserved.

To control the region or processing procedure of image processing, a selected image, graphic, or object is used to mask the processed image (entirely or partially). The specific image or object used for covering is referred to as a mask or template [9]. A mask is a binary image consisting of 0 and 1 s. When a mask is applied in a function,

(a) RGB Image   (b) GRAY Image

(c) RGB Image   (d) HSV Image
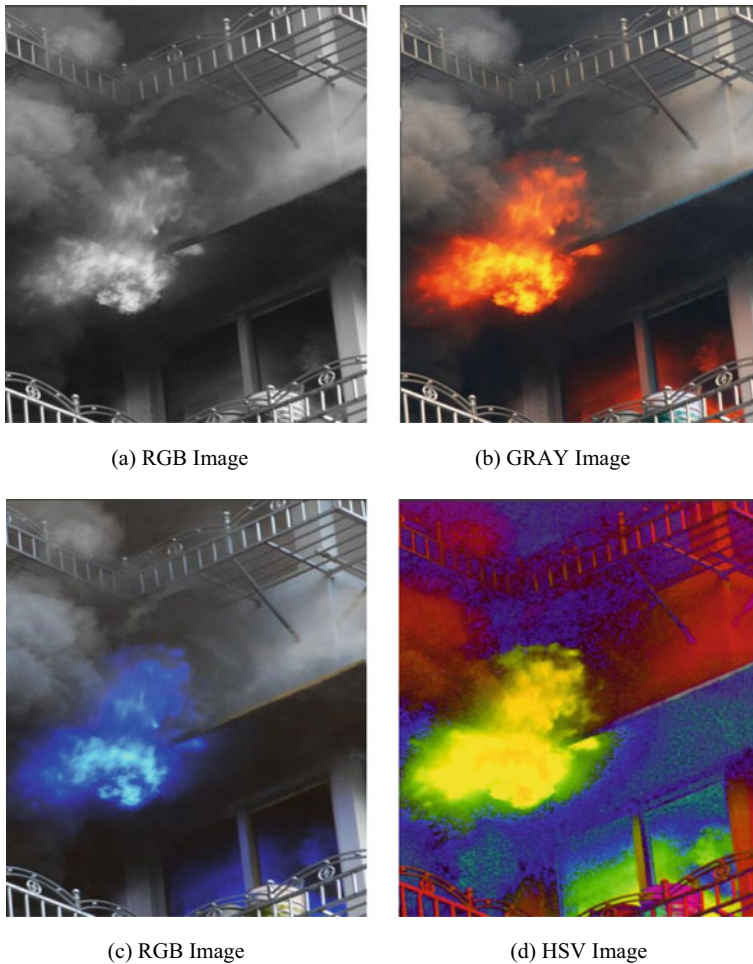
Fig. 18.5 Image format conversion effect

the 1-value region is processed and the masked 0-value region is not included in the calculation. An image mask is defined by a specified data value, data range, limited or infinite values, area of interest, and comment file, or any combination of the above options can be applied as input to create the mask. Each pixel value in the image is recalculated through a mask matrix in OpenCV. The mask matrix controls the influence of the current position of the old image and the surrounding position pixels on the current position pixel value of the new image.

After mask operation, the image processing area is smaller, and the algorithm needs to process fewer pixels, thus reducing the complexity of calculation and improving the processing speed. In addition, the mask operation can exclude pixels that do not belong to the region of interest, thereby reducing noise and background

Fig. 18.6 Image after mold extraction

interference, making subsequent processing more stable and achieving the purpose of thresholding HSV images. The image effect diagram after mask processing is shown in Fig. 18.6.

18.4.2 Image Denoising

In order to obtain more accurate recognition results, images usually need to be denoised. Noise is an unwanted random or intrusive change in an image that may interfere with the process of image analysis and processing. For this purpose, common denoising methods include mean filtering, box filtering, Gaussian filtering, and median filtering, among others [10, 11]. These filtering methods can effectively reduce the noise in the image and improve the reliability and accuracy of subsequent analysis. In Fig. 18.7, we compare the image effects processed by different filtering methods. Through these comparison graphs, we can clearly observe the influence of different filtering methods on the image. According to the image analysis results, the median filter performs well in removing noise, so we choose to use the cv2.medianBlur() function to process the median filter for the image passing through the flame mask.

Despite the filtering process, the flame edge may still have small burrs, cracks, and blurred boundaries. To further improve the quality of the flame image, making it smoother and more suitable for subsequent processing, we apply morphological operations to the image using the cv2.MORPH_OPEN and cv2.MORPH_CLOSE flags of the cv2.morphologyEx() function [12]. In Fig. 18.8, we show the image processing results after morphological manipulation. Through comparison, we can

(a) Mean Filtering

(b) Box Filtering

(c) Gaussian Filter

(d) Median Filter
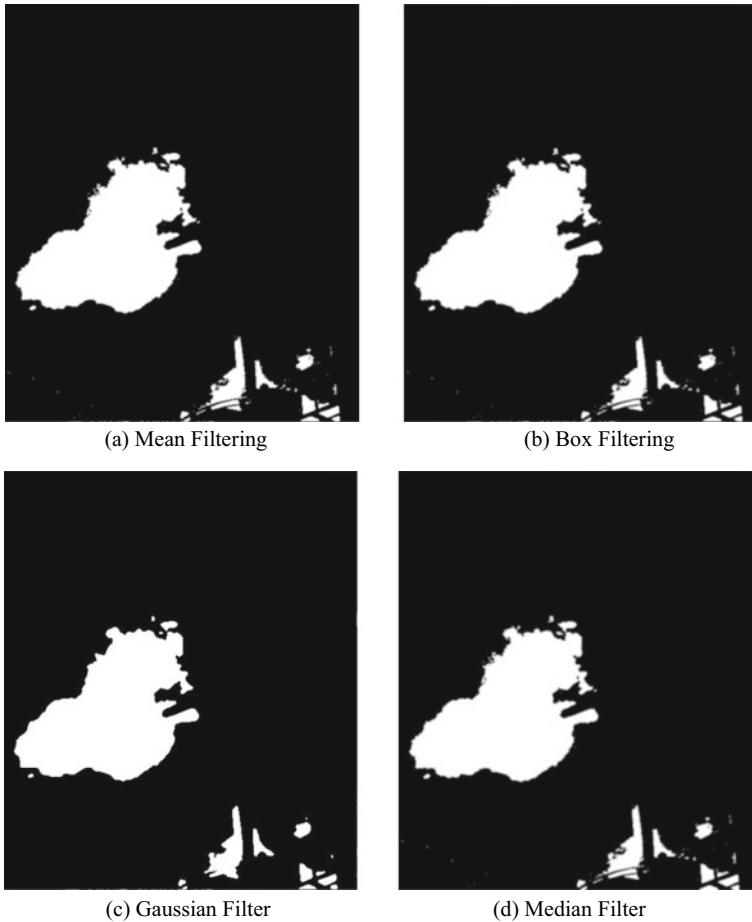
Fig. 18.7   Image filtering effect

clearly observe the effect of morphological manipulation, such as edge smoothness and boundary clarity.

18.5   Target Detection and Locking

In this study, cv2.findContours() function was used to successfully detect the flame region contour after image processing. We then use the cv2.drawContours() function to graphically mark all flame contours on the original image, as shown in Fig. 18.9a. However, since the flame distribution may be uneven when the UAV obtains the image, the detected flame contour area is different. In order to locate the fire source

Fig. 18.8 Morphological
processing of denoised
images

more accurately, we use a sorting algorithm to sort the contour area, and then select
the part with the largest area. Using the cv2.circle() function, we marked the area and
marked the center of the circle to provide firefighters with easy access to fire source
location information. Figure 18.9b shows the labeled results, providing reliable flame
location data for further application to real-world scenarios.

(a) Flame Profile Marking Diagram   (b) Maximum Flame Area Marking Diagram

Fig. 18.9 Flame marking diagram

18.6   Conclusion

In this paper, we deeply discuss the extensive application of image processing technology in air-ground combined fire protection system. Through sufficient research and experiments, we not only confirm the importance of image processing in the field of fire protection but also verify its potential great value. This paper first introduces the basic concept of image processing and then elaborates the practical application of image processing in fire control system. The specific methods and algorithms of fire detection and fire source location by image processing technology are further discussed, and the great potential of these technologies in improving the accuracy and speed of fire detection is deeply revealed. Through a series of experiments, we have fully verified the effectiveness and feasibility of these technologies in practical applications.

To sum up, this paper discusses the application of image processing in the air-ground combined fire protection system in a deeply researched way. This not only provides a useful reference for technological innovation and development in the field of fire protection but also provides a strong theoretical support for the design and optimization of fire protection systems in the future. By integrating image processing technology, we can achieve critical tasks such as fire detection and fire source location more efficiently and accurately, further improving the overall performance of the fire protection system, and protecting people's lives and property safety.

References

1. National Fire and Rescue Bureau. In the past 10 years, residential fires nationwide have resulted in 11,634 fatalities (2022-02-18) [2023-8-15]. https://www.119.gov.cn/gk/sjtj/2022/27328.shtml
2. Ganesan, P., Rajini, V., Sathish, B.S., et al.: HSV color space based segmentation of region of interest in satellite images. In: 2014 International Conference on Control, Instrumentation, Communication and Computational Technologies (ICCICCT), pp. 101–105. IEEE (2014)
3. Liu, C., Liu, G.J., Wang, Z.J., et al.: Multi-feature fusion object tracking algorithm based on HSV. Comput. Simul. **40**(01), 195–199+358 (2023)
4. Bora, D.J., Gupta, A.K., Khan, F.A.: Comparing the performance of L* A* B* and HSV color spaces with respect to color image segmentation (2015). arXiv:1506.01472
5. Xu, T.B.: Research on Large-Scale Space Fire Alarm System Based on Image Processing. East China Jiaotong University (2014)
6. Ge, H.: Research on Biomass Combustion Monitoring Based on Flame Spectrum Analysis and Image Processing. North China Electric Power University (Beijing) (2021)https://doi.org/10.27140/d.cnki.ghbbu.2020.000184

7. Ma, S.C.: Large-Scale Space Firefighting Robot Based on Computer Vision. Fuzhou University (2016)

8. Zhang, R., Jiao, X.Q.: Application of OpenCV-based image processing techniques in traditional Chinese painting. Autom. Instrum. **2019**(09), 226–229 (2019). https://doi.org/10.14016/j.cnki.1001-9227.2019.09.226

9. Ding, T.T., Zhang, N.F., Zhang, Y.X., et al.: Research on de-sharpening dual mask image enhancement method for contraband X-ray images. Appl. Laser **42**(09), 111–117 (2022). https://doi.org/10.14128/j.cnki.al.20224209.111

10. Niu, H.P.: Research on Target Detection Technology for Space-Based Surveillance Systems. University of Chinese Academy of Sciences (Changchun Institute of Optics, Fine Mechanics, and Physics, Chinese Academy of Sciences) (2023). https://doi.org/10.27522/d.cnki.gkcgs.2023.000106

11. Gu, X.J., Yang, B.S., Liu, Q.Y.: Image matching algorithm based on gaussian filtering and AKAZE-LATCH. Semicond. Optoelectron. **44**(04), 639–644 (2023). https://doi.org/10.16818/j.issn1001-5868.2023041601

12. Dong, Y.H., Zhang, X.G.: Quantum implementation and simulation of binary morphological edge detection algorithm. J. Quantum Electron. **40**(05), 654–665 (2023)

Chapter 19
Design and Realization of Mobile Terminal Side Time Synchronization Based on FPGA

Qi Liu, Xiangchao Meng, and Xiaosong Cao

Abstract In order to solve the current demand of high precision time synchronization modularization of mobile terminals, the problem that mobile network standard cannot provide high precision time synchronization ability is solved. Based on the capability of the existing mobile communication system, this project will design a time synchronization module of the mobile terminal side based on field programmable gate array (FPGA) by studying the airport timing and the terminal side's airport timing process.

19.1 Introduction

With the rapid development of network technology and integrated circuits, mobile terminals have also broken free from their constraints and experienced significant growth [1]. In the face of massive interactions and collaborative cooperation among mobile devices, time synchronization has become particularly important, and its accuracy has become a goal pursued by humans. Whether its email communication, telephone billing, campus card authentication, or mobile gaming, time synchronization is essential. Without accurate time synchronization or if the precision is too low, it would lower our quality of life [2]. Nowadays, there are various time synchronization methods such as global navigation satellite system (GNSS), network time protocol (NTP), and precision time protocol (PTP), each shining in their respective domains, but with certain limitations [3]. For example, GNSS is constrained by costs, and NTP lacks high precision. Currently, absolute time synchronization requirements can be

Q. Liu (✉) · X. Cao
Beijing Polytechnic, Beijing, China
e-mail: liuqi@bpi.edu.cn

X. Cao
e-mail: Caoxiaosong@bpi.edu.cn

X. Meng
Beijing Rongzhi Huixin Engineering Co., Ltd, Beijing, China

239

achieved in scenarios like wired symmetric link networks. However, in scenarios with long-distance wireless link networks, due to the instability and asymmetry of the wireless links, most cannot achieve high-precision wireless time synchronization [4], which would negatively impact people's daily lives due to poor user experience.

This paper investigates the timing process on the air interface of mobile terminals and based on the interaction between field programmable gate array (FPGA) and the terminal designs an FPGA-based timing synchronization module for mobile terminals built upon existing mobile network devices and air interface links. The air interface timing not only ensures good measurement of uplink and downlink latency and channel delay in the existing air interface protocol stack (physical layer: PHY, media access control: MAC, etc.) but also achieves higher timing accuracy compared to technologies like NTP and PTP. This simple design enables high-precision time synchronization while ensuring good user experience and accommodating a large number of users. It also reduces costs by utilizing existing or planned network devices such as mobile edge computing (MEC) [5], base stations, and terminals. With the development of 5G, high-speed, low-latency, and high-capacity communication is experiencing vigorous growth. This time synchronization technology can be applied in scenarios such as the Internet of Things and connected vehicles, ushering in a new era with the advent of 5G and allowing everyone to participate in the wireless network world.

19.2 Related Theories

19.2.1 End-to-End Delay Mechanism

The basic principle of PTP synchronization is that the master and slave clocks exchange synchronization messages and record the transmission and reception time of these messages. The round-trip delay between the master and slave clocks is calculated by measuring the time difference between transmitting and receiving the messages. If the network is symmetrical, meaning that the transmission delays in both directions are the same, then the one-way delay is half of the round-trip delay. The clock offset between the master and slave clocks is equal to this one-way delay. By adjusting the local time based on the calculated offset, the slave clock can achieve synchronization with the master clock. The following Fig. 19.1 illustrates the implementation process of the end-to-end delay mechanism in the two-step mode [6].

In the two-step mode of the end-to-end delay mechanism, the timestamp t_1 of the Sync message is carried by the *Follow_up* message, and t_4 and t_5 are carried by the *Pdelay_Req* and *Pdelay_Resp_Follow_UP* messages, respectively.

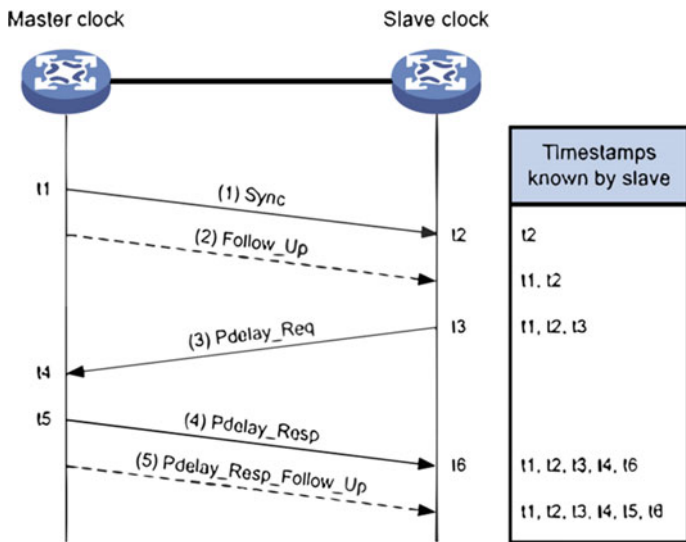The implementation process of the end-to-end delay mechanism in the two-step mode is as follows:

Fig. 19.1   Implementation process of the end-to-end delay mechanism in the two-step mode

- The master clock sends a Sync message to the slave clock and records the transmission time t_1. The slave clock, upon receiving the message, records the reception time t_2.
- After sending the Sync message, the master clock immediately sends the *Follow_up* message containing t_1.
- The slave clock sends a *Pdelay_Req* message to the master clock to initiate the calculation of the reverse transmission delay. The slave clock records the transmission time t_3, and upon receiving the message, the master clock records the reception time t_4.
- Upon receiving the *Pdelay_Req* message, the master clock replies by sending a *Pdelay_Resp* message with t_5 as the transmission time. The slave clock records the reception time t_6 upon receiving this message.
- After replying to the *Pdelay_Req* message, the master clock sends a *Pdelay_Resp_Follow_UP* message containing t_5.

At this point, the slave clock has obtained six timestamps: t_1 to t_6. Using these timestamps, the round-trip delay between the master and slave clocks can be calculated as $[(t_4 - t_3) + (t_6 - t_5)]$, and assuming a symmetrical network, the one-way delay between the master and slave clocks is $[(t_4 - t_3) + (t_6 - t_5)]/2$. Therefore, the clock offset between the slave and master clocks is Offset $= (t_2 - t_1) - [(t_4 - t_3) + (t_6 - t_5)]/2$.

19.2.2 *Air Interface Timing Overview*

At the network level, air interface timing has already had mobile network air links, and the physical layer and data link layer of the air interface protocol stack can ensure relatively good measurement of delay variations and channel delays for uplink and downlink. In future applications, due to the large number of users in air interface timing, there will be significant demand and user volume in areas such as connected vehicles, IoT, and artificial intelligence. Moreover, network equipment such as base stations, terminals, MEC, etc., can utilize existing or upcoming equipment from operators to save costs. Air interface timing can achieve higher timing accuracy using air interface wireless signals, albeit compared to technologies like NTP and PTP which have relatively lower accuracy. Figure 19.2 shows the timing network structure:

In this timing network structure, atomic clock hardware and timing services interact and influence each other. The core network and base stations in the figure achieve time synchronization monitoring and reduce dependence on satellites, thereby achieving higher precision timing using the network. In the future, it can be applied to industries such as autonomous driving in 5G networks and timing for IoT devices.

For the network timing system, the following design plan is proposed, as shown in Fig. 19.3.

Master Clock → Core Network → Base Station/MEC: Using optical network and PTPv2 technology.

Base Station → UE/Gateway: Air interface physical layer for signal timing.

Clock Hierarchy:
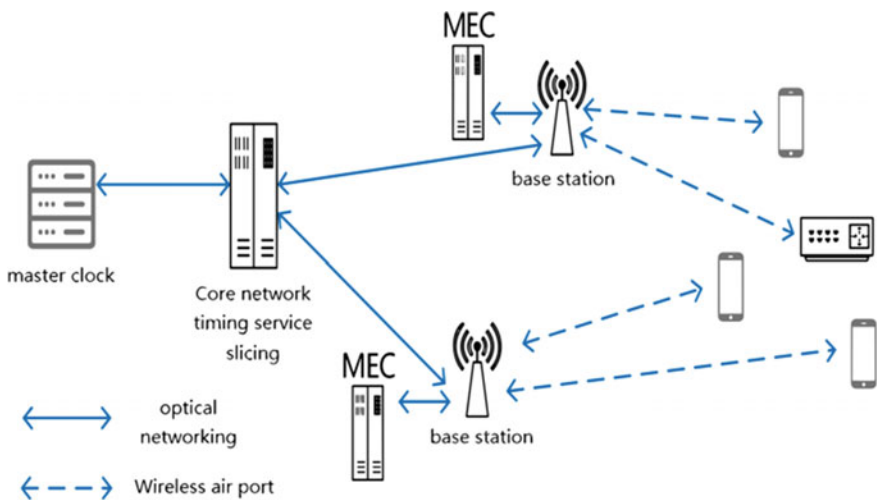
Fig. 19.2 Timing network structure
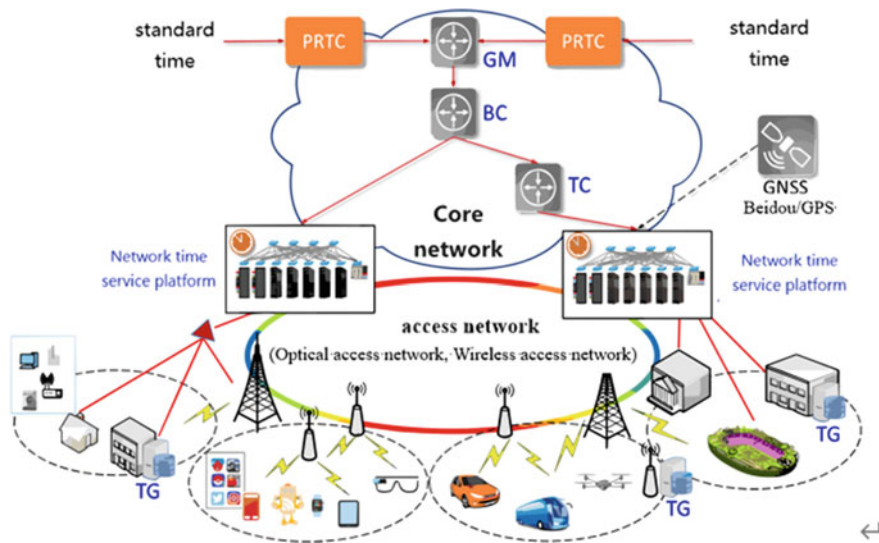
Fig. 19.3   Timing system overview

- GM (Grandmaster Clock): Has the highest stability, precision, and reliability.
- BC (Boundary Clock): Can establish various branch points in different layers of the structure.
- TC (Transparent Clock): Can measure and compensate for the time consumed by PTP event information in the device.

19.2.3   Air Interface Timing Principles and Process

Basic principle: Air interface timing is based on periodic, low-latency physical layer synchronization signals. The base station records the time of the signal transmission and sends that time through a physical broadcast channel or a physical downlink shared channel (PDSCH) channel. The terminal blindly detects the signal and records the received time. Afterwards, the base station provides feedback on the uplink delay measurement through a RandomAccessResponse. The terminal predicts and modifies the timing error.

Fig. 19.4 Flowchart of time synchronization process
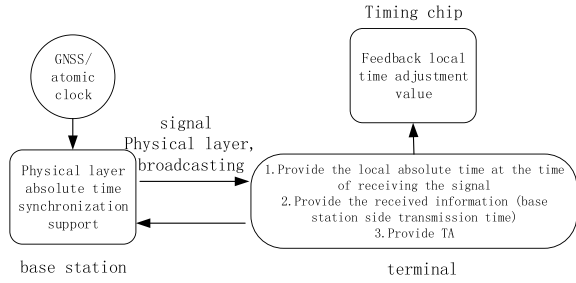
19.3 System Design

19.3.1 Design of Time Synchronization System

Overall scheme of Time Synchronization System based on the studied air interface
timing process on the mobile terminal side, further design of the time synchronization
system is carried out. Figure 19.4 shows the flowchart of the time synchronization
process.

The FPGA in the terminal needs to possess the following three capabilities:

- The FPGA needs to retrieve the terminal's local time when detecting radio resource
  control (RRC) signals, as well as the sending time of the broadcasted signals from
  the base station and the value of n_TA signal in random access response (RAR)
  signals or directly obtain the TimeAdvance value.
- Based on the above data, calculate the adjustment value for the terminal's local
  time.
- Provide feedback of the adjustment value to the terminal.

On the other hand, the terminal needs to open interfaces on the current basis to
provide the aforementioned sending time, local time, and TimeAdvance value. This
enables the terminal to correct its local time based on the adjustment value provided
by the chip. Furthermore, the Verilog [7] language is used to implement the required
functionalities of the FPGA.

19.3.2 FPGA-Based Time Synchronization Module
for Mobile Terminals

Regarding the FPGA-based time synchronization module on the mobile terminal
side, a rough overall design including the terminal's timing system is developed
based on existing resources.

The total TimeAdvance value is recorded to represent the accumulated results from
the timing chip based on all the baseband signals. This result is obtained through

the TimeAdvanceCommand calculation according to the 3GPP standard process, denoted as:

$$TA_{total} = TA_{RA} + \sum_i TA_i \qquad (19.1)$$

Equation (19.1) serves as an estimation of uplink delay. TA_{total} is indicated the total TimeAdvance value. TA_{RA} is indicated the resource allocation of TimeAdvance. TA_i is indicated the Time Advance.

t_0 represents the delay of hardware data transmission and processing, such as the baseband module and timing chip. Since it is relatively fixed and may vary across different hardware, it needs to be determined in advance. If the current channel delay condition is unstable and the Nb timing signals sent by the base station cannot meet the timing conditions set by the chip, the module sends a termination command to the timing chip. The timing chip judges and calculates based on the input system frame number (SFN) and system information block (SIB_t) signals. If the SFN does not match the rSFN in the signal, the current signal is discarded, and the next timing signal is received and processed. For valid timing signals, t_{offset} is calculated based on the formula shown in the figure. The timing chip outputs absolute time information and PPS second pulse based on t_{offset} and ends the current timing process, waiting for the start of the next timing process. The clock adjustment amount for the timing terminal is t_{offset}. Figure 19.5 shows a rough flowchart of the FPGA-based timing process on the mobile terminal side.
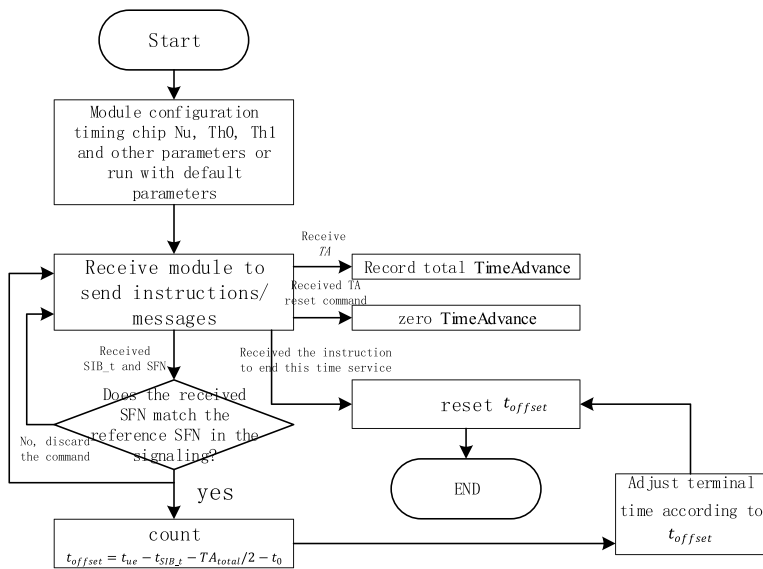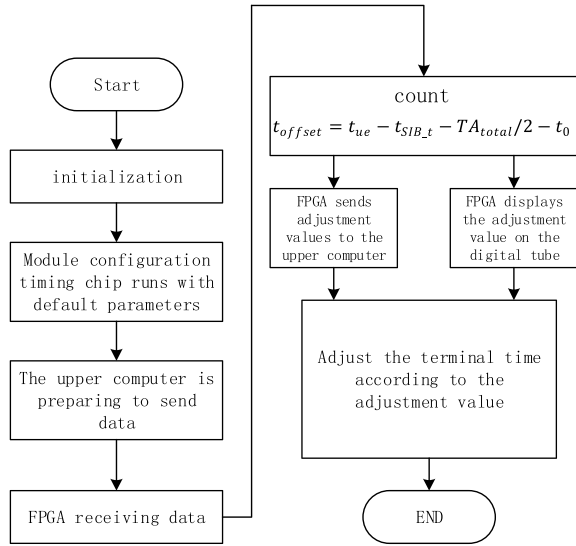

Fig. 19.5 Rough flowchart of FPGA-based timing process on the mobile terminal side

Fig. 19.6 FPGA terminal timing process

It involves measuring the hardware transmission and processing delays of the baseband module and timing chip, estimating the transmission delay TA caused by distance, recording the local absolute time of the receiving end, and responding with the sending time of the transmitting end. Due to network symmetry, the required adjustment for the terminal's time is calculated. The specific design between the FPGA and the terminal is shown in Fig. 19.6: FPGA Terminal Timing Process.

$$t_{\text{offset}} = t_{ue} - t_{\text{SIB}\_t} - \text{TA}_{\text{total}}/2 - t_0 \qquad (19.2)$$

Through the interaction between the FPGA and the terminal, the FPGA obtains TimeAdvance value, value, local reception time, and signal transmission time from the interface. After calculating the adjustment value using Eq. 19.2, the result is displayed on the digital display and returned to the terminal.

19.4 Hardware and Software Resources

The FPGA [8], short for Field Programmable Gate Array, is a type of semiconductor digital integrated circuit that is also a field-programmable gate array, allowing many of its internal circuit functions to be modified based on specific requirements. In the past, PLD (Programmable Logic Device) and ASIC (Application-Specific Integrated Circuit) could only perform their respective roles without fully utilizing their advantages. However, with the emergence of FPGA, it combines the strengths of PLD and ASIC. It can have thousands or even millions of logic gates while still

Fig. 19.7 FPGA structure
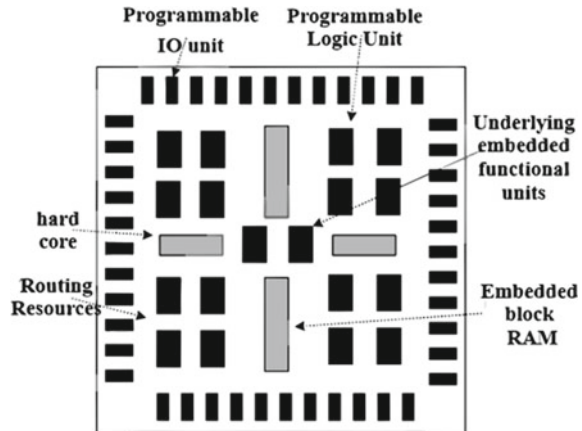
being programmable on the field, enabling larger and more complex functionalities. Additionally, FPGA design costs are relatively lower compared to ASIC, and making changes to previous designs in FPGA is relatively easier. FPGA's main market used to be in the communication and networking fields, but with the passage of time and technological advancements, FPGA applications have explosively grown in consumer electronics, automotive, electrical, and other sectors.

The simplified structure of an FPGA consists of six main components: the FPGA chip itself, programmable Input/Output Modules (IOB) for interfacing with the external world, programmable Logic Modules (CLB), embedded Block RAM (BRAM), interconnect resources for connecting all parts of the FPGA internally, underlying logic elements, and dedicated hard cores. The figure below shows the structure of an FPGA in Fig. 19.7.

In general, the design flow of an FPGA includes several steps, such as defining design inputs according to design specifications, RTL simulation, synthesis of the design, performing placement and routing, conducting timing simulation, analyzing timing, and performing board-level verification. The FPGA design process is shown in Fig. 19.8.

19.5 Interaction Between FPGA and Terminal

In FPGA applications such as traffic lights and digital displays, the system clock cannot be used directly, and sometimes multiple clock pulses of different frequencies are required as driving sources in a digital system. One of FPGA's features is its ability to process clock signals. Therefore, the concept of frequency division comes into being, and the frequency divider has a fundamental and important role in FPGA design. Generally, there is an integrated Phase-Locked Loop (PLL) in FPGA to achieve clock multiplication, frequency division, phase shift, and programmable

Fig. 19.8 FPGA design
process

design specification

Design Input   modify
                                                                 design

RTL simulation

synthesys

Layout and wiring

timing simulation

timing analysis

System Verification

design specification
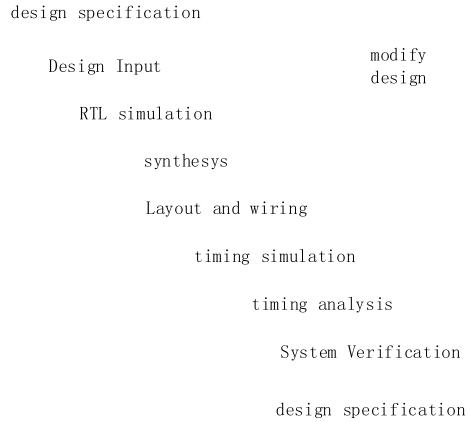
duty cycle functions. However, a PLL or IP core resource can also be excluded in
designs that do not demand high clock accuracy.

Frequency dividers are mainly divided into even and odd divisions, and rela-
tively speaking, even division principles are simple and easier to master. It can be
achieved by counting with a counter. When using N times even frequency division,
the clock triggers the counter for counting, and only needs to flip the output clock
when counting to N/2 − 1, and so on. Figure 19.9 shows the simulation diagram of
a four-fold frequency divider.

For odd frequency division, if you want to implement odd-frequency division with
a 50% duty cycle, you cannot flip the clock at the midway point of the counter as
with even division, as this method cannot obtain a 50% duty cycle clock. If you use a
method similar to even frequency division to trigger the rising edge of a frequency-
divided clock, you will get a clock signal with a duty cycle that is not 50%. If the
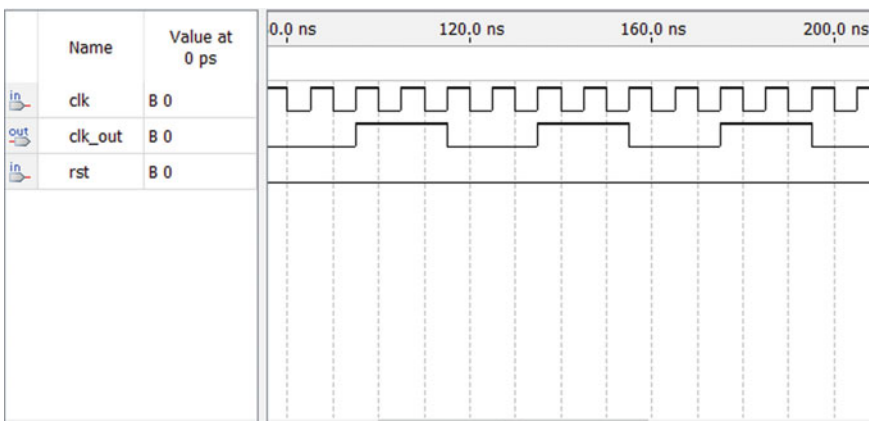
Fig. 19.9 Simulation diagram of four-fold frequency divider
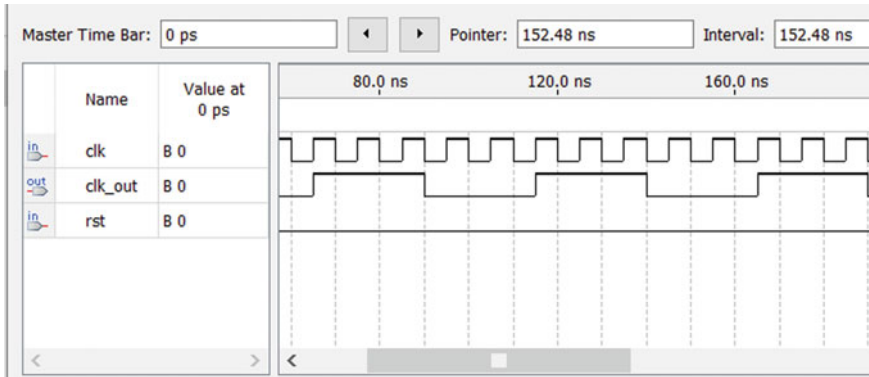
Fig. 19.10 Five-fold frequency divider

clock is triggered again on the falling edge, another clock signal with a duty cycle that is not 50% will be obtained. By performing logical operations on these two clock signals, a clock with a 50% duty cycle can be flexibly obtained. That is, to perform M-fold odd-frequency division on a clock with a duty cycle of 50%, first perform modulo M counting on the rising edge trigger, select a value for clock inversion output, and then perform another clock inversion output on $(M - 1)/2$, obtaining an odd-m frequency clock with a duty cycle that is not 50%. Next, at the same time, perform modulo M counting on the falling edge trigger, and when the clock inversion output value is the same as that selected for the rising edge trigger, start performing clock inversion output on the output clock, and then perform another clock inversion output on $(M - 1)/2$, obtaining an odd-m frequency clock with a duty cycle that is not 50%. Perform logical operations on two m frequency clocks (with a duty cycle not equal to 50%), taking the AND operation for positive periods and the OR operation for negative periods, to obtain an odd-m frequency clock with a duty cycle of 50%. Figure 19.10 shows the simulation diagram of a five-fold frequency divider.

19.6 Software Design for Time Synchronization

Schematic Diagram. In this design, the upper computer (Friendly Serial Debugging Assistant) sends four data to the FPGA in hexadecimal format. These data include the local reception time of the terminal for the signaling, the transmission time of the base station for sending the signaling [9], the TimeAdvance value, and the hardware data transmission and processing delay t_0 of the baseband module, timing chip, and other components. In this design, they are respectively named as A, B, C, and D.

After receiving these four data, the FPGA calculates the adjustment value based on the time synchronization principles and procedures stated in Sect. 19.3, using the formula $A - B - C/2 - D$ [10]. The calculated adjustment value will be displayed
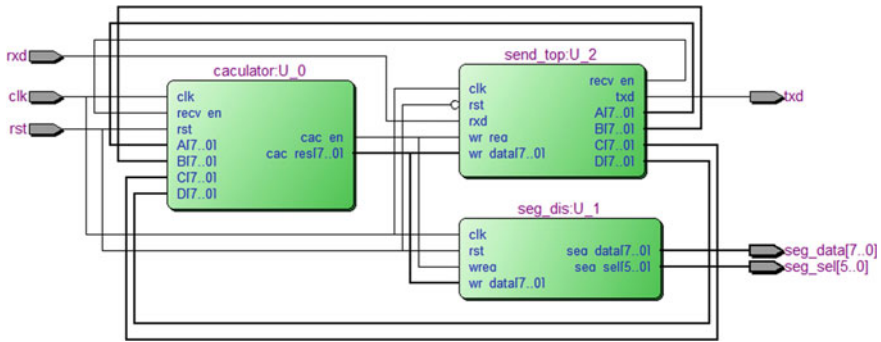
Fig. 19.11 RTL schematic diagram

on the digital display (in decimal format) and sent back to the upper computer (in hexadecimal format). Figure 19.11 shows the RTL schematic diagram of this design.

19.7 Simulation Testing and On-Board Debugging Results

Based on the principles and specific implementation of the above schematic and code, the upper computer in this design sends interface data to the FPGA and completes the calculation of the adjustment value. The adjustment value is then sent back to the upper computer and displayed on the digital display.

The upper computer sends 200, 12, 50, 100 to the FPGA, and after the adjustment value calculation, it is displayed on the digital display [11]. According to the previous formula, the adjustment value should be 63. The hexadecimal representation of 200, 12, 50, 100 is C8, C, 32, 64. The simulation result is shown in Fig. 19.12.

The interface of the Serial Debugging Assistant is shown in Fig. 19.13.

It can be seen that when the upper computer sends the four data in hexadecimal format as C8, 0C, 32, 64 to the FPGA, the FPGA calculates and returns the hexadecimal data 3F, which is equivalent to decimal 63, to the upper computer. Figure 19.14 shows the display on the digital display.

It can be seen that the displayed number on the digital display is 63.

19.8 Conclusions

The upper computer serves as a simulated terminal to provide and send four data to the FPGA, including the local reception time of the received signal at the terminal, the base station sending time of the signal, the delay of hardware data transmission and processing such as baseband module and timing chip, and the TimeAdvance value (estimated value of uplink delay). The FPGA processes and calculates the four data
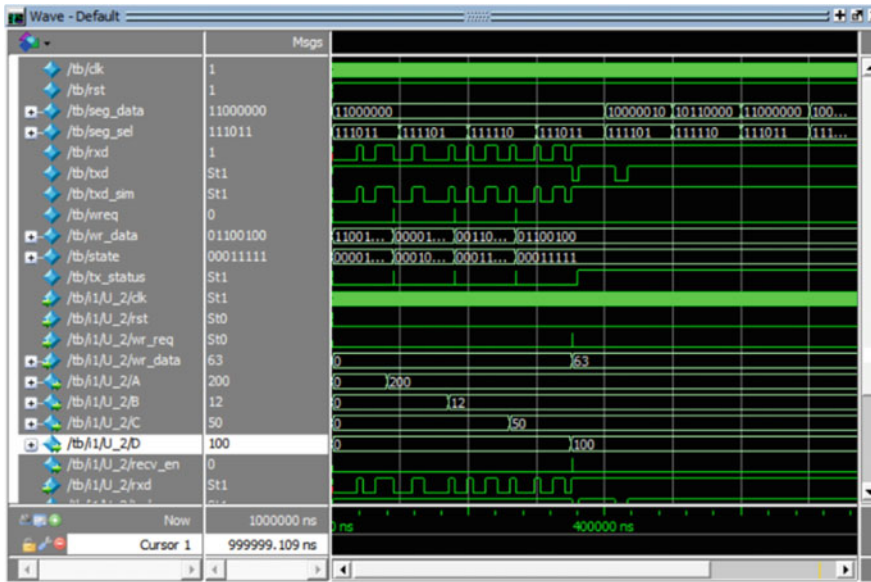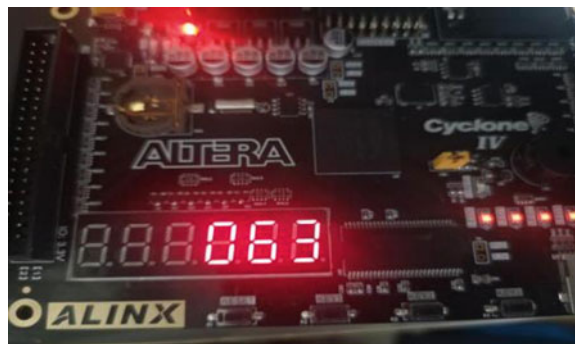
Fig. 19.12 Simulation result

Fig. 19.13 Debugging
assistant interface

Fig. 19.14 Digital display

based on the aforementioned time synchronization principles and sends the calculation result as an adjustment value to the upper computer, which is then displayed on the digital display. This completes the basic process of time synchronization.

Looking ahead, with the continuous advancement of mobile networks, it is expected that more efficient and accurate time synchronization methods will be developed to meet the increasing demands of information exchange and terminal interaction.

References

1. LNCS Homepage, http://www.springer.com/lncs. Accessed 21 Nov 2016
2. Zhang, H., Xu, J., Liu, X., Long, K., Leung, V.C.M.: Joint optimization of caching placement and power allocation in virtualized satellite-terrestrial network. IEEE Trans. Wirel. Commun. (2023). https://doi.org/10.1109/TWC.2023.3257178
3. Chang, Y., Yang, H.X., Zhu, Q.H.: Optimize the deployment and integration for multicast-oriented virtual network function tree. J. Beijing Inst. Technol. **31**(05), 513–523 (2022). https://doi.org/10.15918/j.jbit1004-0579.2022.106
4. Chen, Y., Han, W., Zhu, Q., et al.: Target-driven obstacle avoidance algorithm based on DDPG for connected autonomous vehicles. EURASIP J. Adv. Signal Process. **2022**, 61 (2022)
5. Wu, D.P., Liu, Q.R., Wang, H.G. Wu, D.L., Wang, R.Y.: Socially aware energy-efficient mobile edge collaboration for video distribution. IEEE Trans. Multimed. **19**(10), 2197–2209 (2017)
6. Wu, D.P., Shi, H., Wang, H.G., Wang, R.Y., Fang, H.: A feature based learning system for internet of things applications. IEEE Internet Things J. **6**(2), 1928–1937 (2019)
7. Farooq, U., Baig, I., Alzahrani, B.A: An efficient inter-FPGA routing exploration environment for multi-FPGA systems. IEEE Access **6**, 56301–56310 (2018)
8. Keten, U.: GPS/GNSS independent Time Transfer over Telco IP Core Networks using DTM overlay. In: 2021 IEEE International Symposium on Precision Clock Synchronization for Measurement, Control, and Communication (ISPCS), NA, FL, USA, pp. 1–4 (2021). https://doi.org/10.1109/ISPCS49990.2021.9615348
9. Payal, R., Saxena, A., Chanda, B.: Implementation of smart home through FPGA using Verilog hardware descriptive language. In: 2020 IEEE International Conference on Advent Trends in Multidisciplinary Research and Innovation (ICATMRI), Buldhana, India, pp. 1–6 (2020). https://doi.org/10.1109/ICATMRI51801.2020.9398499
10. Liu, Y., Zhang, W., Zhou, J., Wang, Y., Wang, S., Zhang, L.: A design of encoding arbitration and interrupt request for dynamic reconfigurable high-speed serial bus in cyber physical system. In: 2019 International Conference on Internet of Things (iThings) and IEEE Green Computing and Communications (GreenCom) and IEEE Cyber, Physical and Social Computing (CPSCom) and IEEE Smart Data (SmartData), Atlanta, GA, USA, pp. 627–634 (2019). https://doi.org/10.1109/iThings/GreenCom/CPSCom/SmartData.2019.00122
11. Sun, C., He, Z., Niu, K.: An efficient underwater clock synchronization algorithm based on the principle of firefly synchronization. In: OCEANS 2021: San Diego, Porto, CA, USA. pp. 1–5 (2021). https://doi.org/10.23919/OCEANS44145.2021.9705903

Chapter 20
Exploration of Drone Trajectory Planning in Unknown Environments Using Reinforcement Learning

Yanqiu Wang and Jingya Zhao

Abstract Trajectory planning is a very important problem in UAV base station deployment. The traditional path planning technology based on optimization theory needs to know the environmental information in advance, which cannot be accurately mastered in practice and cannot be applied to complex and changeable scenes. The reinforcement learning technology can make UAV interact with the environment without understanding the global information and then train and learn the optimal trajectory. In this paper, the trajectory problem of a single UAV in unknown user location and channel environment is studied, and the trajectory planning is realized by reinforcement learning method to maximize the throughput. In this paper, the Markov decision process is modeled for the trajectory planning problem of location environment information, and two flight stages are proposed. The actor-critic algorithm is used to solve the problem according to the environmental state and continuity of action of UAV. The result shows that UAV can realize trajectory planning in unknown environment.

20.1 Introduction

UAV can complete the flight task by remote control or internal program control, with good mobility, small size, and flexible deployment. In recent years, it has been widely used in civil and commercial fields. In the field of wireless communication, UAV mainly has two application scenarios. On the one hand, UAV as air base station, relay and access point auxiliary ground node cellular network communication. On the other hand, it can be used as a new type of air users to access cellular networks for communication [1]. Among them, UAVs provide communication services as air

Y. Wang (✉) · J. Zhao
Beijing Polytechnic, Beijing, China
e-mail: wangyanqiu@bpi.edu.cn

J. Zhao
e-mail: zhaojingya@bpi.edu.cn

base stations, which can not only achieve flexible deployment and planning, provide good channel conditions, but also greatly reduce the cost of traditional ground base station deployment, and have broad application prospects [2].

In order to enable comprehensive deployment of UVAs and their role in assisting wireless communication, it is necessary to address the issues of path planning, hovering altitude, and trajectory control for UVAs in complex environments. This paper aims to solve the path planning problem of UAV-BS in a complex environment. In recent years, with the widespread application of machine learning and research and development of path planning algorithms, many scholars have studied the autonomous and intelligent trajectory planning of UVAs. Reinforcement learning has made significant achievements in this field. Due to traditional optimization-based path planning techniques requiring prior knowledge of user location, channel state information, and other information, they are not suitable for many complex and changing practical scenarios. Through reinforcement learning techniques, UVAs can interact with the surrounding environment without prior knowledge of global information, and learn the optimal trajectory. In addition, as UVAs have the continuity characteristics of task space and execution actions, this study selects the actor-critic reinforcement learning method to solve this problem, which can better address the issue of continuity.

20.2 Related Research

20.2.1 Research on UVA Path Planning

Path planning refers to finding an approximate optimal or optimal trajectory from a starting point to an endpoint within certain constraints or criteria in a given area. Path planning problems can be divided into static path planning and dynamic path planning [3]. In recent years, the development of machine learning technology has provided new research directions for path planning problems. The main methods are supervised imitation learning and unsupervised reinforcement learning. Reinforcement learning methods can explore and interact with the environment in unknown environments, learn based on exploration, and obtain the optimal path. In the field of UVA, due to the complexity of the environment, precise mathematical modeling is extremely difficult, so the application of reinforcement learning methods is more extensive. The problem of UVA trajectory planning has been studied in depth with the research of path planning algorithms [4].

Fu Xiaowei et al. used the Dijkstra algorithm to study the correlation between the already flown trajectory and the subsequent trajectory planning [5]. They estimated threat factors such as radar and created distribution maps. Roberge et al. conducted research on the dynamic path planning problem of fixed-wing UVAs in three-dimensional space [6], using intelligent bio-inspired algorithms such as genetic algorithm and particle swarm optimization algorithm. Bellingham et al. studied the

problem of cooperative trajectory planning for multiple UVA swarms [7]. With the continuous development of machine learning theory and related technologies, reinforcement learning theory has also begun to play a role in the problem of UVA trajectory planning. In the research of UVA trajectory planning aiming to maximize service quality, Chen et al. used reinforcement learning to study the static trajectory planning problem of multiple UVAs in a two-dimensional plane [8], where information such as user location and channel state is known. Yin et al. used the Deterministic Policy Gradient (DPG) method to solve the problem of dynamic trajectory planning for single UVAs in three-dimensional space [9], where information such as user location and channel state is unknown.

20.2.2 Reinforcement Learning Research

Minh et al. applied deep reinforcement learning methods to Atari games and introduced the concept of Deep Q Network (DQN). In the following year, Silver et al. proposed the Deterministic Policy Gradient algorithm [10] to address the issue of continuous action spaces, which is a policy-based algorithm. The DeepMind team combined deep learning methods with Monte Carlo methods to develop AlphaGo, which achieved a resounding victory against a renowned Go champion. Subsequently, deep reinforcement learning further evolved and produced more advanced algorithms such as Deep Deterministic Policy Gradient (DDPG) [11] and A3C.

20.3 Related Theories

20.3.1 Reinforcement Learning

Reinforcement learning discusses how an agent maximizes the rewards it receives in a complex and uncertain environment. This is illustrated in Fig. 20.1. It consists of two components: the agent and the environment. In the process of reinforcement learning, the agent and the environment interact continuously. The agent selects and executes an action A_t based on the state S_t of the environment. The environment changes due to this action and provides feedback in the form of a reward R_{t+1} to the agent. The agent then takes the next action based on the updated state S_{t+1} and the received reward R_{t+1}. This iterative process allows the agent to learn how to maximize cumulative rewards through interaction.

Fig. 20.1 The process of
reinforcement learning
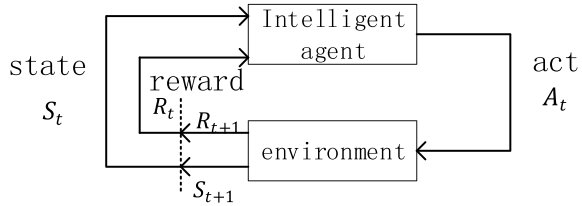
20.3.2 Markov Decision Process and Reinforcement Learning

Reinforcement learning is generally used to solve sequential decision problems, which are often modeled using Markov decision processes. Markov decision processes belong to the class of Markov models, which also includes Markov processes and Markov reward processes. The common characteristic of these models is their Markov property, which means that the current state at a given time only depends on the previous state and action, and is independent of earlier states and actions. This can be represented using conditional probability as follows:

$$P(S_{i+1} \mid S_i, A_i, S_{i-1}, A_{i-1}, \ldots, S_0, A_0) = P(S_{i+1} \mid S_i, A_i) \qquad (20.1)$$

In the equation above, S_i and A_i represent the current state and action at time t, respectively. The influence of actions and states in the reinforcement learning process is persistent, allowing for problem simplification.

In the following text, S represents the state space, A represents action space, "s ∈ S" represents an action belonging to the state space S, similar to action a. R represents the reward feedback from the environment for the current action. P is the probability of state transition, and γ is the reward decay factor. When using reinforcement learning to solve sequential decision problems, the agent's goal is to maximize the expected cumulative reward, even if it requires sacrificing short-term rewards for long-term returns. The discounted cumulative return after time t can be represented as:

$$G_t = R_{t+1} + \gamma R_{t+2} + \gamma^2 R_{t+3} + \cdots = \sum_{k=0}^{\infty} \gamma R_{t+k+1} \qquad (20.2)$$

Policy: It describes how to choose appropriate actions based on input states. Policies can be deterministic or stochastic. A deterministic policy directly selects actions that maximize rewards based on input states, which is a deterministic choice represented by Eq. (20.3). If the probabilities of taking different actions are dependent on input states, the policy becomes stochastic, as shown in Eq. (20.4). The policy distribution is represented by the policy function $\pi(s)$, which indicates the probability distribution of taking action $A_t = a$ in state $S_t = s$ for a specific agent.

$$a^* = \underset{a}{\mathrm{arg}max}\pi(a \mid s) \tag{20.3}$$

$$\pi(a \mid s) = P(A_t = a \mid S_t = s) \tag{20.4}$$

State Value Function ($V(s)$): It represents the expected cumulative reward that can be obtained from state $St = s$ when the policy function is $\pi(s)$. It reflects the average long-term reward and the agent's goal is to maximize the cumulative reward from the initial state to the final state. Since each complete process experiences different states and actions and the immediate rewards are not the same, the expectation operation represents the average cumulative reward for each episode.

$$V_\pi(s) = E_\pi[G_t \mid S_t = s] = E_\pi[\sum_{k=0}^{\infty} \gamma^k R_{t+k+1} \mid S_t = s] \tag{20.5}$$

The relation: $G_t = \sum_{k=0}^{\infty} \gamma^k R_{t+k+1}$ represents the discounted expected return after time t.

State-Action Value Function (Quality of State-Action function) $Q(s, a)$: It represents the expected cumulative reward obtained by being in state $S_t = s$ and taking action $A_t = a$ under the policy function $\pi(s)$. Unlike the state value function, it includes the action as input.

$$Q_\pi(s, a) = |E_\pi[G_t S_t = s, A_t = a]$$
$$= \left| E_\pi \left[\sum_{k=0}^{\infty} \gamma^k R_{t+k+1} S_t = s, A_t = a \right] \right. \tag{20.6}$$

20.3.3 Introduction to Actor-Critic

The Actor-Critic algorithm combines both policy-based and value-based methods. Value-based methods cannot handle continuous space problems, while policy-based methods often use episodic updates, resulting in lower learning efficiency. By combining the advantages of both, a method with good learning capabilities and the ability to handle continuous space problems can be obtained. The actor can be seen as the policy function $\pi(a|s)$, which interacts directly with the environment and learns how to achieve the best evaluation. This evaluation comes from the critic, which can be represented by the value function $Q(s, a)$. The critic learns during the interaction process how to provide appropriate evaluations. As a result, after each execution, the actor receives an evaluation from the critic for updating, while the critic learns to make its evaluations more objective and reliable. This allows for spontaneous convergence towards an optimal reward value and correction of poor action choices.

20.4   Problem Analysis

As shown in the system diagram of the unmanned aerial vehicle (UAV) trajectory planning system in Fig. 20.1, the UAV trajectory planning problem aims to achieve optimal or suboptimal trajectory flight from the starting position to the destination based on the flight mission and constraints, as well as the environment information and the UAV's own flight status. Firstly, the flight mission requirements and constraints of this study are clarified. The scenario assumed in this paper is a single UAV flying at a higher altitude, departing from a specified location, reaching the vicinity of the user area, and providing direct communication services. The UAV's flight actions are constrained to the two-dimensional plane, without changes in altitude. The problem to be solved is how the UAV can approach and hover near the user area in an unknown environment, where information such as user positions and channel statuses are unknown, using the actor-critic reinforcement learning method (Fig. 20.2).

20.4.1   Problem Modeling

There is a single unmanned aerial vehicle (UAV) aerial base station $B-UAV$ flying at a fixed altitude H_0, and at a certain distance, there is a set U consisting of K users. The users are located at a fixed altitude H_1. Assuming sufficient frequency resources, the UAV base station provides services to each user i (where $i \in U$) through frequency division multiplexing. The UAV base station $B-UAV$ can always receive signals from each user i (where $i \in U$), and interference between channels can be handled through other techniques. Without knowing the user positions and channel information, the UAV base station $B-UAV$ can observe the received power and uplink rate from each user. Based on the observed information, the UAV base station learns and makes decisions to fly close to the user area and find a better position to hover for providing services. According to the flight mission and constraints of $B-UAV$, the five-parameter tuple $< S,A,R,P,\gamma >$ in the Markov Decision Process (MDP) is modeled. The state S, action A, and reward R are defined. As for the transition probability P, it is not explicitly modeled as it is difficult to obtain accurate
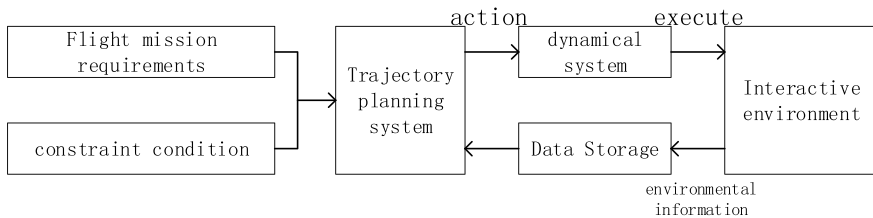

Fig. 20.2   Block diagram of unmanned aerial vehicle trajectory planning system

results even with long-term observations. Instead, the network learns in a model-free manner. The discount factor γ is set to 0.9, mainly considering long-term reward return, but the impact of rewards decreases as the time interval increases.

State Space S:

For the UAV, the state of the environment should be observable and knowable. However, in this problem scenario, the UAV is unaware of the user positions and channel information, including the distance to the users. Instead, the signal power received by the UAV from the users is considered as the observation. By assessing the magnitude of the power, it is possible to determine if the UAV is getting closer to the user area. Since the goal is for the UAV to approach the user area, an increase in power is desired. To make the UAV more sensitive to small changes, the change in received power from the users is chosen as the state. At time t, the UAV can receive the power from each user i in the set U, denoted as $P_{R,i,t}$. Therefore, the state S can be represented as $\{\Delta P_{R,i,t} \mid i \in U\}$.

Action Space A:

Since the UVA's altitude is fixed, its movable range is limited to a two-dimensional plane. Therefore, we choose two orthogonal components to represent the UVA's movement, with a maximum step size restriction. The UVA's movement at time t can be represented as $[\Delta x_t, \Delta y_t]$, where Δx_t and Δy_t denote the projections of the distance moved by the UVA on the two orthogonal components, respectively.

Rewards R:

In addition to measuring power observations, the UVA can also track the throughput during communication. The objective is for the UVA to move towards the user area, indicating an increase in throughput. Therefore, the change in throughput is chosen as the reward, where an increase in throughput is positive and a decrease is negative. This direct reward feedback allows the UVA to better understand the impact of its positional changes on the environment. In this study, the data transmission rate of the uplink link is selected as the metric. At time t, the throughput received by the UVA from user i in the user set U can be denoted as $C_{R,i,t}$. Thus, the reward R can be represented as $\{\Delta C_{R,i,t} \mid i \in U\}$.

Based on the above modeling, the problem can be described as follows: Starting from time t, the UVA observes the environmental state, namely the change in power $\Delta P_{R,i,t}(i \in U)$. It then takes action $[\Delta x_t, \Delta y_t]$ based on the state. Subsequently, the UVA adjusts its decision based on the sum of the changes in user throughput $\sum_{i \in U} \Delta C_{R,i,t+1}(i \in U)$ and the new environmental state information $\Delta P_{R,i,t+1}(i \in U)$, and selects the next action $[\Delta x_{t+1}, \Delta y_{t+1}]$. This process continues until the UVA hovers. The overall goal is to optimize the uplink transmission performance from start to finish, achieving $max \sum_t \sum_{i \in U} \Delta C_{R,i,t}$.

20.4.2   Channel Environment

In this section, we will use the derived state space, namely the power change, and the reward, namely the throughput change, to explain the channel environment.

The power received by the UVA from user i can be represented as:

$$P_{R,i} = P_{T,i} + 10\lg(G_{T,i}G_R) - 10\lg(g(d_i)) - 10\lg(\alpha^2) - x \tag{20.7}$$

where $P_{R,i}$ represents the power received from user i. $P_{T,i}$ represents the power transmitted by user i, set as 1W. $10\lg(G_{T,i}G_R)$ represents the gain at the transmitter–receiver side, set as 1. $10log(g(di))$ represents the large-scale fading (path loss). $10log(\alpha^2)$ represents the small-scale fading, neglecting the influence of multipath. As the UVA's movement speed is considered slow and Doppler effect can be ignored, $10log(\alpha 2) = 0$. x represents the shadow fading, which can be modeled using Gaussian distribution $x \sim N(0, \sigma2)$, where σ2 is between 8 and 10, here set as 9. $g(di)$ represents the path loss, which is the ratio of received power $P_{T,i}$ to transmitted power PR under the influence of distance in free space. Let $L(di) = 10log(g(di))$. Assuming there is a reference distance d_0, when $di > d_0$, the received power $P_{R,i}(d_0)$ is related to the received power $P_{R,i}(di)$. Combining with the logarithmic distance path loss model, we have:

$$L(d_i) = 10nlg(\frac{d_i}{d_0}) + L(d_0) \tag{20.8}$$

In Eq. (20.8), n is set to 4 and f represents the carrier frequency, which is chosen as 2 GHz (4G frequency band). The reference distance d_0 is set to 1 m. For $L(d_0)$, according to

$$P_R(d_0) = \frac{P_T G_T G_R \lambda^2}{(4\pi)^2 d_0^2 L} \tag{20.9}$$

we can obtain

$$L(d_0) = -20\lg(\frac{c}{4\pi}) + 20\lg(f) = 38.4 \tag{20.10}$$

Here L represents the system loss factor, set as 1. In summary, we have:

$$P_{R,i,dB} = -38.4 - 40\lg(d_i) - x \tag{20.11}$$

the throughput:

Considering only the uplink link, which is the data sent by users to the UVA, according to Shannon's theorem, we can derive the uplink data for user i as

$$C_i = \log_2(1 + SINR) \tag{20.12}$$

Here, $SINR = \frac{P_{R,i}}{\sigma^2}$, σ2 represents Gaussian white noise power, σ2 $=-74$ dBm/Hz.

20.5 Problem Solving

Trajectory Planning Based on Actor-Critic Method Algorithm

Algorithm 1: Actor-Critic Algorithm

1: Set the size of experience buffer D to L

Randomly initialize the parameters μ and θ of the action policy network π and the action value network Q

Set the target networks $\hat{\pi}$ and $\hat{Q}$ to have the same parameters as the action networks, i.e., $\theta Q = \theta \hat{Q}$ and $\mu\pi = \mu\hat{\pi}$.

2: Iterate over episodes episode = 1, 2, ..., M:

3: Initialize the user's position randomly to obtain St, and get the action $At = \pi(St) + N(t)$:

4: Execute A_t to obtain R_{t+1} and S_{t+1}, proceed to the next action

5: Save the data $\{S_t, A_t, R_{t+1}, S_{t+1}\}$ to the experience buffer D

6: When the experience buffer D is full, overwrite the previous data with new data

7: Randomly sample N sets of data from the experience buffer:

8: Predict the reward return based on the target network, as in Equation (13)

9: Update the value network Q using gradient descent with the loss function in Equation (14)

10: Update the parameters of the policy network using gradient ascent, as in Equation (15)

11: Every C steps, update $\theta\hat{Q} = \theta Q$ and $\mu\hat{\pi} = \mu\pi$.

Here, π is the action policy network, Q is the action value network, and $\hat{\Pi}$ and $\hat{Q}$ are the corresponding target networks. μ and θ are the parameters of the policy and value networks. To allow for exploration, a random perturbation $N(t)$ is introduced, which decreases gradually with time and training iterations. The entire algorithm flow can be divided into two processes: data interaction collection and network training. Firstly, the network parameters are randomly initialized, and an experience buffer of certain size is set to store the interactive data. Based on the initial environmental state, an action is selected using the policy network with randomly initialized parameters, and after adding a certain perturbation, the UVA executes that action, obtaining a reward and next state information, and the interaction continues. When there are enough data in the buffer, a batch of data is randomly sampled from the buffer for training.

Predict the reward return y for a given state and action based on the sum of the target value network and the reward:

$$y = R_t + \hat{Q}(S_{t+1}, \hat{\pi}(S_{t+1})) \qquad (20.13)$$

Calculate the mean squared error between y and the action value network, yielding the loss function for the action value network:

$$\text{Loss} = \frac{1}{2N} \sum_{i=1}^{N} (y_i - Q(S_i, A_i))^2 \qquad (20.14)$$

Update the parameters of the action value network using gradient descent, minimizing the difference between the estimated reward return and the actual reward return. Update the parameters of the action policy network using gradient ascent, maximizing the rate of the uplink:

$$\nabla_{\theta_\mu} J = \frac{1}{N} \sum_{i=1}^{N} \nabla_{\theta_\mu} \pi(S_i) \nabla_{A_i} Q(S_i, A_i) \qquad (20.15)$$

During this process, the network continues to interact with the environment, and the newly generated data will overwrite the old data in the buffer pool. The parameters of the target network are not updated. After a certain number of training iterations, the parameters of the action network are passed to the target network to update its parameters. Following these steps, continue updating the network parameters until convergence is achieved.

20.6 Simulation Results and Performance

Simulation Environment Analysis. In this study, the unmanned aerial vehicle (UAV) flight space is set in a 400×400 m flying area. The UAV is fixed at a height of 100 m, while there are 30 ground users with a fixed height of 2 m. At the beginning of each simulation, the UAV starts from a fixed three-dimensional coordinate point [100,100,100], and the ground users are randomly initialized and fixed within a 100 $\times$ 100 m range defined by the two three-dimensional coordinate points [300,300,2] and [400,400,2]. The UAV flies close to the user area. Each user has a transmit power of 1W, with no transmit power gain or receive power gain. The channel environment adopts the logarithmic distance loss model mentioned in Eq. (20.8), with a reference distance of 1 m. Doppler shift and multipath effects are not considered. The user's transmitted signal is subject to Gaussian white noise interference, while the interference between users has been handled in other ways. Other parameter settings are the same as those in the channel environment section of 4.2.

20.6.1 Environment Issues and Stability Analysis in the Transition Between Two Phases

Figure 20.3 shows the variations of power and throughput with round number for two independent networks with 20 users. It can be observed that at the transition point
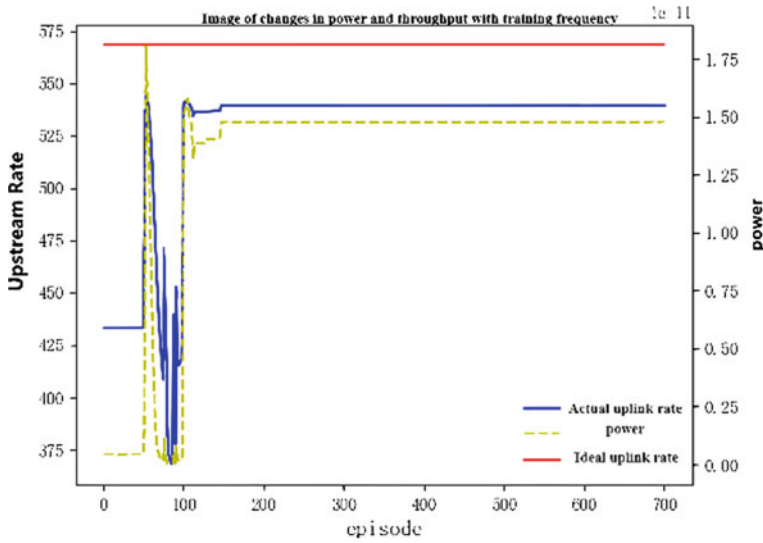
Fig. 20.3 Variations of power and throughput with 20 users

between the first and second phases, the UAV accomplishes the task of approaching the user area in the first phase but does not stabilize at that position. Instead, it moves, resulting in a sudden drop in throughput, and then proceeds to the second flight phase for data collection in the buffer zone. Based on the numerical values, it can be deduced that the discontinuity between the first and second phases results in the starting point of the UAV in the second phase being located further from the user area. This leads to the UAV having to learn both approaching and hovering/ turning back in the second phase, which prolongs the learning and convergence period. Additionally, there are slight fluctuations in power and uplink rate during the convergence phase. The stability of the results is not satisfactory.

It can be analyzed that in this study, there are flaws in the transition between the first and second phases, and the completion of the flight task in the first phase directly affects the implementation effect of the second phase. The network in the first phase has not achieved complete convergence and stability before proceeding to the second phase of learning. This easily leads to unstable movements before the UAV moves in the second phase, thereby affecting subsequent operations.

20.6.2   Simulation Results of User Random Movement

In this subsection, the results of simulations with randomly moving users in the case of two independent networks and dense user distribution will be presented. Figure 20.4 illustrates the trajectory of the UAV at the end of a round when the
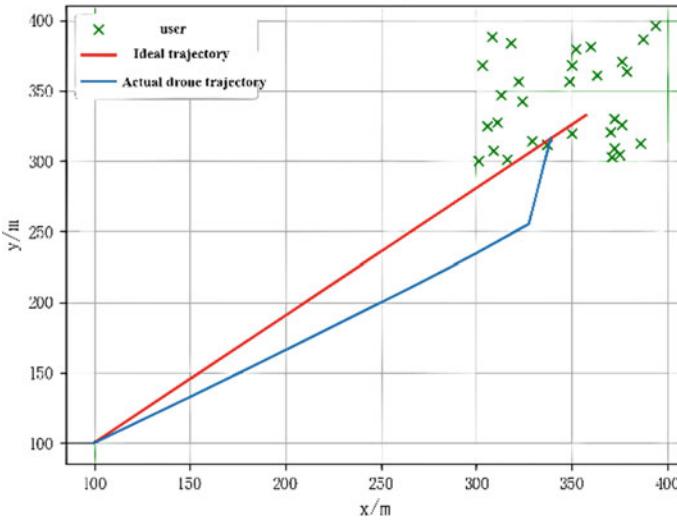
Fig. 20.4 The trajectory of the UAV with 20 users

user positions are randomly moving. It can be observed that even with random user movement, the UAV can still achieve satisfactory trajectory planning results.

Figure 20.5 displays the corresponding variation of cumulative reward with round number. Overall, the trend is consistent with the results when users are stationary. In the first phase, although the user positions are constantly changing, the task objective of approaching remains the same, aiming to achieve a higher cumulative reward and significantly improve throughput. In the second phase, the UAV needs to make slight adjustments to its position, trying to hover above the central area of the user zone. However, due to the random nature of user movement, the optimal hovering point also keeps changing. Thus, the UAV will continuously hover above the user zone, adjusting its position. However, in reality, these adjustments are always lagging behind. Once the UAV determines a better position, the user positions change again, resulting in fluctuations as shown in Fig. 20.5. However, overall, the throughput in the second phase shows a certain improvement compared to the end of the first phase.

20.7   Conclusions

The development of communication technology and the advantages of unmanned aerial vehicles (UAVs) in terms of flexibility and maneuverability have attracted more attention from researchers and scholars in the field of UAV communication. The trajectory planning problem, as an important issue in UAV base station deployment, directly affects the communication quality with ground users. In this paper, the trajectory problem for a single UAV under unknown user positions and channel
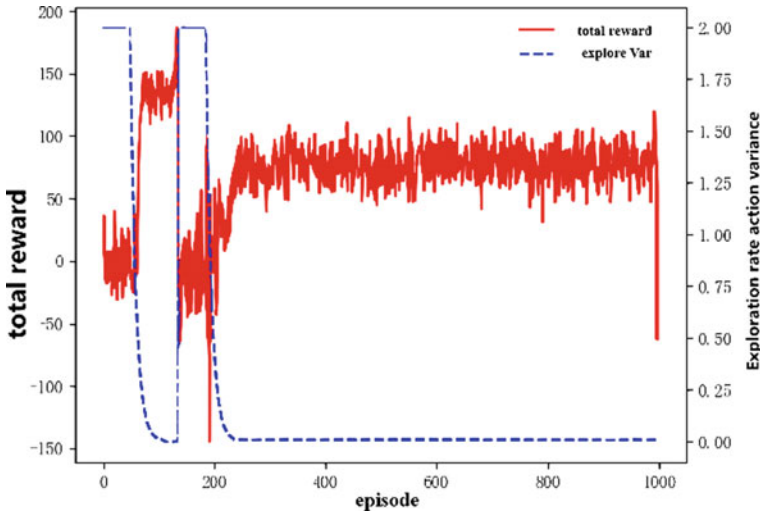
Fig. 20.5 Cumulative reward changes over rounds (number of users: 30)

environments has been studied, and the actor-critic algorithm has been utilized to maximize throughput in solving this problem.

Starting from the perspective of ensuring communication services, UAV trajectory planning has been conducted to maximize throughput, and a two-phase flight approach has been proposed. From the simulation results, it can be observed that reinforcement learning methods can effectively solve the path planning problem in unknown environments. The division into two flight phases can alleviate trajectory deviations to some extent, leading to overall good performance.

The future research directions are as follows: (1) Practical UAV trajectory planning needs to consider issues such as power constraints and obstacle avoidance. Further improvements need to be made according to different scenario requirements. This paper considers the trajectory planning of a single UAV, while in practice, there may be scenarios involving multiple UAVs for cooperative processing. (2) The actual UAV communication environment is more complex, which has been simplified in this paper. (3) From the simulation results, the stability of the network itself is not very good and is susceptible to disturbances caused by randomness. Additionally, further improvements are needed for hovering in dynamic user-changing scenarios.

References

1. Wu, D.P., Yan, J.J., Wang, H.G., Wu, D.L., Wang, R.Y.: Social attribute aware incentive mechanism for device-to-device video distribution. IEEE Trans. Multimedia **19**(8), 1908–1920 (2017)
2. Hossein Motlagh, N., Taleb, T., Arouk, O.: Low-altitude unmanned aerial vehicles-based internet of things services: comprehensive survey and future perspectives. IEEE Internet Things J. **3**(6), 899–922 (2016). https://doi.org/10.1109/JIOT.2016.2612119.
3. Li, D., Wang, P., Du, L.: Path planning technologies for autonomous underwater vehicles-a review. IEEE Access **7**, 9745–9768 (2019). https://doi.org/10.1109/ACCESS.2018.2888617
4. Wang, Y.Q., Zhao, J.Y., Liu, Y., Qinghua, Z.: Research on UAV relay deployment problem for emergency communication. In: 2020 5th International Conference on Mechanical, Control and Computer Engineering (ICMCCE), pp. 640–645. Harbin, China (2020). https://doi.org/10.1109/ICMCCE51767.2020.00142
5. Shen, Y., Liu, J., Luo, Y.: Review of path planning algorithms for unmanned vehicles. In: 2021 IEEE 2nd International Conference on Information Technology, Big Data and Artificial Intelligence (ICIBA), pp. 400–405. Chongqing, China (2021)
6. Roberge, V., Tarbouchi, M., Labonte, G.: Comparison of parallel genetic algorithm and particle swarm optimization for real-time UAV path planning. IEEE Trans. Ind. Inform. **9**(1), 132–141 (2013). https://doi.org/10.1109/TII.2012.2198665
7. Bellingham, J.S., Tillerson, M., Alighanbari, M., How, J.P.: Cooperative path planning for multiple UAVs in dynamic and uncertain environments. In: Proceedings of the 41st IEEE Conference on Decision and Control, vol. 3, pp. 2816–2822. Las Vegas, NV, USA (2002). https://doi.org/10.1109/CDC.2002.1184270.
8. Chen, Z., Zhong, Y., Ge, X., Mia, Y.: An actor-critic-based UAV-BSs deployment method for dynamic environments. In: ICC 2020-2020 IEEE International Conference on Communications (ICC), pp. 1–6. Dublin, Ireland (2020). https://doi.org/10.1109/ICC40277.2020.9148788
9. Yin, S., Zhao, S., Zhao, Y., Yu, F.R.: Intelligent trajectory design in UAV-aided communications with reinforcement learning. IEEE Trans. Veh. Technol. **68**(8), 8227–8231 (2019). https://doi.org/10.1109/TVT.2019.2923214
10. Wu, H., Song, S., You, K., Wu, C.: Neural-network-based deterministic policy gradient for depth control of AUVs. In: 2017 Chinese Automation Congress (CAC), pp. 839–844. Jinan, China (2017). https://doi.org/10.1109/CAC.2017.8242882
11. Zhang, H., Huang, M., Zhou, H., Wang, X., Wang, N., Long, K.: Capacity maximization in RIS-UAV networks: a DDQN-based trajectory and phase shift optimization approach. IEEE Trans. Wirel. Commun (2022)

Chapter 21
A Method for Traffic Flow Prediction Based on Spatiotemporal Graph Network in Internet of Vehicles

Yong Liu and Qinghua Zhu

Abstract In the past, traffic flow prediction, whether using statistical methods or traditional machine learning, only started from the aspect of time or space, so it cannot make good use of the internal characteristics of the collected big data. This paper uses a brand-new prediction model, combines spatial network with temporal network, and selects the emerging technology graph convolution neural network GCN on the spatial side in recent years. On the time side, LSTM and GRU are selected for experiments to collect the data of three subnets. 70% of the data are selected for training and the rest for testing. The experimental results show that after using GCN instead of CNN, the prediction performance has been greatly improved compared with the DMVST-Net model from the same two aspects of time and space, and the MAPE can be controlled at about 3%. At the same time, the selection of LSTM and GRU has little impact on the experimental results. There is a small gap in the three evaluation indexes of MAE, MAPE, and RMSE. The accuracy of LSTM is relatively higher, while the training time of GRU is relatively shorter.

21.1 Introduction

Accurate and real-time traffic prediction is an important part of intelligent transportation system [1], which is of great significance to urban traffic planning, traffic management, and traffic control. However, due to the complex time and space dependence, accurate and real-time traffic prediction has always been a problem of great concern. Among them, time dependence refers to the dynamic change of traffic state with time, which is mainly reflected in its periodicity and trend. Spatial dependence means that the change of traffic state is limited by the topology of urban road network,

Y. Liu (✉) · Q. Zhu
Beijing Polytechnic, Beijing, China
e-mail: liuyong@bpi.edu.cn

Q. Zhu
e-mail: zhuqinghua@bpi.edu.cn

which is mainly reflected in the transmission effect of the traffic state of the upstream section on the downstream section and the backtracking effect of the traffic state of the downstream section on the upstream section. How to learn the spatial topological characteristics and complex temporal characteristics of road network at the same time is the key to achieve accurate traffic prediction.

The K-nearest neighbors (KNN) model is a commonly used model in traditional machine learning and is one of the most commonly used methods in non-parametric regression. The advantages of the K-nearest neighbors' method are obvious—it is easy to implement, easy to adjust (by changing the value of K), and suitable for handling complex high-dimensional problems [2]. However, its disadvantages are unacceptable for practical applications in this problem. The K-nearest neighbors method requires a large amount of data support, and due to the lack of a training process, its computation time is much longer than other algorithms. In the context of traffic prediction, where road conditions and traffic volume information change rapidly, even a large amount of data from the same time period will have little significance if they are separated by a few days. Moreover, exceeding the computing power requirements of other models is also a burden in such scenarios. Therefore, the K-nearest neighbors' method is not suitable for today's traffic flow prediction.

Support Vector Regression (SVR), as discussed in [3], does not demonstrate obvious advantages in terms of robustness to outliers and high prediction accuracy in the context of traffic flow prediction. Meanwhile, its disadvantages include (1) not being suitable for large datasets and (2) exhibiting poor performance when the dataset noise increases and leads to target class overlap. These issues are particularly fatal in the practical application of traffic prediction. Therefore, despite the high-precision estimation characteristics of support vector regression for real-valued functions, we do not consider using it for traffic flow prediction.

ST-Resnet (Deep Spatiotemporal Residual Network), proposed in article [4], addresses three problems overlooked by statistical models and traditional machine learning models: (1) spatial dependence. Regions are not isolated from each other—traffic inflow in one region is influenced by the outflow in adjacent regions, and vice versa. Properly handling this factor's influence and incorporating it into the model is a major focus of traffic flow prediction. (2) Temporal dependence. Population movement in an area or changes in traffic volume are significantly affected by time. For example, congestion during peak hours may extend from 8 o'clock to 9 o'clock, and similar traffic conditions may occur at the same time each day during consecutive work days. This is obviously helpful for better prediction, so capturing the temporal dependence of traffic variations is also essential. (3) External influences, such as weather and major events within the city, also affect pedestrian and traffic flow predictions. This further emphasizes the importance of short-term traffic flow prediction.

In [5], the author used data from Didi Chuxing in Guangzhou, with approximately 300,000 samples per day. In the abstract, the author mentions that traditional traffic flow prediction mainly uses either temporal models or spatial dimension models, focusing on a single dimension of either time (LSTM) or space (CNN). Therefore, the article proposes DMVST-Net, which predicts taxi demand from the perspectives

of time, space, and semantics, enabling resource pre-scheduling. The author introduces the concept of LCNN, which combines Long Short-Term Memory (LSTM) with Convolutional Neural Network (CNN). Since CNN does not represent road conditions well, the author uses a local CNN, which only considers the areas near the prediction location. The results show that the combination of both temporal and spatial dimensions achieves better results compared to other models, while the inclusion of the semantic model has little improvement. Furthermore, the article mentions that CNN does not simulate the spatial structure of the road network satisfactorily. In situations where there is a certain distance between locations but the service demand is the same, CNN ignores the captured features. Therefore, a better grid structure is proposed to simulate the topological structure of the road network and combine it with temporal models.

21.2 Related Technologies

In Sect. 21.1, it was mentioned that the DMVST-Net model uses local CNNs to capture road condition features in spatial dependency, and the experimental results were satisfactory. In this chapter, we will introduce and compare CNN and GCN on spatial dependency, and explain the advantages and disadvantages of the two networks in solving this problem, as well as why we choose graph convolutional neural network. At the same time, we will introduce RNN and its two variations for temporal dependency and explain why we choose LSTM as the final choice.

21.2.1 Selection of Spatial Networks

Graph Convolutional Neural Network (GCN)

The concept of graph neural network (GNN) has a history of many years, but it has not been widely used in practical applications before the concept of graph convolutional neural network (GCN) was proposed. In paper [6] "Semi-Supervised Classification with Graph Convolutional Networks" published in 2016, the concept of GCN was proposed. This paper is also one of the most classic papers in the field of GCN.

Given that the road network has its own unique topology structure in the spatial dimension, which is a typical "non-Euclidean" data, constructing an adjacency matrix to represent this feature using convolutional neural networks (CNN) requires difficult storage and computing, and cannot guarantee data symmetry. As mentioned in the introduction, although CNN is used to represent the spatial structure of the road network in DMVST-Net, it can only grasp local features, and cannot capture the correlation between road conditions that are far apart. Graph convolutional neural networks (GCN) solve the shortcomings of CNN in processing road network distance well. Therefore, in our study, we choose GCN to study the spatial network.

21.2.2 Selection of the Temporal Network

After determining the spatial network using graph convolutional neural networks, we proceed to research and select the temporal network.

Sequential Model—RNN

Recurrent Neural Networks (RNNs) are highly effective in processing data with sequential characteristics. They can deeply analyze temporal information and semantic information within the data. Therefore, for the temporal network, we utilize RNN for learning [7].

The simple model of RNN is depicted in the following Fig. 21.1.

If we remove the "W" part, it becomes a familiar feedforward neural network consisting of input, output, and hidden layers. The function of "W" is shown on the right side of the above figure. To handle sequential data, similar to considering global features in CNN, RNN introduces a "recurrent" component. In other words, given the current input X_t and the current output O_t, we have:

$$Ot = V St \tag{21.1}$$

$$S_t = f(W S_{t-1} + U X_t) \tag{21.2}$$

From this, it can be recursively inferred that:

$$O_t = V f(W f(W f(W f(\cdots + U X_{t-3}) + U X_{t-2}) + U X_{t-1}) + U X_t) \tag{21.3}$$

It can be observed that the current output is related to the past outputs from several time steps ago. This allows for the capture of temporal features among the data, which meets the requirements for time data in traffic flow prediction problems. Therefore, for the temporal network, we adopt RNN for our research, which is consistent with the results in DMVST-Net.
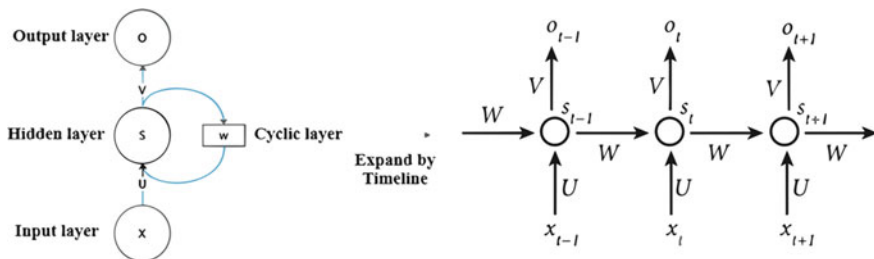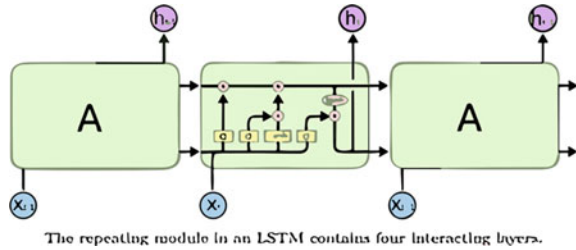

Fig. 21.1 Basic structure of recurrent neural network (RNN)

Fig. 21.2 Basic structure of
LSTM

The repeating module in an LSTM contains four interacting layers.

Long Short-Term Memory Artificial Neural Network (LSTM)

As mentioned earlier, RNN can capture the time characteristics of data, but we find
from Eq. (21.3) that this recursive method can lead to a lower weight value for data
that are farther away in the output, with a possibility of dilution if the distance is too
far. This is known as the "long-term dependency" problem. Additionally, since the
weight matrix for RNN training is circularly multiplied, circulating the same function
itself will inevitably lead to extreme nonlinear behavior. It is clear that RNN suffers
from both gradient vanishing and explosion problems. For practical applications of
predicting traffic flow with large amounts of data, we cannot simply use RNN for
research. Therefore, we choose LSTM as a variant that can solve the above two
problems.

LSTM Technology [8]:

The output components of a traditional RNN node only include weights, biases, and
activation functions. At the same time, all time slices share the same weight, which
is the direct cause of gradient vanishing and explosion. Therefore, LSTM has made
improvements in this area (see Fig. 21.2).

In LSTM, the concept of a forget gate is introduced, which means that the current
node can selectively remember or forget the impact of previous nodes on the hidden
layer. The input gate layer (sigmoid layer) determines which values will be updated
next, and then the tanh layer will create a new vector to update the candidate value in
the state. Then, the two are combined to create a state update, followed by updating
the neuron state, and finally outputting the value.

From the above introduction, we know that LSTM solves the problems of gradient
descent, gradient explosion, and long-term memory in RNN through a more complex
four-layer neural structure, making it suitable for solving the traffic flow prediction
problem studied in this paper.

Gate Recurrent Unit (GRU) [9]:

Although LSTM can solve the two problems of gradient vanishing and explosion and
long-term dependency in RNN, its complex structure also brings pressure to operation
and training. Here, we introduce another variant of LSTM, the gate recurrent unit
(GRU).

Fig. 21.3 Basic structure of GRU
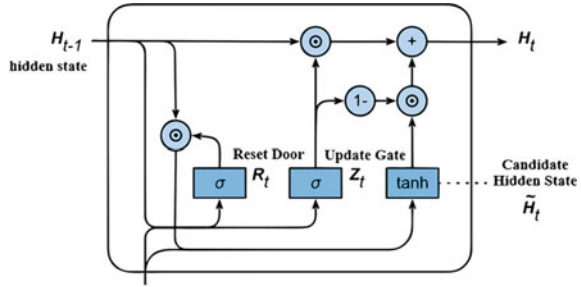
Compared with LSTM, GRU has a simpler structure. Although it still retains the mechanism of the gate, it only retains the reset gate and update gate, so after simplifying the structure, the training difficulty is further reduced and the efficiency is higher (see Fig. 21.3).

As LSTM and GRU are variants of RNN that solve the problems of gradient vanishing, gradient explosion, and long-term dependency, our main research is on LSTM and GRU. Studies have shown that GRU outperforms LSTM in overall performance except for NLP problems. Therefore, this paper will train and compare LSTM and GRU networks separately on the temporal dimension and finally give the results.

21.2.3 Integration of Temporal and Spatial Networks

After selecting the temporal and spatial networks, we construct the most basic T-GCN structure as shown in Fig. 21.4 [10, 11].

The data processing process is as follows: first, collect data to build a dataset. The first part of T-GCN is the spatial network (GCN). After the network captures the topological structure of the road network, the next part is the temporal network, where LSTM or GCN is selected to learn the temporal characteristics of the dataset, and then the traffic flow in the short future can be predicted.

Fig. 21.4 The basic
structure of T-GCN

Fig. 21.4 The basic structure of T-GCN
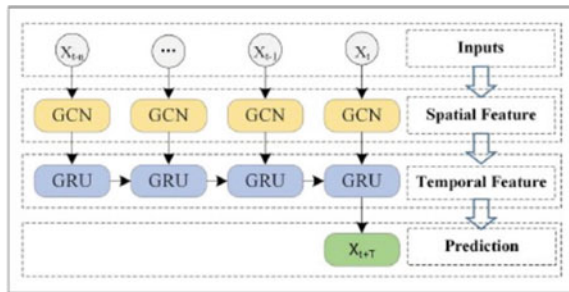
21.3   Model Construction

In this paper, Pycharm is used as the development environment, and the development is based on the Pytorch framework. The construction of neural networks is done using the nn.Module class in Pytorch as much as possible, making the code concise and ensuring program readability.

21.3.1   Implementation Method of Spatial Network

In the research of this problem, the first step is to determine how to model the spatial structure of the road network. Since we are studying traffic flow, which is a property belonging to each road, we focus on the traffic volume, parking volume, average vehicle speed, and other characteristics of each road. Therefore, the modeling approach is not to abstract intersections into points and roads into edges as in visual intuition, but to abstract roads into nodes, where the attributes of each road belong to the corresponding node. The connections between roads are treated as paths between nodes, which facilitates our research and data processing. In the research process of this paper, we specifically select five attributes for road features: traffic volume, average speed of traffic, number of vehicles waiting on the road, number of parked vehicles on the road, and average waiting time for vehicles. The units for these four features are respectively vehicles, meters per second, vehicles, vehicles, and seconds.

Implementation of the GCN Algorithm

First, the data is processed. As mentioned earlier, the data needs to be quantized into vector form. Since there are five features, the data is first read into a string variable called "str". Then, the traffic feature is used as a delimiter to separate and organize each group of data. Each group is then stored in five feature vectors: traffic_data, speed_data, queue_data, parking_data, and waiting_data.

After data preprocessing, the GCN class is defined. The input parameters include three variables: A, in_channels, and out_channels. These variables correspond to the adjacency matrix, input channels, and output channels in the algorithm.

The core algorithm of GCN is as follows:

$$H^{(l+1)} = \sigma(\widetilde{D}^{-\frac{1}{2}} \tilde{A} \tilde{D}^{-\frac{1}{2}} H^{(l)} W^{(l)}) \tag{21.4}$$

$$\tilde{A} = A + I \tag{21.5}$$

$$\tilde{D} = \sum_j A_{ij} \tag{21.6}$$

In Eqs. (21.4)–(21.6), the parameters from left to right represent the following:

- H(l) is the feature matrix of nodes in layer l.
- sigma() is the activation function.
- D_Hat is the degree matrix of the adjacency matrix.
- A_Hat is the self-connected matrix of the adjacency matrix.
- W(l) is the parameter for convolution in the l-th layer.

Here, instead of directly using the adjacency matrix A, we use A_Hat, which is the adjacency matrix with an added identity matrix. This is to preserve the characteristics of the nodes during information propagation. The topology of the road network is captured by multiplying A_Hat with the two-dimensional feature tensor H(l), and then multiplying it with the parameter matrix W(l) and adding a non-linear activation function sigma(). This operation aggregates the feature of adjacent vertices. Since the graph itself has the concept of degrees, vertices with high degrees and vertices with low degrees may have significant differences in feature distribution during propagation. To maintain the original distribution of the feature matrix H(l), A_Hat is normalized during the process. This completes the forward propagation operation in GCN.

In this study, the ReLU function is used as the activation function.

21.3.2   Implementation of Temporal Network

Modeling the Specific Influence of Time in Road Traffic Scenarios:

In real-world scenarios, the influence of time can be well quantified. The time attribute corresponds to each group of data, which includes five values representing road attribute features and the current time feature. By reading the data from the dataset, the time is extracted to be input into the network.

Analysis and Implementation of LSTM and GRU Algorithms:

The nn.Module class in Pytorch already provides pre-built functions for LSTM and GRU. Here, we define the LSTM (GRU) Layer class with input parameters: in_channels, hidden_channels, and out_channels. The feature dimension is set to be the same as in_channels. The number of stacked layers in the temporal network is set to two layers. A network that is too deep can hinder learning and parameter tuning. Finally, the forward propagation function is also defined.

21.3.3   Overlay of Spatio-Temporal Network Model

After constructing the temporal and spatial networks, we define the Net class, which inherits from the GCNConv class and LSTMLayer class. Since this experiment selects data from three road sections as the dataset, we define three channels and weight matrices corresponding to the three road sections. The processing steps are

Fig. 21.5 Model process
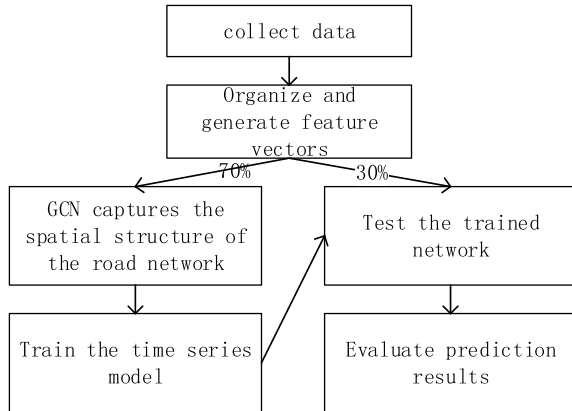
as described in Chap. 2: first, the feature matrix is reshaped using the reshape function, then multiplied by the weight matrix in GCN, generating the output results Y1, Y2, and Y3 for the first part of the spatial network. The lstm function is then applied to generate Y11, Y22, and Y33 for the temporal model. Finally, tensor concatenation is performed to complete the propagation.

The main training process of the model is illustrated in Fig. 21.5.

21.4   Experimental Simulation and Analysis

We will introduce the specific details of the experiments, including the establishment of the dataset, data preprocessing, training process, and comparison of the results of two temporal networks. Finally, we will present the optimal solution for traffic flow prediction in this paper.

21.4.1   Data Acquisition and Dataset Establishment

The dataset used in this paper mainly comes from three sub-regions, totaling 24,846 data samples. The traffic flow at each intersection in the sub-regions is collected every five minutes and merged to form the overall traffic flow file, new.csv. First, the intersections are numbered and a list is created to store the feature indicators. Then, the intersections are traversed, and the time data is read from the dataset. Based on whether the time changes, the counts and feature values are accumulated. If the time changes, the counting starts again. After processing all the data, a graph is plotted with time as the horizontal axis and the respective units as the vertical axis, as shown in Fig. 21.6.
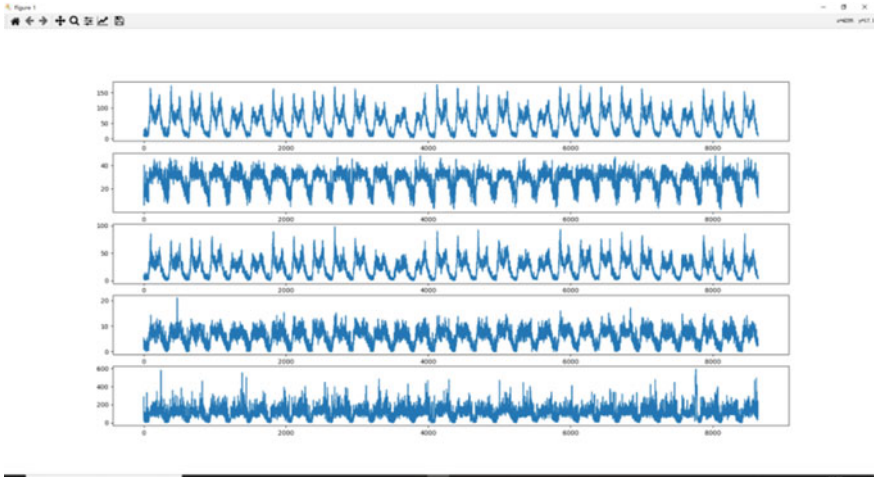
Fig. 21.6 Visualization of the preprocessed dataset

The periodic variation characteristics between the data can be clearly observed, which provides further evidence for studying traffic flow from a temporal perspective.

21.4.2 Traffic Simulation Prediction Experiment and Data Analysis

Data Input and Training Process:

1. Data Processing

First, the values from new.csv (the integrated dataset mentioned earlier) are read and saved into data_csv. The feature values are normalized, and the data_set dataset variable is created. The feature matrix and labels are then combined into ndarrays with sizes of (8102, 15, 5) and (8102, 1), respectively. In this experiment, 70% of the dataset is used as the training set, and the remaining 30% is used as the test set. The data is input into the integrated network.

2. Definition and handling of the loss function

The evaluation criterion, i.e., the loss function, is set as nn.MSEloss(), which represents mean squared error.

$$MSE = \frac{1}{N} \sum_{i=1}^{n} (x_i - y_i)^2 \tag{21.7}$$

In Eq. (21.7), x_i is denoted predictive value, y_i is denoted true value. During each epoch, the loss function is calculated and processed. Backpropagation is performed simultaneously with the forward computation.

3.   Parameter Selection

Since each epoch represents one forward pass and backpropagation process, multiple training iterations are required to make the model fit and converge. Additionally, the dataset needs to be divided into several batches, and in actual training, only a portion of the data is inputted at a time. If the epoch value is too low, the weights may not be sufficient, while increasing the epoch value may lead to transitions from underfitting to fitting to overfitting, especially if the dataset has high diversity.

The parameter batchsize represents the number of training samples in each batch. The size of batchsize determines the performance and convergence speed of the network. When the dataset is relatively small and the computer can handle training with a batch of samples, the convergence effect will be better.

After multiple training iterations, the final parameter values are chosen as epoch = 200, batchsize = 128, and time_step = 3, indicating that the value of the next data point is predicted based on the previous three data points. Since there are three sub-networks, N_nodes are set to 3, and the node feature parameter N_features is set to 5.

4.   Evaluation Metrics

Three evaluation metrics are defined in this experiment:

(1)   Mean Absolute Error (MAE):

$$MAE = \frac{1}{n} \sum_{i=1}^{n} |\hat{y}_i - y_i| \qquad (21.8)$$

In Eqs. (21.8), (21.9), and (21.10), $\hat{y}_i$ is denoted predictive value, and y_i is denoted true value. When the predicted value is identical to the true value, MAE is 0. The larger the deviation between the predicted results and the actual situation, the larger the MAE.

(2)   Mean Absolute Percentage Error (MAPE):

$$MAPE = \frac{100\%}{n} \sum_{i=1}^{n} \left| \frac{\hat{y}_i - y_i}{y_i} \right| \qquad (21.9)$$

When MAPE is 0, it is considered a perfect model. The larger the deviation between the predicted results and the actual situation, the larger the MAPE. A MAPE exceeding 100% indicates a poor model.

(3)   Root Mean Square Error (RMSE):

$$RMSE = \sqrt{\frac{1}{n}\sum_{i=1}^{n}(\hat{y_i} - y_i)^2} \tag{21.20}$$

RMSE is the square root of Mean Squared Error (MSE), providing a more intuitive understanding of the magnitude. Similar to MSE, the larger the deviation between the predicted results and the actual situation, the larger the RMSE.

Data Processing:

After using 70% of the data for training and predicting with the remaining data, the reshape function is used to convert the dimensions. The predicted results of the entire dataset are saved in pred_list and then converted to numpy format. The calculations of three evaluation metrics are performed and printed out. Additionally, the original results and predicted results from the test set are plotted together for visual comparison of the prediction results.

Training Result Evaluation:

①   Learning with LSTM in the temporal network

First, the LSTM function in the nn.Module class is used in the T-GCN file. After training for 200 epochs and making predictions, the output and evaluation metrics are as shown in Fig. 21.7.

Error output using LSTM network:

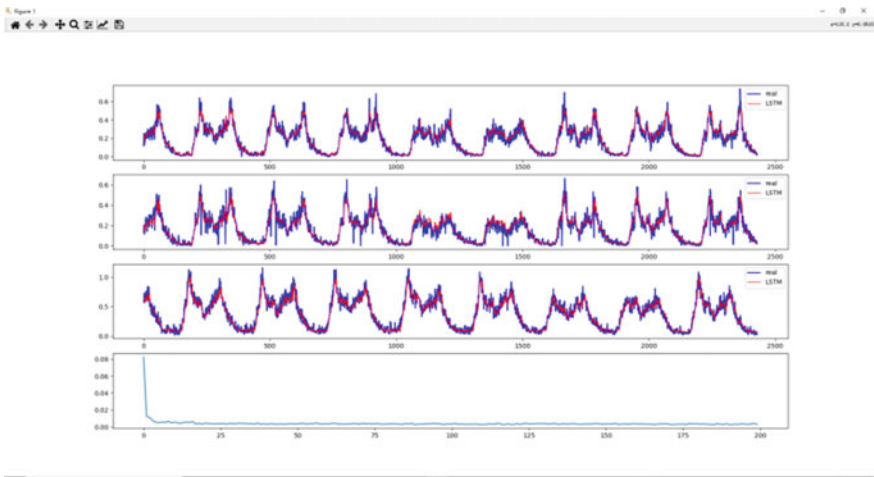Output results: MAE: 0.041408222, MAPE: 0.031441905, RMSE: 0.059112683.

Fig. 21.7 Comparison of predicted results using LSTM network

② Learning with GRU in the temporal network

Then, the LSTM model is replaced with GRU, and the training is performed for 200 epochs.

Error output using GRU network:

Output results: MAE: 0.042373203, MAPE: 0.032359015, RMSE: 0.059946347.

21.4.3   Experimental Results Summary

(1)   Spatial Network

Compared to the DMVST-Net model with MAPE 0.1616 and RMSE 9.642, the advantage of using GCN in the spatial network is evident. Compared to CNN, GCN not only captures local features but also grasps the spatial characteristics of the entire road network. The average absolute percentage error can be stably controlled around 3%. This experiment demonstrates that GCN is a better choice than CNN and showcases the potential of GCN as an emerging neural network in solving graph-related prediction problems.

(2)   Temporal Network

In this experiment, two temporal models, LSTM and GRU, were selected for comparative research. The data comparison is as follows:

It can be observed that LSTM outperforms GRU in all three-evaluation metrics. However, the advantage is not significant, with only a 0.001% difference in the mean absolute percentage error. Therefore, we conclude that both networks have their advantages. If higher accuracy is desired, LSTM is recommended. If larger-scale data needs to be processed, GRU can be chosen.

The superiority of the T-GCN structure lies in simultaneously considering the temporal and spatial networks. It abandons the convolutional neural network and instead adopts the graph convolutional neural network, which can better capture the topological structure of the road network. From the perspective of error metrics, it outperforms most existing models, while the choice between GRU and LSTM for the temporal network has a minimal impact.

(3)   Other Issues

In Fig. 21.8, (a) is shown the real data changes, and (b) is shown the predicted data. In the comparison of prediction results, we found that the model's performance in predicting peak and valley values was not satisfactory (Fig. 21.8).

This is an inherent limitation of the T-GCN model itself. Since the model captures the spatial characteristics of the road network by continuously moving smoothing filters in the Fourier domain, it leads to subtle changes in global predictions. As a result, the predicted curve fluctuates more smoothly compared to actual values and may not predict well during sharp data fluctuations.

Fig. 21.8 Deviation in predicting peak and valley values by the model

	MAE	MAPE	RMSE
LSTM	0.041408222	0.031441905	0.059112683
GRU	0.042373203	0.032359015	0.059946347
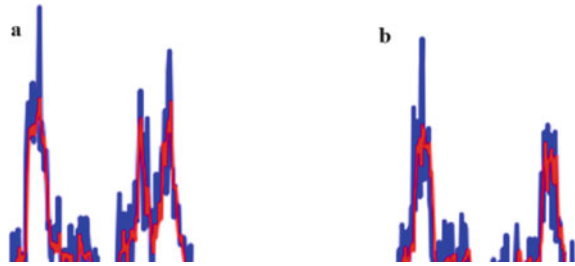
Table 21.1 Error performance comparison between LSTM and GRU

21.5 Conclusions

Starting from the intelligent transportation system (ITS), this paper introduces the problem of traffic flow prediction. We attempt to find a network model that maximizes the utilization of data features to predict actual traffic flow. Two T-GCN models were built in Pytorch, which combined graph convolutional neural networks with LSTM and GRU, respectively, in the hope of obtaining a more optimized network structure. Through parameter settings and multiple rounds of training in experiments, we found that introducing graph convolutional neural networks while abandoning CNN greatly improves the predictive performance of the model. The main reason is that the convolutional kernel of CNN cannot capture the global features of the network well when dealing with "non-Euclidean" data such as road networks. Even in terms of local features, two parts that are far apart may be ignored by CNN. The average absolute percentage error and root mean square error of the DMVST-Net model are 0.1616 and 9.642, respectively, which are significantly improved compared to other models, but still unsatisfactory for practical applications. Both T-GCN models can control the mean absolute percentage error to around 3%, while the root means square error and mean absolute error are related to the dimensional units, so they are not compared here. However, the significant reduction in MAPE indicates that T-GCN is a more superior choice compared to residual neural network models that use CNN. Regarding the selection of time networks, the performance comparison of the two network models is shown in Table 21.1. We found that there is almost no difference in the three error evaluation metrics. As for training time, due to the limited amount of experimental data (only over 24,000 sets of data), the advantage of GRU in saving computing time cannot be highlighted. However, in practical applications, as the amount of data increases, this advantage will also be amplified, while LSTM has its own advantages, namely high accuracy. Each has its own advantages, so the choice of which time series model to use in practical applications needs to be based on actual situations.

References

1. Zhang, H., Xu, J., Liu, X., Long, K., Leung, V.C.M.: Joint optimization of caching placement and power allocation in virtualized satellite-terrestrial network. IEEE Trans. Wirel. Commun. (2023)
2. Wu, D., Shi, H., Wang, H., Wang, R., Fang, H.: A feature-based learning system for internet of things applications. IEEE Internet Things J. **6**(2), 1928–1937 (2019)
3. Mohamad, D., Ossama, M.: SVR approach for predicting vehicle velocity for comfortable ride while crossing speed humps. Alex. Eng. J. **61**, 6119–6128 (2022)
4. Awan, N., et al.: Modeling dynamic spatio-temporal correlations for urban traffic flows prediction. IEEE Access **9**, 26502–26511 (2021). https://doi.org/10.1109/ACCESS.2021.3056926
5. Cao, D., et al.: BERT-based deep spatial-temporal network for taxi demand prediction. IEEE Trans. Intell. Transp. Syst. **23**(7), 9442–9454 (2022)
6. Jiang, B., Zhang, Z., Lin, D., Tang, J., Luo, B.: Semi-supervised learning with graph learning-convolutional networks. In: 2019 IEEE/CVF Conference on Computer Vision and Pattern Recognition (CVPR), Long Beach, CA, USA, pp. 11305–11312 (2019)
7. Zhou, L., Zhang, Q., Yin, C., Ye, W.: Research on short-term traffic flow prediction based on KNN-GRU. In: 2022 China Automation Congress (CAC), Xiamen, China, pp. 1924–1928 (2022)
8. Kang, D., Lv, Y., Chen, Y.Y.: Short-term traffic flow prediction with LSTM recurrent neural network. In: 2017 IEEE 20th International Conference on Intelligent Transportation Systems (ITSC), Yokohama, Japan, pp. 1–6 (2017). https://doi.org/10.1109/ITSC.2017.8317872
9. Chen, C., Liu, Z., Wan, S., Luan, J., Pei, Q.: Traffic flow prediction based on deep learning in internet of vehicles. IEEE Trans. Intell. Transp. Syst. **22**(6), 3776–3789 (2021). https://doi.org/10.1109/TITS.2020.3025856
10. Zhao, L., et al.: T-GCN: a temporal graph convolutional network for traffic prediction. IEEE Trans. Intell. Transp. Syst. **21**(9), 3848–3858 (2020). https://doi.org/10.1109/TITS.2019.2935152
11. Chen, Y., Han, W., Zhu, Q., et al.: Target-driven obstacle avoidance algorithm based on DDPG for connected autonomous vehicles. EURASIP J. Adv. Signal Process. **2022**, 61 (2022)

Chapter 22
Research on Behavior Control Method in 3D Virtual Animation Design

Li Wang, Wenhua Liu, and Lian Bai

Abstract In order to improve the effect of behavior control in 3D animation design, this paper combines 3D intelligent control algorithm to build model. In order to obtain high quality virtual human sign language animation, this paper proposes a new automatic generation technology of virtual behavior animation to realize intelligent control of behavior. According to the behavior control requirements of animation objects, the control model iIE can be constructed. In 3D virtual operation environment, the model and scene are built according to the size and style specified by technicians, and the animation parameters are flexibly adjusted according to the performance effect. After building the model, the method proposed in this paper is evaluated and analyzed with experiments, and the experiments verify that this technology has high applicability.

22.1 Introduction

With the continuous development of 3D modeling technology, 3D modeling methods emerge one after another. Geometry-based modeling is one of the mainstream three-dimensional modeling methods in film production at present, and artists make the required models through Maya, ZBrush, and other three-dimensional software. This method can flexibly create all kinds of complex models, among which human and animal models need a long time to make. Image-based modeling method generates a 3D model with texture by processing the photos of the target object. This method is suitable for generating models of objects and indoor scenes in real life, but there are usually some problems in the generated results, such as holes, uneven distribution of

L. Wang (✉) · W. Liu · L. Bai
School of Software, Shanxi Agricultural University, Taigu Shanxi, Jinzhong 030801, China
e-mail: wangli202311@126.com

L. Wang · L. Bai
College of Creative Arts, Universiti Teknologi MARA, Kedah Branch, 08400 Shah Alam, Malaysia

283

Mesh grids and unclear topological structure, which make it difficult to modify the models and have high algorithm complexity.

The method based on laser scanning modeling uses a laser scanner to scan objects and record their appearance data, obtain a three-dimensional point cloud of the object, and generate a model of the object after processing. The method of laser scanning requires expensive laser scanners, which can only be used for 3D modeling of stationary objects in reality and cannot meet the diverse creative needs of rehearsal production [1].

The application of digital media technology in film and television animation has expanded the development space and pattern of film and television animation [2]. The content of film and television animation is complex and involves a wide range, and there are significant difficulties in the production process. Moreover, the investment cost of traditional film and television animation production is relatively high, and the production technology is relatively backward, which leads to significant limitations in traditional film and television animation and makes it difficult to achieve breakthroughs and innovation [3]. The integration of digital media technology and the film and television animation industry has effectively helped the film and television animation industry overcome difficulties, greatly meeting the public's requirements for film and television animation. At the same time, it has expanded the development space and pattern of the film and television animation industry to a certain extent, gradually showing a trend of popularization and specialization. Based on the background of social development, the market and production environment of the film and television animation industry have also undergone significant changes, and the demand for professional talents is gradually increasing. Due to the widespread application of digital media technology, production techniques and tools are more advanced and convenient, greatly reducing the difficulty of film and television animation production and dissemination [4].

3D space coordinate transformation is the geometric basis of 3D graphics and the basic data theory of Virtual humans motion simulation. It uses vector, matrix, and coordinate system transformation to realize 3D space coordinate transformation, such as the movement change of Virtual humans's arm and body [5]. Design coordinate transformation experiment, master several coordinate transformation methods in rectangular coordinate system, including translation transformation, rotation transformation and compound transformation, and understand the geometric meaning of Homogeneous coordinates transformation through 3D space real-time display experiment [6]. Design a comprehensive experiment on spatial transformation, using coordinate transformations of multiple objects in three-dimensional space to master the mathematical methods of pose transformation of multiple objects in space. In experimental design, Cognitive load is reduced by increasing multiple target degrees of freedom [7].

The inverse Kinematics problem in the motion control of Virtual humans is to know the position and posture of the end of Virtual humans and calculate all the joint variables of the corresponding position of Virtual humans. In the virtual environment provided by the experiment, through the motion control operation of Virtual humans, understand the role of inverse Kinematics in the motion control of Virtual

humans. Through editing, we can design and adjust the joint angle to minimize the system error as far as possible to achieve the basic process of the circular coordinate descent algorithm. Finally, by observing the demonstration of the implementation steps of the circular coordinate descent algorithm in limb space, we can master the basic algorithm principle of Virtual humans motion control and obtain the characteristics of CCD algorithm such as high precision, Real-time computing, fast Rate of convergence, etc. for solving the inverse Kinematics problem of Virtual humans [8]. In experimental design, Cognitive load is reduced by dividing interactive elements and solutions. The cyclic recursive descent algorithm of inverse Kinematics includes multiple loops, which will produce a large Cognitive load if explained in order. You can first explain the calculation operation of each bone node, and then cover the internal loop that continuously tracks up the parent node, and then cover the external loop that constantly adjusts and approaches the target. In this way, the solution can be split according to the problem solving steps, which can reduce the learners' internal Cognitive load [9].

Design Virtual humans motion control experiment, generate Bezer curve by setting control points, and add motion paths for multiple Virtual humans to master the path planning and control of multiple Virtual humans. Set a motion for the virtual character selection and realize the fitting of Virtual humans motion and path through curve interpolation of a motion cycle. Further, through experiencing the virtual simulation system of the Pingchang Winter Olympics Beijing 8-min artistic performance, we can understand the application of multi Virtual humans motion control in the rehearsal simulation of national large-scale activities [10].

The flexible use of dynamic effects is crucial in the production of film and television animations. In the production process of film and television animation, in addition to some Urelement such as character dialogue and theme music, other sound effects can be summarized as dynamic effects. Actions such as sound, combustion flames, and mechanical noise can all be considered as dynamic effects [11]. When creating animation works, flexible use of dynamic effects can make the work more vivid and interesting, while also enriching the audience's viewing experience. When producing animation effects, animation producers must conduct in-depth analysis based on the content of the animation, coupled with reasonable imagination and conception. On the basis of fully grasping the central idea of animation expression, flexible use of animation effects can make the expression of film and television animation more vivid [12]. The widespread application of digital media technology in animation production can enhance the sense of immersion in film and television animation and enhance the expressive power of works. When dealing with the voices of characters, creators can use dynamic effects technology to set up dynamic effects that match the character's personality and highlight the character's image. In addition, the sound of broadcasting, animal calls, electrical equipment operation, noisy squares, and dark environmental sounds can all be produced using dynamic effects technology [13]. It can be seen that dynamic effect technology is widely used in animation production.

In order to improve the behavior control effect in 3D animation design, this paper combines 3D intelligent control algorithm to build a model, so as to improve the

news to intelligent control efficiency of 3D virtual animation and improve 3D sensory effect.

22.2 3D Virtual Animation Behavior Control Model

22.2.1 Animation Generation

Feature points and action information of virtual human are obtained in traditional animation design. After the animation is generated, the action overlap occurs in the action transition process, which seriously affects the animation effect. Therefore, in this study, we will mainly optimize this part of the technology to realize the automatic generation and constraint of virtual human actions.

This article mainly analyzes the difficult character models in animation, which are divided into static and dynamic models. Dynamic models are more difficult, and there are combinations of movement and various complex actions in dynamic models. These actions mainly include spatial translation and rotation, so modeling and analysis are needed for translation and rotation actions.

We assume that there are the frame C_i and the frame D_i in the generated 3D animation, frame windows of these two frames are constructed respectively, and the window length is t. We unify these two frame coordinate systems, align the key skeleton points of the control object, and calculate the distance between frame C_i and frame D_i. The specific calculation formula is as follows:

$$E(C_i, D_i) = \min \sum_{i=1}^{n} \eta_i \left\| u_i - Y_{\overline{\omega},i}; u'_i \right\|^2 \tag{22.1}$$

Among them, u_i represents the processing window generation point of frame C_i, u'_i represents the processing window generation point of frame D_i, and $Y_{\overline{\omega},i}$ represents the linear transformation formula, through which the translation and rotation of key vectors in three-dimensional action are completed. η_i represents the weight of image processing process, and the value of this weight is

$$\sum_{i=1}^{n} \eta_i = 1 \tag{22.2}$$

Taking this weight as the main parameter in the process of motion constraint, combined with linear hybrid algorithm, the motion constraint conditions of 3D animation are set. The usage environment of this constraint is set as follows: (1) The action duration is set to t', and when $t' < 0$, the constraint function is $w(t') = 1$. (2) The termination time of the action target is set to t', and when $t' > t_n$, the constraint function is $w(t') = 0$, and $w(t')$ has continuity. According to the above settings, the

target constraint function can be obtained:

$$w(t') = 2\left(\frac{t'+1}{t_n}\right)^3 - 3\left(\frac{t'+1}{t_n}\right)^2 + 1 \qquad (22.3)$$

On the basis of this formula (22.3), the translation process in the action is limited, and there are:

$$K_t = w(t')K_{t+1} + (1 - w(t'))K_{tn+1} \qquad (22.4)$$

Among them, K_t represents the translation vector in three-dimensional motion. The above settings are sorted out and integrated with the current 3D animation generation technology, so as to realize the automatic generation of 3D animation of virtual human.

22.2.2 3D Virtual Animation Behavior Control Model

The development of simulation animation is transitioning from the video form based on linear playing to the development and design of three-dimensional simulation system. On the one hand, the front-end modeling of equipment is carried out by using three-dimensional software, and it is fully simulated and interacted in the virtual engine. On the other hand, the programming software is used to design the development environment and database, and the bidirectional data feedback between the front-end visual content and the back-end control program is formed so that the operator can watch, move, rotate, and interact freely in this virtual full simulation environment without dead angle.

In the three-dimensional virtual operation environment, the model and scene are established according to the size and style specified by technicians, and the animation parameters, motion track and motion direction of the software virtual camera are flexibly adjusted according to the performance effect. On the basis of determining the material and environmental lighting, the animation is automatically run and generated to form a video with strong authenticity and observability (see Fig. 22.1).

(1) Prepare for modeling. All kinds of data of equipment spot check provided are analyzed, and the technical difficulties and key points are summarized, so as to prepare for the modeling work in the early stage. Through the understanding, analysis, and field investigation of the data, it is determined that the required equipment should be photographed and photographed on the spot, and the technical difficulties and key points should be solved on the spot in time. At the same time, according to the content of each equipment spot check, the original painting script is analyzed and various production materials are accumulated.
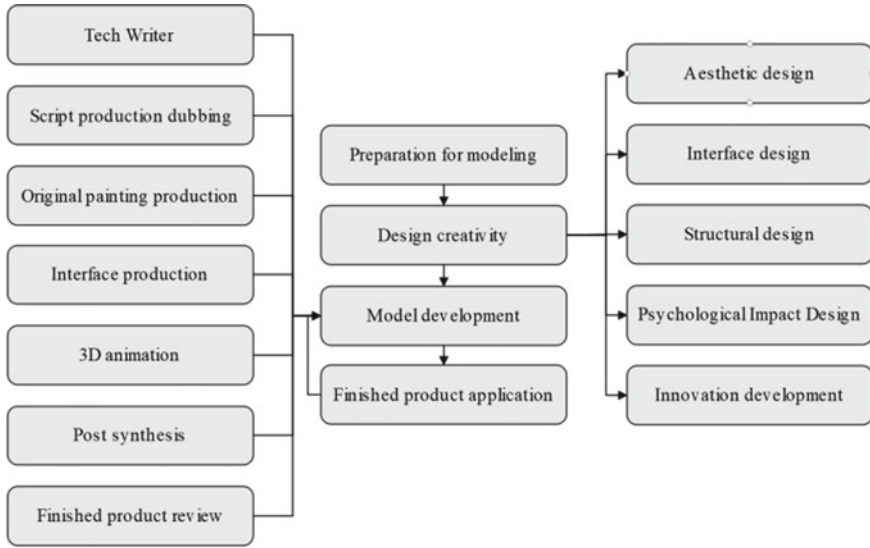
Fig. 22.1 Control scheme of animation design behavior

(2) Creative design. The foreground UI, animation style, interface style, color management, and background program involved in animation are comprehensively designed in aesthetics and structure.

(3) Model development. The whole feasibility analysis of modeling is completed. Under the premise of reaching the index and covering the application points, the scheme is optimized and the final scheme content is determined, so as to carry out targeted development work for each link. At the same time, after the object animation is made, it is necessary to check from the aspects of color matching, knowledge point content and animation performance, and make appropriate adjustments.

The overall framework of the system is designed as shown in Fig. 22.2, which mainly includes four modules: motion capture sensor, human displacement positioning, dance action recognition, and 3D animation display.

Motion capture sensor module is mainly responsible for using magnetometer gyroscope and accelerometer to collect limb information of human body during dance movement including horizontal direction data of sensor vertical axis rotation data and angular velocity data of sensor.

Three-dimensional animation display is responsible for recreating human dance movements. Considering that dance movements are mainly concentrated in human limb joints, this system combines the main joint models of human body, as shown in Fig. 22.3, and selects several joints such as head, neck, and waist to create a three-dimensional human body model, and expresses the dance movements through the human body posture representation method, thus realizing the dance movements display.
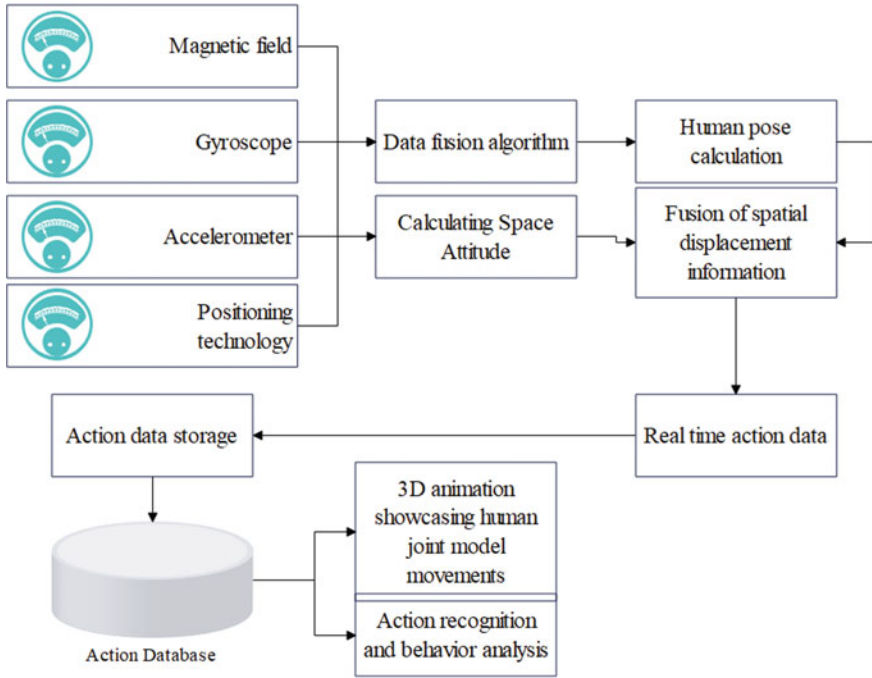
Fig. 22.2 Design drawing of overall system framework

Attitude representation methods mainly include Euler angle, rotation matrix, quaternion, and so on. Among them, the quaternion representation method has low computational complexity and can quickly nested data into coordinate system, thus satisfying the real-time capture of dance movements. Therefore, this system uses quaternion to represent dance movements and postures.

The whole process of animation character behavior recognition and tracking is shown in Fig. 22.4.

The original shape is a series of coordinate information of joints distributed in space. From the trajectory of human behavior, the absolute position of joints is the first-order information of skeleton data. In order to obtain more comprehensive characteristics of joint motion changes, it is necessary to use higher-order skeleton information. Firstly, the spatial and temporal motion characteristics of the original skeleton behavior information are analyzed and transformed twice, and the spatial static structural characteristics and temporal dynamic characteristics are obtained. Secondly, a dual-stream branch input structure is adopted in the shallow network to realize early feature level fusion, thus reducing the number of model parameters and the computational complexity of the model. The overall framework structure of skeleton feature enhancement graph convolution network is shown in Fig. 22.5.

Fig. 22.3 Joint model of
animation characters
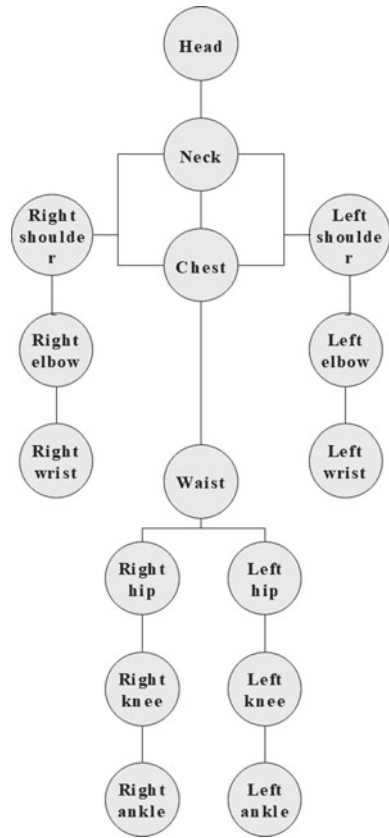
22.3 Experimental Analysis of Behavior Control in 3D Virtual Animation Design

Experimental process and results: in the experiment, NVIDIA GTX1070Ti graphics card is used as hardware, and the deep learning framework is Pytorch1.7.0, Ubuntu 18.0.04 and OpenCV3.4.2. The most common actions are screened out for verification. The selected movements are walking, sitting down, lying down, standing up, running, jumping, and rolling. The training parameters of the learning rate is set to 0.01, and every 10 Epoch, the learning rate is reduced to 0.1 of the original value. After that, the model proposed in this paper is verified, and the behavior control effect of this model is counted, mainly the control accuracy rate is counted, and the experimental results shown in Table 22.1 and Fig. 22.6 are obtained.

From the above analysis, we can see that the behavior control accuracy of 3D virtual animation objects is verified. Through data statistics, we can see that the behavior control method of 3D virtual animation objects proposed in this paper has

Fig. 22.4 The whole process of animation character behavior recognition and tracking
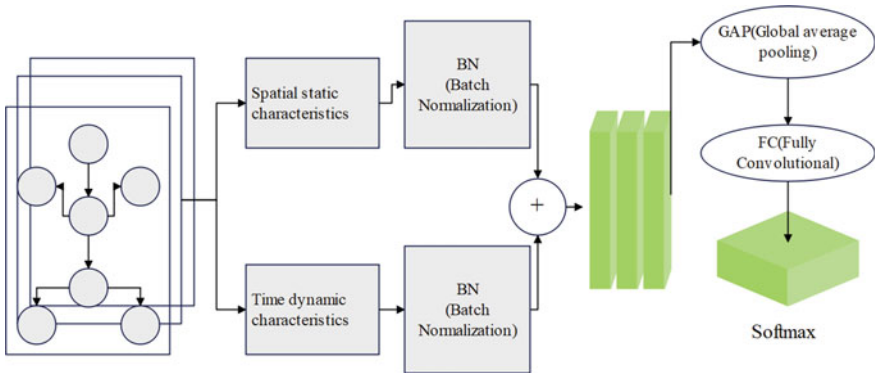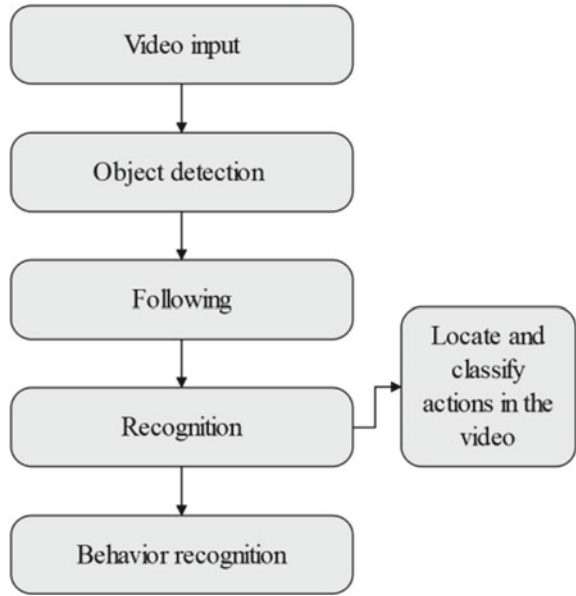
Fig. 22.5 Enhancement of skeleton features

certain effects and can effectively promote the reasonable design of 3D animation objects.

Table 22.1 Statistical table of behavior control accuracy

|	Walk	Sit down	Lie down	Stand up	Running	Hop	Jump	Tumbling
1	98.977	98.239	98.213	99.362	99.544	98.895	99.932	98.341
2	98.242	99.634	99.873	99.195	99.889	98.011	99.524	99.665
3	98.522	98.899	99.307	99.982	98.338	98.061	98.098	98.969
4	99.575	99.050	99.234	98.278	98.420	99.673	99.490	99.516
5	98.887	99.616	99.601	99.821	99.433	98.637	99.253	99.198
6	99.188	98.324	98.892	98.565	98.082	98.462	98.942	99.303
7	98.471	99.149	99.208	98.451	98.729	98.614	98.125	99.228
8	98.380	99.018	99.297	98.080	98.322	98.431	99.184	99.465
9	99.400	99.207	99.165	99.145	98.341	99.305	99.980	98.630
10	98.716	98.590	98.180	98.018	99.452	99.871	98.195	98.553
11	98.548	98.394	98.631	99.882	98.041	99.512	98.323	99.288
12	98.518	99.925	98.926	99.808	99.015	98.440	99.936	99.836
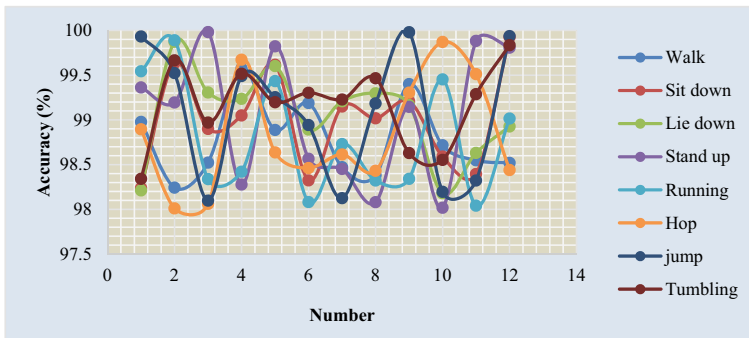
Fig. 22.6 Statistical diagram of behavior control accuracy of 3D virtual animation object

22.4 Conclusion

Traditional film and television animation production techniques are inefficient and the quality of works is uneven. However, digital media technology has an important impact on the production of animation film and television works, and directly affects the production, dissemination, and display of film and television animation works. Moreover, flexible application of digital media technology is conducive to improving the creator's design and editing level and can improve the artistic expression of works. At the same time, it can deepen the expression of emotions, storylines, and themes. In the information age, all walks of life are seeking the organic integration with modern science and technology. The wide application of digital media technology in animation film and television has greatly promoted the progress of animation

film and television industry. In order to improve the effect of behavior control in 3D animation design, this paper constructs a model with 3D intelligent control algorithm. Through the analysis of experimental data, it can be seen that the behavior control method of 3D virtual animation object proposed in this paper has certain effect and can effectively promote the reasonable design of 3D animation object.

The algorithm proposed in this paper is progressiveness to a certain extent, and the animation example test proves the feasibility of the algorithm. In the future, perceptual models will be added to animation instances to add emotional states to each individual, which can improve the realistic behavior generated by group path planning. Therefore, further research will be conducted on this aspect in the future.

References

1. Wang, Y., Wang, Y., Lang, X.: Applied research on real-time film and television animation virtual shooting for multiplayer action capture technology based on optical positioning and inertial attitude sensing technology. J. Electron. Imaging **8**(3), 30–42 (2021)
2. Wu, X., Guo, S., Xing, G., et al.: Information hiding in motion data of virtual characters. Expert. Syst. Appl. **159**(5), 113516 (2020)
3. Ishida, Y., Kumamoto, T., Watanabe, H., et al.: Creation of virtual three-dimensional animation using computer graphic technology for videoscopic transcervical upper mediastinal esophageal dissection. J. Laparoendosc. Adv. Surg. Tech.Laparoendosc. Adv. Surg. Tech. **30**(3), 25–34 (2019)
4. Thies, J., Zollhofer, M., Stamminger, M., et al.: FaceVR: real-time facial reenactment and eye gaze control in virtual reality. ACM Trans. Graph. **37**(2), 25.1–25.15 (2018)
5. Bonomi, M., Boato, G.: Digital human face detection in video sequences via a physiological signal analysis. J. Electron. Imaging **29**(1), 1–12 (2020)
6. Zhang, Z., Wu, Y., Pan, Z., et al.: A novel animation authoring framework for the virtual teacher performing experiment in mixed reality. Comput. Appl. Eng. Educ.. Appl. Eng. Educ. **30**(2), 550–563 (2022)
7. Li, L., Zhu, W., Hu, H.: Multivisual animation character 3D model design method based on VR technology. Complexity **2021**(4), 1–12 (2021)
8. Zhang, L.: Application research of automatic generation technology for 3D animation based on UE4 engine in marine animation. J. Coastal Res. **93**(sp1), 652–666 (2019)
9. Michalski, C., Cowan, M., Bohinsky, J., et al.: Visualization of heart electrocardiographic activity using a mixed reality system. FASEB J. **33**(S1), 444.22–444.34 (2019)
10. Lin, Y., et al.: Blind mesh assessment based on graph spectral entropy and spatial features. Entropy 22(2), 190–201 (2020)
11. Kondratiuk, S.S.: Ukrainian dactyl alphabet gesture recognition using convolutional neural networks with 3d convolutions. Artif. Intell.. Intell. **24**(1–2), 94–100 (2019)
12. Xu, L.: Fast modelling algorithm for realistic three-dimensional human face for film and television animation. Complexity **2021**(2), 1–10 (2021)
13. Cao, D.W., et al.: Research and application of multimedia digital platform in the teaching of college physical education course. J. Intell. Fuzzy Syst. **34**(2), 893–901 (2018)

Chapter 23
Research on Visual Communication Characteristics and Visual Narrative Change of VR News in We-Media Era

Li Meng

Abstract This paper studies the visual communication characteristics and visual narrative changes of VR news in We-Media era, which is aimed at radio and television transmission networks and on-demand and live broadcast application scenarios. The purpose of this study is to summarize the practical and forward-looking information dissemination balance strategy by analyzing and paying attention to virtual reality cases, and put the practical paradigm results into the media and news business practice. Moreover, this paper designs a relatively scientific and reasonable evaluation system, and prepares corresponding news reports in the form of words, visualization and games, and verifies the virtual news system proposed in this paper on the simulation platform. The experimental analysis shows that the visual communication system of VR news proposed in this paper meets the actual needs of people for news in the We-Media era.

23.1 Introduction

New technologies and applications are constantly emerging, and technology has changed from the guarantee element of media to the leading element, which has brought unprecedented revolutionary influence on the way information is generated, disseminated and received. With the continuous popularization of the Internet, new technologies such as 5G and virtual reality are being embedded in human life at an unprecedented speed and depth, and the media industry has also been upgraded and gradually transformed into intelligent media, and great changes have taken place in all aspects of news production.

The meaning of VR news is to use virtual reality technology to report news, mainly through the use of virtual environments and game platforms for documentaries, non-fiction stories, and news transmission on these two carriers. Its greatest purpose is to

L. Meng (✉)
School of Media, Shandong University of Political Science and Law, Jinan 250014, Shandong, China
e-mail: mljn89@163.com

enable the audience to immerse themselves in the scenes described in news reports and documentaries through their own visual perception, and to consider themselves as part of the scene of the news event, fully experiencing everything that happened on the scene, giving them psychological and physical feelings. The purpose is to further strengthen the readers through the correlation between the audience and the news programs produced by these news events [1]. Unlike traditional news production and dissemination methods, the audience can watch news through this special production method, which can greatly solve the audience's indifference towards news reporting, fully mobilize their curiosity and sense of participation. With the lens of the news report, they can perceive the direction and movement of their passage, and feel that they are at the scene of the news event, Virtual reality news is actually a new member of the virtual reality category, which is a news form with active exploration significance and an innovation in the new era news form. It also demonstrates the strong integration of news media and scientific and technological innovation in the new era [2].

The authenticity of news can be said to be the life of news, and maintaining the authenticity of news is the most basic ethical standard for journalists. The various elements presented in news reports must be authentic, that is, the time, place, people, reasons, process, and results of news reports must be verifiable. Technical means will simulate the real world as much as possible, endowing it with new perceptibility [3]. At this point, the information carried by the news event is presented realistically and given new meanings in the process of infinitely approaching the facts of the event. The processing process of data information by computers will be the process of information materialization, and the closer it is to the real experience, the more it can blur people's perception. In the future development of virtual reality technology, research on motion perception, olfactory perception, and taste perception beyond visual perception, auditory perception, and tactile perception will become increasingly focused. With the help of a comprehensive perceptual experience, the realism of virtual news will be infinitely enhanced, and ultimately the virtual world will exist parallel to objective reality, and the boundary between the two will become increasingly blurred. Research has shown that vision plays an absolute role in receiving information, with approximately 83% of normal human brain information obtained through visual information. Therefore, the mature virtual reality devices currently used in the market are virtual reality glasses or virtual reality headworn displays, rather than other virtual reality devices such as virtual reality headphones and virtual reality clothing [4]. The auditory experience is also an important component of virtual reality, and it is second only to visual perception needs. It not only needs to highly match the visual effect, but also has considerable comfort. Virtual reality headphones need to consider the sound effect and sound positioning in the virtual reality environment. It is precisely due to the visual realism brought by virtual reality technology that the audience's aesthetic expectations have been raised. The use of virtual reality technology in news presentation has improved the visual realism of news reporting [5].

Interactive art emphasizes the participation of the audience, which enables works to better communicate with the audience. This allows artists to not only express

personal emotions and reflect their own aesthetic pursuits, but also place the audience's position in a more important position. The functions of artistic works are also more diverse, and they are no longer simply being watched. The introduction of somatosensory hardware in virtual reality technology allows for accurate recognition of gesture movements and can be combined with images produced using 3D technology to achieve better interaction [6]. Currently, the application of virtual reality technology for news reporting may result in better utilization of interactivity in news games due to constraints in production costs, production cycles, and interactive devices. The so-called news game can be roughly explained as a new media product that combines news reporting with video games. Through news games, not only can information be conveyed to users, but they can also have a firsthand experience related to reporting [7].

Since the development of news communication, the communication methods that can be preserved have been honed and optimized over many years. According to the definition of news itself, and according to different forms and categories, it can be divided into many forms, such as news, communication, close-up, reports, comments, etc. News can also be divided into hard news and soft news, sudden news, periodic news, event news, and non-event news, all of which are different forms adopted under the influence of different environmental factors [8]. These different forms can be well applied in different environments, but cannot be copied. For example, for large-scale news events such as the Two Sessions, panoramic presentation technology can be used to produce. However, before sudden reports, panoramic presentation technology cannot be chosen due to production time and various facilities required. Therefore, whether choosing virtual reality news or other forms of news reporting, it is necessary to determine which reporting form is appropriate based on various factors. Virtual news also has certain limitations, with cumbersome production methods and procedures that currently cannot achieve the simplicity and speed of other forms of news promotion. Due to the current level of network bandwidth, data processing technology, data transmission technology, and video players, as well as the inability to promote virtual reality live streaming on a large scale, both domestic and foreign media are still in the exploratory stage of virtual reality live streaming. Therefore, there are still some problems in the application of virtual reality technology in news presentation [9].

The application of virtual reality technology has greatly enriched the form and content of news reporting, especially its contribution to the presentation of news content. It has changed the way news content was presented in the past and made news content more diverse and colorful. However, there are also some ethical and moral issues with the use of virtual reality technology in news reporting. Although some news events have already occurred and we cannot shoot them in the first place, we can use virtual reality technology to restore the incident process [10]. There is a problem in this, such as whether natural disasters, homicides, rape scenes, etc. will be restored, which will cause secondary harm to the parties involved, whether it will leak the privacy of the parties involved in the news, and whether it will induce juvenile delinquency, all of which may constitute news harm. The so-called news injury refers to the possibility or fact of causing certain emotional and spiritual harm

to the parties involved in the news during the process of news interview, editing, and dissemination, or even causing harm to the stakeholders related to the news facts indirectly. Virtual reality technology can enhance the integrity, sense of scene, and feasibility of television programs, enhance the connotation of television programs, and therefore has broad application prospects in news programs and legal education programs. But if virtual reality technology is not applied properly, it can also make programs become false and vulgar synonyms, and may even affect judicial fairness. In order to improve viewership, using unbridled splitting tactics we should learn from this approach. In addition to valuing commercial interests, the media should also shoulder their social responsibilities, promote positive social energy, maintain social fairness and justice, guard against criminals, and pay attention to safeguarding the personal interests of each audience and the common interests of the entire society. If news media only focus on the exciting descriptions of news events and abuse virtual reality technology, it will actually bring negative effects [11].

Although the emergence of virtual reality technology has made news reporting more three-dimensional and realistic, there are still many difficulties and drawbacks in the actual process: firstly, the thinking behind technology is how to enable audiences to watch news within a limited time, rather than relying on technology to gain attention. The second issue is that the cultivation of relevant virtual reality technology talents requires time, and the introduction of relevant equipment by the media requires increased investment in funds. Thirdly, virtual reality news requires further verification and exploration of relevant models from a business perspective [12]. The emergence of virtual reality technology has brought some new thinking, how to shoot news? How to edit virtual reality videos? How to perform sensory stimulation reasonably? How to ensure the authenticity of news? At present, the biggest drawback of virtual reality technology in application is the lack of content, which has become a consensus in the industry. If there is no good content, no matter how good the equipment and funds are, excellent news works cannot be produced. In addition, from a technical perspective, although the data processing capabilities of virtual reality technology are rapidly improving and the technical level has been significantly improved, it has only reached the level that can be applied. From an application perspective, virtual reality technology is far from meeting the needs of users for a comfortable experience [13].

This paper studies the visual communication characteristics and visual narrative changes of VR news in the We-Media era. How to better combine virtual reality technology with news presentation is an important foundation for the future development of news industry.

23.2   Visual Communication Model of VR News

The simulation scenario proposed in this article is a reflection of the objective environment of reality, where "simulation" refers to the collection of news facts by the media and their dissemination to the public in order to form a view of reality. Virtual

reality technology can truly form an interactive three-dimensional virtual environment generated by computers in the process of news dissemination. This environment is a simulated environment formed by the collection and organization of news facts by communication media and the design of participants. Simulated scenes refer to news scenes created by communication media for the public through virtual reality technology based on real news facts. This scene is dedicated to restoring real news scenes. Simulated scenes can be applied to various news events without strict production time requirements. By combining computer technology and 3D graphics technology, news events can be simulated and reproduced in an environmental manner, The application of simulated scenes can enable the public to comprehensively obtain the information contained in news events, further changing the traditional and rigid image of traditional news programs, and subverting the audience in terms of visual effects and scene presentation. This can enable the public to experience the situation and deepen their understanding of news events. The simulation scenario mainly applies virtual reality technology to present real news in a simulated manner. In this presentation process, there is a contradiction between real news events and virtual environments and scenes, as well as a contradiction between the authenticity required in the news dissemination process and the virtuality presented by virtual reality technology. Simulation scenarios need to combine reality and virtuality to form an accurate and realistic dissemination of news events, and to bring the audience into an environment of real news events. Therefore, simulation scenarios have the following three significant characteristics: authenticity, imagination, and selectivity.

Under existing technical conditions, due to the limitations of news editing time, simulation scenarios can be applied to the broadcast of most news events, except for those that require live streaming or have strict requirements for news production time limits. Among various types of news events, there is a type of sudden news. Due to the characteristics of suddenness, contingency, unpredictability, and danger, news events cannot obtain audio-visual information and can only be restored through the later descriptions of parties or witnesses. These news events that cannot provide the public with first-hand audio-visual information about the occurrence of news events are collected, edited, and broadcasted using virtual reality technology. It will greatly enhance the news experience and dissemination effectiveness.

Sudden news that cannot collect audio-visual information mainly includes the following four forms: first, sudden news events, which occur without any regularity, and the scene of the incident can be quite chaotic. Journalists cannot obtain audio-visual information about the entire process of the news event; Secondly, dangerous news events may occur in scenarios such as wars, earthquakes, etc. Journalists are unable to track news through film and television due to safety or technical means; Thirdly, sensitive news events, some of which are sensitive due to political or scientific and technological reasons and cannot be filmed through video or audio, and the scene of such news events cannot be presented; Fourthly, virtual news events, some of which do not actually occur or cannot be physically displayed due to technological means, such as docking with space stations or the effects of trace elements. This type of sudden news is often disseminated in two ways in traditional media reports. One way is to collect information from multiple sources at the time of the news, and

restore the news through the descriptions of the parties or news hosts. The second way is to reproduce the situation based on news materials by the parties or professional actors. With the development of the media industry and the advancement of digital technology, the reproduction requirements of mass news are becoming higher and higher. Simple language descriptions lack visual representation of news facts and scenes, which cannot attract the attention of the audience; On the one hand, the portrayal of news scenes by live actors has serious performance traces, and on the other hand, it is impossible to fully reproduce news facts at all stages. Therefore, the utilization rate of simulation scenes that rely on virtual reality technology to comprehensively restore news events and news scenes is increasing.

The core technology system of virtual reality can be divided into: basic device layer technology, platform tool layer technology and content application layer technology, as shown in Fig. 23.1.

The popularization and development of full-motion video in radio and television is limited by some factors. If the live broadcast channel of broadcast transmission is to ensure the viewing effect of VR video with high quality and definition, the resolution should be at least greater than 3840 × 2160. The bandwidth required for data transmission is huge, and the current transmission channel is difficult to support. Secondly, the way that the user terminal receives, displays and watches VR at home is different from the traditional TV viewing mode. The user needs to wear a head-mounted display, and the receiving terminal needs to be compatible with the
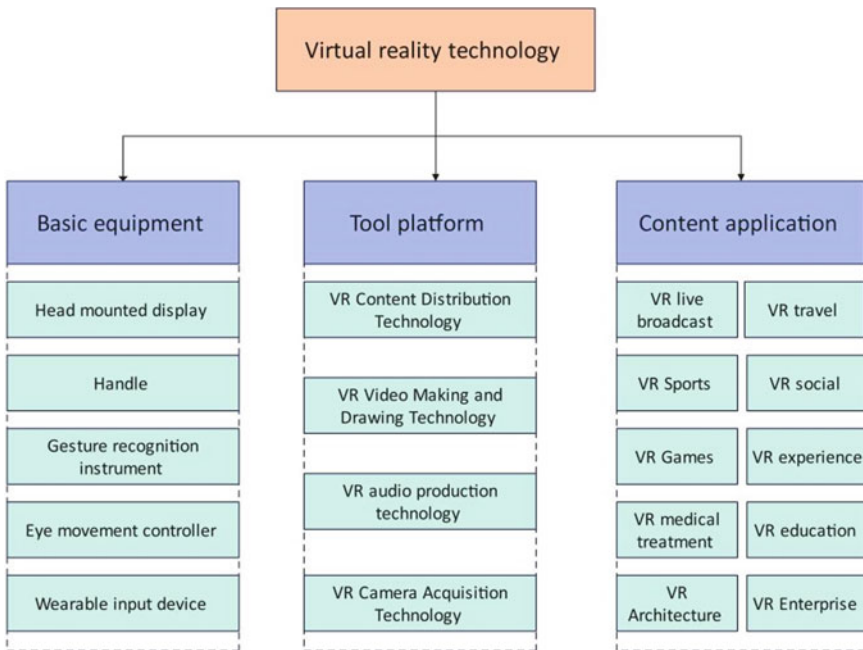

Fig. 23.1 Virtual reality technology system

existing flat-panel TV viewing. Finally, it is necessary to make VR content which is suitable for VR display and popular with users, so as to ensure the viewing of radio and television network users. Therefore, VR full-motion video technology is currently a single-point light and fast experience. If we want to get through the end-to-end link of radio and television, win users, and really bring users the experience of radio and television level, we need to continue to study and advance. Considering the application status and development trend of VR full-motion video technology in China's radio and television industry, this paper designs an end-to-end VR full-motion video transmission system based on wired network. The system architecture is clear, the cost is low, and the effect is good. It can provide VR live broadcast or on-demand service for home users [14].

This paper is aimed at radio and television transmission networks, on-demand and live broadcast application scenarios. At the same time, considering the connection with 4K/8K ultra-high definition resolution, the end-to-end transmission system of VR full-motion video based on wired network is studied and designed, as shown in Fig. 23.2.

In the process of cloud platform architecture design, it is mainly divided into three layers, namely IaaS, PaaS and SaaS. Among them, the main purpose of the IaaS layer is to provide hardware devices, such as network devices, servers and storage
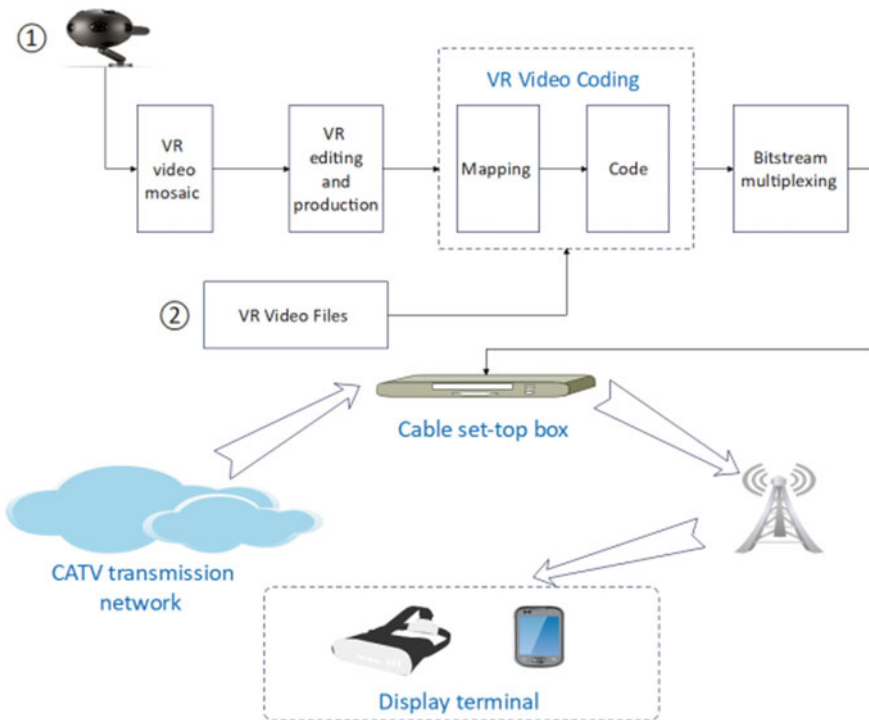

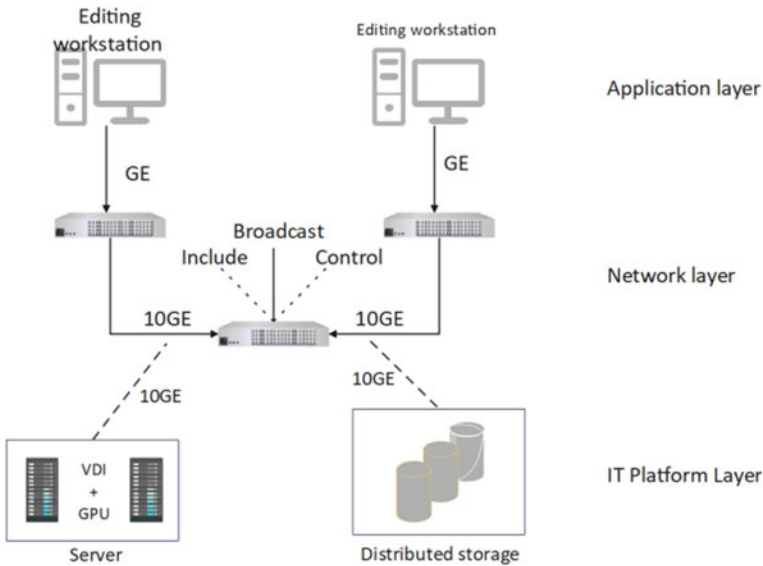**Fig. 23.2** VR full-motion video end-to-end transmission system

Fig. 23.3 Logical architecture of media convergence news production line system

devices. The main purpose of the PaaS layer is to provide middleware services. Simply put, it is to provide virtual operating systems and servers, and some technical staff of the group can develop their own programs and reduce the cost in site and hardware procurement. In addition, the SaaS layer can directly provide software services, and journalists and editors can also directly use browsers to access and use software, which can be used as long as there is a network. Cloud platform architecture determines the construction period, which can effectively improve the production efficiency and resource utilization rate, and also has the characteristics of high flexibility and controllability. Figure 23.3 shows the logical architecture of the media convergence news production line system.

The media convergence news production line system mainly includes five production business systems and two production auxiliary systems. The system platform includes more than 100 sub-functional modules, which can effectively support the news production and release of Weibo, TV, WeChat and App platforms. Compared with the traditional whole network architecture, the advantages of the project are reflected in the newly created news operation and command system, all-media publishing, all-media convergence, media data center and expert database system. The integrated news production platform should also be able to effectively separate application systems, media processing services and hardware, so that the design and deployment of systems and infrastructure can meet the requirements of computer room construction, network and security architecture. The all-media convergence platform has a variety of tools to collect various media resources, and also supports various media resources to enter the all-media content support platform according to the unified interface specification. Among them, the convergence content mainly

includes cooperative media, video websites, user sharing, social networks and mate-
rial collection, and the aggregated content types mainly include audio, video, text,
pictures and Flash. The video files obtained by the aggregation platform can be
processed by the call of the media data center, and the metadata information related
to materials can be intelligently processed and generated. The convergence platform
should use the corresponding interface protocol and the convergence production plat-
form, news command platform and all-media publishing platform in this system to
link with the media data center, so as to provide clues, materials and other services
for the system. Figure 23.4 shows the process of all-media content aggregation and
collection.

As a part of strategy simulation system, virtual news system is not only the
retrieval, merging and broadcasting of video, but also includes the collection, segmen-
tation and management of the video material, the data transmission between service
systems, the data transmission between speech synthesis systems and the message
communication between strategy simulation systems.

The overall structure of software and hardware of the virtual news system is
divided into three levels from bottom to top, as shown in Fig. 23.5. Among them, the
video collection, segmentation and management mainly collect video materials from
multiple video sources, classify and label the video files obtained after segmentation,
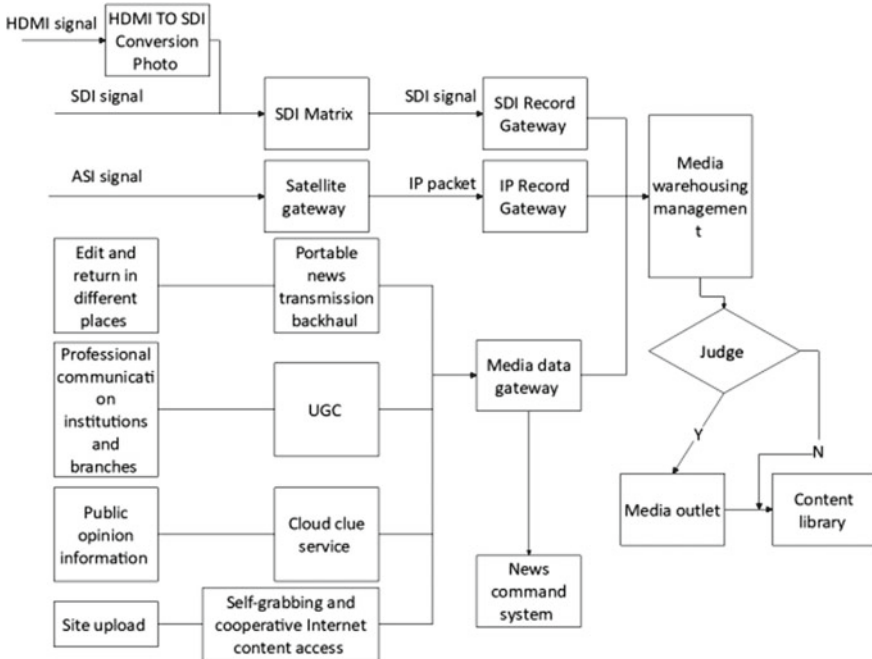and put them into storage management. The virtual news master control and interface

Fig. 23.4 The process of all-media content aggregation and collection

part mainly carries out instructions, sending, receiving and data transmission with other constituent systems or modules. The generation and playing of virtual news is to generate virtual news sequences according to the format defined by users according to decision-making schemes and interactive instructions and transmit them to the video broadcasting server for playing.

On the basis of having news video material files and their annotation information bases, we can start generating virtual news. The generation process of virtual news is shown in Fig. 23.6, and the numbers in the figure are the sequence of the generation process of virtual news. First, the strategy simulation system sends instructions to start generating virtual news. After that, according to the current situation of strategic drills, the virtual news general control retrieves the decision schemes of all parties from the decision scheme library, and extracts the information such as decision types, main participants, time and place, and takes them as the initial virtual news. Secondly, the system selects different virtual news broadcast templates according to different decision-making schemes, corresponding to different video types and press release formats, and adjusts the press release contents of each news broadcast segment according to the decision-making schemes, so that the broadcast sequence of news can be adjusted here. Then, the system retrieves appropriate video materials according to the extracted time and place information, and arranges the video files that can be previewed and retrieved at this time in descending order according to the time length. If it can't accurately reflect the news content, it cannot be selected, or the replacement video can be retrieved again. After that, the system uploads the confirmed broadcast video sequence to the video broadcast server and returns the
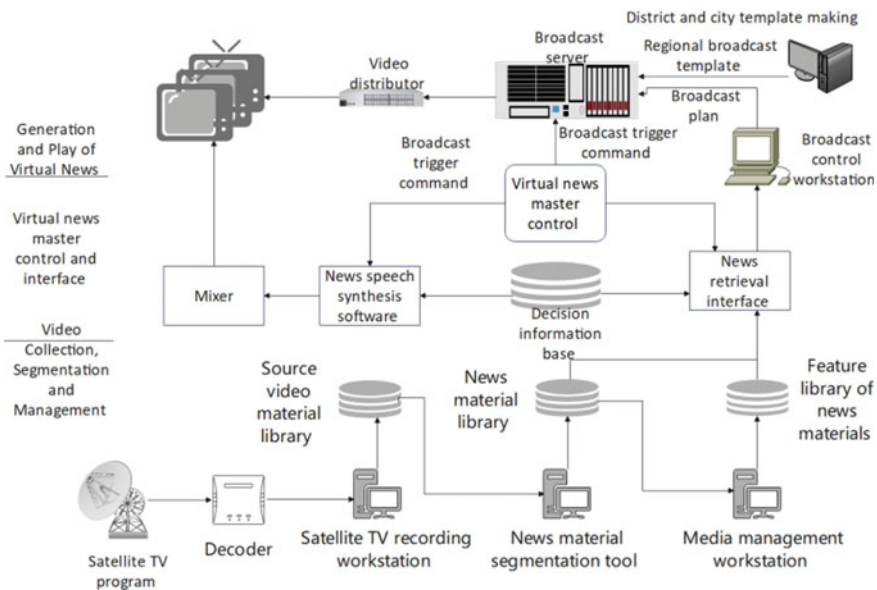

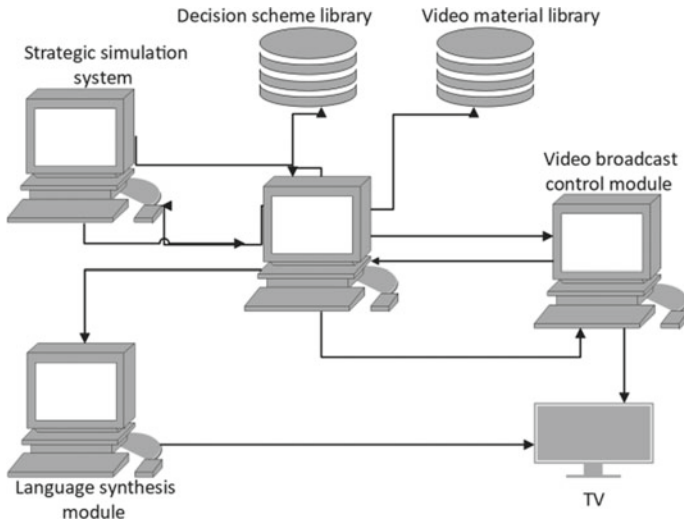**Fig. 23.5** Overall structure diagram of virtual news system

Fig. 23.6 Generation process of virtual news

information to the strategic simulation system, so that the virtual news is ready. After receiving the command of starting news broadcast, the system sends the command of starting broadcast to the broadcast server and transmits it to each decision-making party through the video distributor. At the same time, the system sends the news release content to TTS, and the server broadcasts the voice. After news is played, the judgment condition is that the audio is played, and then the next news is played, so that a complete virtual news is produced.

The main purpose of virtual news control is to control other parts to cooperate with each other to generate virtual news, which is the core of the whole virtual news system. The main purpose of video broadcast server is to imitate the real TV news in the form of playing virtual news. The video area is used to play video clips, and the picture area is used to place static pictures and block some signs of the original news video, and the text area is used for displaying strategic decisions in the form of rolling captions. Besides meeting the needs of broadcasting video clips, the virtual news broadcast template also plays an important role in shielding to avoid great penetration, so that there is no need to do other processing for the retrieved video pictures in the follow-up automation work.

The main purpose of speech synthesis server is to synthesize the text content of press releases into speech imitating real people, which is used to solve the problem that there is no real person imitating the host in virtual news system and there is no real person speech caused by the deletion of audio tracks in the original video. The output is not prepared for outputting video and audio, so ordinary TV sets can meet the requirements.

In the communication mode of immersive scene news, formal and professional news reports need to refer to the communication effect of news when considering

the news value and the communication effect will also determine the content selection and subsequent communication mode of news. Therefore, the research on the communication effect of VR scene news has become an indispensable means and basis for journalists to improve the news presentation mode and news quality. Based on the above analysis and setting of VR scene news effect evaluation system, instinct layer, behavior layer and reflection layer can be classified as the initial design layer of the effect evaluation model, and the effect produced by VR scene news acting on recipients, the relationship between news content and effect, and the influence of media on the effect are set as the performance layer of the system framework, while the information perception, educational reflection, social communication, aesthetic experience and the detailed rules divided under these four effect dimensions corresponding to the performance layer are collectively called the effect layer, and then these three main levels can be combined into the effect evaluation model of VR scene news. Figure 23.7 shows the VR scene news effect evaluation model:

Virtual reality news has developed rapidly and strongly in the past two years, and the research on virtual reality news has gradually changed from shallow analysis on technical level to in-depth research on theoretical latitude. The essence of virtual reality news is a brand-new media transformation force and a new communication logic product relying on technology. Therefore, it is necessary to make a deeper analysis of the communication of virtual reality news based on this level. This paper theoretically analyzes the communication bias of virtual reality news in different latitudes, dissects the influence of virtual reality news on individuals, society and culture according to its communication bias, and explores specific solutions to its problems, so as to build a communication balance mechanism of virtual reality news and give new research reference for the theoretical research of virtual reality news.

Virtual reality technology is a brand-new hope bearing in the media industry. With the empowerment of virtual reality technology, information recipients can fully experience the brand-new "time and space" and "off-site switching" of "region". This
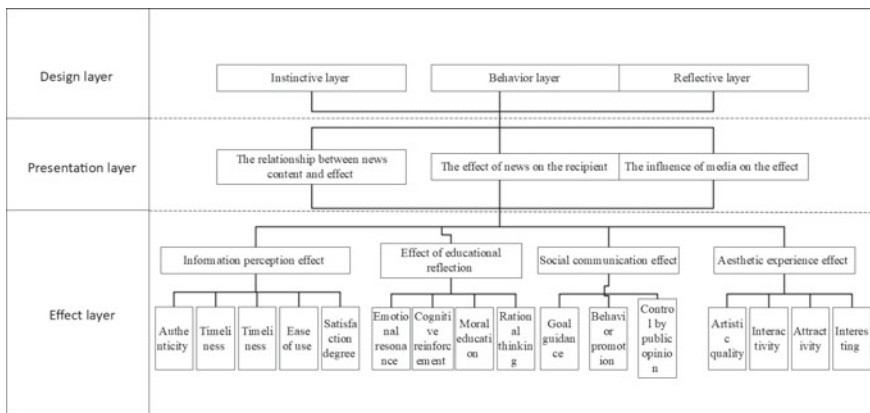

Fig. 23.7 The effect evaluation model of VR scene news

new media mode that can connect human organs and nerves is a brand-new change for the news communication industry. Due to the sustainable development of virtual reality technology, further development of virtual reality news has been put on the agenda, and the media eager to transform are eager to try. However, due to the lack of some theories, the development direction of virtual reality news is blocked.

23.3   Visual Communication Characteristics of VR News

The purpose of this study is to summarize the practical and forward-looking information dissemination balance strategy by analyzing and paying attention to virtual reality cases, and put the practical paradigm results into the media and news business practice.

On the simulation platform, this paper verifies the virtual news system proposed in this paper, and mainly combines the models shown in Figs. 23.1, 23.2, 23.3, 23.4, 23.5 and 23.6 in the second part to verify the visual effect, and evaluates the VR scene news effect through the system structure shown in Fig. 23.7, mainly evaluating the visual effect and communication effect of VR news. The communication effect mainly refers to the impact of the model in this article on the way news is disseminated, including people's acceptance and attractiveness to people. Quantitative analysis is conducted through survey documents, and obtains the results shown in Table 23.1 below.

From the above experimental analysis, we can see that the VR news visual communication system proposed in this paper meets the actual needs of people for news in the We-Media era.

Table 23.1   Visual effect and communication effect of VR news

NO	Visual effect	Communication effect	NO	Visual effect	Communication effect
1	89.262	75.023	13	81.774	78.508
2	82.424	83.548	14	85.507	88.625
3	78.171	77.565	15	83.992	86.856
4	90.933	82.540	16	90.883	77.343
5	89.091	86.758	17	85.857	86.357
6	83.810	84.019	18	86.236	81.121
7	83.102	83.752	19	80.378	87.627
8	90.028	87.446	20	80.570	88.329
9	88.257	87.342	21	91.059	88.923
10	88.507	88.130	22	78.847	88.722
11	83.812	84.582	23	87.860	83.328
12	90.164	81.927	24	79.444	77.837

Compared with visual news and virtual live news, it is found that virtual reality panoramic news has many advantages in the process of news reporting. This kind of news can not only make the audience independent and interactive, but also ensure the authenticity of news in value orientation, enhance the aesthetics of news and enhance the entertainment of news. The virtual reality panoramic technology mainly relies on its own unique advantages to dig news and report in depth.

In the design, the virtual reality panoramic news facing the competition not only follows some basic principles of news content production, but also innovates in interactive design, so that the audience can observe many details of news from different perspectives and roam in space, thus enabling the audience to actively obtain the competition information they are interested in in the virtual reality panoramic news, and meeting the audience's growing demand for "immersive" feeling of news.

In the evaluation of the communication influence of virtual reality panoramic news, the communication influence of virtual reality panoramic news is divided into three aspects from three different levels, and the communication influence is evaluated by means of the data of communication value in a qualitative and quantitative way, and the social value, information value and aesthetic value are included in the evaluation criteria.

23.4   Conclusion

This paper studies the visual communication characteristics and visual narrative changes of VR news in We-Media era, designs a set of relatively scientific and reasonable evaluation system, and prepares corresponding news reports in the form of words, visualization and games, and makes a comparative study to ensure the accuracy of the whole evaluation results. It can be seen that the whole virtual reality panoramic news has obvious advantages in communication influence and outstanding aesthetic value by means of the research and analysis of evaluation data, but it should be further consolidated and made great efforts to break through the bottleneck, give full play to its advantages, subvert the traditional news forms, change the value orientation of news communication and enhance the communication influence of news reports under high technology. Virtual reality panoramic news includes authenticity, interest, design and other characteristics in a news form, which can meet the traditional requirements of news and bring good experience. Therefore, there is an infinite space for development in the future, but there are still shortcomings in many aspects. It is necessary to further invest and strengthen the content construction, fill shortcomings, foster strengths and circumvent weaknesses, and shine increasingly in the era of media integration.

References

1. Brown, P.: SPVS seek feedback on salary survey. Vet. Rec. **185**(16), 512.3–512 (2019)
2. Jin, Y., Li, G., Wu, J.: Research on the evaluation model of rural information demand based on big data. Wirel. Commun. Mob. Comput. **2020**(5), 1–14 (2020)
3. Blowey, R.: Hunting hounds and bovine TB. Vet. Rec. **183**(13), 419.1–419 (2018)
4. Shaw, L.: Make helmets a policy. Vet. Rec. **182**(8), 234.2–234 (2018).
5. Hancox, M.: Badgers caught TB from cows. Vet. Rec. **182**(19), 553.2–553 (2018)
6. Wu, H., Cai, T., Luo, D. et al.: Immersive virtual reality news: a study of user experience and media effects. Int. J. Hum.-Comput. Stud. **147**(4), 102576–102590 (2021)
7. Wu, Y.Z.Z.: Immersive virtual reality news: a study of user experience and media effects. Int. J. Hum.-Comput. Stud. **147**(1), 21–34 (2021).
8. Kweon, S.H., Kim, S.J., Bean, M., et al.: A frame analysis of VR and AR news using semantic network method. Int. J. Adv. Sci. Technol. **110**, 87–98 (2018)
9. Gallardo-Camacho, J., Vanessa, R.: Relationships between law enforcement authorities and drone journalists in Spain. Media Commun. **8**(3), 112–122 (2020)
10. Jeong, S.H., Kim, S., Yum, J.Y., et al.: Effects of virtual reality news on knowledge gain and news attitudes. Int. J. Mobile Commun. **18**(1), 1–12 (2020)
11. Olivia, A.: No news is still good news: well-conducted studies with negative results make for a stronger evidence base. Vet. Rec. **182**(26), 742–743 (2018)
12. Froneman, C.P.E.J.D.: Vrye Weekblad's use of the term Boer to praise and berate in a cultural borderland. Tydskrift vir Geesteswetenskappe **58**(4), 752–769 (2018)
13. Kang, S., Dove, S., Ebright, H. et al.: Does virtual reality affect behavioral intention? Testing engagement processes in a K-Pop video on YouTube. Comput. Hum. Behav. **123**(2), 106875 (2021).
14. Sharma, A., Bajpai, P., Singh, S., et al.: Virtual reality: blessings and risk assessment. Indian J. Sci. Technol. **11**(20), 1–20 (2017)

Chapter 24
Power Internet of Things Sharing Terminal Based on Power Carrier Communication Technology

Shengzhu Li

Abstract With the development of Internet of Things technology and power carrier communication technology, transmission electric field lines are used for load communication, which makes it possible to build a cheap smart home system Intranet. This paper analyzes the sharing terminal of power Internet of Things combined with power carrier communication technology, and constructs a communication model. Aiming at the communication requirements of the scene of distribution Internet of Things and the differentiation of power grid operation and maintenance and extended services, this paper constructs a power line carrier communication model integrating the hierarchical network topology from transformers in the station area to users and families, which is suitable for control services and information collection services in distribution Internet of Things. Moreover, this paper comprehensively uses many advanced information and communication technologies such as cloud computing, big data, Internet of Things, artificial intelligence and edge computing to achieve all-round coverage of data collection, aggregation, processing and application in all links of power production and users. Through the experimental results, we can see that the power Internet of Things shared a terminal system based on the power carrier communication technology proposed in this paper has a good effect.

24.1 Introduction

With the continuous increase of the construction intensity and scale of intelligent power grid, big marketing, big service and big market have gradually become the development goal and trend of power supply enterprises, and intelligent management system, as an intelligent level in the field of power supply, has been widely used in various power supply stations. However, in the traditional power acquisition and control terminal and power marketing system, there are many problems, such as

S. Li (✉)
State Grid Changchun Power Supply Company, ChangchunJilin 13002, China
e-mail: ccjlgd0626@163.com

outdated equipment, large error between actual information and system information, and difficulty in data sharing among systems, which restrict the improvement of service capacity and service efficiency of power supply enterprises to a great extent. Therefore, it is urgent to design a highly intelligent and integrated mining and control terminal and power marketing system.

The application of transmission communication technology in the field of smart grid power collection has effectively promoted the development of the transmission communication industry. Electric field broadband communication can not only be applied in the field of smart grid collection, but also in the fields of smart cities, smart homes, and industrial control. Currently, with the rapid development of the Internet of Things, the scope of the Internet of Things has become an important area of power communication, and the construction of the ubiquitous Internet of Things is expected to become another explosive point of power communication. Reference [1] combines the communication needs of the home internet and the prospects of electric field line carrier technology to explore the specific implementation method of electric field line communication (PLC) in the home internet. Combining the application characteristics and channel characteristics of the Internet of Things industry, it studies encoding and decoding technology and self-organizing network technology to build a set of PLC suitable for the Internet of Things industry.

The power grid can also utilize power line carrier communication technology to fully develop and utilize existing power line resources for data collection, which can not only reduce terminal communication costs but also improve the power grid's ability to deeply perceive [2]. PLC technology, as a representative of the power Internet of Things technology that integrates energy and information, has the advantage of achieving energy and information sharing channel transmission without the need for specialized communication lines, as well as taking into account various functions such as line monitoring and management. However, the complex and variable channel characteristics and noise interference of power lines have also become the main factors hindering the large-scale application of PLC technology in power grids. At present, PLC-IoT technology has made significant breakthroughs in communication performance, which can overcome the difficulties encountered in the application of traditional PLC technology and provide high-speed and reliable communication services with low latency in milliseconds [3]. It can fully meet the communication needs of the power Internet of Things and better promote the gradual coupling and even overlap of the power grid and communication network. It is a successful case of the power Internet of Things technology that integrates energy and information. Based on PLC-IoT technology, in-depth research can seek a more universal path for the integration of energy and information in the Internet of Things technology for large-scale application in the field of power (energy), and promote the construction process of digitalization of power (energy) systems [4].

In the application scenario of ubiquitous power Internet of Things, power perception devices that are fully compatible with communication technology are widely present in all aspects of ubiquitous power Internet of Things. This includes the collection, storage, processing, and transmission of power business data streams, as well as the flexible access and deep integration of various external data. At the same time,

it comprehensively covers multi-level communication networks such as wired, wireless, and satellite, achieving ubiquitous interconnection and interworking of various network resources. The ubiquitous power Internet of Things needs to have strong compatibility in both the network transmission layer and the business application layer, and can be combined with other intelligent networks to break down barriers between different types of business categories, promote deep integration between the power system and other businesses, and strengthen information sharing and intelligent management among power grid companies, government management, users, and other entities [5].

The ubiquitous power Internet of Things has a large number of bottom intelligent terminals and a wide range of power transmission lines. Through the combination of the network layer and the application layer, it jointly realizes the processing of power business data flow. Edge computing extends and expands the computing, storage, and transmission capabilities of the central control of the power system to the edge of the network. It conducts real-time data processing and computing at the terminals and user sides of the network edge, reducing the amount of data transmission between network nodes. This significantly alleviates the processing and computing pressure on the central server and improves the response speed of terminal devices, effectively promoting the ubiquitous interconnection and collaborative processing of the power system [6].

The ubiquitous power Internet of Things comprehensively digitizes and intelligentizes traditional power business through the extensive collection and efficient processing of massive terminal node information in the power system. Strengthening the deep digitization of power grid business provides a reliable guarantee for the safe operation of power equipment. While improving the efficiency of power grid service business, it also solves the problem of equipment status monitoring and quality level evaluation. This not only strongly supports the original traditional business, but also integrates with other external businesses. At the same time, in the process of combining with communication and information technologies such as artificial intelligence, the ubiquitous power Internet of Things combines terminal node distribution coordination and central node unified control to solve the control difficulties and stability issues caused by the large number and wide distribution of nodes in the ubiquitous power Internet of Things to the greatest extent. Promote the deepening application of data-driven power business, and assist in building an intelligent, fast, safe, and effective comprehensive energy system. Artificial intelligence also gives traditional power grids intelligence and adaptability, allowing power business to no longer rely on a single indicator for control, but to make adaptive dynamic decisions and control based on its own situation and network status [7].

Power line communication and wireless communication have their own technological advantages. In the complex topology and communication environment of power line communication networks, the combination of power line communication and wireless communication is one of the best communication modes to complement each other's advantages. The existing research mainly focuses on the performance analysis of PLC and wireless communication hybrid networks at the physical layer, fusion techniques at the MAC layer 190–94, and fusion methods at the network layer.

In terms of research on the physical layer of hybrid networks, authors in reference [8] studied the advantages of parallel use of power line channels and wireless channels to improve the physical layer security of hybrid communication networks. We established mathematical formulas for traversal confidentiality rate and confidentiality interruption probability. When the eavesdropper uses a single data communication interface, the hybrid network has high physical layer security; Reference [9] studies a hybrid model of power line/wireless single relay channels for data communication, and provides a closed form expression for the outage probability of the hybrid network under a certain power spectral density and additive random noise interference, verifying that the performance of the hybrid network is superior to any single communication network; Authors in reference [10] proposes a joint estimation and suppression scheme for pulse noise and narrowband interference in the physical layer of hybrid power line communication and wireless communication networks based on the principle of compressed sensing, in order to improve the performance of the hybrid network; Authors in reference [11] proposes a joint noise suppression algorithm for PLC and wireless communication, which utilizes the spatial correlation between pulse noise and narrowband interference between wireless communication and power lines to transform the discontinuous interference noise problem into a less complex block sparse estimation problem. Using a method based on Bayesian linear minimum mean square error to estimate discontinuous and continuous pulse noise and narrowband interference, and further improving estimation performance based on their second-order statistics. The simulation results show that the hybrid network using the proposed algorithm has advantages over a single communication method; Reference [12] studied the statistical modeling of the frequency response amplitude of a home power line and wireless hybrid communication system in the 1.17-100MHz frequency band. Based on the measurement dataset, a statistical model was established, and the results showed that the channel frequency response amplitude of the home power line and wireless communication hybrid network follows a lognormal distribution.

This paper analyzes the power Internet of Things shared terminal combined with the power carrier communication technology, constructs a communication model, and simulates the model to provide reference for the subsequent application and promotion of power Internet of Things shared terminal.

24.2 Model System

24.2.1 Power Carrier Technology Model

In the sensing layer of power Internet of Things system, the measurement equipment mainly collects the state information and measurement data of various power and energy-related physical sensors, and senses the application site conditions. In the sensing layer, the commonly used sensors include not only smart meters,

but also sensor units that transmit information and data such as voltage, power, temperature and humidity. The optional wired communication modes of these units mainly include: optical fiber, power line carrier, 485 bus and industrial Ethernet. At the same time, the optional wireless communication modes of the unit mainly include: 230MHz wireless private network, 3G/4G/5G wireless public network, satellite communication, Zigbee, wireless micro-power and WiFi technologies. With the development of low-power wide-area communication technology, narrowband Internet of Things, enhanced machine communication and long-distance radio LoRa can also be used in the sensing layer of power Internet of Things system.

If only a single power line carrier technology is used in sensing layer networking, the reliability of data transmission in the sensing layer network will be difficult to guarantee. The existing feasible solution is that because the sensing layer requires higher and higher data transmission reliability, and a single communication technology is difficult to meet the requirements of the sensing layer for transmission success rate, the power line carrier communication technology which has been widely used in large areas is effectively combined with the wireless communication technology with better transmission performance, and a sensing layer fusion network is established to realize complementary advantages.

Electric current communication technology is a special means of communication, which uses electric field lines to transmit voice or data information as a means of information transmission, and can be applied to high voltage electric field lines (usually 35 kV and above), medium voltage lines (10 kV) and low voltage lines (380 V/220 V). It combines the analog or digital information carrier of the secondary device with the high-frequency information carrier, and realizes medium-distance transmission on the electric field line through coupling. Along this line, the power transmission of the remote terminal Internet through the communication carrier communication with the relay node effectively reduces the loss of information data due to very strong attenuation wavelengths, support structures and lines, and can simultaneously transmit the carrier information carrier.

Electrical carrier is a special way of communication in the electrical system. The high-frequency information carrier containing information is loaded on the electric field line through the power transmission module to realize data transmission across the electric field line, then the high-frequency information carrier is separated from the electric field line, and the information carrier is transmitted to the terminal device through the power module. The main body, information terminal and household devices in the smart home system all have a built-in carrier module interfaces, and directly use electric field lines to form the internal Internet. Therefore, the electric field line is not only a kind of energy, but also a means of information and communication, and it is also the embodiment of the advantages of live communication. Its basic structure is shown in Fig. 24.1.

Power Internet of Things is the concrete manifestation of Internet of Things in the field of power (energy). Through the comprehensive use of many advanced information and communication technologies such as cloud computing, big data, Internet of Things, artificial intelligence and edge computing, the data collection, aggregation, processing and application of all links of power production and users can be covered
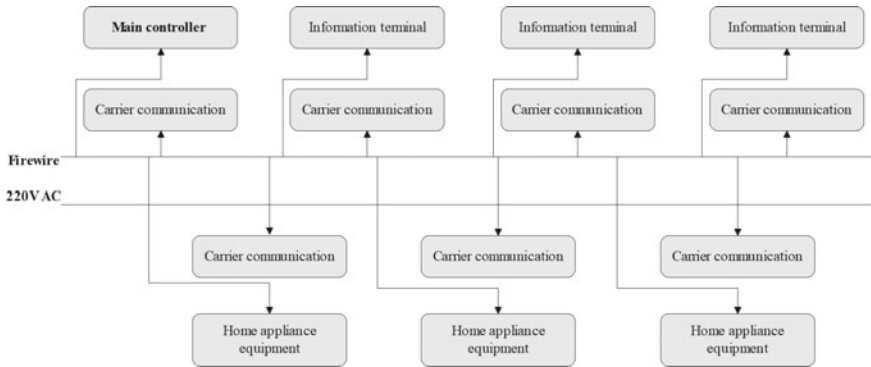
Fig. 24.1 Smart home network composed of power carrier

in all directions, and massive data can drive the power grid to develop towards intelligence and informationization, and effectively meet the challenges of establishing a new power system with new energy as the main body. The technical architecture of power Internet of Things can be divided into four layers: perception layer, network layer, platform layer and application layer, as shown in Fig. 24.2.

Power line carrier communication module is composed of MCU, transmitting carrier amplifier circuit, carrier coupling circuit, receiving carrier filter circuit, receiving carrier demodulation circuit, zero crossing detection circuit, isolation circuit, external crystal, indicator lamp, communication and power interface, power supply and so on. The overall design is shown in Fig. 24.3.

24.2.2 Power Internet of Things Shared Terminal Model Based on Power Carrier Communication Technology

Aiming at the communication requirements of the scene of distribution Internet of Things and the differentiation of power grid operation and maintenance and extended services, this paper constructs a power line carrier communication model integrating the hierarchical network topology from transformers in the station area to users and families, which is suitable for control services and information collection services in distribution Internet of Things. This ensures the reliability of carrier communication under the access environment of a large number of distributed power sources. The layered network topology from the station transformer to the user and the home is shown in Fig. 24.4.

The information transmission flow is shown in Fig. 24.5. The baud rate of data transmission is set to 115,200 Baud. The baud rate of the operation center and the control center are consistent. If the data verification of the transmitted data packet is correct, the transmission is completed. However, if the data verification is different
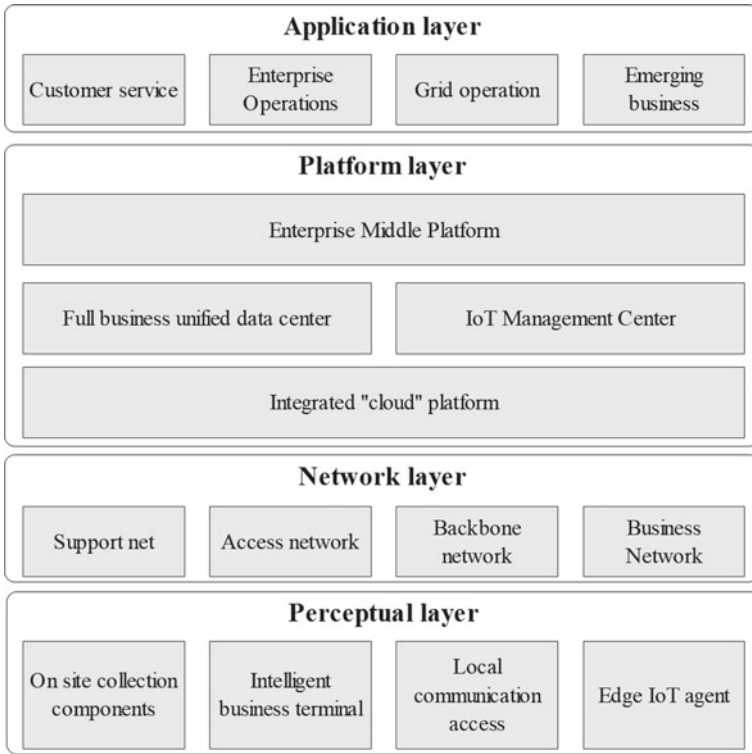
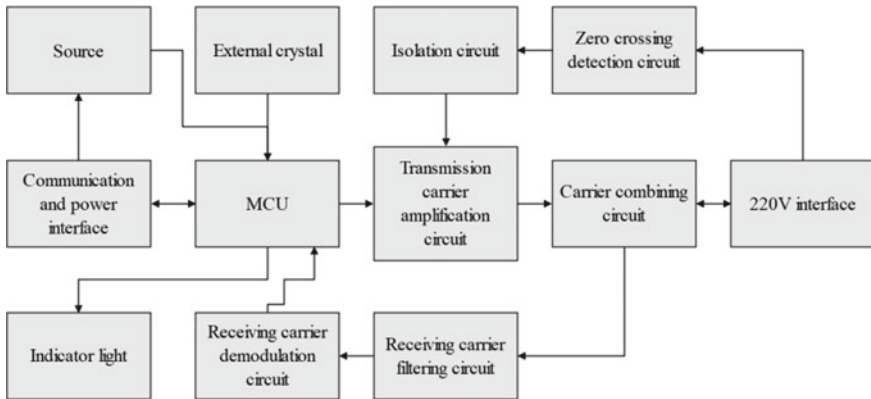**Fig. 24.2** Technical architecture of power internet of things

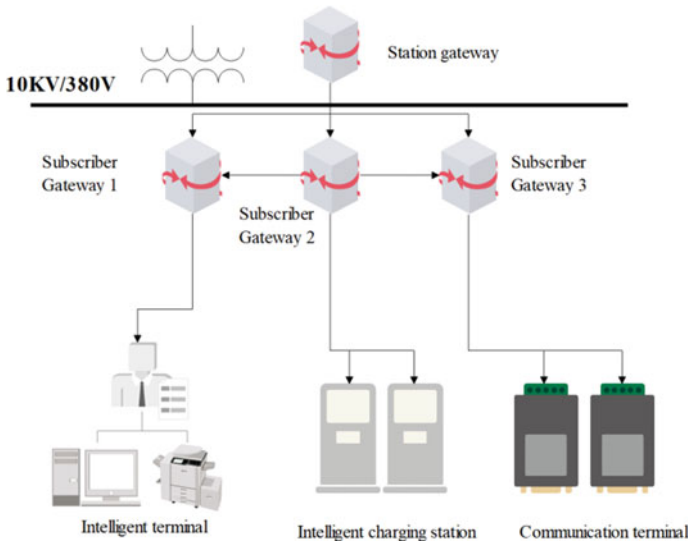**Fig. 24.3** Overall design of power line carrier communication module

Fig. 24.4 Hierarchical network topology

or the data frame is incomplete, the transmission is retransmitted according to the protocol until the receiving end receives complete and correct data information.

24.2.3 *Power Line Channel Modeling*

The topology of power distribution Internet of Things has a great influence on the transmission characteristics of the channel. Therefore, a power line channel model based on transfer matrix is established to study the influence of network topology on the channel transfer function, and strive to improve the comprehensive performance of power line carrier communication. According to the theory of power line transmission, any uniform power line can be represented by a dual-port network. Therefore, a two-port network can be represented by the transmission matrix T, also known as ABCD matrix. The transfer matrix theory is described below, and a common equivalent definition of a dual-port network is as follows

$$\begin{vmatrix} V_1 \\ I_1 \end{vmatrix} = \begin{vmatrix} A & B \\ C & D \end{vmatrix} \begin{vmatrix} V_2 \\ I_2 \end{vmatrix} = T_f \begin{vmatrix} V_2 \\ I_2 \end{vmatrix} \tag{24.1}$$

Among them, V_1 and I_1 represent input voltage and current respectively, V_2 and I_2 represent output voltage and current respectively, and the four coefficients vary with frequency, which can be expressed by the following formula and fully reflect the electrical characteristics of a dual-port network.
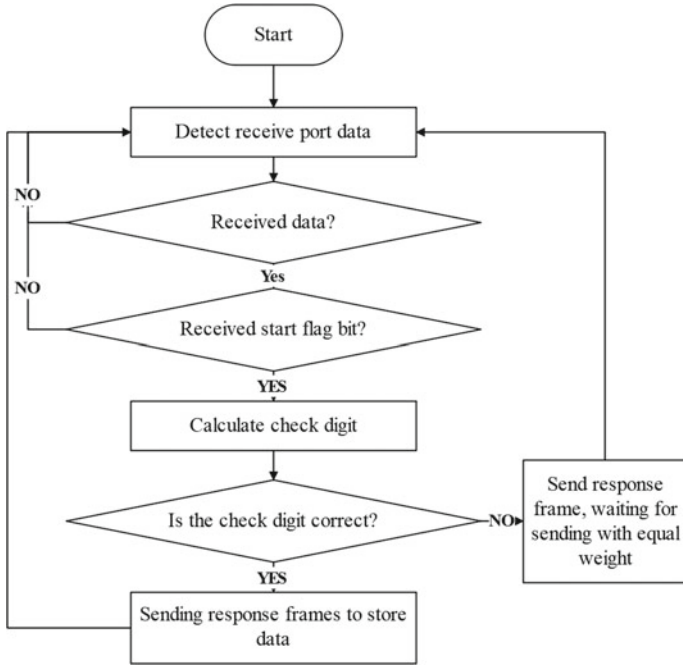
Fig. 24.5 Data transmission

$$A = \left.\frac{V_1}{V_2}\right|_{I_2=0} \quad B = \left.\frac{V_1}{I_2}\right|_{V_2=0}$$
$$C = \left.\frac{I_1}{V_2}\right|_{I_2=0} \quad D = \left.\frac{I_1}{I_2}\right|_{V_2=0} \tag{24.2}$$

In order to express (V_2, I_2) as a function of (V_1, I_1), the ABCD matrix in Eq. (24.2) is inverted to obtain:

$$\begin{vmatrix} V_2 \\ I_2 \end{vmatrix} = \begin{vmatrix} A & B \\ C & D \end{vmatrix}^{-1} \begin{vmatrix} V_1 \\ I_1 \end{vmatrix} = \frac{1}{AD - BC} \begin{vmatrix} D & B \\ C & A \end{vmatrix} \begin{vmatrix} V_1 \\ I_1 \end{vmatrix} = T_b \begin{vmatrix} V_1 \\ I_1 \end{vmatrix} \tag{24.3}$$

Equation (24.1) is called the forward transfer matrix, and Eq. (24.3) is called the reverse transfer matrix T_b.

Figure 24.6 shows a given two-port network. From the figure, the expressions of power supply voltage V_s, load voltage shift V_2 and input impedance Z_{in} in the two-port network can be obtained respectively, which are as follows:

$$Vs = V_1 + I_1 Z_s$$
$$V_2 = I_2 Z_L$$
$$Z_{in}(f) = \frac{AZ_L + B}{CZ_L + D} \tag{24.4}$$

Fig. 24.6 A two-port network
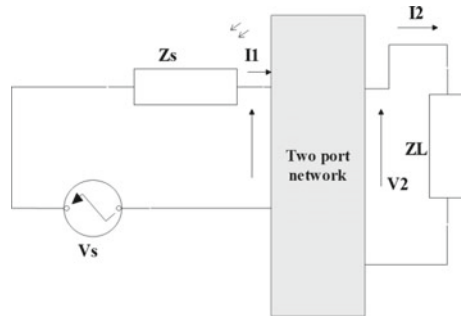
According to the definition of transfer function, the ratio of load voltage to power supply voltage at the receiving end is the channel transfer function of the whole power line, and its expression can be deduced according to ABCD matrix:

$$H(f) = \frac{V_2}{V_s} = \frac{Z_L}{AZ_L + B + CZ_sZ_L + DZ_s} \tag{24.5}$$

24.3 Test Experiment

In this paper, OPENTModel14.5 simulation software on Windows platform is used. CoAP messages are generated by each child node STA and transmitted regularly to the central server CCO in the topology through the proxy node PCO. In order to simulate different network links and generate different levels of network traffic, the simulation parameters are set in Table 24.1.

The same transmission time interval T = 10S is selected, and the change of transmission success rate with the number of nodes N is observed, and the statistical table of transmission success rate shown in Fig. 24.7 is obtained.

Table 24.1 Simulation parameter settings

Parameter	Numerical value
Simulation scenario/m2	100×500
Number of nodes/pieces	[50,100,150,200,250]
Node communication distance/m	100
Link bandwidth Kbp/s	50
Data transmission interval	[2,5,10,15,20,25,30]
Contract size/B	64
Simulation time/s	100
Simulated random SEED value	[64,128,256,512,1024]
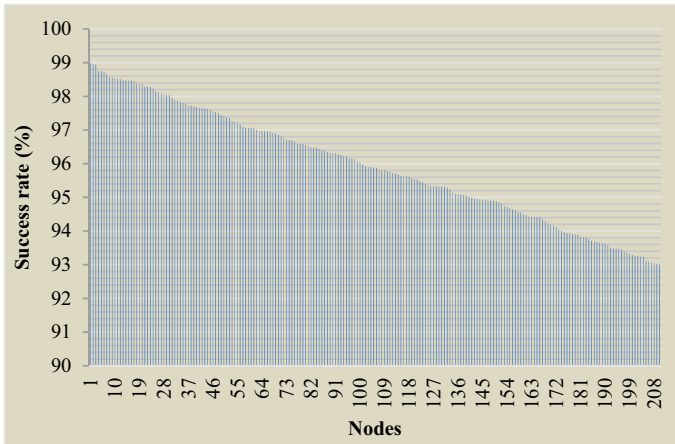
Fig. 24.7 Comparison of packet transmission success rate with different node numbers

As can be seen from Fig. 24.7, the congestion control mechanism estimated by the shared terminal system of power Internet of Things based on power carrier communication technology realizes adaptive estimation, avoids unstable changes of the system, reduces unnecessary retransmission in the network, and ensures high request success rate of the network.

According to the statistics of the data in this article, it can be seen that the average success rate of packet transmission in different node numbers reaches 95.92%. Under the same conditions, a comparison of the methods in reference [5] shows that the average success rate of packet transmission in different node numbers is only less than 80%, indicating that the method in this article has certain advantages.

24.4 Conclusion

With the development of smart grid, a large number of distributed energy devices are accessed, communication terminals are evolving to intelligence, and the emerging services in distribution network and the communication needs in stations and users' homes are increasing. However, the traditional distribution network cannot meet the requirements of reliability and efficiency under the new business. To solve this problem, power line carrier technology for distribution Internet of Things is a good way to solve this problem. This paper introduces the design and control of carrier communication module from two aspects of hardware and software. Each device is integrated with the electric carrier communication module using electric field line as the internal Internet for communication device control and information sharing. Aiming at the communication requirements of the scene of distribution Internet of Things and the differentiation of power grid operation and maintenance and extended

services, this paper constructs a power line carrier communication model integrating the hierarchical network topology from transformers in the station area to users and families. Through the experimental results, we can see that the power Internet of Things shared terminal system based on the power carrier communication technology proposed in this paper has a good effect.

The wireless channel characteristic identification was not originally carried out and was replaced by a universal channel model. Subsequent research work will improve the channel transmission characteristic identification method and apply it to the identification of wireless channel transmission characteristics, and fuse communication based on the actual channel state of the power line and wireless channel.

References

1. Yao, Y., Sun, P., Liu, X., et al.: Simultaneous wireless power and data transfer: a comprehensive review. IEEE Trans. Power Electron. **37**(3), 3650–3667 (2021)
2. Toro, U.S., Wu, K., Leung, V.C.M.: Backscatter wireless communications and sensing in green internet of things. IEEE Trans. Green Commun. Netw. **6**(1), 37–55 (2021)
3. Abdu, T.S., Kisseleff, S., Lagunas, E., et al.: Flexible resource optimization for GEO multibeam satellite communication system. IEEE Trans. Wireless Commun. **20**(12), 7888–7902 (2021)
4. Karimi, M.J., Schmid, A., Dehollain, C.: Wireless power and data transmission for implanted devices via inductive links: a systematic review. IEEE Sens. J. **21**(6), 7145–7161 (2021)
5. Wang, Y., Yan, S., Yang, W., et al.: Energy-efficient covert communications for bistatic backscatter systems. IEEE Trans. Veh. Technol. **70**(3), 2906–2911 (2021)
6. Yu, D., Li, K., Yu, S., et al.: A novel power and signal composite modulation approach to power-line data communication for SRM in distributed power grids. IEEE Trans. Power Electron. **36**(9), 10436–10446 (2021)
7. Zhang, L., Chen, M.Z., Tang, W., et al.: A wireless communication scheme based on space- and frequency-division multiplexing using digital metasurfaces. Nat. Electron. **4**(3), 218–227 (2021)
8. Hayati, M., Kalbkhani, H., Shayesteh, M.G.: Energy-efficient relay selection and power allocation for multi-source multicast network-coded D2D communications. AEU-Int. J. Electron. Commun. **128**, 153522 (2021)
9. Salgals, T., Alnis, J., Murnieks, R., et al.: Demonstration of a fiber optical communication system employing a silica microsphere-based OFC source. Opt. Express **29**(7), 10903–10913 (2021)
10. Tang, X., Cao, C., Wang, Y. et al.: Computing power network: the architecture of convergence of computing and networking towards 6G requirement. China Commun. **18**(2), 175–185 (2021)
11. Chen, Z., Han, C., Wu, Y., et al.: Terahertz wireless communications for 2030 and beyond: a cutting-edge frontier. IEEE Commun. Mag. **59**(11), 66–72 (2021)
12. Wang, H., Asbeck, P.M., Fager, C.: Millimeter-wave power amplifier integrated circuits for high dynamic range signals. IEEE J. Microw. **1**(1), 299–316 (2021)

Chapter 25
An Image-Content-Based Adaptive Tile Partitioning Algorithm

Weiye Jin

Abstract In this paper, an adaptive segmentation algorithm based on image content is proposed, which aims to reduce the encoding loss generated by the process of utilizing the new feature tile in the video coding standard. The algorithm analyzes the regional correlation of the current frame before the encoder performs the current frame encoding, so as to determine the critical area of the correlation change in the frame, divide the tile in the critical area, and ensure that the area with high correlation is not divided by the tile as much as possible. Experimental results show that compared with the case of uniform division of Tile, the proposed algorithm has improved performance.

25.1 Introduction

The establishment of video encoding standards has always been of significant research importance. Nowadays, with the continuous growth in video consumption, the field of video encoding is making persistent efforts to meet the demand for higher resolution, diverse types of videos, and superior quality video application services.

In response to various needs in the video application process, the international video coding standards representing the world's most advanced video encoding technologies began to be established in the 1980s [1]. The two major organizations internationally responsible for setting video encoding standards are the Telecommunication Standardization Sector of the International Telecommunications Union (ITU-T) [2] and the International Organization for Standardization/International Electrotechnical Commission (ISO/IEC). Among them, the coding standards set by ITU-T are the H.26X series, mainly widely applied to video communication in network transmissions like online meetings [3]. In 2003, ISO-IEC and ITU-T jointly developed the H.264/Advanced Video Coding (AVC) [4], and in 2013 they collaborated to

W. Jin (✉)

Microelectronics Research and Development Center, Shanghai University, Shanghai 200444, China

e-mail: 771468917@qq.com

develop the predecessor, H.265/High Efficiency Video Coding (HEVC) [5]. From April 2018 onwards, the Joint Video Experts Team (JVET) began working on the new-generation international video coding standard H.266/Versatile Video Coding (VVC) [6, 7], which was finalized at the end of 2020.

Initially, many private companies also researched their video coding formats, such as the VP8 encoding standard developed by On2 Technologies and acquired by Google in 2009 [8]. Later, Google developed VP9 based on VP8 and completed it in mid-2013. Subsequent improvements aimed at enhancing coding performance led to the proposal of VP10, but its development was halted after some time.

With the growing and diversifying demand for efficient video applications, by 2015, several video on-demand providers and web browser industry companies jointly established AOM. The aim was to develop an open-source, royalty-free next-generation video coding format called AV1. AV1 released its initial version in April 2016 and planned to finalize the ultimate version by mid-2018[8]. Until now, AV1 has occupied a significant portion of the market, as shown in Fig. 25.1. The development goal of AV1 is to ensure high-quality real-time transmission, support devices under various bandwidth conditions, and be reasonably complex for both commercial and non-commercial content, offering a significant performance boost compared to VP9 [9]. The AV1 codec was solidified through consolidating VP9, Daala, and Thor codecs and proposing, testing, and discussing coding tools and functionalities on top of them [9]. The reference software platform for AV1 is libaom, developed in a public repository and disclosing the source code of libaom and related reference information [10]. By early 2018, the design of AV1 coding tools was largely complete, and the reference software platform libaom primarily focused on product application preparation, including but not limited to the design of related optimization algorithms such as early termination to accelerate the codec. Currently, codecs other than libaom are still in the implementation process and may be released later [11].

The primary goal of HEVC is to double the encoding efficiency of H.264/AVC by reducing the bit rate by 50% without compromising video quality. Given that HEVC has inherited several encoding tools from the prior H.264/AVC standard, any gains in coding efficiency are possibly attributed to improvements in these inherited coding tools combined with a new set of coding tools. This results in a very high computational cost. In the H.264/AVC standard, parallelism was explored using Slices; however, Slices require the insertion of additional frame headers along the

Fig. 25.1 Market share proportions
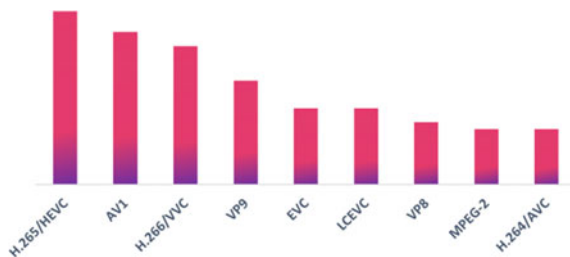
bitstream, leading to unnecessary bitstream overhead. Nevertheless, HEVC introduced a new parallel tool—Tile—to reduce encoding losses. On ultra-high-definition videos, AV1's average encoding efficiency is 30% higher than HEVC/H.265, and it similarly introduces Tiles to mitigate the increase in computational complexity.

Tiles create rectangular partitions in images by defining horizontal and vertical boundaries, utilizing image content better to reduce encoding efficiency losses. These partitions can be uniformly or non-uniformly spaced. In uniform division, the number of Coding Tree Units (CTUs) within a partition is evenly distributed by the encoder. In non-uniform tiles, users can freely set an integer number of CTUs for each tile partition. To support parallelism, Tile breaks dependencies across its boundaries, allowing it to be processed independently. If Tile boundaries partition highly correlated image areas, the decoding loss will be greater. This is because some decoding tools refine based on previously encoded CTUs. By splitting such highly correlated areas, all refinements are discarded, impairing encoding efficiency. Some work exists in the H.264/AVC standard about parallelizing with Slices. In literature [12], the authors improved encoding efficiency by using predictive reference between different Slices but compromised the use of parallel Slices. Since the open-source HEVC/H.265 encoder protocol only supports uniform Tile division, authors in literature [13] only studied the changes in coding efficiency compared to uniform Tile partitioning and other partition structures. However, considering only uniform partitioning leads to significant encoding efficiency losses. In literature [14], the authors proposed a content-based Tile partitioning algorithm, which reduced encoding losses resulting from using Tiles by leveraging video attributes during the Tile partitioning process. In literature [15], the authors introduced an efficient HEVC/H.265 decoder parallelization adaptive Tile division algorithm. By effectively balancing the workload of different Tiles in the kernel, it improved both decoding performance and video quality. In literature [16], the authors presented an algorithm for adaptive Tile division based on CTU encoding time (Time-based Tile Load Balancing, TTLB), which shortened the encoding time. However, it yielded significant gains only for sequences moving in specific frames and was less pronounced for sequences moving throughout the frame.

In summary, various encoders have some issues when using parallelism tools like Slice/Tile. Considering the encoding performance of the AV1 encoder surpasses that of HEVC, this paper selects the AV1 encoder for research. Addressing these issues, we propose an adaptive algorithm that defines Tile parameters based on image attribute features (variance), allowing for the dynamic selection of appropriate Tile partitions to cluster highly correlated image samples. In doing so, we reduce the impact on encoding efficiency brought about by using Tiles, enhancing the encoding performance of the AV1 video standard.
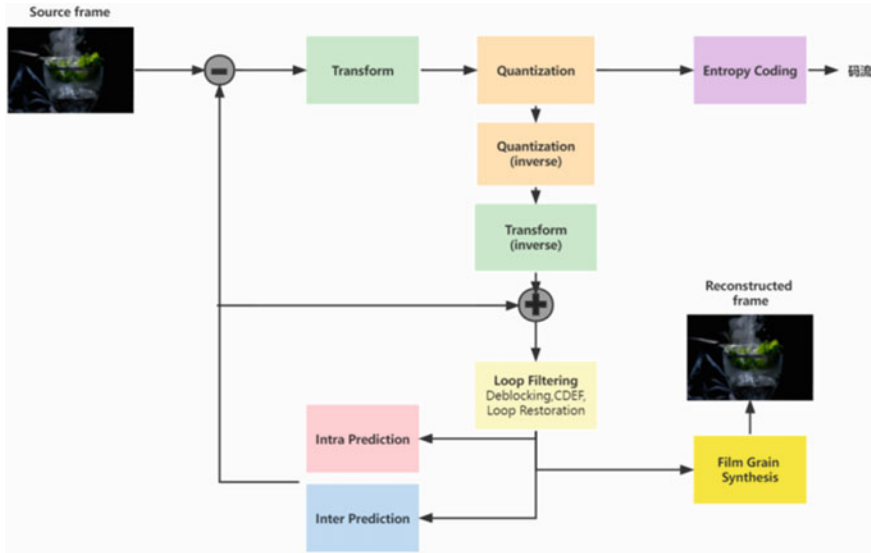
Fig. 25.2 AV1 encoder and decoder framework

25.2 Background Knowledge

The encoding framework used by AV1 is shown in Fig. 25.2. First, each frame in the video is divided into multiple coding blocks. Then, the encoding process is sequentially completed through modules such as prediction, transformation, quantization, entropy coding, and filtering.

The AV1 standard's encoding tools can encode images into Tiles made up of multiple SuperBlocks. All intra-frame prediction references and probability model updates within the Tile are confined to the Tile itself. As defined by encoding parameters, Tiles can be uniform or non-uniform. They can be encoded and decoded independently, and each Tile can be encoded and decoded in any order without affecting one another, demonstrating good parallelism.

25.3 Tile Partitioning Scheme Based on Frame Inherent Statistical Data

(1) Analysis of Intra-Frame Prediction Correlation in Data Compression:

After pixel blocks undergo predictive compression encoding, the original pixel values are transformed into residuals through calculations with the predicted values, achieving the removal of spatial redundancy. The residual is then used for further compression. The reason for using prediction errors as the object for subsequent

processing, and the ability of spatial redundancy to be removed through predictive coding, is due to numerous experimental conclusions indicating that there is a very strong correlation between neighboring pixels in the same image. That is, the pixel values between adjacent pixels are very similar, and the possibility of a sudden change in pixel values between adjacent pixels is very small. This means that the residuals between adjacent pixels are very small values, or even 0, allowing for the transmission of the same information with fewer bits.

From an information theory perspective, because the distribution of errors is concentrated, only a small area is distributed with most of the errors, while the vast majority of error areas are around 0. This means that the entropy values of the source symbols in those large error areas are relatively small. Without predictive coding, the distribution of the original pixels would be more uniform, resulting in a higher entropy value. Thus, the process of predictive coding is essentially a transformation from a high entropy value to a lower one, facilitating subsequent encoding.

(2)   Proposed Algorithm:

Intra-frame prediction is an essential component of the AV1 video standard. The basic idea is to use the correlation of neighboring pixels within a frame to eliminate spatial redundancy. However, the use of Tiles can interrupt this dependency, leading to a loss in encoding efficiency. If the boundaries of the Tiles happen to partition highly correlated image areas, the encoding loss will be even more severe. To reduce these encoding losses, Tile division based on frame complexity can be defined, seeking the intersection of highly correlated image areas and dividing areas with different attributes.

By analyzing the image attributes based on the original video frame, the highly correlated areas of the image can be deduced. The variance data of all SuperBlocks in the original frame of the 1080p video sequence, Aspen, is shown in Table 25.1. These areas can be located by analyzing abrupt changes in variance, indicating that effective prediction hasn't been applied in that area. Since intra-frame prediction uses spatial redundancy, when there's a change in variance (spatial attributes), the intra-frame prediction will also change accordingly.

Based on the aforementioned analysis, we propose an adaptive Tile partitioning algorithm based on the correlation of the current frame's regions, utilizing image information to define the Tile partitions for each encoded frame. The variance map of the image can be used as an input parameter, thereby pinpointing the highly correlated areas in each image. This ensures that during partitioning, areas with correlation are not split apart, which would result in encoding losses. The detailed algorithm flowchart is shown in Fig. 25.3.

Table 25.1 Variance values of superblocks in the aspen video sequence

No	1	2	3	4	5	6	7	8	9
1	193.4	86.0	115.3	296.5	174.9	591.9	42.6	38.1	15.8
2	642.0	453.9	54.4	26.6	609.8	480.2	130.7	1.5	1.5
3	565.4	504.1	162.9	12.6	856.4	97.1	138.4	305.8	452.9
4	151.0	448.4	265.1	438.0	208.7	230.4	164.8	251.7	301.0
5	12.9	2.5	99.8	337.9	54.1	127.7	108.4	93.2	394.4
6	11.6	1.5	2.1	311.3	91.6	53.5	85.5	186.5	396.9
7	11.3	1.6	1.6	98.4	266.7	119.4	179.1	806.3	261.2
8	11.4	1.9	2.0	1.7	113.8	328.5	128.9	27.3	795.4
9	58.4	120.1	257.0	276.0	226.9	180.4	97.4	122.6	40.0
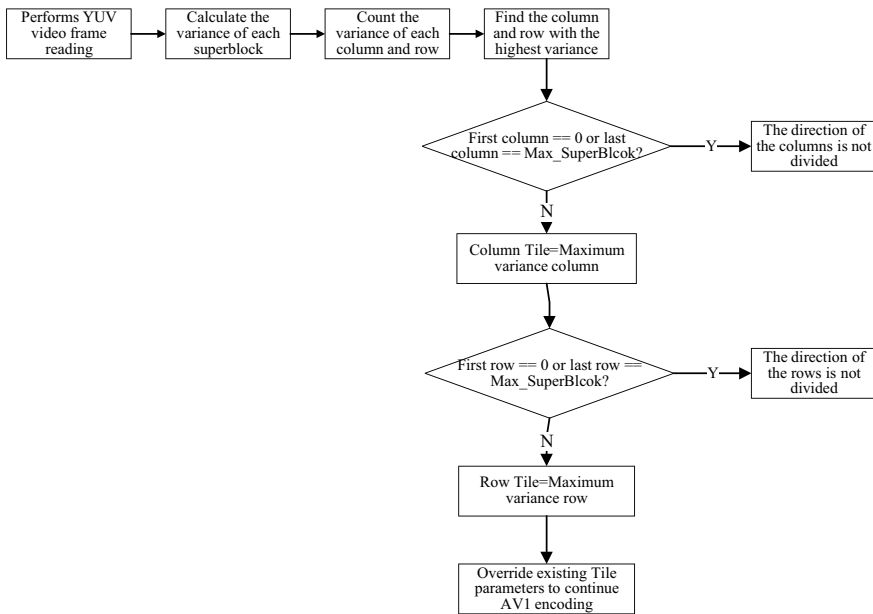
Fig. 25.3 Algorithm flowchart

This algorithm consists of two independent phases: the first phase acquires the coordinates of the vertical boundaries, and the second phase obtains the coordinates of the horizontal boundaries. In the first step of the first phase, the variance of each SuperBlock needs to be calculated, generating a two-dimensional variance matrix for the current frame using SuperBlock as the unit. Subsequently, the variance of each row of the matrix is summed up, forming a row variance sum. From this, the row with the largest variance sum is selected. It can be determined that the current row has the highest degree of non-correlation and is suitable to be used as the Tile

partition boundary. This approach mitigates the impact on image continuity caused by Tile partitioning, thereby minimizing the effect on quality. The variance matrix of the current frame with SuperBlock as the unit, the variance matrix of the current frame with SuperBlock rows as the unit, and the variance matrix of the current frame with SuperBlock columns as the unit are represented by formulas (25.1), (25.2), and (25.3), respectively. Among them, VarMtx represents the variance matrix, i and j represent the number of rows and columns of the matrix, SpBlk is the abbreviation of SuperBlock, $\text{VarMtx}_{\text{RowSum}}$ represents the row variance matrix, and $\text{VarMtx}_{\text{RowSum}}$ represents the column variance matrix. The SuperBlock row and SuperBlock column with the largest variance selected from the variance matrices of formulas (25.2) and (25.3) are represented by formulas (25.4) and (25.5), respectively. $\text{Selected}_{\text{Row}}$ and $\text{Selected}_{\text{column}}$ are the calculated rows and columns respectively.

$$
\text{VarMtx}_{i,j} = \begin{pmatrix} \delta^2(\text{SpBlk}_{0,0}) & \cdots & \delta^2(\text{SpBlk}_{0,\text{width\_in\_sb}}) \\ \vdots & \ddots & \vdots \\ \delta^2(\text{SpBlk}_{\text{height\_in\_sb},0}) & \cdots & \delta^2(\text{SpBlk}_{\text{height\_in\_sb},\text{width\_in\_sb}}) \end{pmatrix} \quad (25.1)
$$

$$
\text{VarMtx}_{\text{RowSum}} = \begin{vmatrix} \sum_{i=0}^{\text{width\_in\_sb}} \delta^2(\text{SpBlk}_{0,i}) \\ \sum_{i=0}^{\text{width\_in\_sb}} \delta^2(\text{SpBlk}_{1,i}) \\ \vdots \\ \sum_{i=0}^{\text{width\_in\_sb}} \delta^2(\text{SpBlk}_{\text{width\_in\_sb},i}) \end{vmatrix} \quad (25.2)
$$

$$
\text{VarMtx}_{\text{clmSum}} = \\ \left| \sum_{j=0}^{\text{height\_in\_sb}} \delta^2(\text{SpBlk}_{j,0}), \cdots, \sum_{j=0}^{\text{height\_in\_sb}} \delta^2(\text{SpBlk}_{j,\text{height\_in\_sb}}) \right| \quad (25.3)
$$

$$
\text{Selected}_{\text{Row}} = \text{Max}(\text{VarMtx}_{\text{RowSum}_0}, \text{VarMtx}_{\text{RowSum}_1}, \ldots, \text{VarMtx}_{\text{RowSum}_{\text{width\_in\_sb}}}) \quad (25.4)
$$

$$
\text{Selected}_{\text{column}} = \text{Max}(\text{VarMtx}_{\text{clmSum}_0}, \text{VarMtx}_{\text{clmSum}_1}, \ldots, \text{VarMtx}_{\text{clmSum}_{\text{height\_in\_sb}}}) \quad (25.5)
$$

The Tile partitioning in the vertical direction is (0, SelectedRow) and (SelectedRow + 1, width_in_sb). In the horizontal direction, the partitioning is (0, Selectedcolumn) and (Selectedcolumn + 1, height_in_sb).

25.4 Experiment

(1) Experimental Setup:

To validate the efficacy of the method proposed in this section, the algorithm was integrated into the reference software of the AV1 video encoding standard, libaom3.0. The testing conditions utilized six common 1080p test sequences: Aspen, Blue_sky, BasketballDrive, BQTerrace, Cactus, and MarketPlace. The QP test points selected were: 22, 27, 32, and 37.

When evaluating the performance of video codecs, the Rate-PSNR curve is typically used. Here, "Rate" represents the bitrate of the video, and PSNR (Peak Signal Noise Ratio) represents the peak signal-to-noise ratio between the encoded reconstructed video and the original video. The calculation method for it is shown in formula (25.6), MAXI represents the maximum value of the image point color while MSE represents the mean square error. The Rate-PSNR curve is also known as the R-D curve, which stands for Rate-Distortion. The BD-rate metric is a performance parameter derived from the R-D curve [17], indicating the variations in bitrate and PSNR of the video encoded by the new algorithm relative to the original one. When encoding video, a lower bitrate indicates greater compression, while a higher PSNR indicates better objective quality. Hence, for a coding algorithm, if the compressed video bitrate is reduced and the PSNR value is increased, the algorithm exhibits good performance. However, typical video coding algorithms will lead to a quality loss while increasing compression, i.e., as the bitrate decreases, the PSNR value may also decrease simultaneously. In such cases, the BD-rate is employed for assessment.

$$\text{PSNR} = 10 \cdot \log_{10}\left(\frac{\text{MAX}_\text{I}^2}{\text{MSE}}\right) = 20 \cdot \log_{10}\left(\frac{\text{MAX}_\text{I}}{\sqrt{\text{MSE}}}\right) \tag{25.6}$$
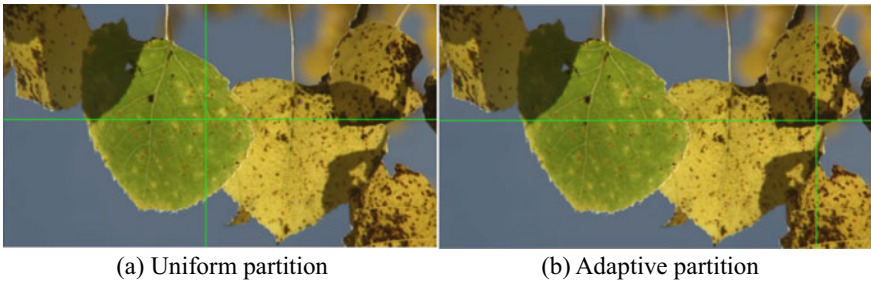
(2) Experimental Results:

Table 25.2 presents the specific scenarios and BD-rate improvements for the 6 test sequences using both uniform Tile partitioning and our adaptive Tile partitioning algorithm. Considering the differences in video sequences, using uniform partitioning leads to significant encoding efficiency losses. The partitioning situation of uniform Tile and adaptive Tile for one of the video sequences, Aspen, is illustrated in Fig. 25.4, where the green solid line indicates the Tile partition.

From Fig. 25.4a, it can be observed that for the uniform partitioning case, the image content complexity is not taken into account. Partitioning of the frame into Tiles is done uniformly solely based on user settings. Horizontally, there are a total of 15 SuperBlocks, and it's set such that after the first 7 SuperBlocks from the left, there's a vertical boundary for Tile partitioning. Vertically, there are 9 SuperBlocks, and after the first 4 SuperBlocks from the top, there's a horizontal boundary for Tile partitioning. Both the vertical and horizontal boundaries together partition the image into 4 Tiles. Figure 25.4b illustrates the scenario after adaptive Tile partitioning,

Table 25.2 BD-rate improvement with adaptive partitioning

Stream	Uniform tile partitioning	Adaptive tile partitioning	BD-rate improvement (%)
Aspen	Horizontal 7/8 Vertical 4/5	Horizontal 13/2 Vertical 4/5	1.08
Blue_sky	Horizontal 7/8 Vertical 4/5	Horizontal 3/12 Vertical 1/8	1.76
BasketballDrive	Horizontal 7/8 Vertical 4/5	Horizontal 2/13 Vertical 1/8	0.60
BQTerras	Horizontal 7/8 Vertical 4/5	Horizontal 11/4 Vertical 5/4	0.17
Cactus	Horizontal 7/8 Vertical 4/5	Horizontal 11/4 Vertical 5/4	0.26
MarketPlace	Horizontal 7/8 Vertical 4/5	Horizontal 5/10 Vertical 1/8	1.31

(a) Uniform partition   (b) Adaptive partition

Fig. 25.4 Illustration of tile partitioning

where the horizontal direction is divided into a combination of 13 and 2 SuperBlocks, with the vertical direction remaining unchanged.

Table 25.3 presents the PSNR and Bitrate values for the 6 test sequences using both uniform Tile partitioning and our adaptive Tile partitioning algorithm, the quality control parameter QP selection points are 22, 27, 32, and 37 (QP test points are usually selected in this way in the general test environment of coding and decoding standards).

Table 25.3 Experimental results (PSNR is based on the average of Y, U, and V values, unit in dB; Bitrate is in kbps)

Stream	Quality control parameters	Original PSNR	Adaptive tile partitioning PSNR	Original bitrate	Adaptive tile partitioning bitrate
Aspen	Q22	42.337	42.341	1409.8	1407.0
	Q27	42.902	42.898	1944.4	1952.5
	Q32	43.356	43.381	2736.6	2683.3
	Q37	43.921	43.908	4281.3	4258.4
Blue_sky	Q22	42.087	42.096	2230.1	2114.3
	Q27	42.953	42.960	2789.9	2773.8
	Q32	43.691	43.705	3633.1	3591.9
	Q37	44.254	44.275	4633.2	4597.5
BasketballDrive	Q22	39.120	39.114	2719.5	2692.1
	Q27	39.701	39.703	3706.2	3684.6
	Q32	40.202	40.203	5168.0	5146.5
	Q37	40.675	40.676	7584.7	7540.7
BQTerras	Q22	36.715	36.726	2616.8	2628.6
	Q27	37.241	37.246	3835.0	3847.8
	Q32	37.900	37.903	7056.7	7067.0
	Q37	39.113	39.096	16,275.1	16,148.2
Cactus	Q22	37.849	37.847	3072.1	3068.1
	Q27	38.397	38.401	4126.5	4123.1
	Q32	38.845	38.846	5587.0	5564.6
	Q37	39.261	39.259	8029.6	7978.8
MarketPlace	Q22	39.722	39.710	2163.3	2151.1
	Q27	40.220	40.237	2895.1	2857.4
	Q32	40.703	40.710	3856.7	3841.9
	Q37	41.063	41.068	5241.5	5223.9

25.5   Conclusion

This paper proposes an algorithm for adaptive Tile partitioning based on the complexity of the current frame, thereby achieving the effect of reducing encoding efficiency loss. The algorithm utilizes the image variance map to cluster highly correlated regions into the same Tile. Results indicate that compared to the situation where uniform partitioning is directly applied without considering image content, the proposed algorithm can achieve a BD-rate improvement of up to 1.76%. Along this research direction, there are still some issues that need to be resolved for this research. In order to enhance the accuracy of the complexity model, the influence of various encoding factors should be considered, and how to achieve a more effective

trade-off between decoding performance and video quality should be thought about. These are things we are considering for future work.

References

1. Wan, S., Yang, F. Z.: Next-Generation Efficient Video Coding H.265/HEVC. Electronic Industry Press (2014)
2. Wu, C. Y.: The application of video coding and decoding technology in the security industry. China Secur. (7), 7 (2022)
3. Ghanbari M.: Video coding for low bit rate communications (H.263). IET Digital Library (2003)
4. Bi, H.J.: Next-Generation Video Compression Coding Standard: H.264/AVC. People's Posts and Telecommunications Press (2005)
5. Yu, H., Wang, W., Ma, Z., et al.: Palette mode in high efficiency video coding (HEVC) screen content coding (SCC): U.S. Patent 10,038,908 (2018)
6. Zouidi, N., Belghith, F., Kessentini, A., et al.: Complexity reduction of versatile video coding standard: a deep learning approach. J. Electron. Imaging **30**(2), 023002–023002 (2021)
7. Choi, K.: A Study on fast and low-complexity algorithms for versatile video coding. Sensors **22**(22), 8990 (2022)
8. Grois, D., Nguyen, T., et al.: Coding efficiency comparison of AV1/VP9, H.265/MPEG-HEVC, and H.264/MPEG-AVC encoders. In: 2016 Picture Coding Symposium (PCS). IEEE, pp.1–5 (2016)
9. Chen, Y., Murherjee, D., Han, J, et al.: An overview of core coding tools in the AV1 video codec. In: 2018 Picture Coding Symposium (PCS). IEEE, pp. 41–45 (2018)
10. Zhang, M. L.: Research on AV1 Intra-Frame Inter-Prediction Coding Algorithm. Xi'an University of Electronic Science and Technology (2021)
11. Mukherjee, D., Han, J., Yue, C., et al.: Novel inter and intra prediction tools under consideration for the emerging AV1 video codec. In: Applications of Digital Image Processing XL. SPIE, 10396, 54–66 (2017)
12. Franche, J. F., Coulombe, S.: A multi-frame and multi-slice H.264 parallel video encoding approach with simultaneous encoding of prediction frames. In: 2012 2nd International Conference on Consumer Electronics, Communications and Networks (CECNet). IEEE, pp. 3034–3038 (2012)
13. Chi, C.C., Alvarez-Mesa, M., Juurlink, B., et al.: Parallel scalability and efficiency of HEVC parallelization approaches. IEEE Trans. Circuits Syst. Video Technol. **22**(12), 1827–1838 (2012)
14. Blumenberg, C., Palomino, D., Bampi, S., et al.: Adaptive content-based tile partitioning algorithm for the HEVC standard. In: 2013 Picture Coding Symposium (PCS). IEEE, pp. 185–188 (2013)
15. Baik, H., Song, H.: A complexity-based adaptive tile partitioning algorithm for HEVC decoder parallelization. In: 2015 IEEE International Conference on Image Processing (ICIP). IEEE, pp.4298–4302 (2015)
16. Koziri, M., Papadopoulos, P.K., Tziritas, N., et al.: Adaptive tile parallelization for fast video encoding in HEVC. In: 2016 IEEE International Conference on Internet of Things (iThings) and IEEE Green Computing and Communications (GreenCom) and IEEE Cyber, Physical and Social Computing (CPSCom) and IEEE Smart Data (SmartData). IEEE, pp. 738–743 (2016)
17. Bjontegaard, G.: Calculation of average PSNR differences between RD-curves. ITU SG16 Doc. VCEG-M33 (2001)

Author Index